UNIVERSITY OF CALIFORNIA SAN DIEGO

Investigating the impacts of aerosol sources upon coastal clouds

A dissertation submitted in partial satisfaction of the requirements for the degree Doctor of Philosophy

in

Chemistry

by

Gavin Christopher Cornwell

Committee in charge:

Professor Kimberly Prather, Chair
Professor Rommie Amaro
Professor Andrew Martin
Professor Joel Norris
Professor Robert Pomeroy
Professor Wei Xiong

2019

The Dissertation of Gavin Christopher Cornwell is approved, and it is acceptable in quality and form for publication on microfilm and electronically:

_____

_____

_____

_____

_____

_____

Chair

University of California San Diego

2019

DEDICATION

To my wonderful family, Aileen, Tim, and Zoë, for their love and support in this and all endeavors.

TABLE OF CONTENTS

LIST OF ABBREVIATIONS AND SYMBOLS

A	particle surface area
AA	ammonium to amine ratio
AAE	aerosol angstrom exponent
AIDA	Aerosol Interaction and Dynamics in the Atmosphere facility
AIS	automated ice spectrometer
AMB	ambient
APC	aerosol preparation chamber
APS	aerodynamic particle sizer
ARO	atmospheric river observatory
ARs	atmospheric river
ART-2A	adaptive resonance theory, version 2a
ASD	Argentinian soil dust
ATD	Arizona test dust
ATOFMS	aerosol time-of-flight mass spectrometer
A-ATOFMS	aircraft aerosol time-of-flight mass spectrometer
BAM	beta attenuation monitor
BC	black carbon
BB	Biomass burning
BBY	Bodega Bay, California
Bio	biological
BML	Bodega Marine Laboratory
BSD	Bachli soil dust

CAM5	Community Atmospheric Model v5
CARB	California Air Resources Board
CBJ	coastal barrier jet
CCN	cloud concentration nuclei
CDNC	cloud droplet number concentration
CESM	Community Earth System Model
CF	cold front
CFDC	continuous flow diffusion chamber
CFS	Climate Forecast System
CN	condensation nuclei
CO	carbon monoxide
Cr	*C. reinhardtii*
CSU	Colorado State University
CTL	control time periods
CV	California's Central valley
Cv	*C. Vulgaris*
CZC	Cazadero
D_a	aerodynamic diameter
D_p	mobility diameter
D_p	physical diameter
Dt	*D. tertiolecta*
D_{va}	vacuum aerodynamic diameter
D_{10}	Diameter at 10^{th} percentile

D_{25}	Diameter at 25th percentile
D_{50}	Diameter at 50th percentile
EC	elemental carbon
ECOC	elemental carbon organic carbon
EF	enrichment factor
ESRL	Earth System Research Laboratory
ETH	echo top height
EVSD	Ethiopian soil dust
f_{dust}	fraction of dust
FIN-1	Fifth Ice Nucleation Workshop
f_{SSA}	fraction of sea spray aerosol
H1	hypothesis 1
H2	hypothesis 2
HMS	Hydroxymethanesulfonate
ICF	ice nucleating particle concentration factor
ICP-MS	inductively coupled plasma mass spectrometry
IN	ice nucleation
INEs	ice nucleating entities
INP(s)	ice nucleating particle(s)
INX	Illite-NX
IS	ice spectrometer
KF	K-Feldspar
KIT	Karlsruhe Institute of Technology

LLJ	lower level jet
LRT	long range transport
MAM3	Modal Aerosol Module
MART	marine aerosol reference tank
MBL	marine boundary layer
MERRA	Modern Era Retrospective Analysis for Research and Applications
MSL	meters above sea level
miniMART	miniature marine aerosol reference tank
mPGF	meteorological Petaluma gap flow
MSD	Morroccan soil dust
M18	parameterization from McCluskey et al., (2018)
NADH	nicotinamide adenine dinucleotide
nAPS	median APS number concentration
Nd:YAG	Neodymium:YAG laser
NCSU	North Carolina State University
N_{INPs}	number concentration of ice nucleating particles
NOAA	National Oceanic and Atmospheric Administration
NPS	National Park Service
n_s	ice nucleation active site density
N06	Neiman et al., 2006
N12	parameterization from Niemand et al., (2012)
N500	number of particles greater than 500 nm
OC	organic carbon

OC/EC	organic carbon to elemental carbon ratio
OPC	optical particle counter
OSL	ocean surface layer
PCVI	pumped counterflow virtual impactor
Pf	*P. fluorescens*
PGF	Petaluma gap flow
PMT(s)	photomultiplier tube(s)
PM2.5	particulate matter below 2.5 microns
Pp	*P. purpera*
Ps	*P. syringae*
PSLs	polystyrene latex spheres
P18	exponential fit of data from Price et al., (2018)
RASS	radio acoustic sounding system
RH	relative humidity
RH_w	relative humidity with respect to water
RPA	relative peak area
S16	parameterization from Steinke et al., (2016).
Sd	*S. dimorphus*
Se	*S. elongates*
SFBA	North San Francisco Bay Area
SMPS	scanning mobility particle sizer
SN	sulfate to nitrate ratio
SO	Southern Ocean

SPMS	single particle mass spectrometer
SSA	sea spray aerosol
SSML	sea surface microlayer
SS_w	supersaturation with respect to water
TBL	terrestrial boundary layer
TE	transmission efficiency
TOF	time of flight
TPII	total positive ion intensity
VOCs	volatile organic compounds
UCSD	University of California, San Diego
UTJ	upper tropospheric jet
UF-ATOFMS	ultra-fine aerosol-time-of-flight mass spectrometer
WIBS	wideband integrated bioaerosol sensor
ΔAC	albedo change
σATN	aerosol absorption coefficient

LIST OF FIGURES

LIST OF TABLES

ACKNOWLEDGEMENTS

First of all, I would like to thank Professor Kimberly Prather for her support as my graduate advisor and the chair of my committee. I have learned and grown so much during my time working for her, and I am grateful for the opportunities and resources that she has afforded me. One of the things I have really admired about Kim is her desire and push to always make the research more important and relevant, and I hope to take that drive with me throughout the rest of my career.

I would also like to thank my doctoral committee members Professor Rommie Amaro, Professor Andrew Martin, Professor Joel Norris, Professor Robert Pomeroy, and Professor Wei Xiong for their advice and feedback during my exams and graduate school tenure.

Beyond the research, working in the Prather Lab has been a pleasure due to the intelligent, curious, talented, and generally awesome people who make up the team. Their support, friendship, guidance, and hard work have helped inspire me through paper writing, exam preparations, field studies, lab experiments, and instrumental headaches. Thank you to: Hashim Al-Mashat, Dr. Jessica Axson, Charlotte Beall, Dr. Jack Cahill, Dr. Doug Collins, Dr. Louise Kristensen, Chris Lee, Dolan Lucero, Dr. Andrew Martin, Kathryn Mayer, Brock Mitts, Alexia Moore, Kathryn Moore, Matt Pendergraft, Robin Richardson, Matt Ruppel, Dr. Olivia Ryder, Mitchell Santander, Jon Sauer, Bas Schaap, Dr. Camille Sultana, Dr. Kaitlyn Suski, Kara Voss, and Dr. Xiaofei Wang. Special thanks to Joe Mayer for his calm, no-nonsense manner, his ability to solve 90% of my problems by asking me to repeat the problem, and then the remaining 10% as well, and to Monica Castrejon for her good cheer, relentless professionalism, and incredible competence at overcoming all administrative and logistical problems.

Outside of the Prather Lab, I have been fortunate to work with some truly outstanding people. My research, and scientific growth have undoubtedly been bettered through my

collaboration with them, thank you to: Dr. Paul DeMott, Dr. Tom Hill, Dr. Ezra Levin, Dr. Christina McCluskey, Dr. Gregg Schill, Dr. Natalie Mahowald, Dr. Marje Prank, Dr. Jessie Creamean, Dr. Forrest Cannon, Professor Markus Petters, Professor Sonia Kreidenweis, Sam Atwood, Dr. Nicholas Rothfuss, Hans Tayor, Professor Hari Mix, and Sean Reilly.

Finally, I would like to thank my family. My parents, Aileen and Tim, have always pushed me to be curious, open-minded, and fair. My sister Zoë has been a source of inspiration for her strength and resiliency. All of them have been incredibly patient in listening to me vent, supporting me when I needed it, and pushing me when I needed that instead. This whole process would not have been possible without their unconditional love and support. I would also like to thank my friends for keeping me (mostly) sane, and in particular I would like to thank Dan Steward, Sarah Armenta, and Dave Meyers who I have not mentioned yet.

Chapter 2, in full, is a reprint of material as it appears in Atmospheric Chemistry and Physics 2017. Martin, A. C., Cornwell, G. C., Atwood, S. A., Moore, K. A., Rothfuss, N. E., Taylor, H., DeMott, P. J., Kreidenweis, S. M., Petters, M. D., Prather, K. A. (2017). Transport of pollution to a remote coastal site during gap flow from California's interior: impacts on aerosol composition, clouds, and radiative balance. Atmospheric Chemistry and Physics 17:1491-1509. Reproduced with permission of the European Geophysical Union. Professor Andrew Martin and the dissertation author are co-first authors of this manuscript.

Chapter 3, in full, is a reprint of material that has been accepted for publication in Atmospheric Chemistry and Physics. Martin, A. C., Cornwell, G. C., Beall, C. M., Cannon, F., Reily, S., Schaap, B., Lucero, D., Creamean, J. M., Ralph, F. M., Mix, H., Prather, K. A. (2019). Contrasting Local and Long-Range Transported Warm Ice-Nucleating Particles During an

Atmospheric River in Coastal California, USA. Reproduced with permission of the European Geophysical Union.

Chapter 4, in full, is currently being prepared for submission for publication of the material. Cornwell, G. C., Sultana, C. M., Petters, M. D., Al-Mashat, H., Rothfuss, N. E., Taylor, H. P., DeMott, P. J., Martin, A. C., Kreidenweis, S. M., Prather, K. A. (2019), "Improved discrimination between dust and bioaerosol by aerosol time-of-flight mass spectrometry" Dr. Camille Sultana and the dissertation author are co-first authors of this manuscript.

Chapter 5, in full, has been submitted to *Journal of Geophysical Research: Atmospheres* for publication of the material. Cornwell, G. C., M., McCluskey, C. S., Levin, E. J. T., Suski, K. J., DeMott, P. J., Kreidenweis, S. M., Prather, K. A. (2019), "Direct on-line mass spectrometry measurements of ice nucleating particles at a California coastal site." The dissertation author is the primary investigator and author of this manuscript.

Chapter 6, in full, is currently being prepared for submission for publication of the material. Cornwell, G. C., Rothfuss, N. E., Taylor, H. P., Petters, M. D., DeMott, P. J., Prather, K. A. (2019), "Assessing contributions to ice nucleating particle concentrations at a coastal site in California using single particle mass spectrometry." The dissertation author is the primary investigator and author of this manuscript.

Chapter 7, in full, is currently being prepared for submission for publication of the material. Cornwell, G. C., Sultana, C. M., Prank, M., Cochran, R. E., Hill, T. C. J., Schill, G. P., DeMott, P. J., Mahowald, N., Prather, K. A., (2019). "Ejection of dust from the ocean as a novel source of marine ice nucleating particles." The dissertation author is the primary investigator and author of this manuscript.

VITA

2007 Bachelor of Science, University of Texas at Dallas, cum laude

2007-2009 Research associate, Kirkegaard & Perry Laboratories

2009-2013 Associate Scientist, Johns Hopkins University Applied Physics Laboratory

2013-2019 Research Assistant, University of California San Diego

2019 Doctor of Philosophy, University of California San Diego

AWARDS

Graduate Assistance in Areas of National Need (GAANN) Fellow, UCSD, 2015-2016.

School of Global Policy & Strategy (GPS) Science Policy Fellow, UCSD, 2015-2016.

PUBLICATIONS

Mix, H. T., Reilly, S. P., Martin, A., & Cornwell, G. (2019). Evaluating the Roles of Rainout and Post-Condensation Processes in a Landfalling Atmospheric River with Stable Isotopes in Precipitation and Water Vapor. *Atmosphere*, *10*(86), 1–13.

*Martin, A. C., *Cornwell, G. C., Atwood, S. A., Moore, K. A., Rothfuss N. E., Taylor H., DeMott P. J., Kreidenweis, S. M., Petters, M. D., Prather, K. A. (2017) Transport of pollution to a remote coastal site during gap flow from California's interior: impacts on aerosol composition, clouds, and radiative balance. *Atmos Chem Phys* 17(2):1491–1509.

McCluskey C. S., Hill, T. C. J., Malfatti, F., Sultana, C. M., Lee, C., Santander, M. V., Beall, C. M., Moore, K. A., Cornwell, G. C., Collins, D. B., Prather, K. A., Jayarathne, T., Stone, E. A., Azam, F., Kreidenweis, S. M., DeMott, P. J. (2017) A dynamic link between ice nucleating particles released in nascent sea spray aerosol and oceanic biological activity during two mesocosm experiments. *J Atmos Sci* (2017):*JAS*-D-16-0087.1.

Sultana CM, Cornwell GC, Rodriguez P, Prather KA (2017) FATES: a flexible analysis toolkit for the exploration of single-particle mass spectrometer data. *Atmos Meas Tech* 10(4):1323–1334.

Forestieri, SD, Cornwell, GC, Helgestad, TM, Moore, KA, Lee, C, Novak, GA, Sultana, CM, Wang, X, Bertram TH, Prather, KA, and Cappa, CD. (2016) Linking variations in sea spray aerosol particle hygroscopicity to composition during two microcosm experiments. *Atmos Chem Phys*, 16, 9003-9018.

Lee C, Sultana CM, Collins DB, Santander MV, Axson JL, Malfatti F, Cornwell GC, Grandquist JR, Deane GB, Azam F, Grassian VH, Prather KA. (2015) Advancing model systems for

fundamental laboratory studies of sea spray aerosol using the microbial loop. *J Phys Chem A* 119(33):8860–8870.

Wang X, Sultana CM, Trueblood J, Hill T.C.J., Malfatti F, Lee C, Laskina O, Moore KA, Beall CM, McCluskey CS, Cornwell GC, Zhou Y, Cox JL, Pendergraft MA, Santander MV, Bertram TH, Cappa CD, Azam F, DeMott PJ, Grassian VH, Prather KA. (2015) Microbial control of sea spray aerosol composition: a tale of two blooms. *ACS Cent Sci* 1(3):124–131.

Zhao, K., Ippolito, G, Wang, LL, Price, V, Kim, MH, Cornwell, G, Fulenchek, S, Breen, GA, Goux, WJ, D'Mello, SR. Neuron-selective toxicity of tau peptide in a cell culture model of neurodegenerative tauopathy: essential role for aggregation in neurotoxicity. *Journal of Neuroscience Research*, 88(15), 3399-3413, 2010.

*Co-first authors.

PRESENTATIONS

Cornwell, GC, Kristensen, LJ, Voss, K, Campbell, L, Al-Mashat, H, Hill, TCJ, Levin, E, Barry, K, Suski, KJ, Leung, R, Martin, AC, DeMott, PJ, Prather, KA, (2018), Long range vs marine sources of aerosols and their effects upon landfalling atmospheric rivers in California, Abstract A14C-03 presented at 2018 Fall Meeting, AGU, Washington, D.C., 10-14 Dec.

Cornwell, GC, DeMott, PJ, Hill, TCJ, Taylor, H, Petters, M, Prather, KA, (2018) Identifying marine biological particles at Bodega Bay, CA using single-particle measurements, presented at 2018 International Atmospheric Rivers Conference, La Jolla, Calif., 25-28 June.

Cornwell, GC, Sultana, CM, Schill, GP, Hill, TCJ, Cochran, RE, DeMott, PJ, Prather, KA, (2017), Resuspended dust as a novel source of marine ice-nucleating particles, Abstract A11L-06 presented at 2017 Fall Meeting, AGU, San Francisco, Calif., 11-15 Dec.

Cornwell, GC, McCluskey, CS, Levin, EJ, Suski, KJ, DeMott, PJ, Kreidenweis, SM, Prather KA, (2016), First direct on-line mass spectrometry measurements of marine ice nucleating particles, Abstract A54C-07 presented at 2016 Fall Meeting, AGU, San Francisco, Calif., 11-15 Dec.

Cornwell, GC, Martin AM, Petters M, Rothfuss, NE, Taylor H, Prather, KA, (2015), Gap-flow Mediated Transport of Pollution to a Remote Coastal Site: Effects upon Aerosol Composition, Abstract A51L-0243 presented at 2015 Fall Meeting, AGU, San Francisco, Calif., 14-18 Dec.

ABSTRACT OF THE DISSERTATION

Investigating the impacts of aerosol sources upon coastal clouds

by

Gavin Christopher Cornwell

Doctor of Philosophy in Chemistry

University of California San Diego, 2019

Professor Kimberly Prather, Chair

Aerosols can affect climate and precipitation through their ability to serve as cloud seeds. Of particular interest to this dissertation are the sources of aerosols impacting storms that cross the coast of California. Ice nucleating particles (INPs) are particles capable of triggering heterogeneous ice formation in the atmosphere. Even though they are rare, they can have an outsized effect due to their ability to trigger cloud glaciation even at low concentrations. In this dissertation, the effect of aerosol sources and microphysical properties, particularly those of INPs, upon coastal clouds are studied using a combination of lab experiments, field measurements, remote sensing, and atmospheric modeling. Measurements of ambient particles showed that specific meteorological conditions can lead to the transport of anthropogenic pollution particles to the coast of California from the Central Valley, potentially modifying properties of coastal clouds.

The role of meteorological conditions in dictating particle source during a winter storm was also investigated by analyzing precipitation samples and remote sensing of clouds. The features of single particle mass spectrometer measurements of dust and bioparticles are explored and characterized. The findings from these lab experiments are used to develop a novel decision tree for the identification of bioparticles in ambient measurements. For the first time, single particle measurements of marine and coastal INP composition were performed. The major source of INPs active at T = -30 ºC was dust, while sea spray aerosol (SSA) and bioparticles were minor sources. SSA that activated into ice crystals were found to be enriched in organics. A novel methodology was developed to estimate INP sources without using direct measurements of INPs. Bioparticles are found to dominate INPs active at T = -20 ºC. Finally, a series of experiments showed that dust can be resuspended from the ocean and still be able to nucleate ice. Aerosol transport simulations of this phenomenon showed that this process may be important for INP populations in the Southern Ocean.

Chapter 1. Introduction

1.1 Aerosols

Aerosols are liquid or solid particles suspended in the atmosphere. In addition to affecting human health and air quality, they can have a tremendous impact upon climate through their ability to directly interact with light and modify cloud properties. Atmospheric aerosols can range in diameter from 1 nm to 100 μm and are typically grouped into three size regimes: the Aitken mode (1-100 nm), the accumulation mode (100-1000 nm), and the coarse mode (>1 μm). The effects of aerosol particles on climate are highly contextual and dependent upon their size, chemical composition, morphology, and number (Seinfeld & Pandis, 2006).

1.2 Aerosol sources

Aerosols are produced from a variety of natural or anthropogenic sources, and can be directly emitted as particles into the atmosphere ("primary aerosol") or formed through the condensation of reacted gases ("secondary aerosol"). Dust is produced via mechanical erosion induced by winds and is comprised of crustal elements including but not limited to aluminum, iron, titanium, sodium, potassium, and barium (Choobari et al., 2014). Sea spray aerosol (SSA) particles are produced by the bursting of bubbles generated by breaking waves, and are a complex mixture of inorganic salts, organic compounds, and particulate species such as bacteria or viruses (Cochran et al., 2017; Lewis & Schwartz, 2004). Particles of biogenic origin such as bacteria, fungi, pollen, and viruses can be directly aerosolized into the atmosphere (Fröhlich-Nowoisky et al., 2016). Black carbon (sometimes referred to as elemental carbon) and biomass burning particles are produced by the incomplete combustion of fuel sources (Bond et al., 2013; Briggs & Long, 2016; Ni et al., 2014). Volatile organic compounds (VOCs) can be oxidized in the atmosphere and then condense into the particle phase, forming secondary organic aerosol (SOA; Altieri et al.,

2008; Montoya et al., 2017; Virtanen et al., 2010). Aerosol composition, size, and other properties can be transformed post-emission through coagulation with other particles, heterogeneous reactions with reactive species such as NOx, aqueous-phase processing in clouds, and condensation of semi-volatile gases onto the particles (Seinfeld & Pandis, 2006).

1.3 Aerosol effects on climate

Aerosols can influence climate through two mechanisms. The first is through the absorption or scattering of incoming solar radiation by aerosol particles themselves (i.e "direct effect"). The second mechanism is through the nucleation of cloud droplets and the subsequent modification of cloud properties (i.e "indirect effect"). For instance, clouds with more particle seeds (such as commonly found in polluted airmasses) have more numerous, smaller cloud droplets. Higher cloud droplet concentrations lead to an increase in back-scattered solar radiation and results in a net cooling effect, known as the "Twomey effect" (Twomey, 1974, 1977). An increase in clouds seeds and subsequent decrease in cloud droplet size also results in reduced or delayed precipitation and, and thus increased cloud lifetime, i.e. the "Albrecht effect" (Albrecht, 1989). The presence of ice nucleating particles (INPs) in clouds at temperatures amenable to heterogeneous ice nucleation (ranging from -2 to -38 °C) can cause clouds to glaciate. Ice crystals grow more quickly and efficiently compared to liquid cloud droplets which can lead to decreased cloud lifetimes because they precipitate more quickly (DeMott et al., 2010). As a result, the indirect effect is currently the greatest source of uncertainty in understanding and predicting global climate change (IPCC, 2013).

1.4 Cloud condensation nuclei

When the atmosphere becomes supersaturated with respect to water (i.e. relative humidity greater than 100%) aerosol particles can nucleate cloud droplets by providing a surface for the

water vapor to condense on to (Pruppacher & Klett, 2010). The ability of a particle to act as a cloud condensation nuclei (CCN) at a given supersaturation is a function of both its size and composition. Köhler theory was developed to describe this relationship thermodynamically (Kohler, 1936).

$$S = \left(1 - \frac{B}{D^3}\right) exp\left(\frac{A}{D}\right)$$

In which S is the supersaturation, D is the radius of the particle, and A and B are defined by the following expressions

$$A = \frac{4M_w\sigma}{RTp_w} \qquad\qquad B = \frac{3imM_w}{4\pi M_s p_w}$$

in which M_w is the molar mass of water, σ is the droplet surface tension, R is the ideal gas constant, T is the temperature, p_w is the density of water, i is the van 't Hoff factor (degree of disassociation), M_s is the molecular weight of the solute, and m_s is the mass of the solute (Seinfeld & Pandis, 2006). Kohler theory has been extended in recent years to develop a single-parameter, κ, to describe the hygroscopicity of the particle (Petters & Kreidenweis, 2007). Following this κ-Kohler theory, the supersaturation of the particle can be described as

$$S = \frac{D^3 - D_d^3}{D^3 - D_d^3(1-\kappa)} \exp\left(\frac{A}{D}\right)$$

in which D_d is the dry diameter of the particle.

1.5 Ice nucleating particles

INPs are aerosol particles that are capable of initiating heterogeneous ice crystal formation (Schaefer, 1946). Without an INP present, an ice crystal will not form at temperatures warmer than the homogeneous freezing point (approximately -38 °C). However, if an INP is present ice can form at temperatures as warm as -2 °C (Maki et al., 1974). Even though they are rare (typically in the free troposphere ~1 in 10^5 out of all aerosols are capable of acting as INPs), INPs can cause clouds to glaciate even at low concentrations and thus can have an outsized impact upon both

climate and precipitation processes (DeMott et al., 2010). The properties that cause particles to form ice crystals is still not well understood and an area of active research.

The ice nucleation active site density (n_s) concept assumes that ice formation is, to a first approximation, time-independent and elicited by specific sites on the particle surface, while the number of these sites is dependent upon either the temperature or ice supersaturation (Vali, 1971). There is a strong size bias for ice nucleation because larger particles have greater surface areas and are more likely to have an ice-active site. The n_s facilitates comparisons between different particle types by accounting for this surface area and can shed insight into the efficacy of different IN-sources. The n_s is also useful because it can be measured in lab (Niemand et al., 2012; Ullrich et al., 2017) and field experiments (McCluskey, Ovadnevaite, et al., 2018; Price et al., 2018) and extended to the simulation of INP emission and transport (Vergara-Temprado et al., 2017; Vergara-Temprado et al., 2018a; Vergara-Temprado et al., 2018b).

1.5.1 Sources of INPs

Mineral dust is thought to be the most important source of INPs globally because of its high atmospheric burden (Andreae and Rosenfeld, 2008) and because it is IN-active at temperatures cooler than -15 ºC (Atkinson et al., 2013; Boose et al., 2016; Boose et al., 2016; Murray et al., 2011; Murray et al., 2012; Niemand et al., 2012). Soil dust is emitted from agricultural fields and has demonstrated IN-activity at temperatures as warm as -6 ºC (Garcia et al., 2012). The increased IN-activity for soil dust relative to mineral dust has been attributed to internal mixing with organic matter (Hill et al., 2016; Tobo et al., 2014). Primary biological aerosol particles such as bacteria, fungi, and pollen have also proven to be potent ice nucleators at temperatures warmer than -10 ºC (Alpert et al., 2011; Huffman et al., 2013; Knopf et al. 2011; Mason et al., 2015), though the importance of these particles as INPs on the global or regional

scale is unclear due to uncertainties about their emission rates, as well as the considerable spread in IN-activity (Kanji et al., 2017). There is mixed evidence for the efficacy of biomass burning and other combustion particles serving as INPs with some studies observing activity (Levin et al., 2016; McCluskey et al., 2014; Petters et al., 2009) and some observing no activity (Schill et al., 2016; Vergara-Temprado, 2018a). Finally, while aerosol emitted from the ocean have not traditionally been considered to be a significant source of INPs, recent research has shown that elevated INP production may be associated with phytoplankton blooms (DeMott et al., 2016; McCluskey et al., 2017). This increase in IN-activity in lab studies has been attributed to the incorporation of surface-active molecules such as proteins or long-chain fatty acids (DeMott et al., 2018; McCluskey et al., 2018).

1.5.2 Measurements of INP concentrations

INP concentrations can be measured using offline or online methods. For offline methods, a sample is collected over a given period of time, either through filtering air, impacting aerosol into a liquid, or by collecting precipitation samples (Creamean et al., 2018; Hill et al., 2014; Hill et al., 2016; Petters & Wright, 2015; Wright et al., 2014). These samples are typically resuspended in water and then dispensed into small droplets which are subjected to decreasing temperatures. The number of droplets frozen can be used to calculate the INP concentration at each temperature. Due to the long collection times (often 8-12 hours), these measurements possess poor temporal resolution; however, this technique can be used to derive the entire ice nucleation activity across a range of temperatures.

In contrast, online methods can measure INP concentrations with much higher temporal resolutions. One such instrument is a continuous flow diffusion chamber (CFDC; Rogers, 1988). CFDCs measure INP concentrations by introducing a sample of air to a cold and wet chamber,

which is configured such that the temperature of the inner and outer walls can be controlled separately. Through the manipulation of the temperatures of the two walls, the temperature and supersaturation which the aerosol are subjected to can be controlled. In this environment, particles that are capable of nucleating into ice crystals (i.e. INPs) at that temperature will do so. After traversing a subsaturated region to evaporate non-frozen droplets, these nucleated ice crystals are counted by an optical particle counter (OPC). This method is capable of measuring INP concentrations with a high degree of temporal resolution, but for only one freezing temperature at a time. Offline and online measurements thus provide complementary information with their own advantages and disadvantages.

1.5.3 Measurements of INP composition

Identifying INP composition and sources is a particularly demanding analytical problem due to their rarity—1 in 10^5 out of all atmospheric particles are estimated to be able to act as INPs (DeMott et al., 2010). Some have attempted to solve this problem by correlating INP concentrations to other measurements or tracers (Huffman et al., 2013; Mason et al., 2015). Another approach is to filter the sample, subject it to heat, or some other chemical test and observe the difference in IN-activity, thus identifying particle types and/or components important to the ice nucleation process (Hill et al., 2016; Suski et al., 2018; Tobo et al., 2014). This approach can be particularly useful for identifying particles with biogenic components, as those are generally thought to be the most sensitive. Finally, some studies have attempted to isolate INPs by first nucleating them into ice crystals using in-situ measurements such as a CFDC. These ice crystals can either be impacted onto substrates for characterization via microscopy (McCluskey et al., 2018; Suski et al., 2018) or isolated using a counter-flow virtual impactor, which screens out small particles (i.e. non-activated particles), and then passed on to some other measurement technique

(Corbin et al., 2012; Cziczo et al., 2003; DeMott et al., 2003; Richardson et al., 2007). Of these approaches, the last is the most desirable because it is a direct measurement of the particle's composition.

1.6 Measuring single particle composition with ATOFMS

The aerosol time-of-flight mass spectrometer (ATOFMS) was developed to measure the size-resolved composition of individual particles in real-time (Gard et al., 1997). An aircraft-compatible ATOFMS (A-ATOFMS; (Pratt et al., 2009) has also been designed, and has been deployed to measure atmospheric aerosol and cloud residuals aloft (Cahill et al., 2012; Creamean et al., 2013; Pratt et al., 2010; Rosenfeld et al., 2014). Particles are introduced into the instrument through the inlet and then collimated and focused with either a series of skimmers or an aerodynamic lens. The focused particles are accelerated past two continuous wave lasers (532 nm) located 6 cm apart. As particles traverse the laser beam they scatter light, which is collected by ellipsoidal mirrors and focused onto photomultiplier tubes (PMTs). The signals from the PMTs are used to calculate particle velocity which can be used to determine particle size via external calibration with polystyrene latex spheres (PSLs) of known diameter. The particle velocity is also used to fire a pulsed 266 nm laser (typically operated from 1.0-1.3 mJ/pulse) to desorb and ionize particles. Both positive and negative ions are generated by each laser pulse, and these ions are extracted into a dual polarity time-of-flight (TOF) mass spectrometer, and ion signals are measured using microchannel plate detectors. For each analyzed particle, the time, size and spectra for positive and negative ions are recorded.

Methods of grouping similar particles are needed due to the size of a typical ATOFMS ambient dataset (>1,000,000 particles). For this dissertation, particle mass spectra and size data were imported into Matlab (The MathWorks, Inc.) and analyzed via the software toolkit FATES

(Sultana et al., 2017). Traditional analysis of ATOFMS datasets has been performed by clustering particles based upon their mass spectral features using an adaptive neural network (Rebotier & Prather, 2007; Song et al., 1999). Clusters are then regrouped into particle types based upon spectral studies using previous lab and field studies as references.

1.7 Aerosol-cloud-precipitation interactions

Aerosols can affect cloud properties such as droplet number, size, and phase by acting as surfaces onto which water and ice can condense. As described in section 1.3, clouds with more seeds in them (such as commonly found in polluted airmasses) have more numerous, smaller cloud droplets. Smaller more numerous droplets leads to delayed onset of precipitation because it takes longer for cloud droplets to grow to the critical size where they precipitate (Rosenfeld et al., 2008; Rosenfeld & Givati, 2006). In addition to particle number, clouds precipitation properties can vastly change due to the presence of INPs. Ice crystals grow more quickly and efficiently compared to liquid cloud droplets which can lead to decreased cloud lifetimes because they precipitate more quickly (DeMott et al., 2010). Aerosols may also affect storm dynamics through the release of latent heat and subsequent invigoration of updrafts (Altaratz et al., 2014; Fan et al., 2016; Rosenfeld et al., 2008). The sum of these effects is highly contextual and remains poorly understood.

1.7.1 Landfalling atmospheric rivers in California

Atmospheric rivers (ARs) are storms that are typified by the strong horizontal transport of water vapor (Zhu & Newell, 1998). While they are global phenomena, these storms are known to deliver copious amounts of precipitable water to the western United States. They are particularly important for California because as few as 2-3 of these storms can deliver 50% of the state's annual water budget (Dettinger et al., 2011). Thus, understanding the role that aerosols play in affecting

the amount, phase, and spatial distribution of precipitation during these storms is critically important for optimal water management (Ralph et al., 2016). Understanding how aerosol sources influence AR's led to the initiation of the CalWater field campaign in which aerosol size, number, composition, and microphysical processes were measured at a site in the Sierra Nevada during the winters of 2009-2011. Similar measurements were also collected on a series of 28 research flights in the winter of 2011. Research flights were conducted out of McClellan air base in Sacramento, CA and sampled clouds and ambient aerosol all over the state of California.

The CalWater campaigns showed that dust, transported long-range from Asia and Africa, can affect cloud phase over California, potentially increasing the amount of precipitation from ARs (Ault et al., 2011; Creamean et al., 2013). An additional "dust-biological" type was observed in the cloud and precipitation residuals, though the extent to which these particles were truly bioaerosols is not well understood. Regardless, ARs are associated with their own population of marine aerosols (Creamean et al., 2013), and will also interact with coastal and terrestrial aerosols as they proceed across the state. Thus, characterizing the sources and microphysical properties of marine and coastal aerosol in California is important for determining the sum total aerosol effect upon ARs.

1.8 Goals of dissertation

This dissertation focuses upon the sources and properties of aerosols and their impacts on clouds and precipitation. Special focus is placed on coastal systems in California to determine when and if these aerosols are being incorporated into landfalling ARs.

The main questions that will be addressed include:

1. What are the sources of aerosols impacting storms that cross the coast of California? How does particle source affect clouds and precipitation processes?

2. Which aerosols impact clouds in landfalling ARs? Are long range or local aerosols more important and how do they evolve over the course of a storm?
3. Is it possible to distinguish between dust and biological aerosols, and their mixtures, using the ATOFMS?
4. What are the major sources of ice nucleating particles in coastal CA environments? What are the relative abundances of these particles in the atmosphere and what are the factors controlling these concentrations?
5. How important are ocean-derived INPs to marine clouds?

1.9 Synopsis of dissertation

This dissertation attempts to address these questions by combined lab experiments, field measurements, remote sensing, and atmospheric modeling. Chapter 2 of this dissertation shows that specific meteorological conditions can lead to the transport of large numbers of anthropogenic pollution particles to the Californian coast. Particle number, composition, and microphysical properties were shown to be greatly affected under these conditions. The effect of these transported aerosols on cloud droplet number concentrations were modeled and the corresponding change in albedo were estimated to be 16-28%.

Chapter 3 of this dissertation investigates how meteorological conditions affect the incorporation of warm INPs (active at $T \geq -10$ ºC) into a landfalling AR through the analysis of time-resolved precipitation samples collected at a coastal site and a downwind mountain site. Warm INPs were measured in precipitation samples during periods in which meteorological conditions elevated cloud tops to the level of the upper tropospheric jet, and which may contain trans-Pacific aerosol. In contrast, the downwind site measured warm INPs through most of the storm and were likely due to warm INP production via the "bioprecipitation feedback" (Huffman

et al., 2013; Morris et al., 2014). Clouds above the mountain site were more likely to be glaciated compared to the coastal site, indicating that these INPs were incorporated into the storm and affected cloud properties.

Chapter 4 of this dissertation investigates how to better distinguish between dust and bioaerosol using single particle mass spectrometry. The mass spectral features of dust and bioaerosol are explored and characterized using the ATOFMS, and key ion markers that may aid in their separation are identified and discussed. The findings from these lab experiments are used to develop a novel decision tree for the identification of bioaerosol in ambient measurements, which are found to correlate well with auxiliary measurements of bioaerosol and warm INP concentrations.

Chapter 5 of this dissertation describes the integration of a CFDC with an ATOFMS for the characterization of INPs. This integrated system was deployed to a coastal site in California to measure INP composition. Despite the fact that SSA was the dominant particle type measured by the ATOFMS during ambient sampling, INP residuals were determined to be primarily dust particles. The active site density was calculated for SSA and dust and found to agree well with previously determined parameterizations. These measurements were also able to highlight the fact that enhanced organic markers are important for the IN-activity of SSA.

Chapter 6 of this thesis describes the methodology for decomposing the sources and abundances of INPs using the ATOFMS. A methodology for predicting the relative abundances of INPs from dust and SSA using tandem measurements of single particle composition and size distributions is developed. Likewise, INP contributions from bioaerosols are predicted using single-particle measurements of bioaerosol concentrations. This methodology suggests that the

primary source of INPs at the site were bioaerosol, while dust was a secondary source. SSA were not determined to be a significant source of INPs.

Finally, Chapter 7 explores the resuspension of dust from the ocean and its ability to act as INPs. Tandem measurements of single particle composition and IN-activity from laboratory experiments utilizing realistic SSA generation methods show that dust can be resuspended after deposition to the surface of the ocean. This resuspended dust maintains IN-activity and may constitute an entirely unconsidered source of INPs in marine systems. Global emission and transport simulations were conducted and the Southern Ocean identified as a location where resuspended dust could be a potentially important source of INPs. Overall, the contents of this dissertation provide insight into the role atmospheric aerosols may play in modifying cloud properties.

1.10 Acknowledgements

Jon Sauer and Kathryn Mayer are acknowledged for their assistance in editing this chapter.

1.11 References

Albrecht, B. A. (1989). Aerosols, cloud microphysics, and fractional cloudiness. Science, 245(4923), 1227–1230. https://doi.org/10.1126/science.245.4923.1227

Alpert, P. A., Aller, J. Y., & Knopf, D. a. (2011). Ice nucleation from aqueous NaCl droplets with and without marine diatoms. Atmospheric Chemistry and Physics Discussions, 11(3), 8291–8336. https://doi.org/10.5194/acpd-11-8291-2011

Altaratz, O., Koren, I., Remer, L. A., & Hirsch, E. (2014). Review: Cloud invigoration by aerosols-Coupling between microphysics and dynamics. Atmospheric Research, 140–141, 38–60. https://doi.org/10.1016/j.atmosres.2014.01.009

Altieri, K. E., Seitzinger, S. P., Carlton, a. G., Turpin, B. J., Klein, G. C., & Marshall, a. G. (2008). Oligomers formed through in-cloud methylglyoxal reactions: Chemical composition, properties, and mechanisms investigated by ultra-high resolution FT-ICR mass spectrometry. Atmospheric Environment, 42, 1476–1490. https://doi.org/10.1016/j.atmosenv.2007.11.015

Andreae, M. O., & Rosenfeld, D. (2008). Aerosol-cloud-precipitation interactions. Part 1. The

nature and sources of cloud-active aerosols. *Earth-Science Reviews*, *89*(1–2), 13–41. https://doi.org/10.1016/j.earscirev.2008.03.001

Atkinson, J. D., Murray, B. J., Woodhouse, M. T., Whale, T. F., Baustian, K. J., Carslaw, K. S., … Malkin, T. L. (2013). The importance of feldspar for ice nucleation by mineral dust in mixed-phase clouds. Nature, 500(7463), 490–490. https://doi.org/10.1038/nature12384

Ault, A. P., Williams, C. R., White, A. B., Neiman, P. J., Creamean, J. M., Gaston, C. J., … Prather, K. a. (2011). Detection of Asian dust in California orographic precipitation. Journal of Geophysical Research, 116(D16205), 1–15. https://doi.org/10.1029/2010JD015351

Bond, T. C., Doherty, S. J., Fahey, D. W., Forster, P. M., Berntsen, T., Deangelo, B. J., … Zender, C. S. (2013). Bounding the role of black carbon in the climate system: A scientific assessment. Journal of Geophysical Research: Atmospheres, 118, 5380–5552. https://doi.org/10.1002/jgrd.50171

Boose, Y., Sierau, B., Isabel García, M., Rodríguez, S., Alastuey, A., Linke, C., … Lohmann, U. (2016). Ice nucleating particles in the Saharan Air Layer. Atmospheric Chemistry and Physics, 16(14), 9067–9087. https://doi.org/10.5194/acp-16-9067-2016

Boose, Y., Welti, A., Atkinson, J., Ramelli, F., Danielczok, A., Bingemer, H. G., … Lohmann, U. (2016). Heterogeneous ice nucleation on dust particles sourced from nine deserts worldwide - Part 1: Immersion freezing. Atmospheric Chemistry and Physics, 16(23), 15075–15095. https://doi.org/10.5194/acp-16-15075-2016

Briggs, N. L., & Long, C. M. (2016). Critical review of black carbon and elemental carbon source apportionment in Europe and the United States. Atmospheric Environment, 144, 409–427. https://doi.org/10.1016/j.atmosenv.2016.09.002

Cahill, J. F., Suski, K., Seinfeld, J. H., Zaveri, R. a., & Prather, K. a. (2012). The mixing state of carbonaceous aerosol particles in northern and southern California measured during CARES and CalNex 2010. Atmospheric Chemistry and Physics, 12, 10989–11002. https://doi.org/10.5194/acp-12-10989-2012

Choobari, O. A., Sturman, A., Choobari, A. O., Zawar-Reza, P., & Sturman, A. (2014). The global distribution of mineral dust and its impacts on the climate system : A review. Atmospheric Research, 138, 152–165. https://doi.org/10.1016/j.atmosres.2013.11.007

Cochran, R. E., Laskina, O., Trueblood, J. V., Estillore, A. D., Morris, H. S., Jayarathne, T., … Grassian, V. H. (2017). Molecular Diversity of Sea Spray Aerosol Particles: Impact of Ocean Biology on Particle Composition and Hygroscopicity. Chem, 2(5), 655–667. https://doi.org/10.1016/j.chempr.2017.03.007

Corbin, J. C., Rehbein, P. J. G., Evans, G. J., & Abbatt, J. P. D. (2012). Combustion particles as ice nuclei in an urban environment: Evidence from single-particle mass spectrometry. Atmospheric Environment, 51, 286–292. https://doi.org/10.1016/j.atmosenv.2012.01.007

Creamean, J. M., Kirpes, R. M., Pratt, K. A., Spada, N. J., Maahn, M., de Boer, G., … China, S. (2018). Marine and terrestrial influences on ice nucleating particles during continuous springtime measurements in an Arctic oilfield location. Atmospheric Chemistry and Physics, 18, 18023–18042. https://doi.org/10.5194/acp-2018-545

Creamean, J. M., Suski, K. J., Rosenfeld, D., Cazorla, A., DeMott, P. J., Sullivan, R. C., … Prather, K. a. (2013). Dust and biological aerosols from the Sahara and Asia influence precipitation in the western U.S. Science (New York, N.Y.), 339(2013), 1572–8. https://doi.org/10.1126/science.1227279

Cziczo, D. J., DeMott, P. J., Brock, C., Hudson, P. K., Jesse, B., Kreidenweis, S. M., … Murphy, D. M. (2003). A Method for Single Particle Mass Spectrometry of Ice Nuclei. Aerosol Science and Technology, 37(5), 460–470. https://doi.org/10.1080/02786820300976

DeMott, P. J., Cziczo, D. J., Prenni, A. J., Murphy, D. M., Kreidenweis, S. M., Thomson, D. S., … Rogers, D. C. (2003). Measurements of the concentration and composition of nuclei for cirrus formation. Proceedings of the National Academy of Sciences, 100(25), 14655–14660. https://doi.org/10.1073/pnas.2532677100

DeMott, P. J., Hill, T. C. J., McCluskey, C. S., Prather, K. A., Collins, D. B., Sullivan, R. C., … Franc, G. D. (2016). Sea spray aerosol as a unique source of ice nucleating particles. Proceedings of the National Academy of Sciences, 113(21), 5797–5803. https://doi.org/10.1073/pnas.1514034112

DeMott, P. J., Mason, R. H., McCluskey, C. S., Hill, T. C. J., Perkins, R. J., Desyaterik, Y., … Prather, K. A. (2018). Ice nucleation by particles containing long-chain fatty acids of relevance to freezing by sea spray aerosols. Environmental Science: Processes and Impacts, 20(11), 1559–1569. https://doi.org/10.1039/c8em00386f

DeMott, P. J., Prenni, A. J., Liu, X., Kreidenweis, S. M., Petters, M. D., Twohy, C. H., … Rogers, D. C. (2010). Predicting global atmospheric ice nuclei distributions and their impacts on climate. Proceedings of the National Academy of Sciences, 107(25), 11217–11222. https://doi.org/10.1073/pnas.0910818107

Dettinger, M. D., Ralph, F. M., Das, T., Neiman, P. J., & Cayan, D. R. (2011). Atmospheric Rivers, Floods and the Water Resources of California. Water, 3(4), 445–478. https://doi.org/10.3390/w3020445

Engelstaedter, S., Tegen, I., & Washington, R. (2006). North African dust emissions and transport. Earth-Science Reviews, 79(1–2), 73–100. https://doi.org/10.1016/j.earscirev.2006.06.004

Fan, J., Wang, Y., Rosenfeld, D., & Liu, X. (2016). Review of Aerosol–Cloud Interactions: Mechanisms, Significance, and Challenges. Journal of the Atmospheric Sciences, 73(11), 4221–4252. https://doi.org/10.1175/JAS-D-16-0037.1

Fröhlich-Nowoisky, J., Kampf, C. J., Weber, B., Huffman, J. A., Pöhlker, C., Andreae, M. O., …

Pöschl, U. (2016). Bioaerosols in the Earth system: Climate, health, and ecosystem interactions. Atmospheric Research, 182, 346–376. https://doi.org/10.1016/j.atmosres.2016.07.018

Garcia, E., Hill, T. C. J., Prenni, A. J., DeMott, P. J., Franc, G. D., & Kreidenweis, S. M. (2012). Biogenic ice nuclei in boundary layer air over two U.S. high plains agricultural regions. Journal of Geophysical Research Atmospheres, 117(17), 1–12. https://doi.org/10.1029/2012JD018343

Gard, E., Mayer, J. E., Morrical, B. D., Dienes, T., Fergenson, D. P., & Prather, K. A. (1997). Real-Time Analysis of Individual Atmospheric Aerosol Particles: Design and Performance of a Portable ATOFMS. Analytical Chemistry, 69(20), 4083–4091. https://doi.org/10.1021/ac970540n

Hill, T. C. J., Demott, P. J., Tobo, Y., Fröhlich-Nowoisky, J., Moffett, B. F., Franc, G. D., & Kreidenweis, S. M. (2016). Sources of organic ice nucleating particles in soils. Atmospheric Chemistry and Physics, 16(11), 7195–7211. https://doi.org/10.5194/acp-16-7195-2016

Hill, T. C. J., Moffett, B. F., DeMott, P. J., Georgakopoulos, D. G., Stump, W. L., & Franc, G. D. (2014). Measurement of ice nucleation-active bacteria on plants and in precipitation by quantitative PCR. Applied and Environmental Microbiology, 80(4), 1256–1267. https://doi.org/10.1128/AEM.02967-13

Huffman, J. A., Prenni, A. J., Demott, P. J., Pöhlker, C., Mason, R. H., Robinson, N. H., … Pöschl, U. (2013). High concentrations of biological aerosol particles and ice nuclei during and after rain. Atmospheric Chemistry and Physics, 13(13), 6151–6164. https://doi.org/10.5194/acp-13-6151-2013

IPCC, 2013: Climate Change 2013: The Physical Science Basis. Contribution of Working Group I to the Fifth Assessment Report of the Intergovernmental Panel on Climate Change [Stocker, T.F., D. Qin, G.-K. Plattner, M. Tignor, S.K. Allen, J. Boschung, A. Nauels, Y. Xia, V. Bex and P.M. Midgley (eds.)]. Cambridge University Press, Cambridge, United Kingdom and New York, NY, USA, 1535 pp, doi:10.1017/CBO9781107415324.

Kanji, Z. A., Ladino, L. A., Wex, H., Boose, Y., Burkert-Kohn, M., Cziczo, D. J., & Krämer, M. (2017). Overview of Ice Nucleating Particles. Meteorological Monographs, 58, 1.1-1.33. https://doi.org/10.1175/AMSMONOGRAPHS-D-16-0006.1

Knopf, D. A., Alpert, P. A., Wang, B., & Aller, J. Y. (2011). Stimulation of ice nucleation by marine diatoms. Nature Geoscience, 4(2), 88–90. https://doi.org/10.1038/ngeo1037

Kohler, H. (1936). The nucleus in and the growth of hygroscopic droplets. Transactions of the Faraday Society, 32(2), 1152–1161. https://doi.org/10.1134/S002016850605013X

Levin, E. J. T., Mcmeeking, G. R., Demott, P. J., Mccluskey, C. S., Carrico, C. M., Nakao, S., …

Kreidenweis, S. M. (2016). Journal of Geophysical Research : Atmospheres, 5888–5903. https://doi.org/10.1002/2016JD024879.Received

Maki, L. R., Galyan, E. L., Chang-Chien, M. M., & Caldwell, D. R. (1974). Ice nucleation induced by pseudomonas syringae. Applied Microbiology, 28(3), 456–459. https://doi.org/10.1111/1462-2920.12668

Mason, R. H., Si, M., Li, J., Chou, C., Dickie, R., Toom-Sauntry, D., … Bertram, A. K. (2015). Ice nucleating particles at a coastal marine boundary layer site: Correlations with aerosol type and meteorological conditions. Atmospheric Chemistry and Physics, 15(21), 12547–12566. https://doi.org/10.5194/acp-15-12547-2015

McCluskey, C. S., DeMott, P. J., Prenni, A. J., Levin, E. J. T., McMeeking, G. R., Sullivan, A. P., … Kreidenweis, S. M. (2014). Characteristics of atmospheric ice nucleating particles associated with biomass burning in the US: Prescribed burns and wildfires. Journal of Geophysical Research, 119(17), 10,458-10,470. https://doi.org/10.1002/2014JD021980

McCluskey, C. S., Hill, T. C. J., Malfatti, F., Sultana, C. M., Lee, C., Santander, M. V., … DeMott, P. J. (2017). A dynamic link between ice nucleating particles released in nascent sea spray aerosol and oceanic biological activity during two mesocosm experiments. Journal of the Atmospheric Sciences, 74(2017), JAS-D-16-0087.1. https://doi.org/10.1175/JAS-D-16-0087.1

McCluskey, C. S., Hill, T. C. J., Sultana, C. M., Laskina, O., Trueblood, J., Santander, M. V., … DeMott, P. J. (2018). A Mesocosm Double Feature: Insights into the Chemical Makeup of Marine Ice Nucleating Particles. Journal of the Atmospheric Sciences, 75(7), 2405–2423. https://doi.org/10.1175/JAS-D-17-0155.1

McCluskey, C. S., Ovadnevaite, J., Rinaldi, M., Atkinson, J., Franco, B., Ceburnis, D., … Demott, P. J. (2018). Marine and Terrestrial Organic Ice Nucleating Particles in Pristine Marine to Continentally-Influenced Northeast Atlantic Air Masses. Journal of Geophysical Research: Atmospheres, 123, 1–17. https://doi.org/10.1029/2017JD028033

Montoya, J., Horne, J. R., Hinks, M. L., Fleming, L. T., Perraud, V. V., Lin, P., … Nizkorodov, S. A. (2017). Secondary Organic Aerosol from Atmospheric Photooxidation of Indole. Atmospheric Chemistry and Physics Discussions, 30(March), 1–31. https://doi.org/10.5194/acp-2017-270

Morris, C. E., Conen, F., Alex Huffman, J., Phillips, V., Pöschl, U., & Sands, D. C. (2014). Bioprecipitation: A feedback cycle linking Earth history, ecosystem dynamics and land use through biological ice nucleators in the atmosphere. Global Change Biology, 20(2), 341–351. https://doi.org/10.1111/gcb.12447

Murray, B. J., Broadley, S. L., Wilson, T. W., Atkinson, J. D., & Wills, R. H. (2011). Heterogeneous freezing of water droplets containing kaolinite particles. Atmospheric Chemistry and Physics, 11(9), 4191–4207. https://doi.org/10.5194/acp-11-4191-2011

Murray, B. J., O'Sullivan, D., Atkinson, J. D., & Webb, M. E. (2012). Ice nucleation by particles immersed in supercooled cloud droplets. Chemical Society Reviews, 41(19), 6519. https://doi.org/10.1039/c2cs35200a

Ni, M., Huang, J., Lu, S., Li, X., Yan, J., & Cen, K. (2014). A review on black carbon emissions, worldwide and in China. Chemosphere, 107, 83–93. https://doi.org/10.1016/j.chemosphere.2014.02.052

Niemand, M., Möhler, O., Vogel, B., Vogel, H., Hoose, C., Connolly, P., … Leisner, T. (2012). A Particle-Surface-Area-Based Parameterization of Immersion Freezing on Desert Dust Particles. Journal of the Atmospheric Sciences, 69(10), 3077–3092. https://doi.org/10.1175/JAS-D-11-0249.1

Petters, M. D., & Kreidenweis, S. M. (2007). A single parameter representation of hygroscopic growth and cloud condensation nucleus activity - Part 2: Including solubility. Atmospheric Chemistry and Physics, 7, 1961–1971. https://doi.org/10.5194/acp-8-6273-2008

Petters, M. D., Parsons, M. T., Prenni, A. J., Demott, P. J., Kreidenweis, S. M., Carrico, C. M., … Moosmüller, H. (2009). Ice nuclei emissions from biomass burning. Journal of Geophysical Research Atmospheres, 114(7), 1–10. https://doi.org/10.1029/2008JD011532

Petters, M. D., & Wright, T. P. (2015). Revisiting ice nucleation from precipitation samples. Geophysical Research Letters, 42(20), 8758–8766. https://doi.org/10.1002/2015GL065733

Pratt, K. A., Twohy, C. H., Murphy, S. M., Moffet, R. C., Heymsfield, A. J., Gaston, C. J., … Prather, K. A. (2010). Observation of playa salts as nuclei in orographic wave clouds. Journal of Geophysical Research Atmospheres, 115(15), 1–17. https://doi.org/10.1029/2009JD013606

Pratt, K. a, Mayer, J. E., Holecek, J. C., Moffet, R. C., Sanchez, R. O., Rebotier, T. P., … Su, X. Y. (2009). Development and Characterization of an Aircraft Aerosol Time-of-Flight Mass Spectrometer Development and Characterization of an Aircraft Aerosol Time-of-Flight Mass Spectrometer. Analytical Chemistry, 81(5), 1792–1800. https://doi.org/10.1021/ac801942r

Price, H. C., Baustian, K. J., McQuaid, J. B., Blyth, A., Bower, K. N., Choularton, T., … Murray, B. J. (2018). Atmospheric Ice-Nucleating Particles in the Dusty Tropical Atlantic. Journal of Geophysical Research: Atmospheres, 123(4), 2175–2193. https://doi.org/10.1002/2017JD027560

Pruppacher, H. R., & Klett, J. (2010). Microphysics of Clouds and Precipitation (Vol. 18). https://doi.org/10.1007/978-0-306-48100-0

R. Lewis, E., & Schwartz, S. (2004). Sea Salt Aerosol Production: Mechanisms, Methods, Measurements and Models—A Critical Review. Washington DC American Geophysical

Union Geophysical Monograph Series, 152, 3719-.

Ralph, F. M., Prather, K. A., Cayan, D., Spackman, J. R., Demott, P., Dettinger, M., … Intrieri, J. (2016). Calwater field studies designed to quantify the roles of atmospheric rivers and aerosols in modulating U.S. West Coast Precipitation in a changing climate. Bulletin of the American Meteorological Society, 97(7), 1209–1228. https://doi.org/10.1175/BAMS-D-14-00043.1

Richardson, M. S., DeMott, P. J., Kreidenweis, S. M., Cziczo, D. J., Dunlea, E. J., Jimenez, J. L., … Lersch, T. L. (2007). Measurements of heterogeneous ice nuclei in the western United States in springtime and their relation to aerosol characteristics. Journal of Geophysical Research Atmospheres, 112(2), 1–16. https://doi.org/10.1029/2006JD007500

Rogers, D. C. (1988). Development of a continuous flow thermal gradient diffusion chamber for ice nucleation studies. Atmospheric Research, 22(2), 149–181. https://doi.org/10.1016/0169-8095(88)90005-1

Rosenfeld, D., Chemke, R., Prather, K., Suski, K., Comstock, J. M., Schmid, B., … Jonsson, H. (2014). Polluting of winter convective clouds upon transition from ocean inland over central California: Contrasting case studies. Atmospheric Research, 135–136, 112–127. https://doi.org/10.1016/j.atmosres.2013.09.006

Rosenfeld, D., & Givati, A. (2006). Evidence of orographic precipitation suppression by air pollution-induced aerosols in the western United States. Journal of Applied Meteorology and Climatology, 45(7), 893–911. https://doi.org/10.1175/JAM2380.1

Rosenfeld, D., Lohmann, U., Raga, G. B., O'Dowd, C. D., Kulmala, M., Fuzzi, S., … Andreae, M. O. (2008). Flood or drought: how do aerosols affect precipitation? Science (New York, N.Y.), 321(5894), 1309–13. https://doi.org/10.1126/science.1160606

Rosenfeld, D., Woodley, W. L., Axisa, D., Freud, E., Hudson, J. G., & Givati, A. (2008). Aircraft measurements of the impacts of pollution aerosols on clouds and precipitation over the Sierra Nevada. Journal of Geophysical Research Atmospheres, 113(15), 1–23. https://doi.org/10.1029/2007JD009544

Schaefer, V. J. (1946). The Production of Ice Crystals in a Cloud of Supercooled Water Droplets. Science, 104(2707), 457–459.

Schill, G. P., Jathar, S. H., Kodros, J. K., Levin, E. J. T., Galang, A. M., Friedman, B., … DeMott, P. J. (2016). Ice-nucleating particle emissions from photochemically aged diesel and biodiesel exhaust. Geophysical Research Letters, 43(10), 5524–5531. https://doi.org/10.1002/2016GL069529

Seinfeld, J. H., & Pandis, S. N. (2006). Atmospheric chemistry & physics: from air pollution to climate change. Hoboken, NJ: Wiley Interscience.

Suski, K. J., Hill, T. C. J., Levin, E. J. T., Miller, A., DeMott, P. J., & Kreidenweis, S. M. (2018). Agricultural harvesting emissions of ice-nucleating particles. Atmospheric Chemistry and Physics, 18(18), 13755–13771. https://doi.org/10.5194/acp-18-13755-2018

Tobo, Y., Demott, P. J., Hill, T. C. J., Prenni, A. J., Swoboda-Colberg, N. G., Franc, G. D., & Kreidenweis, S. M. (2014). Organic matter matters for ice nuclei of agricultural soil origin. Atmospheric Chemistry and Physics, 14(16), 8521–8531. https://doi.org/10.5194/acp-14-8521-2014

Twomey, S. (1974). Pollution and the Planetary Albedo. Atmospheric Environment, 8, 1251–1256. https://doi.org/10.1016/j.atmosenv.2007.10.062

Twomey, S. (1977). The Influence of Pollution on the Shortwave Albedo of Clouds. Journal of the Atmospheric Sciences, 34, 1149–1152.

Ullrich, R., Hoose, C., Möhler, O., Niemand, M., Wagner, R., Höhler, K., … Leisner, T. (2017). A New Ice Nucleation Active Site Parameterization for Desert Dust and Soot. Journal of the Atmospheric Sciences, 74(3), 699–717. https://doi.org/10.1175/JAS-D-16-0074.1

Vali, G. (1971). Quantitative Evaluation of Experimental Results an the Heterogeneous Freezing Nucleation of Supercooled Liquids. Journal of the Atmospheric Sciences. https://doi.org/10.1175/1520-0469(1971)028<0402:QEOERA>2.0.CO;2

Vergara-Temprado, J., Holden, M. A., Orton, T. R., O'Sullivan, D., Umo, N. S., Browse, J., … Murray, B. J. (2018). Is Black Carbon an Unimportant Ice-Nucleating Particle in Mixed-Phase Clouds? Journal of Geophysical Research: Atmospheres, 123(8), 4273–4283. https://doi.org/10.1002/2017JD027831

Vergara-Temprado, J., Miltenberger, A. K., Furtado, K., Grosvenor, D. P., Shipway, B. J., Hill, A. A., … Carslaw, K. S. (2018). Strong control of Southern Ocean cloud reflectivity by ice-nucleating particles. Proceedings of the National Academy of Sciences, 201721627. https://doi.org/10.1073/pnas.1721627115

Vergara-Temprado, J., Murray, B. J., Wilson, T. W., O'Sullivan, D., Browse, J., Pringle, K. J., … Carslaw, K. S. (2017). Contribution of feldspar and marine organic aerosols to global ice nucleating particle concentrations. Atmospheric Chemistry and Physics, 17(5), 3637–3658. https://doi.org/10.5194/acp-17-3637-2017

Virtanen, A., Joutsensaari, J., Koop, T., Kannosto, J., Yli-Pirilä, P., Leskinen, J., … Laaksonen, A. (2010). An amorphous solid state of biogenic secondary organic aerosol particles. Nature, 467(7317), 824–827. https://doi.org/10.1038/nature09455

Wright, T. P., Hader, J. D., McMeeking, G. R., & Petters, M. D. (2014). High relative humidity as a trigger for widespread release of ice nuclei. Aerosol Science and Technology, 48(11), i–v. https://doi.org/10.1080/02786826.2014.968244

Zhu, Y., & Newell, R. E. (1998). A Proposed Algorithm for Moisture Fluxes from Atmospheric Rivers. Monthly Weather Review, 126, 725–735. https://doi.org/10.1175/1520-0493(1998)126<0725:APAFMF>2.0.CO;2

Chapter 2. Transport of pollution to a remote coastal site during gap flow from California's interior: impacts on aerosol composition, clouds and radiative balance

2.1 Abstract

During the CalWater-2015 field campaign, ground-level observations of aerosol size, concentration, chemical composition, and cloud activity were made at Bodega Bay, CA on the remote California coast. A strong anthropogenic influence on air quality, aerosol physicochemical properties, and cloud activity was observed at Bodega Bay during periods with special weather conditions, known as Petaluma Gap flow, in which air from California's interior is transported to the coast. This study applies a diverse set of chemical, cloud microphysical and meteorological measurements to the Petaluma Gap flow phenomenon for the first time. It is demonstrated that the sudden and often dramatic change in aerosol properties are strongly related to regional meteorology and anthropogenically-influenced chemical processes in California's Central Valley. In addition, it is demonstrated that the change in airmass properties from those typical of a remote marine environment to properties of a continental regime has the potential to impact atmospheric radiative balance and cloud formation in ways that must be accounted for in regional climate simulations.

2.2 Introduction

The remote northern California coast experiences a Mediterranean climate (Aschmann, 1973, Lentz and Chapman, 1989) and warm, dry summers. The vast majority of yearly precipitation occurs during winter (Regonda et al., 2005), when the north Pacific extratropical storm track extends southward and brings periodic pressure falls and rain to the region. (Gyakum et al., 1998). Also during the winter months, conditions known as channeled gap flow can transport airmasses from much further inland to the remote coast. These episodic periods result when very

low near-surface buoyancy and an onshore-directed gap-parallel pressure gradient co-occur in one of several prominent gaps in the coastal mountain ranges (Overland and Walter, 1981; Neiman et al., 2006; Loescher et al., 2006; Colle et al., 2006). One such prominent gap is located near the town of Petaluma in Sonoma County, CA and can act to channel air from the North San Francisco Bay Area (SFBA), the Sacramento River Delta and California's Central Valley (CV) to coastal Northern California (see schematic in Figure 2.1, Neiman et al., 2006 – hereafter N06). N06 described the regional weather patterns and lower tropospheric dynamic meteorology associated with Petaluma Gap Flow (PGF) using 62 cases observed during the multi-winter deployment of a 915 MHz wind profiling radar to Bodega Bay, CA. N06 describe PGF as a near-surface shallow (~500m) stably-stratified quasi-Bernoulli flow which can lead to increased static stability, increased density, lower relative humidity and increased anthropogenic pollutants near Bodega Bay and offshore.

Evidence presented in N06 for the proliferation of anthropogenic pollutants at the coast during PGF included horizontal coast-normal transects and low-troposphere vertical profiles of Carbon Monoxide (CO) mixing ratio from a trace gas analyzer on-board just one research flight of the National Oceanographic and Atmospheric Administration (NOAA) P-3 aircraft. During the coast-normal transect CO mixing ratio doubled from 120 ppbv to 240 ppbv across a 20 km wide gradient that was located approximately 75 km offshore of Bodega Bay and Point Reyes, CA. It was inferred that when the near-surface airmass during PGF episodes travelled from the polluted Central Valley region before arriving at the coast, the airmass would acquire properties commensurate with combustion, transportation, agriculture and manufacturing (e.g. the observation of elevated CO concentration).

When transport occurs, PGF should cause large measurable impacts on the coastal environment via an abrupt but significant change in trace gas and aerosol chemistry. Expected impacts include:

- An increase in absorption of solar shortwave radiation by black carbon aerosol, which have much greater emission sources on the continental side of the Petaluma Gap. An increase in black carbon mass may also be associated with more freshly emitted soot. Together, these factors may lead to a relative decrease in both externally mixed and internally mixed organic to elemental carbon ratios. (e.g. Chung et al., 2012; Cahill et al., 2012).
- A brightening in near-shore marine stratocumulus clouds through the cloud albedo indirect effect (Twomey, 1977; Solomon, 2007), since the inferred PGF airmass contains more numerous pollution aerosol particles, a portion of which will serve as cloud condensation nuclei.
- Increased deposition of nitrogen containing particulate matter to the local ecosystem which may lead to increased eutrophication along the coastal shelf (Paerl, 1995; Paerl, 1997), because particles transported during PGF may have formed or have been aged in a nitrous-oxide and ammonia enriched environment (Seinfeld and Pandis, 2012).

As part of the CalWater-2 experiment (Lueng et al., 2014; Ralph et al., 2015), measurements of trace gas concentrations, aerosol physicochemical properties and lower tropospheric meteorology were taken at the University of California, Davis Bodega Marine Laboratory during January, February and March, 2015. Using this dataset, described in section 2.3, we report the abrupt changes in trace gases and particulate matter observed during five PGF events and establish composite aerosol size distributions, aerosol chemical sources, trace gas concentrations, and cloud condensation nuclei activation curves. We also identify particle aging through the accumulation of ammonium and nitrate during PGF using detailed single particle mass spectrometry

measurements. The analysis methods presented in section 2.4, and their results, presented in section 2.5, verify the above hypotheses and present a nuanced picture of the secondary heterogeneous chemistry active in aerosol particles that travel to the coast in the PGF airmass. Fine details of particle aging are location specific, but conclusions drawn from the increase in aerosol number, changes in aerosol source, brightening of marine clouds and impact on aerosol absorption are generally applicable to many other coastal regions that periodically experience channeled offhsore flow through a mountain gap.

2.3 Data Sources

2.3.1 Bodega Marine Laboratory

Measurements and samples were collected January 14, 2015 to March 9, 2015 at Bodega Marine Laboratory (BML, 38° 19'N, 123° 4') in Bodega Bay, California. Measurements were collected continuously unless otherwise noted. BML is located south-southwest of the northern California coastal mountain ranges and north of Point Reyes National Seashore (Fig. 2.1). More detailed information regarding instrumentation deployed to BML follows below.

The sampling site at BML included two instrumented trailers located ~100 m ENE of the seashore, and ~30 m north of the northernmost BML permanent building. The Beta Attenuation Monitor (BAM), for measuring particulate matter mass for particles smaller than 2.5 μm ($PM_{2.5}$), and IMPROVE (Eldred et al., 1997) filters for collecting $PM_{2.5}$ and particles smaller than 10 m (PM_{10}) were placed at an ancillary site ~15 m Southwest of the trailers. The IMPROVE samples are not used in the analysis that follows. Aerosol composition and ice nucleating particle concentrations were measured in the trailer owned by the California Air Resources Board (CARB) and operated by the University of California, San Diego (UCSD). Aerosol sizing, gas phase tracer concentrations, black carbon mass, cloud condensation nuclei concentrations were measured in the

trailer owned by the National Park Service (NPS) and operated by Colorado State University (CSU). Ambient aerosol particles were collected nearby using filters for subsequent laboratory measurement of droplet freezing temperature. A more extensive description of these instruments and the data processing, quality control and archiving is given by Petters et al.[1] A meteorology station operated by the Earth System Research Laboratory, National Oceanic and Atmospheric Administration (NOAA/ESRL) was located ~100 m North of the two trailers. The NOAA/ESRL 449 MHz wind profiling radar, radio acoustic sounding system (RASS), and 10m surface meteorology tower were operated during the two study periods and are used for the analysis presented in later sections. Descriptions of these instruments and the NOAA/ESRL Bodega Bay meteorology station (BBY) can be found in White et al. (2013).

2.3.2 Aerosol composition

Size-resolved aerosol composition at Bodega Bay was measured with an aerosol-time-of-flight mass spectrometer (ATOFMS) and an ultrafine aerosol-time-of-flight mass spectrometer (UF-ATOFMS). The UF-ATOFMS used a diluting stage with an approximate dilution of 5x to increase aerosol ionization efficiency during periodic high particle concentrations. The use of these instruments in tandem allows the direct measurement of single-particle composition for particles in the aerodynamic diameter range 0.15-3.0 μm. The design and operating principles of these instruments have been described elsewhere (Gard et al., 1997; Su et al., 2004), thus we provide only a short overview here. Particles were dried prior to introduction to the instrument with silica-diffusion dryers in order to improve the ionization efficiency and thus improve the acquired spectra quality. Particles enter the vacuum system through either a converging nozzle or an aerodynamic

[1] Petters, M. D., Taylor, H. P., Attwood, S., Kreidenweis, S. M., DeMott, P. J., Rothfuss, N. E., Prather, K. A. Martin, A.: Aerosol characteristics in and around landfalling Atmospheric Rivers and marine air intrusions observed during the Calwater-2015 campaign.

lens, wherein they are accelerated to their terminal velocities. After reaching this terminal velocity, they enter the sizing region where travel through two continuous wave laser beams (diode-pumped, Nd:YAG at 532 nm) separated by a vertical distance of 6 cm, and oriented orthogonal to each other. Because the distance is known, particle velocity can be determined by measuring the time difference between the two scattering signals. These velocities can be converted to vacuum aerodynamic diameter (D_{va}) through a calibration curve generated with polystyrene latex spheres (PSLs). The velocity is also used to calculate the time when a particle will arrive in the ion source region. Upon arrival in the source region, a 266-nm Nd:YAG laser is triggered to fire upon the particle, desorb it, and generate positive and negative ions whose mass spectrum are measured with dual-polarity time-of-flight mass spectrometer.

2.3.3 Size distributions

Aerosol size distributions at BML were measured using a scanning mobility particle sizer (SMPS, TSI Inc. Model 3936) and an aerodynamic particle sizer (APS, TSI Inc. Model 3321). The SMPS was operated with a pump flow of 0.3 lpm and a sheath flow of 3.0 lpm so that the dynamic size range varied from 13.6 to 736.5 nm. The APS operated with a sample flow rate of 1.0 lpm and a sheath flow of 4.0 lpm and measured particle sizes from 0.6 to 20 μm. The APS was externally calibrated using Polystyrene Latex Spheres (PSLS). Particles were not dried prior to sizing, but the relative humidity (RH) of the sample line was monitored with a RH sensor (Vaisala, HMP110). The RH in the sample line varied from 7.5% to 54.7% during measurement periods with a mean value of 35.5%. Nearly 97% of the sampling periods occurred while sample line RH was below 47% (0.4% of LOCAL, 4.7% of CTL and 0% of PGF) the efflorescence humidity of sodium chloride particles (Gupta et al., 2015). Because the RH was below the efflorescence point of sodium chloride (chosen as a proxy for sea spray) for >95% of the sampling periods the humidity

likely had little bearing on the composite size distributions used in this analysis. Assuming spherical particles, the measured mobility diameter (D_m) is equivalent to physical diameter (D_p). APS measurements were adjusted from aerodynamic diameter (D_a) to D_p assuming spherical particles and an effective density of 1.8 g cm^{-3}. Both APS and SMPS size distributions were combined to ten-minute mean distributions from their operational 1 and 5 minute scan frequency.

2.3.4 Aerosol and BC mass concentration

$PM_{2.5}$ mass was determined using a beta attenuation monitor (BAM, Met One Instruments Inc., Model BAM 1020). The mass was recorded hourly. Black carbon (BC) mass concentration and attenuation were determined with a 7-channel aethalometer (Magee Scientific Corp., Model AE16-ER-P3-F0), operating in AE-30 mode.

2.3.5 Cloud activation properties

Size-resolved (also referred to as "diameter scan") cloud condensation nuclei concentrations were measured using a streamwise cloud condensation nuclei counter (Droplet Measurement Technologies Inc., CCN-100) coupled with an SMPS. The SMPS (TSI 3080 long column) was operated at a sheath-to-sample flow rate of 5 (L min-1)-to (1.3 L min-1). Raw counts were recorded in Labview and inverted as described previously (Nguyen et al. 2014; Petters et al. 2009). The inversions account for temperature and pressure changes inside the DMA, contribution of multiply charged particles and losses through the inlet system. The CCN was operated at a sample flow rate of 0.3 L min-1 and sheath-to-sample flow ratio of 10:1. Supersaturation is calibrated using atomized, dried ammonium sulfate aerosol (Christensen and Petters 2012). The control software cycles through an automated 12 point sequence varying supersaturation between 0.06% and 0.67%. Activation diameters are obtained for normalized activation curves (Petters et al. 2009) and the apparent hygroscopicity parameter at standard state, κ is calculated from the

supersaturation and activation diameter (Christensen and Petters 2012; Petters and Kreidenweis 2007).

2.3.6 Gas-phase measurements

Concentrations of gas-phase pollutants were determined using a suite of gas-phase instruments, collocated with the aethalometer, CCN counter, and the sizing instruments. A NO-NO_2-NO_x analyzer (TEI Inc., Model 42C), ozone analyzer (TEI Inc., Model 49C), sulfur dioxide analyzer (TEI Inc. Model 43C), and carbon monoxide monitor (Horiba Inc., APMA-370) were all utilized in this study. Gas phase measurements were recorded every second and converted to 10-minute mean time resolution.

2.3.7 Remotely sensed cloud properties

Level 2 MODIS cloud products (Platnick et al., 2003) are used to estimate the range of marine stratocumulus cloud optical depth offshore from BML during PGF episodes with clear sky above low clouds, and to verify that the clouds in near-shore MODIS scenes are low-level cumulus or stratocumulus clouds.

2.4 Methods

2.4.1 Method of compositing by measurement period

Composite aerosol size distributions, trace gas and aerosol type concentrations, indicators of secondary chemical aging, and CCN activation spectra corresponding to PGF periods and control periods are derived as a primary tool for addressing the hypotheses posed in this study. Herein, we define a control period (CTL) to be any hourly period which does not fit the definition for flow through the Petaluma Gap arriving at BML found in N06 (hereafter mPGF) and does not occur during short-lived episodes of concentrated local anthropogenic pollution. In this study, mPGF periods that also meet a minimum threshold for concentrated non-local anthropogenic

pollution will be called PGF. Observed causes of local anthropogenic pollution included nearby brush fires, vehicle activity at BML, and "seabreeze resampling". During the latter, high concentrations of anthropogenic pollution from either a local source or from further inland that was previousy transported offshore returned to the measurement site via the afternoon sea-breeze. Since the polluted airmass may have up to 18 hours of modification by the near BML marine environment just before seabreeze resampling episodes, these were classified as local anthropogenic pollution and were removed from the PGF and CTL composites.

We followed the methodology of N06 in identifying Petaluma Gap flow using the BBY 449 MHz vertically profiling radar and 10 m anemometer (see section 4a in N06). Briefly, this methodology includes identifying continuous periods at least 6 hours in length during which wind speed and direction criteria are met both at the surface (10 m anemometer at BML) and in the lowest retrieved layer (approx. 100 to 350 m MSL) of the BML 449 MHz radar. If the conditions from the N06 methodology were met, we declared the period mPGF. It is important to note that while 449 MHz wind profiles are collected hourly, all other data from the study are collected more frequently, therefore we classified local conditions in hourly intervals.

To choose local conditions based on an indicator of anthropogenic pollution, we examined CalWater-2015 observations of CO, NO_x, SMPS number concentration integrated from 13.6 nm to 736.5 nm (CN), and $PM_{2.5}$ (collectively, peripherals). During mPGF, the interquartile range of CO, and NO_x was higher than the interquartile range of the same measurements during periods that did not fit mPGF (not shown). In addition, for indicators of fine particulate concentration (CN, $PM_{2.5}$), the median value during PGF is higher than the upper quartile value during all periods. For all anthropogenic pollutant indicators, the maximum observation and much of the upper quartile range is higher than any observation taken during mPGF, and occurred during local anthropogenic

pollution periods. An example is shown in Figure 2.2, which contrasts lower tropospheric horizontal wind and virtual potential temperature (θ_v), selected peripheral measurements and EC and SS particle subtypes (see methods for particle typing, later this section) during a period when neither mPGF was observed nor anthropogenic pollutants were high (Fig. 2.2a), a period when it is suspected local anthropogenic pollutants were sampled (Fig. 2.2b) and a mPGF period (Fig. 2.2c). Note that during the local pollutant episode, CN and CO were elevated to the same levels as during the mPGF period for a few hours. The onset of the elevated pollutant period occurs near the maximum in onshore sea-breeze (NNW 200 m wind near 03 UTC on February 12th). Pollutant concentrations decrease again a few hours after local sunset, when the offshore land-breeze become established. The period February 12, 2015 @ 0300 UTC through February 12, 2015 @ 11 UTC is an example of a seabreeze resampling period.

In order to exclude local or sea-breeze resampled anthropogenic pollutants from CTL periods, we imposed an additional requirement based upon CO concentration - hourly mean CO concentration must be above the CalWater-2015 mean plus two standard deviations (138.1 ppbv). Along with mPGF, this requirement forms the basis of a decision table (Table 2.1) that allows the separation of CalWater-2015 measurements into 4 composites. We choose CO concentration as our additional discriminator because its interquartile range during mPGF is entirely above the interquartile range from all other periods, because its overall variability is the lowest among peripheral measurements and because elevated near-surface CO concentration was observed by aircraft during a PGF event reported in N06. Table 2.1 allows the compositing of observational period by PGF (mPGF and elevated CO conditions met), CTL (neither mPGF nor elevated CO conditions met), LOCAL (mPGF not met, elevated CO met), and DIFFUSE (mPGF met, elevated

CO not met). In this light, Figs. 2.2a, b and c can be seen as examples of CTL, LOCAL and PGF periods, respectively.

2.4.2 Derivation of angstrom absorption exponent from aethalometer observations

The attenuation recorded by the aethalometer was used to derive the aerosol absorption coefficient (σATN) at the instrument's native 5 minute resolution following the method described in Collaud Cohen et al. (2010) (see their equation 2). This value was not corrected and thus not reported directly, as techniques for correcting aethalometer measurements require a coincident multi-channel measurement of aerosol scattering in order to determine backscattering by the filtered particles, and this additional measurement was not taken during CalWater-2015. It is noted that values of σATN generally fall in the range reported by previous studies in continental regions (e.g. Table 1 in Chung et al., 2012). The hourly mean aerosol absorption coefficient in the channels 470 nm, 520 nm, 590 nm, and 660 nm were used to derive the Angstrom absorption exponent (AAE), using the relation σ_ATN (λ)=C_0 λ^(-AAE). AAE is calculated by regression to the uncorrected σATN(λ). Note that Weingartner et al. (2003) estimated that errors in σATN are only a very weak function of wavelength in the channels used, thus it is expected that instrument errors do not contribute significantly to the estimate of AAE.

2.4.3 Assigning particle type to ATOFMS spectra

ATOFMS and UF-ATOFMS can provide information on size and chemical composition (via mass spectra) for an individual particle. Generally, positive spectra reveal particle source while negative spectra provide information on the atmospheric processing a particle has undergone (Guazzotti et al., 2001; Sullivan et al 2007; Prather et al., 2008). ATOFMS, but not UF-ATOFMS spectra were filtered for periodic radio frequency interference caused by a sub-optimally operating instrument component. A total of 115,416 particles were scattered and hit during PGF events, and

1,835,387 during the control time periods (see section 2.4.1 for definition of PGF and control periods).

Single particle spectra and size data were loaded into Matlab (The MathWorks, Inc.) and analyzed via the software toolkit YAADA (http://www.yaada.org/). Particles were divided into clusters based on their mass spectral features via an adaptive neural network (ART-2a, vigilance factor 0.8, learning rate 0.05 and 20 iterations regroup vigilance factor of 0.85) (Rebotier and Prather, 2007; Song et al., 1999). Greater than 95% of art2-a analyzed particles were grouped were recombined into 11 types based upon their characteristic mass spectra and size distributions. Similar to previous field studies using ATOFMS (Sullivan et al., 2007; Pratt et al., 2009; Cahill et al., 2012, Qin et al., 2012), particle types were assigned by a human operator based upon similarity to known types from previous field and laboratory studies. Calculated standard error in particle fraction were less than 1% for all particle types and thus were not included in the discussion. These results are summarized in Table 2.2.

2.4.4 Determining aging mechanisms using ATOFMS

It is important to describe not only particle sources, but also secondary aging impacts as the aging mechanism will change the light absorption cross-section of carbonaceous aerosols. For instance, a sulfate coating can increase the light-absorbing properties of soot by a factor of 1.6 (Moffett and Prather, 2009). Internally-mixed EC and OC have greater absorption profiles compared to homogeneously mixed particles of either species. (Schnaiter et al., 2005). Additionally, aging can increase particle hygroscopicity through condensation and reaction of gases like NOx or SO2 (Wang et al., 2010; Mochida et al., 2006; Zuberi et al., 2005; Zhang et al., 2008) or oxidation of carbonaceous species (Zuberi et al., 2005; Kotzick et al., 1997). Increased particle hygrospocity can increase the CCN activity of particles and their growth factor, profoundly

impacting radiative effects. Finally, accumulation of nitrogen species on particles can lead to increased deposition of nitrate and ammonium and impact oceanic biology (Paerl, 1995; Paerl et al., 1997).

The ATOFMS is a powerful tool to measure particle aging because of its ability to measure single-particle composition and directly determine the type and extent of particle aging. For similar particles of the same type, relative peak areas (RPA) qualitatively reflect the amount of a species on a particle in relation to other species (Bhave et al., 2002; Gross et al., 2000; Prather et al., 2008) and thus can be used to investigate the mechanism of aging (Cahill et al., 2012). During this study, the mixing state of single particles with secondary markers was investigated by identifying and comparing peak areas for ammonium ($^{18}NH_4^+$), amines ($^{58}C_2H_5NHCH_2^+$, $^{59}NC_3H_9^+$, $^{86}(C_2H_5)_2NCH_2^+$), sulfate ($^{97}HSO_4^-$, $^{195}H_2SO_4HSO_4^-$), nitrate ($^{46}NO_2^-$, $^{62}NO_3^-$, $^{125}H(NO_3)_2^-$), elemental carbon ($^{12}C^+$, $^{36}C^+$, $^{60}C^+$), and organic carbon ($^{27}CHN/C_2H_3^+$, $^{29}C_2H_5^+$, $^{37}C_3H^+$, $^{43}C_2H_3O^+/CHNO^+$). Other markers of heterogeneous processing were investigated, but no notable patterns emerged. For this analysis, a particle was considered to be an internal mixed with a species if it had an RPA greater than 0.5% for the characteristic ion markers, similar to the methodology employed by Cahill et al. (2012).

2.4.5 Estimates of cloud droplet number concentration and marine stratocumulus albedo change

Size distribution, hygroscopicity, and CCN concentration measurements were collated from periods classified as PGF and CTL. Cumulative CCN supersaturation spectra, defined as median CCN concentration as a function of supersaturation were constructed from the integrated CCN and size distribution data. The spectra were fit to a two mode hypergeometric model (Cohard et al., 1998) to estimate cloud droplet number concentration for a range of updraft velocity.

The albedo change (ΔA_c) of near-shore marine stratocumulus during PGF episodes was determined using equation 7 in Platnick and Twomey (1994):

$$\Delta A_c = \left[A_C(1 - A_C)\left(\chi^{\frac{1}{3}} - 1\right)\right]\left[A_C\left(\chi^{\frac{1}{3}} - 1\right) + 1\right]^{-1},$$

where $\chi = N_{PGF}/N_{CTL}$ is the ratio of CDNC in PGF conditions to CDNC in CTL periods. This analytical formulation relies upon the assumptions of conservative scattering, nearly invariant asymmetry parameter, and constant liquid water path. Furthermore, the estimate we present herein of albedo change during PGF episodes assumes that marine stratocumulus clouds are present near Bodega Bay during PGF and that they are not overtopped by higher cloud layers. The validity of each assumption will be briefly discussed.

- Conservative scattering: This assumption is commonly invoked in studies that estimate cloud albedo susceptibility or change (Twomey, 1991; Platnick and Towmey, 1994; Hill et al., 2008a,b; Hill et al., 2009; Chen et al., 2011). Liquid cloud particles are generally conservative (single scattering albedo ~ 1.0) for small to moderate cloud optical depth ($\tau_c < 23.0$). As we will demonstrate, marine cumulus and stratocumulus cloud layers are nearly always below this threshold during PGF.
- Invariant asymmetry: For visible light, cloud droplet scattering asymmetry varies weakly with particle size (Kokhanovsky, 2004). For liquid drops, the variation is primarily by approximately 5% over the range of effective radius from 6 μm to 19 μm. We will demonstrate that the estimated change in liquid drop effective radius during and near PGF periods lies well within this range.
- Constant liquid water path: This is the least likely of the above listed assumptions to be valid. Cloud albedo is susceptible to changes in both cloud droplet number concentration and cloud liquid water path. The latter can also vary with cloud droplet number concentration through

cloud dynamics pathways including the so-called "evaporation-entrainment" and "sedimentation-entrainment" effects (Lu et al., 2005; Wood et al., 2007; Hill et al., 2009; Chen et al., 2011). The impact of these feedbacks to cloud albedo through the dynamics that control cloud liquid water path vary strongly with environmental conditions, and in some cases can cancel the direct increase in cloud albedo resulting from an increase in cloud droplet number concentration. Environmental conditions during PGF (greater likelihood of very dry air above the marine boundary layer, and an increase in large-scale subsidence and thus increased low-level static stability) have been found to favor competing effects on susceptibility through the entrainment effects (e.g. Wood et al., 2007; Chen et al., 2011) The strength of the entrainment feedbacks is strongly dependent on sea surface temperature as well. PGF can occur under a wide range of sea-surface temperatures arising from natural variability in the northeastern Pacific Ocean. To disentangle the total susceptibility which may arise from these competing liquid water path feedbacks, a series of large-scale eddy simulations, similar to those in Lu et al. (2005) and Chen et al. (2011), are required. This is beyond the scope of the current study, thus we will only estimate the so-called "Twomey Effect" (or cloud albedo first aerosol indirect effect) on albedo which corresponds to the increase in cloud albedo due to an increase in CCN concentration when liquid water path is held fixed.

The MODIS level-2 cloud products provide swath-level retrievals of liquid cloud optical depth, liquid cloud effective radius, and cloud top pressure twice daily during daylight hours from descending (Terra – 10:15 local time) and ascending (Aqua – 13:45 local time) sun-synchronous orbits. The level 2 cloud products have a nominal spatial resolution of 20 km. For this study, daytime retrievals during PGF conditions from the expanded catalogue (N06 PGF events plus Table 2.3 from this study) during the MODIS operational period (2002 – present) were screened

to remove pixels over land or more than 75 km from the coast (offshore extent of PGF airmass found by aircraft and reported in N06) and pixels which likely did not correspond to low-level cumulus or stratocumulus. We followed the cloud type definitions (e.g. Figure 2 from Rossow and Schiffer, 1999) from the International Satellite Cloud Climatology Project (ISCCP) that rely upon thresholds of both cloud top pressure and cloud optical depth. Pixels for which no cloud information was retrieved were also discarded (no cloud present, or retrieval algorithm failed). The retrieved effective radius was also retained to judge the suitability of the invariant asymmetry assumption. The cloud albedo change reported is thus the estimate of the Twomey effect on albedo during PGF episodes when marine cumulus or stratocumulus are present with clear sky above marine low level clouds.

2.5 Results and discussion

2.5.1 Description of PGF cases observed during CalWater-2015

Table 2.3 lists all cases which fit the mPGF requirements during CalWater -015. Hereafter, these will be referred to as PGF(1-5). Some key parameters which describe the PGF layer flow measured by the 449 MHz radar are also summarized in Table 2.3, along with their 67 case rank (62 cases from N06 plus 5 from CalWater-2015). Note that in all 5 cases, both mPGF and elevated CO are met for a majority of the period, however the listed start time and duration in Table 2.3 is for mPGF, and in some cases the duration for PGF may be shorter than that listed when the additional elevated CO constraint is enforced.

2.5.2 Airmass properties during PGF

Figure 2.3 shows a box and whisker plot for the peripheral instrument data. So that all measurements fall on the same scale, each measurement has been normalized according to its all-study mean (μ_{all}) and has been plotted according to its natural logarithm. For CO, NO_x, and CN,

the interquartile range during PGF lies entirely above (or nearly so in the case of CN) the interquartile range during CTL. The difference in normalized concentration is most dramatic for NO_x, for which the minimum hourly concentration during PGF is nearly the median CTL concentration and the maximum CTL concentration is nearly the median PGF concentration. Median APS number concentration integrated from 542 nm to 19,810 nm (n^{APS}) is not preferentially higher during PGF, CTL or ALL hourly periods, though the range of n^{APS} for each period varies slightly. $PM_{2.5}$ is more likely to be elevated during PGF, but its interquartile range overlaps with the interquartile range of $PM_{2.5}$ during CTL and ALL hourly periods. Mean PM2.5 during ALL hourly periods is estimated to be 14.7±11.6 μg m^{-3}. Mean PM2.5 during CTL periods is estimated to be 14.0±11.9 μg m^{-3}. This estimate increases to 22.9±16.0 μg m^{-3} during PGF, a mean increase of 64 percent.

Figure 2.3 also displays wind rose diagrams for ALL and CTL periods. The distribution of wind directions and speeds during CTL suggest that these periods are dominated by the land-sea breeze diurnal cycle (BML is situated just east of a shoreline oriented NNW to SSE). The wind rose for PGF is not shown, since wind direction was used in the algorithm for defining PGF.

The range of normalized hourly $\sigma_{ATN}(\lambda)$ values measured during PGF, CTL and LOCAL periods are shown in Figure 2.4. The normalization method follows that used in Fig. 2.3. As discussed in the methods section, absolute values are uncorrected and thus not reported. The median and upper/lower quartile values of σ_{ATN} were compared to published work (Table 1, Chung et al., 2012) and it was found that they are reasonable for the location and concentration/type of aerosols measured. It should be noted that absorption coefficient median and interquartile ranges are highest during PGF, followed by LOCAL and CTL and that highest maximum values of σ_{ATN} are observed during LOCAL. The AAE derived from the visible light channels for each period is reported in

the figure annotation. The AAE (0.98 +/- 0.21) during PGF is very close to 1.0, which is widely accepted to be indicative of fresh soot (Chung et al., 2012). Fig. 2.4 shows that AAE during CTL (0.87 +/- 0.10) decreases during PGF. AAE is expected to decrease with soot particle age (accumulation of organic and nitrate on the particle surfaces). A possible explanation for the decrease in CTL AAE wrt. PGF is that during PGF direct lower tropospheric transport through the Petaluma Gap brings CV and SFBA brings more freshly emitted soot particles to the measurement site. During CTL periods, fewer soot particles are present (lower absorption coefficient), and those that are measured by the aethalometer have been further aged. In section 2.5.4, this conclusion is supported by single particle mixing state analysis which shows that organic to elemental carbon ratio decreases during PGF periods compared to CTL. The AAE during LOCAL periods is highest at 1.17 +/- 0.11. This value is closer to that reported for biomass burning (Clarke et al., 2007; Lewis et al., 2008) than is the AAE during PGF or CTL.

Figure 2.5 shows the average merged size distributions for PGF and CTL sampling periods. CTL periods were marked by lower particle concentrations in the submicron mode and higher in the coarse mode (D_p > 1.0 μm). CTL periods often experienced westerly flows and would be expected to be dominated by marine aerosol from the Pacific Ocean. The marine boundary layer over the remote ocean is typified by low particle concentrations and a significant supermicron mode (Quinn et al., 2015). Integrated average supermicron counts on the APS during CTL periods were 14.9 cm^{-3}, compared to 2.4 cm^{-3} for PGF periods, a decrease of 84%. The Fig. 2.5b is a $\log_{10}$-$\log_{10}$ plot of D_p, and shows supermicron particles concentrations approximately an order of magnitude greater. Single particle composition data from the ATOFMS during these time periods, discussed more in section 2.5.3, confirmed that the increase in coarse mode particles could be attributed to greater concentrations of marine-type particles.

PGF events, in contrast, showed a large increase in the number of particles with $D_p < 1.0$ μm, and a new ultrafine mode with mode diameter $D_p = 36$ nm. The Fig. 2.5a shows this relationship more clearly, and the corresponding decrease in coarse mode particles. CN increased by 110% during PGF compared to CTL, from 311.0 cm^{-3} to 650.9 cm^{-3}, These results were also expected, because continental, anthropogenically-influenced airmasses typically contain smaller and more numerous particles (Tunved et al., 2005). This increase in particle number during PGF events was correlated with the increase in $PM_{2.5}$ as shown in Fig. 2.2.

2.5.3 Aerosol particle types

PGF conditions coincide with a shift in particle type away from marine and towards continental. Figure 2.6 shows pie charts of the sub- and super-micron particle populations for CTL vs PGF. Percentages indicate the number fraction of particles assigned to the corresponding particle type. The total hit rate for all particles were 20.8%. Panels (a) and (b) show the submicron (0.2-1.0μm) particle number fraction by type during CTL (1,222,274 particles) and PGF (164,952 particles), respectively. PGF had approximately the same level of submicron biomass burning particles (BB). However, there was a large increase in elemental carbon/organic carbon (ECOC) (20-28%) and ammonium nitrate (AN) (10-28%) particle types. These two types have both been linked to anthropogenic activity. The ECOC type has been observed before with the aging of fuel emissions (Hughes 2000) in the Los Angeles basin during stagnant conditions with high pollutant concentrations. Similarly, the California Central Valley is an area of elevated hydrocarbon fuel emissions and frequent long-lived lower tropospheric inversions, and might be expected to support the formation of ECOC particles. AN particles have been linked to the accumulation of ammonia and nitric acid on particles (Qin et al., 2012) and nucleation by reactions between ammonia and nitric acid (Russell and Cass, 1986; Hughes et al., 2002), gases strongly correlated with

anthropogenic activity. Marine aerosols make up a sizable fration of submicron particles during CTL (SS and Aged SS). However, these particles are much less prominent during PGF. The increase in ECOC and AN and decrease in marine particle types reinforce the conclusion that PGF airmasses originate continentally and have strong anthropogenic character.

The clearest delineation in particle type was observed in the supermicron fraction (1.0-3.0 μm). Panels (c) and (d) of Fig. 2.6 show that over 90% of CTL supermicron particles (544,612 total particles) were either fresh or aged marine particles, while less than 20% were of marine origin during PGF. During PGF, supermicron particles (25,457 total particles) were comprised of primarily BB, ECOC, AN and elemental carbon (EC), a byproduct of fuel combustion. Additionally, the majority of PGF marine particles showed markers of reacting with nitric acid (Gard et al., 1998). This contrasts CTL marine particles, which were primarily unreacted.

The Dust and Dust/Bio types also increased during PGF. The CV, despite its agricultural production, is a semi-arid environment and can be a significant source of dust. Conversely, BML airmasses during CTL periods were heavily influenced by the Pacific Ocean and thus were not expected to contain much dust. The shift in supermicron particles composition away from marine particles to anthropogenic and dust particle types supports the conclusion that PGF airmasses likely originate from the CV.

2.5.4 Aging processes observed through secondary species markers

Figure 2.7 shows the sulfate:nitrate ratio (SN) of particles separated by type. Unmodified peak ratios are dependent upon which peak is in the denominator, i.e. whether or not the ratio is greater than 1, thus potentially skewing the data. To account for this, we calculated the normalized peak ratio by the following: ratio > 1, normalized peak ratio = 1-(1/ratio); ratio < 1, normalized peak ratio = ratio -1; and ratio = 1, normalized peak ratio = 0. As ratios approach −1 or 1, they are

exponentially increasing, while close to zero, the RPA of each species is essentially the same. This results in a broader range of ratios for bins near −1 or 1, while the bins near 0 bins include a smaller range of ratios. The left panel depicts the SN for CTL particles. The majority of particles showed higher SN ratios, indicating that aging primarily occurred through the accumulation of sulfate. The exception to this rule was the SS type, which can react with NOx species in a displacement reaction to liberate HCl (Gard et al., 1998; Cahill et al., 2012). PGF particles showed a SN ratio biased toward nitrate accumulation, indicating that the primary and most important aging mechanism was through NOx pathways.

In addition to probing the partitioning of acidic species, basic species like amines and ammonium were investigated. Figure 2.8 shows the normalized ratio for amines:ammonium ratio (AA). The AA for CTL particles shows fairly equal partitioning for all particle types. During PGF the average peak area of amine peaks (58C2H5NHCH2+, 59NC3H9+, 86(C2H5)2NCH2+) in particles actually increased, but the AA ratio shifted toward ammonium because the ammonium content of particles increased much more. The area surrounding BML contains animal husbandry, but no industrial-scale farming. The shift in basic species partitioning indicates that PGF particles originate from a large source of ammonium. The CV region contains many more industrial-scale farms where ammonium is employed, and thus this change in aging shows that the PGF airmass likely originates within the CV.

Previous studies (Cahill et al., 2012) have used the ATOFMS to determine the internal mixing state of carbonaceous particles. Figure 2.9 shows the organic carbon:soot ratio as calculated by the ATOFMS, seperated by particle type. CTL particles appear to have relatively higher amounts of OC, most notably in the Amine particle types and, unsurprisingly, the OC type. Amines consist of organic carbon chains bound to Nitrogen atoms, so it is also unsurprising that these

particles would have high OC:EC ratios. The ratio plot indicates that PGF particles contain more EC relative to CTL particles. This is despite the appearance of the AN particle type, which had greater OC character. These OC/EC ratio plots agree with the aethalometer-derived AAE, which suggest that the soot was less aged during PGF than during CTL periods.

In summary this analysis shows that the preeminent aging mechanisms associated with PGF are the accumulation of ammonium and nitrate, in accordance with previous studies on Central Valley particle composition (Qin et al., 2006). Amine accumulation was also observed in ECOC and AN particless, but was determined to not be as significant as ammonium. Accumulation of nitrogen species on aerosol particles is important as it increases the risk of nitrogen deposition into coastal waters, which can lead to ecosystem degradation (Ryther and Dunstan, 1971; Paerl, 1995; Paerl, 1997). The shift toward internal mixtures containing elemental carbon and away from particulate matter containing primarily organic carbonaceous species during PGF suggests that gap flow may cause increased solar absorption by near surface aerosols, especially in visible wavelengths. This potential impact is corroborated by the aethalometer PGF and CTL measurements.

2.5.5 CCN and cloud droplet spectra

Figure 2.10 displays the cumulative CCN supersaturation spectrum (versus liquid supersaturation) transformed from the size-resolved CCN data and the cloud droplet number concentration (CDNC) for updraft velocities between 0.1 m s-1 and 10 m s-1. CCN concentration is enhanced during PGF by 2.8 to 3.0 for a wide range of supersaturations. The increase in CCN is remarkably consistent across the range due to the confluence of two factors. First, the hygroscopicity parameter – or the contribution of particle chemistry to CCN activation – does not change significantly between PGF and CTL (0.21 vs. 0.20). Second, particle concentrations are

larger for all sizes D < 500 nm during PGF events (Fig. 2.5). These sizes dominate the spectra in Fig. 2.10a. As a consequence CDNC increases across all considered cloud updraft speeds during PGF episodes. Figure 2.10b shows that CDNC increases between 125% and 145%, and that this relative increase is expected for all possible cloud types. In the results to follow concerning cloud albedo change during PGF, CDNC increases are considered as a ratio (i.e. $\chi = N\_PGF/N\_CTL$). In this framework, the average ratio, χ, is 2.35.

2.5.6 Impact of PGF on marine cumulus and stratocumulus albedo

During expanded catalog (see Methods) PGF episodes the observed cloud albedo ranged from 0.01 to 0.63, with upper (lower) quartile values of 0.43 (0.17). Using the observed Ac = 0.43 (0.17) and χ~2.35, equation 7 from Platnick and Twomey (1994) estimates that $\Delta A\_C/A\_C=0.28$ (0.16). Therefore, clouds that condense on PGF CCN without concomitant changes in liquid water path are expected to be 16% to 28% more reflective when considering the Twomey aerosol indirect effect. As discussed in the methods section, the values reported here correspond to PGF episodes where marine cumulus or stratocumulus are present within 75 km of the shoreline and when clear the marine cloud layer is topped by clear sky.

2.6 Summary

Measurements taken at Bodega Bay, CA during the CalWater-2015 intensive observing period were used to investigate the impacts of Petaluma Gap Flow on local air quality and marine cloud albedo. The kinematics of PGF and its relation to synoptic scale weather patterns and the Central Valley cold pool has been perviously described in N06. This study is the first attempt to quantify the impact of PGF on the boundary layer airmass and particle chemistry.

Vertically resolved lower tropospheric wind observations and carbon monoxide concentration were used to identify PGF periods during the CalWater-2015 intensive observing

period and separate these from CTL periods, during which the BML airmass was neither influenced by PGF or heavy pollutant loads from a local source. Five PGF events were identified during Calwater-2015 and were compared to the PGF catalog published in N06 by means of their local weather attributes.

During Calwater-2015 PGF periods, several measures of anthropogenic pollution, including CO, NO_x CN, and black carbon mass concentration estimated by a multi-channel Aethamometer, were consistently elevated when compared to CTL periods. Using SMPS and APS aerosol size spectrometers, we found that aerosol number concentrations increase by 110% in the submicron size range, while decreasing 84% in the supermicron size range. Both PGF and CTL periods presented size distributions with a similar accumulation mode near 100 nm. The PGF period composite size distribution contained a prominent mode below 50 nm which was not present in the CTL composite. This fine mode indicates that particle source and/or degree of particle chemical aging may be significantly different during PGF periods. The particle chemistry of this fine mode could not be investigated because the relevant size are below the lower detection limit of the UF-ATOFMS PGF periods contained 84% fewer coarse mode particles than did CTL periods. The relative lack of particles at these sizes is related to a significant change in super-micron particle chemistry found by analyzing single particle mass spectra. Taken together, the above results demonstrate the change in aerosol physicochemical properties during PGF events.

Single particle chemical mixing state during PGF events was investigated using UF-ATOFMS and ATOFMS Measurements. It was found that submicron particle populations change during PGF to favor ECOC, BB, AN, and EC types at the expense of SS types. The large difference in supermicron particle mixing state is likely related to the shift in prominent wind direction during PGF. The analysis of secondary aging also showed that carbonaceous particles are more likely to

contain elemental carbon than organic carbon during PGF episodes. Aethalometer-derived AAE also suggested that observed soot was less aged during PGF periods but total absorption and total black carbon mass were greater than during CTL. The above results reinforce the hypothesis that PGF could lead to an increase in absorption of solar shortwave radiation by black carbon aerosol, which may be associated with more freshly emitted soot.

PGF and CTL single particle mass spectra relative peak area ratios were used to investigate particle aging mechanism. PGF particles were much more likely to acquire nitrate than CTL particles, which preferentially contained sulfate. This was especially true for AN, ECOC, BB, and EC particle types during PGF, but may not appply to SS and Aged SS, which showed a preference for nitrate aging even during CTL periods. The aging of SS by nitrate is a well-documented phenomenon that was also regularly observed during CalWater-2015. Relative peak area analysis also showed that particles are much more likely to chemically age by ammonium than by amines during PGF. This tendency appeared especially strong for BB, EC and ECOC types. While OC type particles increased in relative number during PGF episodes, they appeared to favor the amine aging pathway even during PGF. Together the above results reinforce the hypothesis that PGF could lead to increased deposition of nitrogen containing particulate matter to the local ecosystem near and offshore of Bodega Bay. This result may also be true in other coastal locations which are periodically influenced by offshore gap flow originating in a NO_x and ammonia enriched airmass (e.g. the nearby Salinas Valley, and offshore of the Golden Gate). If increased nitrogen deposition is occurring during PGF episodes, it could lead to eutrophication and algal blooms, as suggested by Paerl (1995; 1997).

Particle hygroscopicity, as shown by size-resolved CCNc measurements, was nearly invariant between PGF and CTL periods. The model of Cohard et al. (1998) was used to estimate

the cloud droplet number concentration resulting from the derived CCN activation curves (section 2.4.5). The increase found in CDNC was stable across a wide range of updraft velocities. The marine cloud albedo change in response to PGF CCN was estimated using MODIS level 2 cloud products and equation 7 from Platnick and Twomey (1994). To first order (assuming constant liquid water path) it is estimated that near shore marine clouds will brighten by 16% to 28% percent (interquartile range) in visible wavelengths during PGF events. This finding supports the hypothesis that PGF conditions may lead to a brightening in near-shore marine stratocumulus clouds through the cloud albedo indirect effect.

The conclusions reached in addressing the three hypotheses posed in this study represent only the first attempt to characterize the impact of Petaluma Gap Flow on the aerosol direct effect, aerosol indirect effect and coastal environment in Northern Central California. Due to the relatively short CalWater-2 intensive observing campaign, these results were drawn from only 5 PGF events. The data necessary to investigate these hypotheses was drawn from a large multi-agency effort including many specialized and operator intensive measurements, which by nature must be short in duration. Longer term observation, perhaps by less detailed but targeted chemical observations at similar locations could significantly augment the findings presented here.

During this study, we attempted to detect inter-event differences in relative peak area ratios for secondary aging indicators, but no significant change was observed. In addition, the authors wish to comment that many of the assumptions made (e.g. constant liquid water path) in estimating the impact of PGF on marine cloud albedo change can only be discarded through airborne observations or modeling studies. These were considered beyond the scope of this study, but may be valuable future investigations to fully describe the impact of polluted offshore-directed gap flow on marine cloud brightness.

The findings presented herein demonstrate that PGF can impact aerosol number, chemical aging pathways, shortwave absorption and the number of CCN available to near-shore marine clouds. These findings are the first of their kind that result from direct observation of an intermittent weather phenomenon that brings anthropogenic pollutants to an otherwise remote region. While the findings follow from in-situ observations representative of a small region, we note that the meteorological factors causing Petaluma Gap flow (pooling of cold continental air, an onshore, mountain-normal directed pressure gradient, a narrow low-elevation gap in the coastal mountain range) certainly exist in other regions. Thus, the introduction of anthropogenically influenced continental air to remote marine environments may modify air quality, aerosol direct and indirect effects in other regions experiencing regular offshore gap flow as well. The authors argue that further study of the chemical composition of continental outflow in other regions is necessary to refine current understanding of the impact of human activities on the environment.

2.7 Acknowledgements

The authors thank all other CalWater and ACAPEX 2015 participants including those from Pacific Northwest National Laboratories, The National Oceanic and Atmospheric Administration, NASA Jet Propulsion Laboratory, the Naval Research Laboratory, University of California, Davis, Scripps Institution of Oceanography, Colorado State University and North Carolina State University. The authors would also like to thank the UC Davis Bodega Marine Laboratory for the use of laboratory and office space and shipping and physical plant support while collecting data, as well as the California Air Resources Board and the National Park Service for the trailers used for sampling. This research was funded by NSF award number 1451347 (ACM, GCC, KAM, KAP), NSF award number 1450690 (MDP, NR, HT), and NSF award number 1450760 (SAA, SMK, PJD).

Chapter 2, in full, is a reprint of material as it appears in Atmospheric Chemistry and Physics 2017. Martin, A. C., Cornwell, G. C., Atwood, S. A., Moore, K. A., Rothfuss, N. E., Taylor, H., DeMott, P. J., Kreidenweiss, S. M., Petters, M. D., Prather, K. A. (2017). Transport of pollution to a remote coastal site during gap flow from California's interior: impacts on aerosol composition, clouds, and radiative balance. Atmospheric Chemistry and Physics 17, 1491-1509. Reproduced with permission from the European Geophysical Union.

2.8 Figures

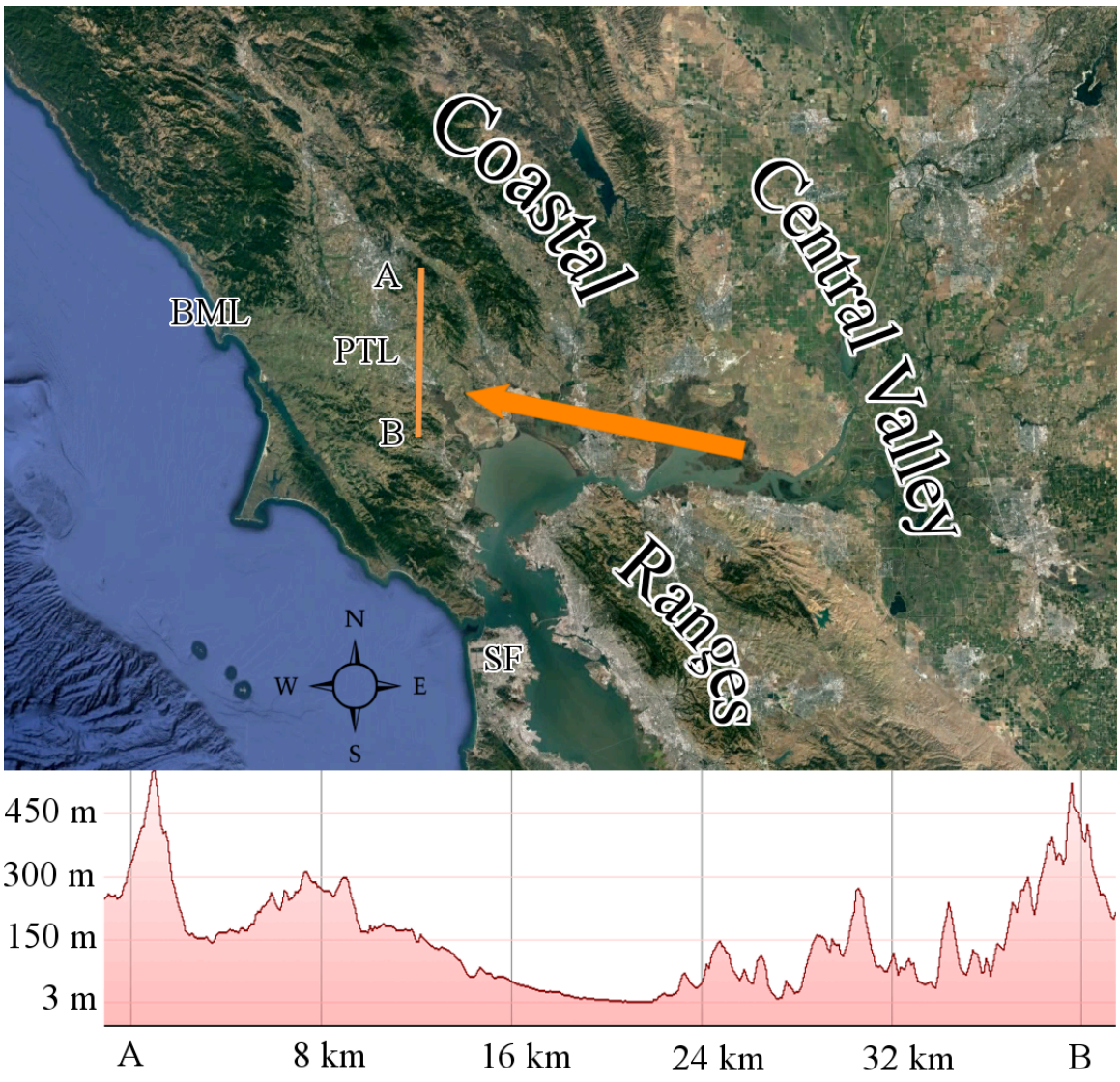

Figure 2.1. Regional map displaying the location of BML, the town of Petaluma, CA (PTL), San Francisco, CA (SF), the Central Valley and the Coastal Ranges. The Orange Arrow depicts the direction of typical flow during PGF conditions. Line A-B traces a path across the Petaluma Gap. The inset at bottom displays the cross-gap terrain profile along line A-B.

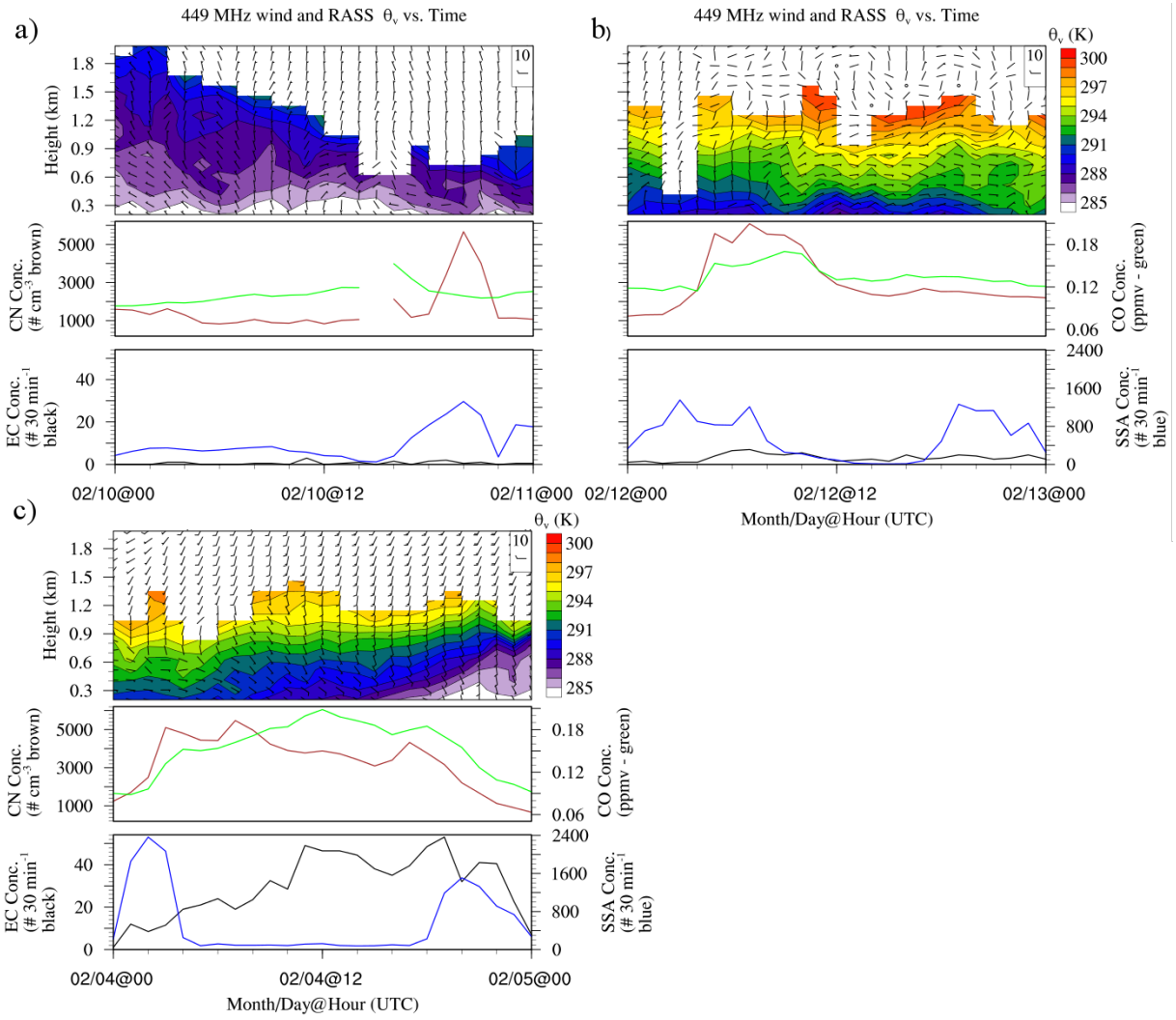

Figure 2.2. a) Horizontal wind barb and θ_v every 100 meters from 300 m AGL to 1900 m AGL from NOAA-ESRL 449 MHz wind prifiling radar and RASS at BBY (top), hourly CO concentration (ppmv – green) and CN (# cm^{-3} – brown) (middle), Number particles classified as EC or Aged EC (black) and SS or Aged SS (blue) per 30 minute interval from ATOFMS (bottom) during a 24 hour period (02/10/2015) calssified as CTL. b) as in a, except for a 24 hour period (02/12/2015) classified as LOCAL. c) as in a, except for the 24 hours surrounding PGF 4.

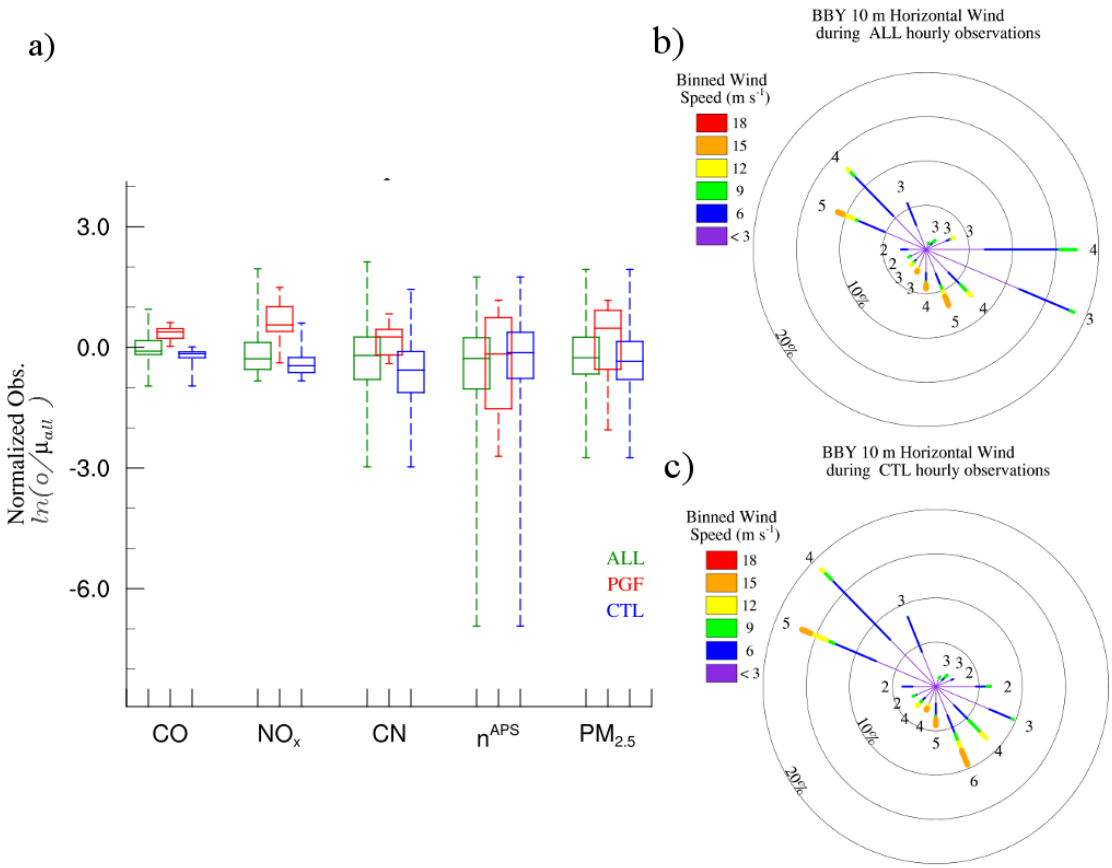

Figure 2.3. a) Box and whisker plot displaying normalized peripheral measurements during all (ALL – green) hourly CalWater-2015 periods, PGF (PGF – red) periods, and CTL (CTL – blue) periods. b) BBY 10 m wind rose diagram for ALL. Rings represent probability of wind from displayed direction, petals represent relative distribution of wind speeds (color bar - m s^{-1}) from the given direction. c) As in b, except for CTL periods.

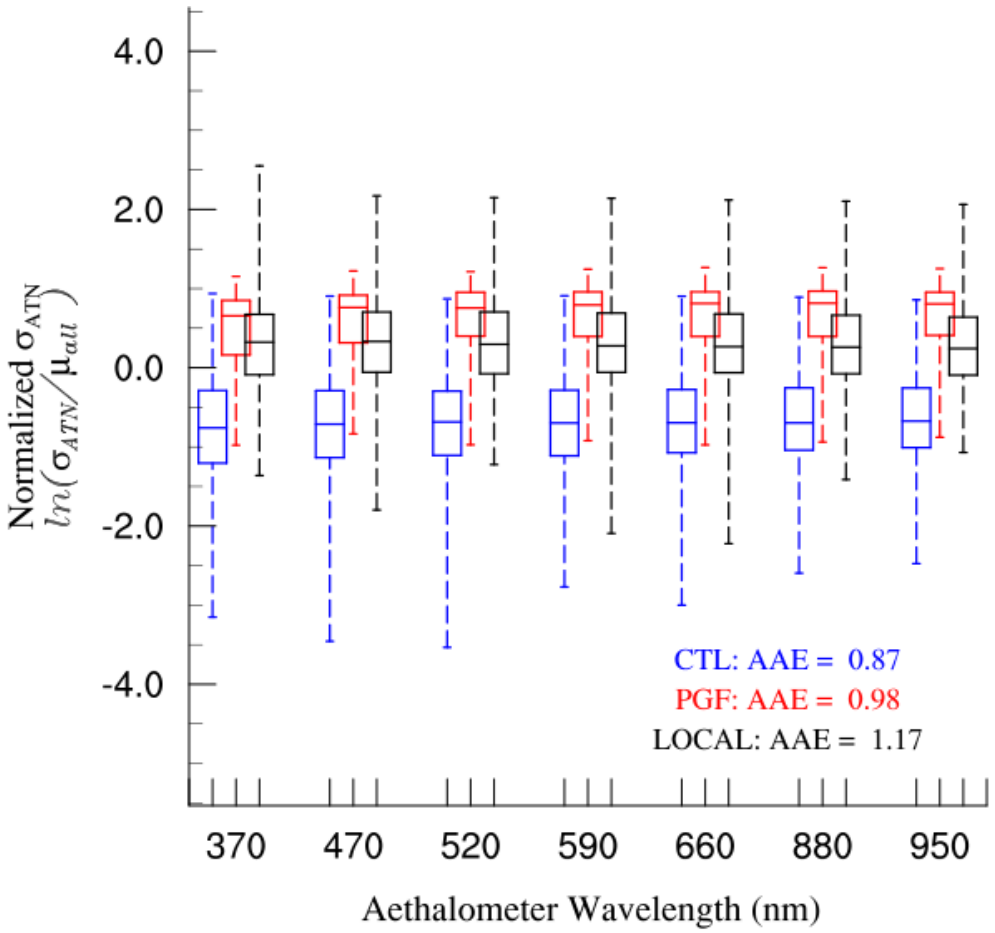

Figure 2.4. Normalized Aethalometer Light Absorption Coefficient at seven wavelengths for hourly periods classified as CTL (blue), PGF (red) and LOCAL (black). Upper/Lower box bounds represent upper/lower 25% values, respectively. Upper/Lower whiskers represent max/min values respectively. Box middle represents median value. Also displayed are the AAE values found by regression during each period.

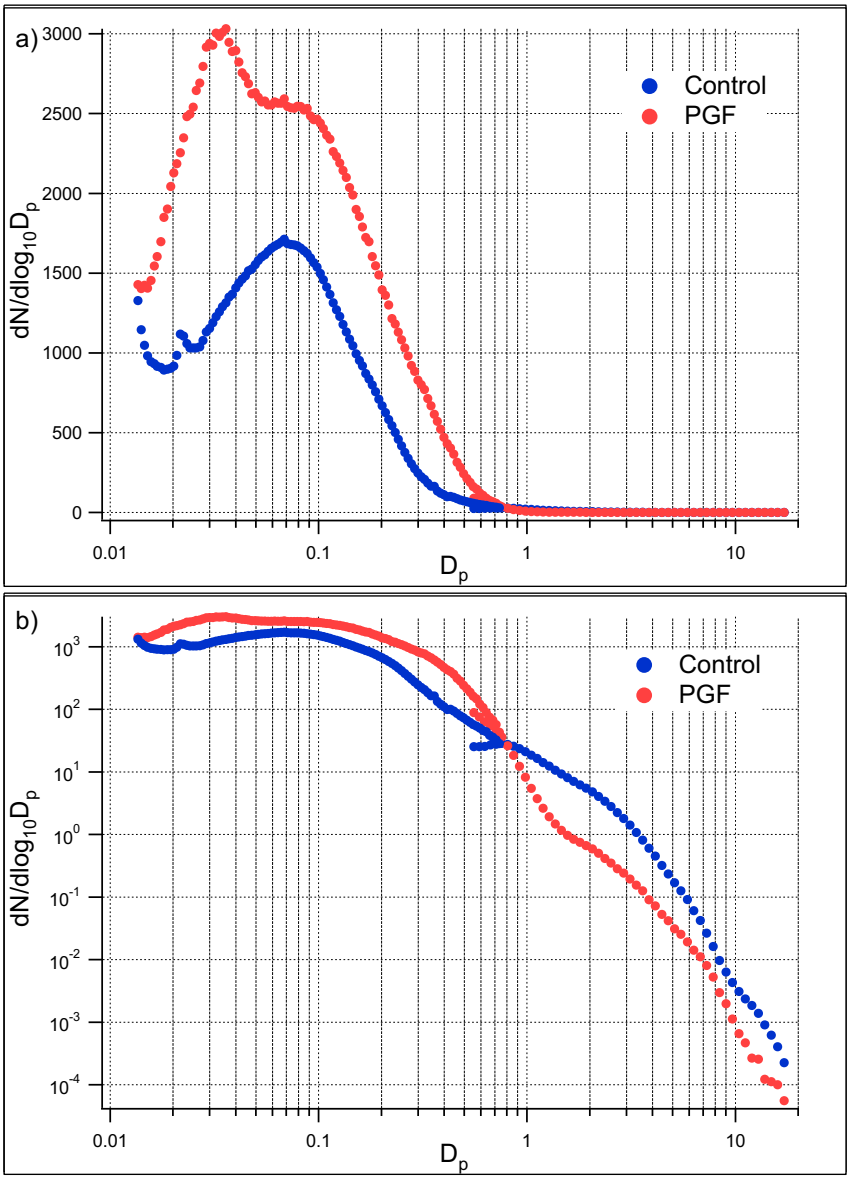

Figure 2.5. a) Composite merged SMPS-APS size distribution displayed as $dN/dlog10D_p$ for PGF (red) and CTL (blue) periods. b) as in a, except displayed on a log-axis.

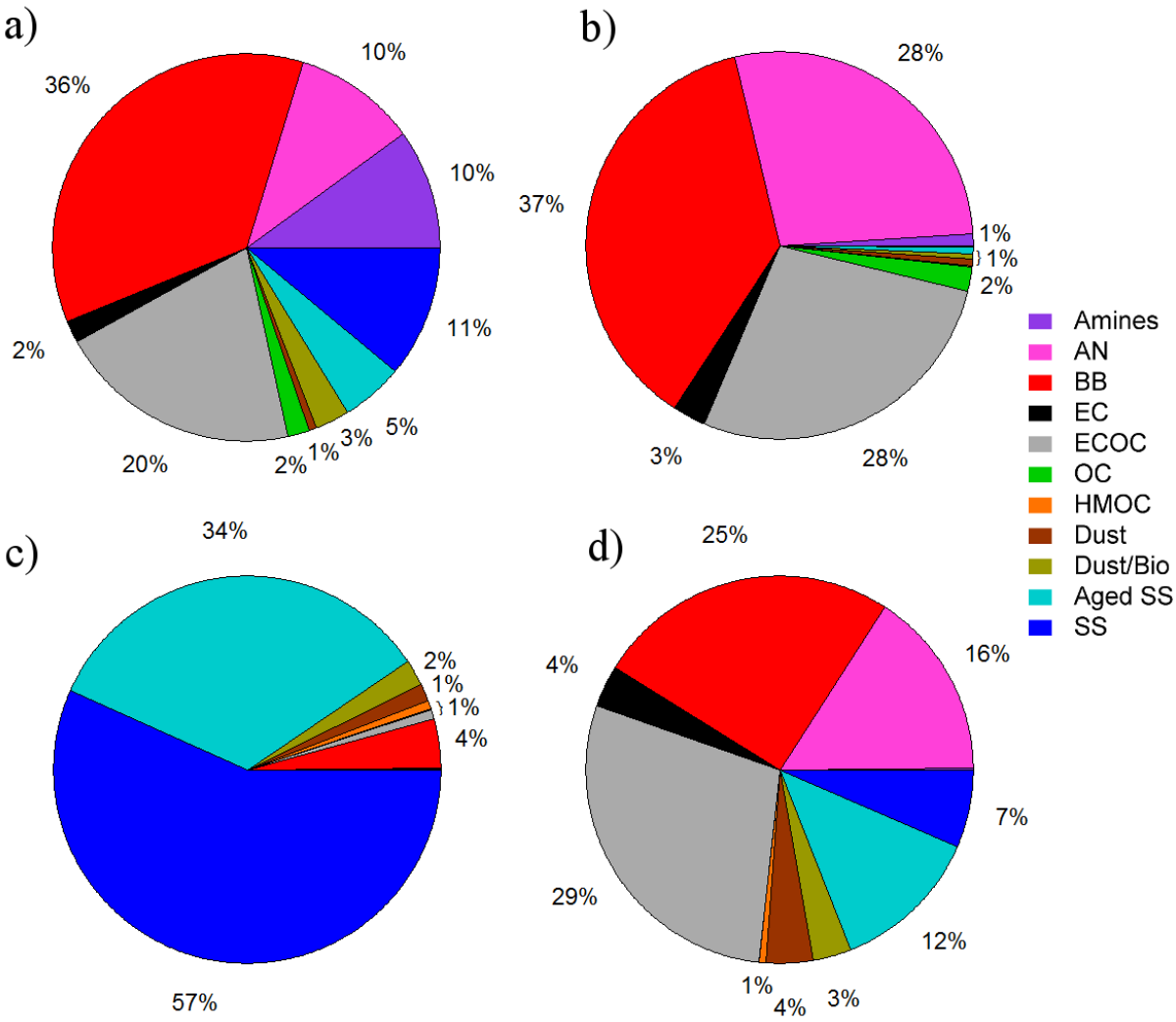

Figure 2.6. Pie charts for sub- (top panels) and supermicron (bottom panels) particle types for CTL (left panels) and PGF (right panels). Description of particle classifications can be found in Table 2.2.

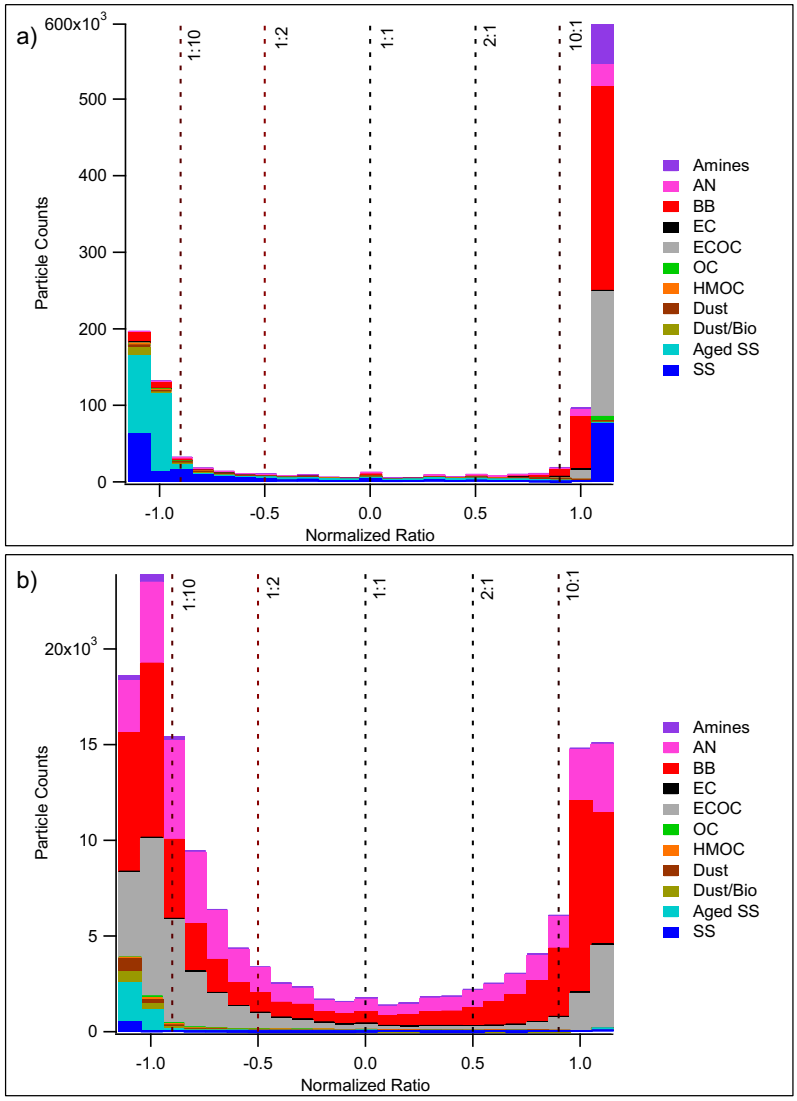

Figure 2.7. a) Particle sulfate:nitrate ion ratio distribution for CTL periods. Values <0 indicate more nitrate than sulfate and values>0 indicate more sulfate than nitrate. Ratios representing 1:1, 2:1, and 10:1 are shown by vertical dashed lines. Significant particle types are represented by separate colors. b) as in a), except during PGF periods.

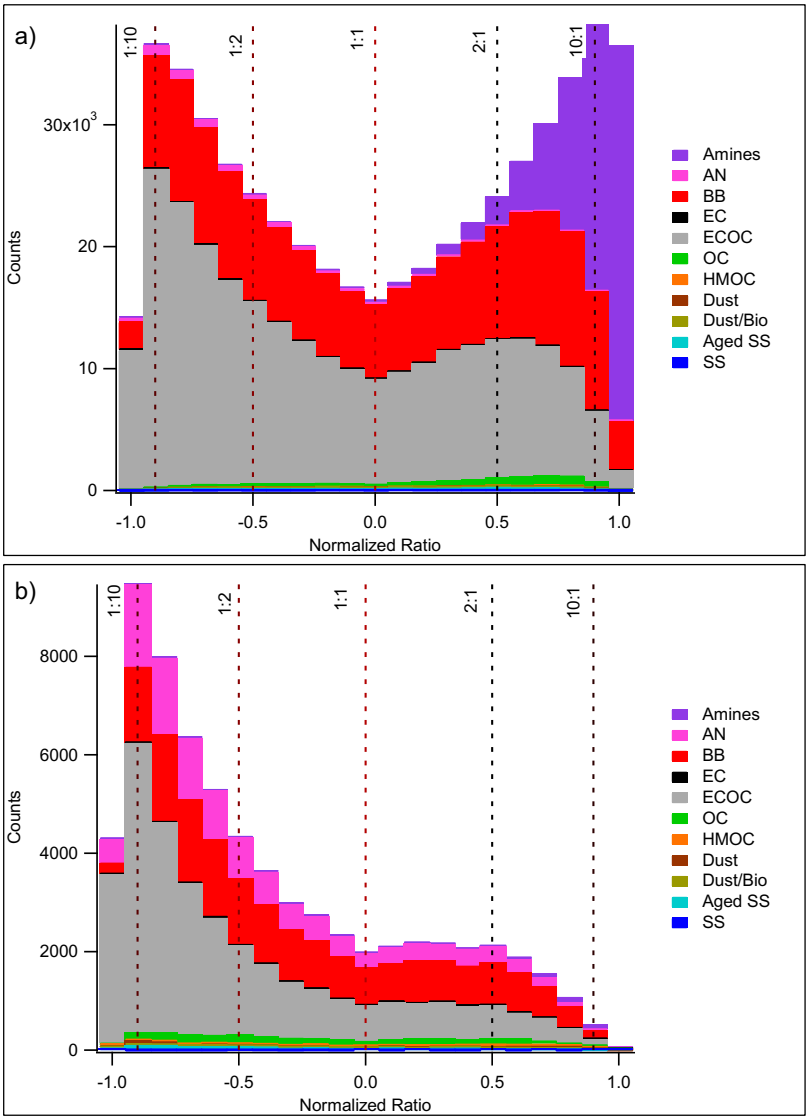

Figure 2.8. As in Figure 2.7, except amines:ammonium ion ratio distributions are shown.

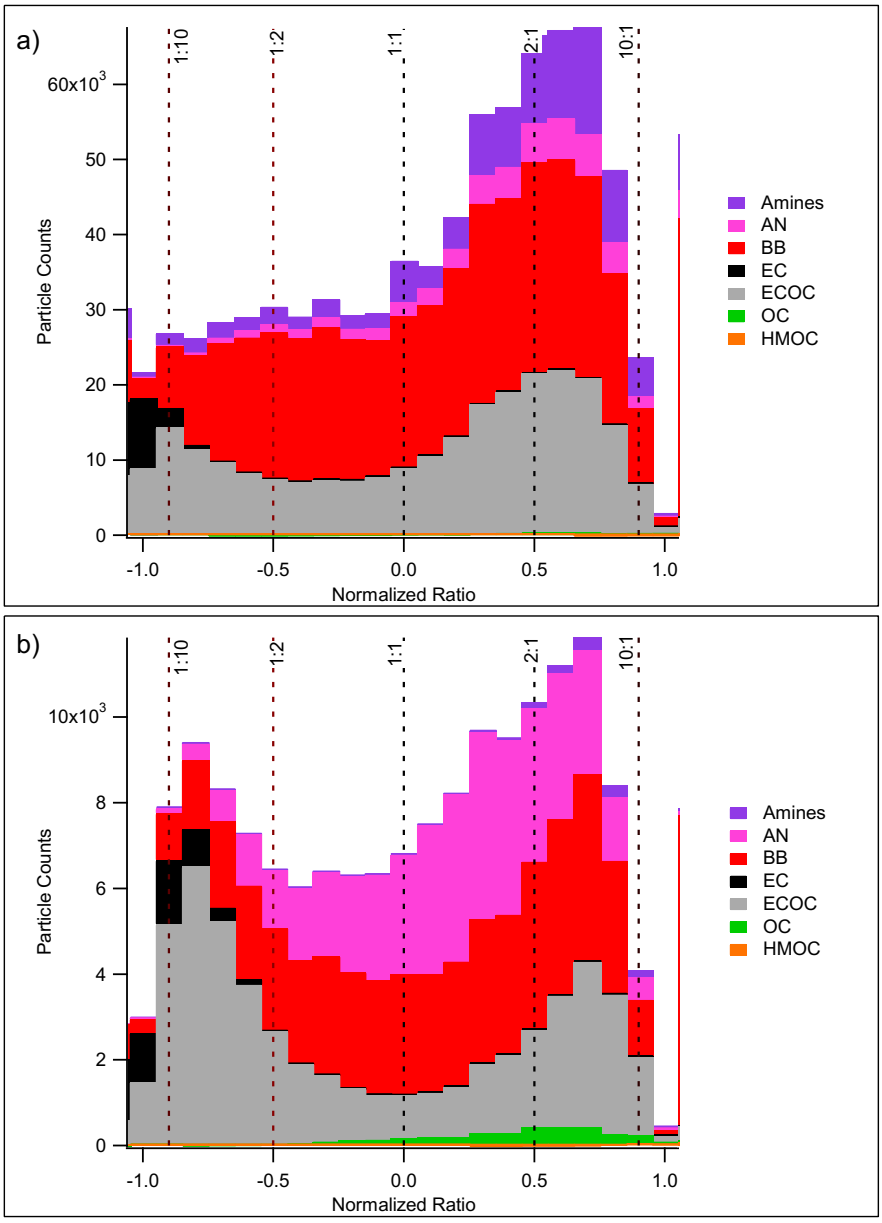

Figure 2.9. As in Figure 2.7, except OC:soot ion ratio distributions are shown.

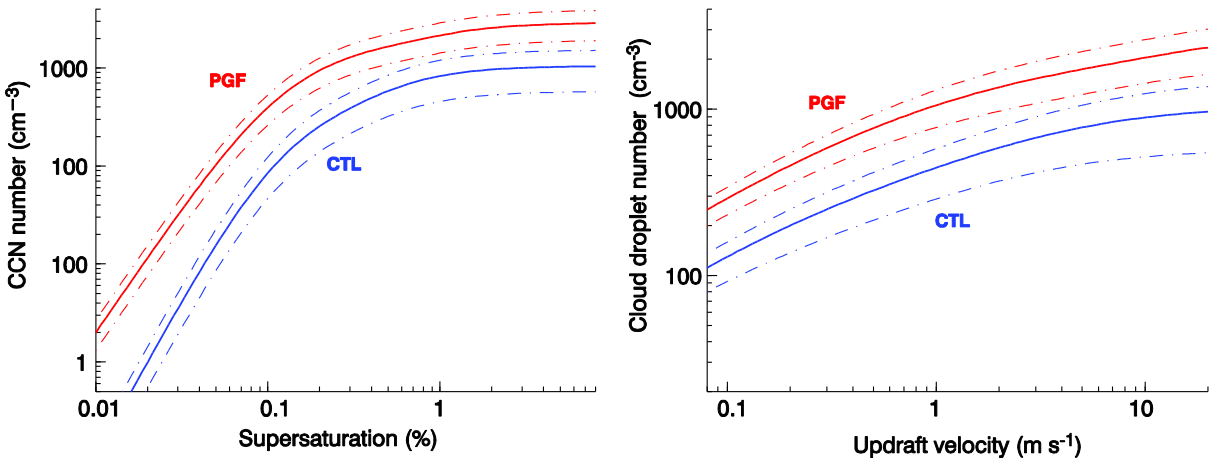

Figure 2.10. Left) cumulative median CCN supersaturation spectrum PGF periods (blue) and CTL (yellow). Dashed lines approximate the interquartile range. Right) as in left, except for predicted cloud droplet number concentration as a function of updraft velocity.

2.9 Tables

Table 2.1. Decision tree used for filtering measurement periods, and the resulting number of hourly periods (/total) in each category.

Decision Criteria	3 PGF Criteria at BBY (Neiman et al., 2006)		
CO conc. greater		Y	N
than $\mu + 2\sigma$	Y	PGF (55/1248)	Local (407/1248)
(138.1 ppbv)	N	Onset/Diffuse (11/1248)	CTL (775/1248)

Table 2.2. Summary of particle types determined by ATOFMS and their characteristic ion markers.

Particle Type	Characteristic Peaks
Amines	$^{58}C_2H_5NHCH_2^+$, $^{86}(C_2H_5)_2NCH_2^+$ (Angelino *et al.,* 2001; Pratt *et al.,* 2009; Qin *et al.,* 2012).
Ammonium nitrate (AN)	$^{18}NH_4^+$, $^{30}NO^+$, $^{46}NO_2^-$, $^{62}NO_3^-$, $^{97}HSO_4$-, $^{125}(HNO_3)NO_3^-$ (Pastor *et al.,* 2003; Qin *et al.,* 2012).
Biomass burning (BB)	Strong $^{39}K^+$ and $^{97}HSO_4^-$, less intense $^{12}C^+$, $^{26}CN^-$, $^{46}NO_2^-$, $^{62}NO_3^-$, $^{125}H(NO_3)_2^-$ (Silva *et al.,* 1999).
Elemental carbon (EC)	Carbon Clusters at C_n^+ and C_n^- (Moffett and Prather, 2009; Spencer and Prather, 2006).
Elemental carbon/organic carbon (ECOC)	$^{12}C^+$, $^{24}C_2^+$, $^{27}C_3^+$, $^{36}C_3^+$, $^{37}C_3H^+$, $^{43}CH_3CO^+/CHNO^+$ (Moffet and Prather 2009; Qin et al., 2012).
Organic carbon	$^{27}C_2H_3^+/CHN^+$, $^{37}C_3H^+$, $^{43}CHNO^+$ (Silva and Prather, 2000; Spencer and Prather, 2006; Qin et al., 2012).
High mass organic carbon (HMOC)	$^{37}C_3H^+$, $^{43}CHNO^+$, differences of 14-16 past 150 m/z, $^{46}NO_2^-$, $^{62}NO_3^-$, $^{97}HSO_4^-$ (Denkenberger et al., 2007; Qin et al., 2006)
Dust	Inorganic ions $^{6/7}Li^+$, $^{27}Al^+$, $^{39}K^+$, $^{40}Ca^+$, $^{48/64}Ti/TiO^+$, $^{54/56}Fe^+$, $^{60}SiO_2^-$, $^{76}SiO_3^-$, $^{79}PO_3^-$ (Silva et al., 2000).
Dust/bio	Same as Dust, but also with biological markers $^{26}CN^-$, $^{42}CNO^-$
Aged marine (Aged SS)	Same as Fresh Marine but also with $^{108}Na_2NO_3^+$, $^{46}NO_2^-$, $^{62}NO_3^-$, $^{147}Na(NO_3)_2^-$ (Gard *et al.,* 1998).
Fresh marine (SS)	$^{23}Na^+$, $^{24}Mg^+$, $^{39}K^+$, $^{40}Ca^+$, $^{81,83}Na_2Cl^+$, $^{35,37}Cl^-$, $^{58}NaCl^-$, $^{93,95,97}NaCl_2^-$, $^{151,153,155}Na_2Cl_3^-$ (Gard et al., 1998).

Table 2.3. PGF events observed during CalWater-2015 and their significant parameters following N06. Ranks are out of 67 (62 cases from N06 plus 5 from CalWater-2015).

Start date @ time (UTC)	Duration (hr) (rank)	Jet altitude (m MSL) (rank)	Jet maxima (m/s) (rank)	Jet dir. (degree)	Gap folding height (m MSL) (rank)	Vertical shear across folding alt (m/s) (rank)	Precipitation at BBY (mm) (rank)
1/14/2015 @ 1300	31 (5)	307 (47)	10.0 (16)	96	622 (20)	12.8 (46)	0 (67)
1/25/2015 @ 1100	8 (44)	1146 (1)	15.7 (2)	79	1776 (1)	3.7 (67)	0 (67)
1/26/2015 @ 1200	10 (33)	202 (47)	8.6 (37)	98	517 (28)	12.4 (48)	0 (67)
2/04/2015 @ 0700	9 (38)	202 (47)	8.8 (33)	122	517 (28)	7.8 (62)	0 (67)
3/05/2015 @ 1300	8 (44)	412 (6)	7.6 (56)	119	727 (12)	11.6 (50)	0 (67)

2.10 References

Aschmann, H.: Distribution and peculiarity of Mediterranean ecosystems, in: Mediterranean type ecosystems, pp. 11–19, Springer, 1973.

Bhave, P. V., Allen, J. O., Morrical, B. D., Fergenson, D. P., Cass, G. R., and Prather, K. A.: A field-based approach for determining ATOFMS instrument sensitivities to ammonium and nitrate, Env. Sci. & Tech., 36, 4868–4879, 2002.

Cahill, J., Suski, K., Seinfeld, J., Zaveri, R., and Prather, K.: The mixing state of carbonaceous aerosol particles in northern and southern California measured during CARES and CalNex 2010, *Atmos. Chem. Phys.*, 12, 10 989–11 002, 2012.

Chen, Y.-C., Xue, L., Lebo, Z., Wang, H., Rasmussen, R., and Seinfeld, J.: A comprehensive numerical study of aerosol-cloud-precipitation interactions in marine stratocumulus, Atm. Chem. Phys., 11, 9749– 9769, 2011.

Christensen, S. I. and Petters, M.: The role of temperature in cloud droplet activation, J. Phys. Chem. A, 116, 9706–9717, 2012.

Chung, C., Kim, S.-W., Lee, M., Yoon, S.-C., and Lee, S.: Carbonaceous aerosol AAE inferred from in-situ aerosol measurements at the Gosan ABC super site, and the implications for brown carbon aerosol, Atm. Chem. Phys., 12, 6173–6184, 2012.

Clarke, A., McNaughton, C., Kapustin, V., Shinozuka, Y., Howell, S., Dibb, J., Zhou, J., Anderson, B., Brekhovskikh, V., Turner, H., et al.: Biomass burning and pollution aerosol over North America: Organic components and their in- fluence on spectral optical properties and humidification response, J.Geo. Res.: Atmos., 112, 2007.

Cohard, J.-M., Pinty, J.-P., and Bedos, C.: Extending Twomey's analytical estimate of nucleated cloud droplet con- centrations from CCN spectra, J. Atmos. Sci., 55, 3348–3357, 1998.

Collaud Coen, M., Weingartner, E., Apituley, A., Ceburnis, D., Fierz-Schmidhauser, R., Flentje, H., Henzing, J., Jen- nings, S. G., Moerman, M., Petzold, A., et al.: Minimizing light absorption measurement artifacts of the Aethalome ter: evaluation of five correction algorithms, Atmos. Meas. Techn., 3, 457–474, 2010.

Colle, B. A., Loescher, K. A., Young, G. S., and Winstead, N. S.: Climatology of barrier jets along the Alaskan coast Part II: Large-scale and sounding composites, Mon. Weather Rev., 134, 454–477, 2006.

Dockery, D. W. and Pope, C. A.: Acute respiratory effects of particulate air pollution, Ann. Rev. Pub. Health., 15, 107–132, 1994.

Eldred, R. A., Cahill, T. A., and Flocchini, R. G.: Composition of PM2. 5 and PM10 Aerosols in the IMPROVE Network, J. Air Waste Ma., 47, 194–203, 1997.

Gard, E., Mayer, J. E., Morrical, B. D., Dienes, T., Fergenson, D. P., and Prather, K. A.: Real-time analysis of individual atmospheric aerosol particles: Design and performance of a portable ATOFMS, Anal. Chem., 69, 4083–4091, 1997.

Gard, E. E., Kleeman, M. J., Gross, D. S., Hughes, L. S., Allen, J. O., Morrical, B. D., Fergenson, D. P., Dienes, T., Ga¨lli, M. E., Johnson, R. J., et al.: Direct observation of heterogeneous chemistry in the atmosphere, Science, 279, 1184–1187, 1998.

Gross, D. S., Gälli, M. E., Silva, P. J., and Prather, K. A.: Relative sensitivity factors for alkali metal and ammonium cations in single-particle aerosol time-of-flight mass spectra, Anal. Chem., 72, 416–422, 2000.

Guazzotti, S. A., Whiteaker, J. R., Suess, D., Coffee, K. R., and Prather, K. A.: Real-time measurements of the chemical composition of size-resolved particles during a Santa Ana wind episode, California USA, Atmos. Env., 35, 3229–3240, 2001.

Gupta, D., Kim, H., Park, G., Li, X., Eom, H.-J., and Ro, C.-U.: Hygroscopic properties of NaCl and $NaNO_3$ mixture particles as reacted inorganic sea-salt aerosol surrogates, Atmos. Chem. Phys., 15, 3379-3393, 2015.

Gyakum, J. R., Anderson, J. R., Grumm, R. H., and Gruner, E. L.: North Pacific cold-season surface cyclone activity: 1975-1983, Mon. Weather Rev., 117, 1141–1155, 1989.

Hill, A. and Dobbie, S.: The impact of aerosols on non-precipitating marine stratocumulus. II: The semi-direct effect, Q. J. Roy. Meteor. Soc., 134, 1155–1165, 2008.

Hill, A., Dobbie, S., and Yin, Y.: The impact of aerosols on non-precipitating marine stratocumulus. I: Model descrip- tion and prediction of the indirect effect, Q. J. Roy. Meteor. Soc., 134, 1143–1154, 2008.

Hill, A. A., Feingold, G., and Jiang, H.: The influence of entrainment and mixing assumption on aerosol-cloud interactions in marine stratocumulus, J. Atmos. Sci., 66, 1450–1464, 2009.

Hughes, L. S., Allen, J. O., Bhave, P., Kleeman, M. J., Cass, G. R., Liu, D.-Y., Fergenson, D. P., Morrical, B. D., and Prather, K. A.: Evolution of atmospheric particles along trajectories crossing the Los Angeles basin, Env. Sci. & Tech., 34, 3058–3068, 2000.

Hughes, L. S., Allen, J. O., Salmon, L. G., Mayo, P. R., Johnson, R. J., Cass, G. R.: Evolution of nitrogen species air pollutants along trajectories crossing the Los Angeles area, Env. Sci. Tech., 36, 3928-3925, 2002.

Kokhanovsky, A.: Optical properties of terrestrial clouds, Earth-Sci. Rev., 64, 189–241, 2004.

Kotzick, R., Panne, U., and Niessner, R.: Changes in condensation properties of ultrafine carbon particles subjected to oxidation by ozone, J. Aero. Sci., 28, 725–735, 1997.

Lentz, S. J. and Chapman, D. C.: Seasonal differences in the current and temperature variability over the northern California shelf during the Coastal Ocean Dynamics Experiment, J. Geo. Res.: Oceans (1978– 2012), 94, 12 571–12 592, 1989.

Leung, L., Prather, K., Ralph, F., Rosenfeld, D., Spackman, J., Fairall, C., DeMott, P., Fan, J., and Zhao, C.: The CalWater 2-ARM Cloud Aerosol Precipitation Experiment (ACAPEX), in: AGU Fall Meeting Abstracts, vol. 1, p. 01, 2014.

Lewis, K., Arnott, W. P., Moosmüller, H., and Wold, C. E.: Strong spectral variation of biomass smoke light ab- sorption and single scattering albedo observed with a novel dual-wavelength photoacoustic instrument, J. Geo. Res.: Atmos., 113, 2008.

Loescher, K. A., Young, G. S., Colle, B. A., and Winstead, N. S.: Climatology of barrier jets along the Alaskan coast.

Part I: Spatial and temporal distributions, Mon. Weather Rev., 134, 437–453, 2006.

Lu, M.-L. and Seinfeld, J. H.: Study of the aerosol indirect effect by large-eddy simulation of marine stratocumulus, J. Atmos. Sci., 62, 3909–3932, 2005.

Mochida, M., Kuwata, M., Miyakawa, T., Takegawa, N., Kawamura, K., and Kondo, Y.: Relationship between hy- groscopicity and cloud condensation nuclei activity for urban aerosols in Tokyo, J. Geo. Res.: Atmos., 111, 2006.

Moffet, R. C. and Prather, K. A.: In-situ measurements of the mixing state and optical properties of soot with im- plications for radiative forcing estimates, PNAS, 106, 11 872–11 877, 2009.

Neiman, P. J., Ralph, F. M., White, A. B., Parrish, D. D., Holloway, J. S., and Bartels, D. L.: A multiwinter analysis of channeled flow through a prominent gap along the northern California coast during CALJET and PACJET, Mon. Weather Rev., 134, 1815–1841, 2006.

Nguyen, T., Petters, M., Suda, S., Guo, H., Weber, R., and Carlton, A.: Trends in particle-phase liquid water during the Southern Oxidant and Aerosol Study, Atmos. Chem. Phys., 14, 10 911–10 930, 2014.

Overland, J. E. and Walter Jr, B. A.: Gap winds in the Strait of Juan de Fuca, Mon. Weather Rev., 109, 2221– 2233, 1981.

Paerl, H. W.: Coastal eutrophication in relation to atmospheric nitrogen deposition: current perspectives, Ophelia, 41, 237–259, 1995.

Paerl, H. W.: Coastal eutrophication and harmful algal blooms: Importance of atmospheric deposition and groundwa- ter as “new” nitrogen and other nutrient sources, Limnol. Oceanogr., 42, 1154–1165, 1997.

Petters, M. and Kreidenweis, S.: A single parameter representation of hygroscopic growth and cloud condensation nucleus activity, Atmos. Chem. Phys., 7, 1961–1971, 2007.

Petters, M. D., Carrico, C. M., Kreidenweis, S. M., Prenni, A. J., DeMott, P. J., Collett, J. L., and Moosmüller, H.: Cloud condensation nucleation activity of biomass burning aerosol, J. Geo. Res.: Atmos., 114, 2009.

Platnick, S. and Twomey, S.: Determining the susceptibility of cloud albedo to changes in droplet concentration with the Advanced Very High Resolution Radiometer, J. App. Meteor., 33, 334–347, 1994.

Platnick, S., King, M. D., Ackerman, S., Menzel, W. P., Baum, B., Riedi, J. C., Frey, R., et al.: The MODIS cloud products: Algorithms and examples from Terra, Geoscience and Remote Sensing, IEEE Transactions on, 41, 459– 473, 2003.

Prather, K. A., Hatch, C. D., and Grassian, V. H.: Analysis of atmospheric aerosols, Annu. Rev. Anal. Chem., 1, 485–514, 2008.

Pratt, K. A. and Prather, K. A.: Real-time, single-particle volatility, size, and chemical composition measurements of aged urban aerosols, Env. Sci. Tech., 43, 8276–8282, 2009.

Qin, X., Pratt, K. A., Shields, L. G., Toner, S. M., and Prather, K. A.: Seasonal comparisons of single-particle chemical mixing state in Riverside, CA, Atmos. Env., 59, 587–596, 2012.

Qin, X., Prather, K.A.: Impact of biomass emissions on particle chemistry during the California Regional Particulate Air Quality Study, Int. J. Mass Spect. 258, 142-150, 2006.

Quinn, P. K., Collins, D. B., Grassian, V. H., Prather, K. A., and Bates, T. S.: Chemistry and related properties of freshly emitted sea spray aerosol, Chem. Rev., 115, 4383–4399, 2015.

Ralph, F., Prather, K., Cayan, D., Spackman, J., DeMott, P., Dettinger, M., Fairall, C., Leung, R., Rosenfeld, D., Rutledge, S., et al.: CalWater Field Studies Designed to Quantify the Roles of Atmospheric Rivers and Aerosols in Modulating US West Coast Precipitation in a Changing Climate., B. Am. Meteorol. Soc., 2015.

Rebotier, T. P. and Prather, K. A.: Aerosol time-of-flight mass spectrometry data analysis: A benchmark of clustering algorithms, Anal. Chim. Acta, 585, 38–54, 2007.

Regonda, S. K., Rajagopalan, B., Clark, M., and Pitlick, J.: Seasonal cycle shifts in hydroclimatology over the western United States, J. Clim., 18, 372–384, 2005.

Rossow, W. B. and Schiffer, R. A.: Advances in understanding clouds from ISCCP, B. Am. Meteorol. Soc., 80, 2261–2287, 1999.

Russell, A. G. and Cass, G. R.: Verification of a Mathematical Model for Aerosol Nitrate and Nitric Acid Formation and Its Use for Control Measure Evaluation, Atmos. Env., 20, 2011-2025, 1986.

Ryther, J. H. and Dunstan, W. M.: Nitrogen, phosphorus, and eutrophication in the coastal marine environment, Science, 171, 1008–1013, 1971.

Schnaiter, M., Linke, C., Möhler, O., Naumann, K.-H., Saathoff, H., Wagner, R., Schurath, U., and Wehner, B.: Absorption amplification of black carbon internally mixed with secondary organic aerosol, J. Geo. Res: Atmos., 110, 2005.

Seinfeld, J. H. and Pandis, S. N.: Atmospheric chemistry and physics: from air pollution to climate change, John Wiley & Sons, 2012.

Solomon, S.: Climate change 2007-the physical science basis: Working group I contribution to the fourth assessment report of the IPCC, vol. 4, Cambridge University Press, 2007.

Song, X.-H., Hopke, P. K., Fergenson, D. P., and Prather, K. A.: Classification of single particles analyzed by ATOFMS using an artificial neural network, ART-2A, Anal. Chem., 71, 860–865, 1999.

Su, Y., Sipin, M. F., Furutani, H., and Prather, K. A.: Development and characterization of an aerosol time-of-flight mass spectrometer with increased detection efficiency, Anal. Chem., 76, 712–719, 2004.

Sullivan, R., Guazzotti, S., Sodeman, D., and Prather, K.: Direct observations of the atmospheric processing of Asian mineral dust, Atmos. Chem. Phys., 7, 1213–1236, 2007.

Tunved, P., Nilsson, E., Hansson, H.-C., Ström, J., Kulmala, M., Aalto, P., and Viisanen, Y.: Aerosol characteristics of air masses in northern Europe: Influences of location, transport, sinks, and sources, J. Geo. Res.: Atmos., 110, 2005.

Twomey, S.: The influence of pollution on the shortwave albedo of clouds, J. Atmos. Sci., 34, 1149–1152, 1977.

Twomey, S.: Aerosols, clouds and radiation, Atmos. Env. A-Gen, 25, 2435–2442, 1991.

Wang, L., Khalizov, A. F., Zheng, J., Xu, W., Ma, Y., Lal, V., and Zhang, R.: Atmospheric nanoparticles formed from heterogeneous reactions of organics, Nat. Geoscience, 3, 238–242, 2010.

Weingartner, E., Saathoff, H., Schnaiter, M., Streit, N., Bitnar, B., and Baltensperger, U.: Absorption of light by soot particles: determination of the absorption coefficient by means of aethalometers, J. Aero.Sci., 34, 1445–1463, 2003.

White, A., Anderson, M., Dettinger, M., Ralph, F., Hinojosa, A., Cayan, D., Hartman, R., Reynolds, D., Johnson, L., Schneider, T., et al.: A twenty-first-century California observing network for monitoring extreme weather events, J. Atmos. Ocean Tech., 30, 1585–1603, 2013.

Wood, R.: Cancellation of aerosol indirect effects in marine stratocumulus through cloud thinning, J. Atmos. Sci., 64, 2657–2669, 2007.

Zhang, R., Khalizov, A. F., Pagels, J., Zhang, D., Xue, H., and McMurry, P. H.: Variability in morphology, hygroscop- icity, and optical properties of soot aerosols during atmospheric processing, PNAS, 105, 10 291–10 296, 2008.

Zuberi, B., Johnson, K. S., Aleks, G. K., Molina, L. T., Molina, M. J., and Laskin, A.: Hydrophilic properties of aged soot, Geo. Res. Let., 32, 2005.

Chapter 3. Contrasting local and long-range transported warm ice-nucleating particles during an atmospheric river in coastal California, USA

3.1 Abstract

Ice nucleating particles (INPs) have been found to influence the amount, phase, and efficiency of precipitation from winter storms, including atmospheric rivers. Warm INPs, those that initiate freezing at temperatures warmer than -10 °C, are thought to be particularly impactful because they can create primary ice in mixed-phase clouds, enhancing precipitation efficiency. The dominant sources of warm INP during atmospheric rivers, the role of meteorology in modulating transport and injection of warm INP into atmospheric river clouds and the impact of warm INP on mixed-phase cloud properties are not well-understood. In this case study, time-resolved precipitation samples were collected during an atmospheric river in Northern California, USA during winter 2016. Precipitation samples were collected at two sites, one coastal and one inland, which are separated by about 35 km. The sites are sufficiently close that airmass sources during this storm were almost identical, but the inland site was exposed to terrestrial sources of warm INP while the coastal site was not. Warm INP were more numerous in precipitation at the inland site by an order of magnitude. Using FLEXPART dispersion modelling and radar-derived cloud vertical structure, we detected influence from terrestrial INP sources at the inland site, but did not find clear evidence of marine warm INP at either site. We episodically detected warm INP from long-range transported sources at both sites. By extending the FLEXPART modelling using a meteorological reanalysis, we demonstrate that long-range transported warm INP were observed only when the upper tropospheric jet provided transport to cloud tops. Using radar-derived hydrometeor classifications, we demonstrate that hydrometeors over the terrestrially-influenced inland site were more likely to be in the ice phase for cloud temperatures between 0 °C and -10

°C. We thus conclude that terrestrial and long-range transported aerosol were important sources of warm INP during this atmospheric river. Meteorological details such as transport mechanism and cloud structure were important in determining warm INP source and injection temperature, and ultimately the impact of warm INP on mixed phase cloud properties.

3.2 Introduction

Atmospheric Rivers (ARs) are responsible for significant precipitation in many extratropical regions (Ralph et al., 2006; Neiman et al., 2011; Ralph and Dettinger, 2012; Dettinger, 2013; Lavers and Villarini, 2013). On the windward side of some continents, including the US state of California, ARs are responsible for up to 50% of the annual rainfall (Dettinger et al., 2011; Lavers and Villarini, 2015) It has long been known that naturally occurring tropospheric aerosols can influence precipitation by serving as heterogeneous ice nucleating particles (INPs) (Vali, 1971; Pitter and Pruppacher, 1973; Maki et al., 1974; DeMott et al., 2011). INPs may also influence precipitation from ARs. Ault et al. (2011) compared two dynamically similar ARs that impacted California and found that precipitation residues classified as dust or biological were more plentiful in the AR that produced more precipitation and more mountain snow. By extending similar analyses, Creamean et al. (2013) showed a relationship between the amount of dust and biological precipitation residues and the precipitation amount and phase. Creamean et al. (2013, 2015) also found that precipitation occurring after the storm's cold front passed was more enriched in these residue types. Numerical weather prediction experiments (Fan et al., 2014) have demonstrated that dust aerosols can invigorate precipitation in California AR by enhancing snow formation in mixed-phase orographic clouds.

Several studies have suggested that long-range transported dust aerosols are often mixed with biological remnant material (Conen et al., 2011; Murray et al., 2015; O'Sullivan et al., 2016).

The source of the remnant material may allow dust/biological mixtures to serve as "warm" INPs. Herein, we define warm INPs as particles that cause freezing of supercooled liquid cloud droplets through immersion nucleation at temperatures warmer than -10 °C (Stopelli et al., 2015). Several other types of biological aerosol particles of terrestrial or marine origin may also serve as warm INPs. These particle types may include pollen, viruses, bacteria or microscopic plant material (Schnell and Vali, 1973, 1976; Pruppacher et al., 1998; Hoose et al., 2010; Murray et al., 2012). Terrestrial warm INPs can be found in high concentrations near agricultural regions (Tobo et al., 2014), forests (Tobo et al., 2013), and in biomass burning (Petters et al., 2009). Recent studies suggest terrestrial INPs can induce "bioprecipitation feedback" (Huffman et al., 2013; Prenni et al., 2013; Morris et al., 2014; Bigg et al., 2015), whereby rainfall stimulates emission of INPs from some types of terrestrial biota and rainfall efficiency and INP concentration are thereafter increased. Marine INPs are thought to be an important source for the global INP budget (Burrows et al., 2013). Indeed, it has been shown that biological material ejected to the atmosphere in sea-spray may contribute to immersion mode freezing at temperatures as warm as -5 °C (DeMott et al., 2016; Wilson et al., 2015; McCluskey et al., 2018).

ARs often exist near upper tropospheric jet streams and can generate deep clouds whose tops may access airmasses containing long-range transported (LRT) dust or dust/bio INPs. Both Ault et al. (2011) and Creamean et al. (2013) hypothesized that INPs arrived to their storms near cloud top and showed through back-trajectory analysis that the likely sources of these INPs were Asiatic, Arabian and African desert regions. The degree to which terrestrial or marine warm INPs enter AR clouds is less well-established, though good evidence that marine aerosols and terrestrially emitted pollutant aerosols enter the clouds in ARs over California has been provided (Rosenfeld et al., 2008, 2014).

The impact warm INPs have on AR clouds is likewise not established. ARs support a wide variety of clouds, cloud structures and kinematic features that could allow warm INPs to encounter supercooled liquid droplets. Past authors have noted that ARs regularly generate stratiform orographic clouds containing a large amount of supercooled liquid water (Heggli et al., 1983; Heggli and Rauber, 1988), and that AR orographic clouds regularly form seeder-feeder structures (Robichaud and Austin, 1988) wherein falling ice hydrometeors grow rapidly by riming in the warmest supercooled layers (Neiman et al., 2002; White et al., 2003; Creamean et al., 2013). In the seeder-feeder model, the altitude or temperature of warm INP injection to the cloud may lead to differing hydrometeor growth outcomes by changing the relative importance of processes such as riming, ice multiplication, and/or the Wegener-Bergeron-Findeisen process (Pruppacher et al., 1998). Further complicating matters, the type of cloud, depth of cloud and amount of supercooled liquid water may vary considerably during a given AR and could depend upon local topography and short-lved kinematic regimes such as barrier jets, low-level jets and cold fronts (Kingsmill et al., 2006; Ralph et al., 2005; Kingsmill et al., 2013).

While the authors mentioned above and others have collected INPs in AR clouds and precipitation and found important links between INP source and ARs, additional contrast between local marine and terrestrial and LRT warm INP sources is needed. In addition, coincident analyses of warm INPs with cloud injection temperature and hydrometeor properties is necessary to establish that warm INPs impact AR clouds rather than simply becoming removed by below-cloud precipitation. Hereafter, we will refer to local marine and terrestrial warm INPs as simply "marine" and "terrestrial". LRT will refer to all other warm INPs.

For the current study, we examined hourly precipitation samples collected at two Northern CA, USA locations during an AR during 5 - 6 March, 2016. During an extended period of this

event, the coastal site - Bodega Marine Laboratory, CA - was directly upwind of the inland site - Cazadero, CA by approximately 35 km. We will demonstrate that the geometry of the flow during this AR and the geography of the two sites create a natural contrast whereby both sites were exposed to marine and long-range transported aerosol sources, but only the inland site was exposed to terrestrial aerosol sources. We will additionally demonstrate that the temperature lapse rates of this storm and partial beam blocking by the coastal mountain range near the measurement sites constrained weather service radar such that retrieved signal was from hydrometeors with temperatures $-9.2\ ^{\circ}C < T \leq 0.8\ ^{\circ}C$. The remotely sensed hydrometeors thus approximately overlap with the temperatures of warm INP activation. We used these unique properties to inform analyses of the amount and activation spectra of ice nuclei in precipitation, cloud hydrometeor phase, kinematic regime, and cloud-terminating airmass source. These analyses allowed us to address the following questions:

1. What roles do terrestrial, marine and LRT sources have in determining the warm INPs during this AR?
2. What are the transport and cloud injection mechanisms for each of these sources?
3. When warm INPs are present in precipitation, are cloud microphysics impacted?

The rest of this study will be organized as follows. We present data sources and the study location in section 3.3. Methodology, including the detection of kinematic forcing regime; Lagrangian dispersion modelling; and radar analyses are presented in section 3.4. We will review the atmospheric river event and present our findings in section 3.5. Finally, we review how our findings address the above questions in section 3.6.

3.3 Data sources and study locations

3.3.1 Atmospheric river observatory

The coastal atmospheric river observatory (ARO) was developed by the National Oceanic and Atmospheric Administration Earth System Research Laboratory (NOAA-ESRL) to better observe kinematic forcing, cloud and precipitation processes during landfalling ARs. The ARO is comprised of two sites in Northern CA commonly exposed to AR conditions during the winter months. A coastal site at Bodega Marine Laboratory in Bodega Bay, CA (BBY; 15 m MSL; 38.32 °N, 123.07 °W) and a mountain site in Cazadero, CA (CZC; 478 m MSL; 38.61°N, 123.22 °W), together measure nearly coincident weather conditions during landfalling ARs (White et al., 2013). During the event described herein, both sites had a tipping bucket rain gauge, near-surface (10 m) anemometer, GPS receiver capable of estimating integrated water vapor by means of radio occultation, and a vertically oriented radar for vertical sensing of atmospheric properties. BBY had a 449 MHz wind profiling radar and CZC had a S-band precipitation radar (See table 3.1 for a list of all ARO measurements and their technical references). The CZC S-Band radar was used to determine the echo top height (ETH - see 3.4.4) during the AR. Neiman et al. (2002) contains a description of the coastal ARO, and application of the measurements to AR kinematics, cloud properties and precipitation.

3.3.2 Precipitation samples

Precipitation samples were collected hourly from 00 UTC on 5 March to 00 UTC on 7 March, 2016. Precipitation was captured by the Teledyne ISCO model 6712 commercial water samplers, (Teledyne ISCO, Inc., US) connected by tygon tubing to a 300 mL funnel. Precipitation was dispensed into one of twenty-four 350 mL glass jars with hourly collection time interval. Sampling began by manually initiating the program on the sampler at BBY and by triggering from the Teledyne ISCO 674 rain gauge, set to 0.5 mm threshold, at CZC. Two ISCO samplers, programmed to sample sequentially, were placed at each site, enabling a 48-hour continuous

collection period. Prior to collection, glass jars were cleaned with acetone, methanol, and ultrapure milli-Q water (18 MΩ cm^{-1}) and peripheral hardware (funnel, tubing, distributor arm, etc.) was rinsed with milli-Q water. Precipitation samples analyzed in the automated ice spectrometer (section 3.3.5) were separated into 40-mL glass scintillation vials, frozen and stored at -20 °C for approximately 4 months before they were thawed for analysis.

3.3.3 Balloon-borne soundings

Helium balloon-borne GPS-rawinsondes (Vaisaila model RS-41) were launched from BBY at irregular intervals varying from 60 to 180 minutes during the AR. Each rawinsonde carried a package of meteorological instruments to measure ambient temperature, humidity, latitude, longitude and altitude. This data was broadcast to a ground-based antenna at BBY during balloon flight. Two-dimensional horizontal wind was derived automatically from the time-derivative of rawinsonde position. Vaisala model MW41 DIGICORA sounding system software was used to postprocess and archive data from each rawinsonde. The relevant soundings used in analysis of the AR event are listed in Table 3.2.

3.3.4 Climate Forecast System

NOAA Climate Forecast System (CFS) global short-duration ($t < 6$ hr) forecasts (Saha et al., 2014) were used as threedimensional atmospheric forcing datasets for FLEXPART (Section 3.4.2). CFS was also used to identify large scale meteorological features such as ARs and the Pacific upper tropospheric jet stream.

3.3.5 Automated ice spectrometer

INP concentrations and freezing activation spectra were determined via the droplet freezing method (Hill et al., 2014) using the automated ice spectrometer (AIS; Beall et al., 2017). Precipitation samples were distributed directly in microliter aliquots into a 96-well polypropylene

assay plate. The assay plates were loaded into the AIS, which was slowly cooled until the samples are frozen. Cooling of each hourly precipitation sample was repeated in triplicate, along with a milli-Q water sample as control for contamination from the loading process. Though the homogeneous freezing point of water is -38 ºC, freezing of milli-Q samples typically started at -25 to -27 ºC, effectively setting the cold limit at which freezing due to INPs in precipitation can be determined. Cumulative droplet freezing activity spectra, INP(T) (mL^{-1} rainwater), were calculated using the fraction of unfrozen wells f per given temperature interval: $INP(T) = \ln(f)/V$, where V is the volume of the sample in each well (Vali, 1971). The fraction of unfrozen wells f was adjusted for contamination by subtracting the number of frozen milli-Q water wells per temperature interval from both the total number of unfrozen wells and the total number of wells of the sample. The limit of detection for the AIS under these laboratory conditions was 0.70 mL^{-1}. Warm INP concentration, INP_{-10}, is herein defined as the cumulative concentration at T = -10 ºC.

A companion set of precipitation samples were heated prior to introduction to the AIS to detect ice-nucleating biological material that is sensitive to heat (Hill et al., 2014). Heated precipitation samples were subjected to heat via immersion in a hot water bath (90 ºC) for 20 minutes prior to analysis with the AIS. In analysis presented later, if heated INP(T) decreased compared to un-heated INP(T) drawn from the same precipitation sample for T < -10 ºC, we consider a portion of warm INPs from that sample as bio-INP.

3.4 Methods

3.4.1 INP source and impact hypothesis testing

There is much concerning INPs we cannot directly observe during this event. Specifically, we cannot analyze INP chemical composition separately from the ambient aerosol or condensation nuclei population. The primary inferences about terrestrial INP therefore come from the contrast

between the AIS-measured freezing temperature and number of INPs in the coastal and inland site precipitation. We also cannot observe ice nucleation events in cloud above our collection sites. To address the goals of this study related to INP sources upwind of both sites (Marine and LRT) and impacts on cloud microphysics, we performed backward Lagrangian airmass modeling using the FLEXPART model and analysis of weather service radar derived hydrometeor type in clouds above our precipitation collection sites.

Each of these analysis methods has its own shortcomings. Accordingly, results emerging from the FLEXPART and radar analyses will be supported by constructing and rejecting alternate hypotheses. These hypotheses and their accompanying experimental design will be briefly described in tandem with the FLEXPART and weather service radar technical methods.

3.4.2 FLEXPART

We used the FLEXPART Lagrangian dispersion model (Stohl et al., 2005) to simulate backward dispersion from discrete cloud layers (see section 3.4.3 for definition of layers) over the ARO. FLEXPART version 9.0.2 was run in serial processor mode on a Unix workstation. Backward simulation of FLEXPART iteratively solves for element position (latitude, longitude and altitude) as a function of time prior to release. It should be noted that the distance separating BBY and CZC is approximately 35 km, and is less than the horizontal resolution of the CFS grid (0.5 degree latitude by 0.5 degree longitude). However, FLEXPART performs several operations designed to resolve motions at less than grid scale (Stohl et al., 2005). We ran FLEXPART simulations for each site separately, but with small exception did not find significant difference in element position or transport patterns. Therefore, unless noted we present only the result of FLEXPART backward simulations ending at CZC.

3.4.3 FLEXPART experiments

The FLEXPART model was employed to simulate the sources of air arriving in subfreezing cloud layers over the ARO. The 15 simulations were motivated by the following hypothesis.

– H1: warm INP content in precipitation is limited by the cloud's access to airmasses containing the specific source.

For example, LRT warm INPs will be present only if collected precipitation is falling from clouds with temperature suitable for ice nucleation that can entrain air transported from terrestrial regions across the Pacific Ocean. Note that we cannot run a full global source-receptor model to address this hypothesis, because emission and removal of warm INPs are poorly simulated processes. Therefore, in performing the FLEXPART modeling we are assuming that the INP sources contained in given airmass are closely associated with the history of the airmass as it traveled through the atmosphere before arriving in cloud. To construct an airmass history related to LRT sources, we examined simulated airmass residence in the upper tropospheric jet (UTJ) and the atmospheric river (AR). Each is a persistent and horizontally extensive feature located near the ARO during this event and contains fast horizontal winds directed from remote regions to the measurement sites. Each is therefore capable of efficiently transporting remote airmasses to the cloud layers over the ARO. To construct an airmass history related to marine sources, we examined simulated residence in the Northeast Pacific Ocean marine boundary layer (MBL). To construct an airmass history related to local terrestrial sources, we examined simulated residence in the terrestrial boundary layer (TBL) over California.

Warm INPs can initiate freezing in any cloud with subfreezing temperatures, but they are expected to have greatest impact where temperatures are warmer than -10 °C. We separately examined injection to mixed-phase clouds (10 °C ≤ T ≤ 0 °C) and cloud tops (T ≤ -20 °C for the majority of this event) by simulating the position of FLEXPART elements released from each

layer. Because the atmosphere is highly stratified, we expect airmass sources entering mixed-phase and cloud top layers to differ. We also expect that the AR kinematic regime (e.g. barrier jet, low-level jet, post cold-frontal) will both modulate the atmospheric stratification and limit the pathways available to transport air to each cloud layer by serving as the final airflow link between clouds and the largescale weather pattern. We used rawinsondes to define the upper and lower geopotential height boundaries of the mixed-phase and layer and to identify contiguous periods of dominant kinematic regime (hereafter "kinematic periods") within our storm (see section 3.4.4). Cloud top height boundaries were assigned by perturbing the S-Band radar echo top height (ETH) by ± 500 m. Separate FLEXPART simulations were performed by releasing 2000 FLEXPART elements from each kinematic period and cloud layer and allowing the model to simulate the element position backward in time for 120 hours. We examined H1 by calculating the probability of instantaneous element residence, P_{res}, in each feature (UTJ, AR, MBL, TBL). Element position was considered an instantaneous sample from a set of elements that would end in the mixed-phase (cloud top) layer over the ARO. The quantity P_{res} was calculated as the fraction of the set of positions that could be assigned to the feature, $P_{res} = n_{res}/n_{rel}$ 10, where n_{res} is the number element positions residing in the desired feature, and n_{rel} is the total number released from the given layer above the ARO.

3.4.4. Identifying kinematic periods and airmass history features in atmospheric data

Definitions of cloud layer, airmass history, and kinematic forcing features are described herein with a short summary of identification methodology using study datasets.

1. Atmospheric river (AR): FLEXPART elements resided in the AR when CFS integrated vapor transport (IVT) exceeded 250 kg m s−1 (Rutz et al., 2014) and relative humidity exceeded 85% (Ralph et al., 2005).

2. Coastal barrier jet (CBJ): The CBJ forms as onshore-directed wind is deflected by the coastal mountain topography. It was identified as a time-height maximum in along-slope water vapor flux occurring below the local terrain height - (450 m Neiman et al. (2004)). Along-slope water vapor flux was calculated similarly to terrain-normal water vapor flux, except the formula is expressed $|\mathbf{a}|q_v$, where $|\mathbf{a}|$ is the magnitude of the horizontal wind projected to the along-slope direction (â). See a hypothetical along-slope wind barb depicted in Fig. 3.1. Rawinsonde observations of two-dimensional wind speed and q_v were temporally interpolated to a constant 60-minute time series using cubic-spline before water vapor flux calculations were performed.

3. Echotop Height (ETH): The echo top approximates the upper boundary of the cloud layer sensed by the S-Band radar at CZC. See White et al. (2013) for details.

4. AR low-level jet (LLJ): The LLJ was defined as a time-height maximum in terrain-normal water vapor flux occurring below 3 km MSL (Neiman et al., 2002; Ralph et al., 2005). Terrain-normal water vapor flux was calculated from rawinsondes following the formula $|\mathbf{u}|q_v$, where q_v is the water vapor mixing ratio (g kg^{-1}) and $|\mathbf{u}|$ is the magnitude of the horizontal wind (m s^{-1}) projected along the terrain-normal (upslope) direction for the ARO local terrain (Neiman et al., 30 2002). A hypothetical wind barb directed along the upslope direction (û) is depicted in Fig. 3.1.

5. Marine boundary layer (MBL): The MBL was defined where CFS geopotential height (m MSL) was less than the FLEXPART planetary boundary layer depth and the FLEXPART latitude and longitude are over the Northeast Pacific Ocean.

6. Terrestrial boundary layer (TBL): The TBL was defined similarly to the MBL, expect latitude and longitude must have been over the US state of California.

7. Pacific upper tropospheric jet stream (UTJ): The UTJ was identified using CFS data when horizontal wind speed exceeded 50 m s^{-1} between an altitude of 6.5 and 11 km MSL (hereafter referred to as the UTJ layer). The UTJ layer was defined by visual identification of the UTJ in latitude-vertical cross-sections along the longitudes 135, 150, 165 °W extending from 25 °N to 60 °N during 05 March and 06 March, 2016. It was confirmed that the UTJ remained quasi-stationary during 05-06 March, 2016.

8. Polar cold front: The polar cold front was identified using rawinsonde data by the directional wind shear in the lowest 5 km of the troposphere. The discontinuity between horizontal wind veering/backing with height (Neiman et al., 1991) is considered to mark the transit of the cold front across the ARO.

3.4.5 KDAX weather service radar

The KDAX weather service radar (Heiss et al., 1990) located in Sacramento, CA was used to evaluate hydrometeor phase and precipitation intensity in a shallow mixed-phase cloud layer over BBY and CZC. The location of KDAX relative to BBY and CZC is shown in Fig. 3.2a. During each azimuthal scan, the lowest beam elevation (0.51 degree) from KDAX is partially blocked by the coastal mountain range. The result of the beam blockage is that signal is only returned from a narrow vertical slice of the scan above BBY (CZC). Figure 3.2b depicts the blocked and unblocked portions of the beam above both sites. The highest and lowest altitudes of

the KDAX unblocked layers are 2850 and 3650 m, respectively. During this storm, rawinsondes measured the temperature range corresponding to these altitude limits (Table 3.2). Hydrometeors sensed by KDAX in the unblocked layer over BBY and CZC were in the temperature range 0.8 °C to -9.2 °C. Therefore, information retrieved from the KDAX unblocked layer such as hydrometeor type and radar reflectivity were indicative of mixed-phase clouds during the storm. WSR-88D Polarimetric weather service radars (including KDAX) retrieves hydrometeor type (Park et al., 2009) containing 11 classifications: biological (animals, not particles), clutter, ice, dry snow, wet snow, light rain, heavy rain, big drops, graupel, hail, and unknown. We designed our KDAX experiment (section 3.4.6) to operate on binary information: frozen and not-frozen. We grouped the classifications ice, dry snow, wet snow, and graupel into the frozen hydrometeor category. All other classifications beside unknown were categorized as "not frozen".

3.4.6 Radar experiments

After grouping and discarding the unknown classification, we were left with binary categorical information (frozen / not frozen) from the KDAX radar retrievals. We applied a Chi-Square independence test to the frozen / not frozen category time series to test the hypothesis:

– H2: The likelihood of detecting frozen hydrometeors in the mixed-phase cloud layer differed above the coastal and inland sites during the storm.

To confirm that the KDAX retrieval category time series were sufficient to test this hypothesis, we verified that the data passed the Chi-Square rule of thumb for minimum expected populations and that the result of the test did not change under Yates' correction (Haviland, 1990). The result of this test is only of interest if the CZC and BBY categorical data is drawn from remotely sensed hydrometeors at the same range of temperatures, namely the range of temperatures in the unblocked layer (Table 3.2). To preserve the same upper and lower unblocked

layer altitudes over both sites, we retained only one range gate, nearest the CZC site, from the CZC azimuth. We retained the 45 range gates from the BBY azimuth that complete the red trapezoid in Fig. 3.2b. The KDAX radial resolution is 250 m, thus the BBY azimuth retrievals correspond to the unblocked layer over BBY along a great circle toward KDAX extending 11.5 km.

We do not possess independent observations of temperature in the KDAX unblocked layer over each site. Instead, we assume that the temperatures T_{top} KDAX (T_{bot} KDAX) are equivalently representative of both sites. Each rawinsonde's ground location was tracked to an altitude of 3650 m. The mean ground location in the height range of the KDAX unblocked beam layer varied by sounding but was nearly equidistant from both sites at a distance approximately 19.44 (26.48) km to BBY (CZC). We note that local effects related to airflow over a mountain barrier (Minder et al., 2011) could preferentially cool the lower troposphere above CZC more than above BBY. If this effect is strong, the unblocked beam layer above CZC could contain cooler air than it does over BBY. Following the methodology of Minder et al. (2011), we performed semi-idealized simulations of flow over a 2-dimensional hill of approximate height (500 m) and half-width (10 km) of the mountain ridge at CZC using rawinsondes from this study as the upstream boundary condition. Simulated temperatures above the CZC proxy mountain were not cooler than those above the BBY proxy coast by more than 0.25 °C.

3.5 Results

3.5.1 Overview of atmospheric river event

An Atmospheric River caused heavy rain in Northern California during 5-6 March, 2016. AR conditions, measured by a combination of the 449 MHz wind profiling radar and the GPS receiver, (Ralph et al., 2013) were present at the ARO from 15 UTC on 5 March, 2016 to 06 UTC on 6 March, 2016. Rawinsonde measurements show that IVT reached a peak value of 956 kg m^{-1}

s^{-1} near 02 UTC on 6 March (see Table 3.2). This value is well above the range of expected peak IVT estimates for ARs impacting this region (Ralph et al., 2018) Total precipitation at CZC during AR conditions was 72 mm, placing this event in the top 20% of all events published in Ralph et al. (2013).

3.5.2 Kinematic periods

Time-vertical meteograms of along-slope and upslope vapor flux (g kg^{-1} s^{-1}) over the ARO are shown in Fig. 3.3a. Along-slope (upslope) vapor flux is here used to indicate transport of water vapor consistent with a coastal barrier jet (AR low-level jet) - see section 3.4.4. CBJ vapor transport reached its maximum between 21 and 23 UTC on 5 March. Maximum values in along-slope vapor transport were located between the surface and 400 m MSL. The LLJ vapor transport maxima occured later, between 23 UTC on 5 March and 01 UTC on 6 March. the LLJ vertical maxima was located above the height of the coastal mountains, near 750 m MSL. This spatio-temporal evolution of the CBJ and LLJ is consistent with previous studies. In particular, Neiman et al. (2004) found that the barrier jet typically forms before the arrival of maximum vapor transport, in response to blocking of the flow by local topography. Kingsmill et al. (2013) described the AR low-level jet as forced upward over the top of an antecedent barrier jet, with typical location near 1 km MSL.

Fig 3.3b shows horizontal wind (m s^{-1}) vectors from balloon-borne radiosondes. The top axis indicates the time of soundings measuring IVT values of (514, 736, and 956) kg m^{-1} s^{-1}, respectively. Also indicated on the top axis is the time of sounding indicating the transit of the cold front. Wind barbs back with height in the lowest 5 km of the troposphere for this and following sondes, further indicating the cold front has passed. The strength of each the coastal barrier jet, the low-level jet and the cold front, along with their interchange in a short period of time suggests that

the kinematic forcing for orographic clouds during this AR may have changed rapidly several times. We will hereafter use the dominance in vapor flux by the CBJ (LLJ) and the transit of the cold front to segment the AR into four kinematic periods (see Table 3.3).

3.5.3 Warm INPs, rainfall, and cloud top height

Figure 3.4a shows the time series of INP_{-10} (box-and-whiskers) and accumulated precipitation (solid lines) during the event at BBY (CZC). Note that INP_{-10} at CZC is consistently between 1 and 4 mL^{-1} before 21 UTC on 5 March and between 10 and 15 mL^{-1} thereafter (Barrier Jet period). INP_{-10} content was only occasionally above detection limit at BBY. INP_{-10} at CZC was at least an order of magnitude higher than that at BBY with rare exception. The only samples for which the AIS registered INP_{-10} above detection limit at BBY occurred between 22 - 23 UTC on 5 March and near 5 UTC on 6 March. The sample collected at BBY at 22 UTC contained INP_{-10} = 2.67 mL^{-1}, the highest at BBY. The heaviest rainfall occurred between 21 UTC 5 March and 3 UTC 6 March at both sites (Barrier Jet and Peak AR periods).

The S-Band radar derivation of ETH and the relative humidity at 5 km MSL (RH_{5km} - %) are displayed in Fig. 3.4b. ETH was variable during the storm. S-Band retrievals are intermittently missing between 15 UTC and 21 UTC on 5 March. Where not missing, the median value of ETH was near 5 km MSL. ETH rose sharply after 21 UTC on 5 March, reaching an event maximum value just over 8 km MSL. After 23 UTC on 5 March, ETH fell to a minimum value of approximately 4 km MSL 25 at 02 UTC on March 6. This time corresponds to the maximum measured IVT (Table 3.2). ETH rose again near cold front passage, passing 7 km MSL. After 5 UTC on 6 March, ETH fell precipitously. After 6 UTC, S-Band retrievals of ETH ceased.

After 18 UTC on March 5, ETH and RH_{5km} are qualitatively well correlated. ETH rose (fell) in the range 4 km MSL to 8 km MSL as RH_{5km} rose (fell). This suggests that the availability

of moisture was a factor controlling the presence of upper cloud layers during the Barrier Jet and Peak AR periods. It is noteworthy that the strongest IVT and heaviest rainfall occurred when mid-levels were dry, cloud tops were lower, and INP_{-10} were absent at BBY. We will explore whether warm INPs in BBY precipitation is related to cloud top altitude in sections 3.5.6 and 3.5.7.

While both sites experienced very similar weather conditions during the AR, warm INPs were much more prevalent in precipitation at CZC than at BBY. The enhancement in INP_{-10} (Fig. 3.4a) was more than a factor of during most of the storm. While INP_{-10} remained elevated throughout the latter three periods in CZC precipitation, INP_{-10} presence in BBY precipitation was ephemeral. These two findings suggest that the two sites were exposed to different warm INP sources, experienced different cloud injection mechanisms, or both.

3.5.4 Droplet freezing spectra at BBY and CZC and their response to heat treatment

Figure 3.5a,c show the droplet freezing activation spectra, INP(T), as measured by the AIS from precipitation samples at BBY and CZC, respectively. Vertical lines at -10 °C are provided so that the number of warm INPs is visually enhanced. In CZC samples, significant freezing events occurred for T > -10 °C in all periods. Concentrations from CZC in the temperature range -15 °C < T ≤ -5 °C are consistent with precipitation samples containing terrestrial bio-INPs as reported in Petters and Wright (2015). In the Barrier Jet and Peak AR periods, freezing events were detected at temperatures as warm as -5 °C. In agreement with Fig. 3.4a, few BBY samples from the Barrier Jet period and one sample from the Post CF period similarly contained material that froze at T > -10 °C. As time passed, the maximum INP(T) and INP_{-10} both increased in precipitation collected at CZC. Concentrations were greater during the Peak AR period than during Barrier Jet; and Barrier Jet concentrations were greater, in turn, than during Early AR. Rainfall also accumulated over time, with the sharpest increase in rain rate between the Early AR and Barrier Jet periods.

Though the increase in rainfall rate and in INP_{-10} are concurrent, we do not have sufficient analysis to confidently ascribe the increasing trend in INP_{-10} to bioprecipitation feedback.

Further difference in INPs between BBY and CZC is found in the shapes of the freezing spectra. The freezing spectra for T < -10 °C at BBY (Fig. 3.5a) are log-linear and negatively sloped with temperature. This agrees with models predicting immersion mode freezing of dust published by DeMott et al. (2010) and Niemand et al. (2012). Fig. 3.5c, by contrast, shows freezing spectra from CZC that cannot be modeled by a simple log-linear temperature relationship. This is consistent with immersion freezing of bio-INPs (Murray et al., 2012; Tobo et al., 2013, 2014; Petters and Wright, 2015).

Figures 3.5b,d show the fractional change in INP(T) after precipitation samples from BBY and CZC, respectively, were heated (see section 3.3.5). This is expressed as ΔINP(T)/INP(T), where ΔINP(T) is the concentration from the unheated sample minus the concentration at matching temperature from the heated sample. Heating the precipitation samples prior to measuring their freezing activation de-natures biological material that would otherwise have supported ice nucleation (Hill et al., 2014, 2016). It may also cause insoluble inorganic material to break apart. In some cases, this fracturing of insoluble material can lead to increases in INP(T) (McCluskey et al., 2018). For T < -15 °C, the combination of these effects may lead to a mixture of positive and negative ΔINP(T). Additionally, heat treatment may completely nullify the ability of some bio-INPs to support freezing but may not render other types (e.g. cellular fragments) freezing inactive. At both sites, heating nullified most freezing for T > -10 °C. The exception is for samples during the Peak AR period at CZC. Some CZC Peak AR samples partially, but not completely, lost their freezing activity for T > -10 °C after heating. The issue of mixed trend in ΔINP(T) for T < -15 °C is apparent in samples from both sites. INP(T) increased after heating in 23% (11%) of samples

collected at BBY (CZC), respectively. Heat treatment and INP(T) functional form support the conclusion that biological material contributed to warm INP concentrations at CZC for most samples. However, biological material contributed to warm INP concentration at BBY only for a few samples.

Results from sections 3.5.3 and 3.5.4 show a large difference in INP_{-10} between sites, with many more collected in precipitation at CZC. Later analysis will address hypotheses related to source and impact on clouds of these INP, but here the authors feel it is prudent to address the possibility that sample or instrument contamination led to the failure to detect warm INP at BBY. While we cannot test the chemical composition of individual INP, we were able to classify chemical type of the collected insoluble precipitation residues using the aerosol time of flight mass spectrometer (ATOFMS). We have included ATOFMS methods, concepts of operation and particle type classification in supplemental material (section 3.10). ATOFMS was used to classify single insoluble residue particles into four separate types, including a bioparticle type. The particle classification method and bioparticle type have been published in previous studies, with references provided in the 3.10. Figure 3.8 shows that the bioparticle type was the most numerous at both coastal and inland sites during all kinematic periods. While we cannot separate these bioparticles according to their marine or terrestrial sources, their ubiquity and similar concentration at both coastal and inland sites during strong onshore flow suggest that a significant number are from marine sources. These bioparticles are related to warm INP in that all freezing events triggered for T > -10 °C in the AIS should be caused by insoluble residue bioparticles, but not all insoluble residue bioparticles are capable of triggering freezing in the AIS (e.g. IN inactive bioparticles). Thus, Fig. 3.8 demonstrates that marine bioparticles were collected and preserved for laboratory

analysis from both sites, while the low number warm INP collected at the coastal site reflects the inability of the marine bioparticles collected there to trigger freezing events at T > -10 °C.

3.5.5. Qualitative transport patterns and their association with warm INPs in precipitation

The location and altitude of FLEXPART elements released in the mixed-phase and cloud-top layers for each of the four periods are displayed in Fig. 3.6. Of note for understanding LRT warm INPs during the AR, Fig. 3.6b,d display the element position for releases made during the Barrier Jet and Post CF periods. During these periods, many elements ending in the cloud top layer travelled along the upper tropospheric jet stream. Recall from section 3.4.4 that the jet stream is located between altitudes of 6.5 and 11 km MSL, therefore yellows, oranges and reds in Fig. 3.6 indicate appropriate jet altitudes. By contrast, element positions for cloud-top releases during Early AR (Fig. 3.6a) and Peak AR (Fig. 3.6c) periods do not visually show transport influence from the jet stream. The difference in degree of jet stream influence between the three pre-cold frontal periods likely comes from cloud-top layer altitude (Table 3.2). Elements ending in the cloud-top layer during the Post-CF period likewise appear to have travelled along the Pacific upper tropospheric jet even though cloud tops were lower during much of this period. Subsidence in the post cold-frontal airmass may have linked the high-altitude UTJ and relatively lower cloud tops during the Post CF period. The Barrier-Jet and Post-CF periods were the only periods during which warm INPs were detected in precipitation collected at BBY (Fig. 3.5a). Figures 3.5a and 3.6 together suggest some long-range transported warm INPs may have arrived to the AR cloud tops by travelling across the Pacific Ocean on the upper tropospheric jet stream. This result is in broad agreement with findings in Ault et al. (2011) and Creamean et al. (2013). From Fig. 3.6 it is also apparent that elements nearing the ARO primarily travelled along the AR during the final hours of

their flight. The AR played a smaller role in transport to the cloud layers during the Post CF period, when lower tropospheric airmasses arrived to the ARO from the cold-sector, or from the west of the cold front and AR, just glancing the AR upon arrival.

3.5.6 Quantitative relationships between airmass source, transport mechanism, and cloud injection temperature

Table 3.4 presents the probability of element residence (section 3.4.3) in the UTJ, AR, MBL and TBL. From Table 3.4, one can verify many of the broad qualitative findings from Fig. 3.6. Namely, elements were much more likely to arrive in the cloud-top layer after travelling in the UTJ during the Barrier Jet and Post CF periods; airmasses arriving in the mixed-phase layer had the largest marine boundary layer influence during the Barrier Jet and Peak AR periods; and the probability that an element passed through the AR before arriving in the clouds above CZC is smallest for the Post CF period.

Table 3.4 also offers insight to which periods were most likely to have terrestrial boundary layer air drawn into the mixed-phase cloud layer. The probability that an element both travelled through the terrestrial boundary layer and ended in either cloud layer during the Early AR period is zero. Likewise, there is zero probability that elements travelled through the terrestrial boundary layer and entered the cloud-top layer during any period. The probability that an element travelled through the terrestrial boundary layer and ended in the mixed phase cloud layer above CZC during the Barrier Jet, Peak AR and Post CF periods is 0.062, 0.083, and 0.044, respectively. Note that all elements arrived at CZC in both layers from the west or southwest (offshore) during all periods, and thus had a very short trip over or through terrestrial boundary layers. These directions of travel were the same for FLEXPART simulations over BBY (not shown). The location of BBY directly on the coastline thus yields $P_{TBL} = 0$ for all layers and all periods. BBY clouds were never

downwind of a nearby landmass during the AR. We interpret the P_{TBL} results to mean that approximately 4% to 8% of the air arriving in the mixed-phase clouds over CZC also spent time in the nearby terrestrial boundary layer. If terrestrial biomes were a source of warm INPs, mixed phase clouds were able to entrain warm INPs into layers that could support heterogeneous freezing. Note that the concentration of INP_{-10} at CZC increased markedly from the Early AR period to the other periods considered (Fig. 4a), following the trend in increasing P_{TBL}.

We can now address questions related to warm INP source and injection mechanism. Both sites were downwind of marine particle sources for the entire storm and the cloud layers above each site received significant contributions from the marine boundary layer during all storm periods. Only CZC precipitation contained warm INPs during all periods. The only persistent difference in airmass influence between the cloud layers over the two sites was that inflowing air to CZC passed through the terrestrial boundary layer before arriving. Thus, we conclude that the warm INPs present in CZC precipitation are predominantly terrestrial in origin, and that terrestrial warm INPs are not found in BBY precipitation. There is no mechanistic explanation for the simultaneous presence (lack) of warm INPs at CZC (BBY) if the warm INP source is marine. LRT warm INPs were ephemerally present, likely at both sites. LRT warm INPs were injected at cloud top and their transport and injection were highly modulated by large-scale meteorology (e.g. the UTJ), kinematic forcing mechanism and the availability of mid-tropospheric moisture.

Table 3.4 demonstrates that a transport pathway existed for terrestrial boundary layer air, potentially containing terrestrial INPs, to become injected to mixed phase clouds. The activity of this pathway (P_{TBL}) was modulated by kinematic forcing regime. For example, it was inactive during the Early AR period but became active through the rest of the storm. The reader may wonder whether it is reasonable for the warm INP content of precipitation to so strongly respond (order

magnitude increase, see Fig. 3.4a) to the onset of air parcels from the terrestrial boundary layer, given the fractional contribution of these parcels to the cloud-inflowing airmass is at most 8%. It is prudent to note that the ambient concentration of warm INP in the terrestrial boundary layer upstream of CZC is unknown, but work on bioprecipitation feedback (Huffman et al., 2013; Prenni et al., 2013; Morris et al., 2014; Bigg et al., 2015) demonstrates that warm INP emission often rises dramatically in response to precipitation, thus the FLEXPART analysis alone cannot estimate the increase in number concentration of cloud-inflowing terrestrial warm INP. Additionally, Stopelli et al. (2015) argue that INP are removed much more efficiently by precipitation than are other condensation nuclei. We can thus expect that the precipitation INP content will respond in a highly non-linear fashion to changes in the ambient warm INP concentration of cloud-inflowing air. Indeed, because the ice-phase microphysical processes governing removal of INP by precipitation may vary independently from airmass source, we need not expect the precipitation INP content to strongly covary with changes in terrestrial boundary layer residence.

3.5.7 Impact of warm INPs on mixed-phase cloud microphysics

Figure 3.7 displays the time series of the fraction of returns with frozen hydrometeors in the BBY azimuth, (P_{frz}^{BBY}), for each scan. The all-storm value of P_{frz}^{CZC} is displayed as a horizontal reference line. For the majority of the AR, P_{frz}^{BBY} was much less than the storm-mean P_{frz}^{CZC}. The likelihood that KDAX observed frozen hydrometeors in the unblocked layer above CZC during the storm is P_{frz}^{CZC} = 0.615. The same likelihood over BBY is P_{frz}^{BBY} = 0.165. A two-category, two-site Chi-square independence test was performed using all available hydrometeor class retrievals from each site. The null hypothesis, that the likelihood of observing frozen hydrometeors is independent of site, is rejected with P = 4.3×10^{-38}. This result is insensitive to Yates' correction. By visual inspection of Fig. 3.7 and by the result of the Chi-square independence test, we adopt

H2 and note that frozen hydrometeors were more likely at equivalent temperatures over CZC than over BBY. As we have seen, warm INPs were also consistently more numerous, by as much as a factor of 10, in CZC precipitation. Also of note in Fig. 3.7, P_{frz}^{BBY} did not increase during the Barrier Jet period, though Barrier Jet period precipitation samples from BBY contained higher INP_{-10}. It is possible that warm INPs over BBY were only injected through cloud top at colder temperatures, supporting the activation of other INP sources. If so, LRT warm INPs may have minimally impacted the presence of frozen hydrometeors in the mixed-phase layer. This explanation is consistent with the LRT source and injection mechanisms found for BBY in prior analyses.

Because we cannot directly measure the impact of warm INPs on P_{frz}^{BBY} (P_{frz}^{CZC}), we must attempt to exclude the possibility alternate processes explain the difference in P_{frz}^{BBY} (P_{frz}^{CZC}). After noting that we ensured that the KDAX hydrometeor type sample corresponds to the same temperature range over both sites, we address the possibility that any difference in P_{frz}^{BBY} (P_{frz}^{CZC}) was caused by a difference in the rate of frozen hydrometeors falling from above the KDAX unblocked layer. To address this possibility, we conducted analysis of the reflectivity in the KDAX unblocked layer over each site. For this analysis only, we relaxed the constraint on temperatures above each site in favor of also retaining 45 gates from the CZC azimuth. Radar reflectivity is closely related to the precipitation rate, thus a strong association between the KDAX unblocked reflectivity and P_{frz}^{BBY} (P_{frz}^{CZC}) is considered to indicate that frozen hydrometeors are primarily falling from higher and colder layers. Radar power is also returned more strongly for liquid hydrometeors than for ice hydrometeors. Therefore, in the absence of any relationship between strength of precipitation rate and likelihood of frozen hydrometeors, we should expect a weak negative relationship between reflectivity and the likelihood of frozen hydrometeors in the unblocked layer. We also note that intersite comparisons of reflectivity are not appropriate, since

the degree of beam blockage is different over each site and we do not perform any correction to retrieved beam power based on the blockage geometry (e.g. Qi et al., 2014). The relationship between P_{frz}^{BBY} (P_{frz}^{CZC}) and mean unblocked layer reflectivity for all scans is shown in Fig. 3.8. Note there is little to no correlation between mean reflectivity and P_{frz} for either site. R^2 is 0.004 (0.006) for BBY (CZC). We thus conclude that the precipitation rate had very little effect on the chance of observing frozen hydrometeors in the unblocked layer over both sites.

3.6 Conclusions

In this study, we examined the freezing spectra of time-resolved rainfall samples from two Northern CA sites, one coastal (BBY) and one inland (CZC), during an AR with significant regional impact. We compared these spectra and their warm INP concentration (INP_{-10}) across sites and across kinematic with varying cloud depth, airmass source and transport mechanisms. These analyses were performed to address the following questions. What roles do terrestrial, marine and LRT aerosols play in determining the warm INPs during this AR? What are the transport and cloud injection mechanisms for each of these sources? When warm INPs are present in precipitation, are cloud microphysics impacted? In summary, we found

1. Using the AIS, that terrestrial warm INPs are abundant in precipitation at the inland site. It is possible that bioprecipitation feedback contributes to terrestrial warm INP source for the inland site.

2. Through quantitative analysis of FLEXPART element residence times, we do not see evidence of marine warm INPs at either site during this storm.

3. Through similar analysis, that long-range transported warm INPs may additionally be present in precipitation at both sites, but only when airmass transport patterns and kinematic regime enable cloud tops to access high altitude transported airmasses.

4. Using the analysis of FLEXPART residence times and radar hydrometeor classifications, we found evidence that terrestrial warm INPs impacted precipitating hydrometeors in mixed phase clouds during this storm.

The unique flow geometry and geography of the precipitation collection sites during this AR formed a critical element supporting these findings. Both sites are downwind of marine particle sources for the entire storm and the cloud layers above each site receive significant airmass contribution from the marine boundary layer during all storm periods (Table 3.4). However, only the inland site shows warm INPs in precipitation during all periods (Fig 3.4a and Fig 3.5a,c). The only difference in airmass influence between the cloud layers over the two sites is that inflowing air to mixed phase clouds over the inland site (CZC) passes through the terrestrial boundary layer before arriving (Table 3.4). When warm INPs are present in coastal site precipitation, their presence can be explained mechanistically by transport patterns and cloud top altitude favorable for LRT aerosols to become injected at cloud top. Conversely, we cannot provide an alternate hypothesis for ephemeral injection of marine warm INPs into coastal site clouds. Here we must note that it is possible that suppressed emission of marine warm INPs in nearby source regions or offshore removal led to the absence of detectable marine warm INPs during this storm but that marine INPs may be important for other ARs.

The KDAX radar hydrometeor retrievals (Fig. 3.7) were likewise a critical element supporting these findings KDAX analyses show that the precipitating hydrometeor phase in clouds with -10 °C < T ≤ 0 °5 C is significantly different at CZC than at BBY, with a higher probability of frozen hydrometeors over CZC. As we have seen (Fig. 3.4a), warm INPs were also consistently more numerous, by as much as a factor of 10, in CZC precipitation. We can thus hypothesize that

terrestrial warm INPs became injected into mixed-phase clouds over CZC and impacted cloud hydrometeor populations through in-situ ice-phase microphysics.

As we have seen in multiple analyses presented herein, the role of meteorology in modulating warm INP source, transport and cloud injection mechanism is complex. It depends upon large-scale weather features, kinematic forcing mechanisms such as barrier and low-level jets, and the availability of moisture near cloud top. These are just the processes that determine the warm INPs in the single AR studied herein. ARs as important mechanisms for the removal of trace atmospheric constituents of remote origin and the impact of terrestrial and marine warm INPs on mixed-phase clouds and precipitation are topics deserving further study. Finally, this study demonstrated that polarimetric precipitation radar can be a useful tool to study cloud microphysics given well-constrained conditions. Future studies into the impact of aerosols on cloud microphysics may benefit from targeted polarimetric radar observations conducted in tandem with tropospheric soundings and laboratory analysis of cloud and precipitation material. It is certainly possible to enhance the analysis methods herein and deploy similar methods for multiple storms so that these or future findings may be generalized to other regions or other weather scenarios.

3.7 Acknowledgements

The authors would like to acknowledge the UC Davis Bodega Marine Laboratory in Bodega Bay, CA for providing space for sample collection, laboratory work and housing while the field phase of this study was completed. Many thanks to Drs. Paul DeMott and Thomas Hill of Colorado State University for helpful guidance regarding AIS analyses. National Science Foundation Grants 25 AGS-145147, AGS-1632913, and US Army Corps of Engineers Grant W912HZ-15-2-0019 provided funding for this work. J. Creamean was supported through funding from NOAA Physical Sciences Division.

Chapter 3, in full, has been accepted for publication in Atmospheric Chemistry and Physics. Martin, A. C., Cornwell, G. C., Beall, C. M., Cannon, F., Reily, S., Schaap, B., Lucero, D., Creamean, J. M., Ralph, F. M., Mix, H., Prather, K. A. (2019). Contrasting Local and Long-Range Transported Warm Ice-Nucleating Particles During an Atmospheric River in Coastal California, USA.

3.8 Figures

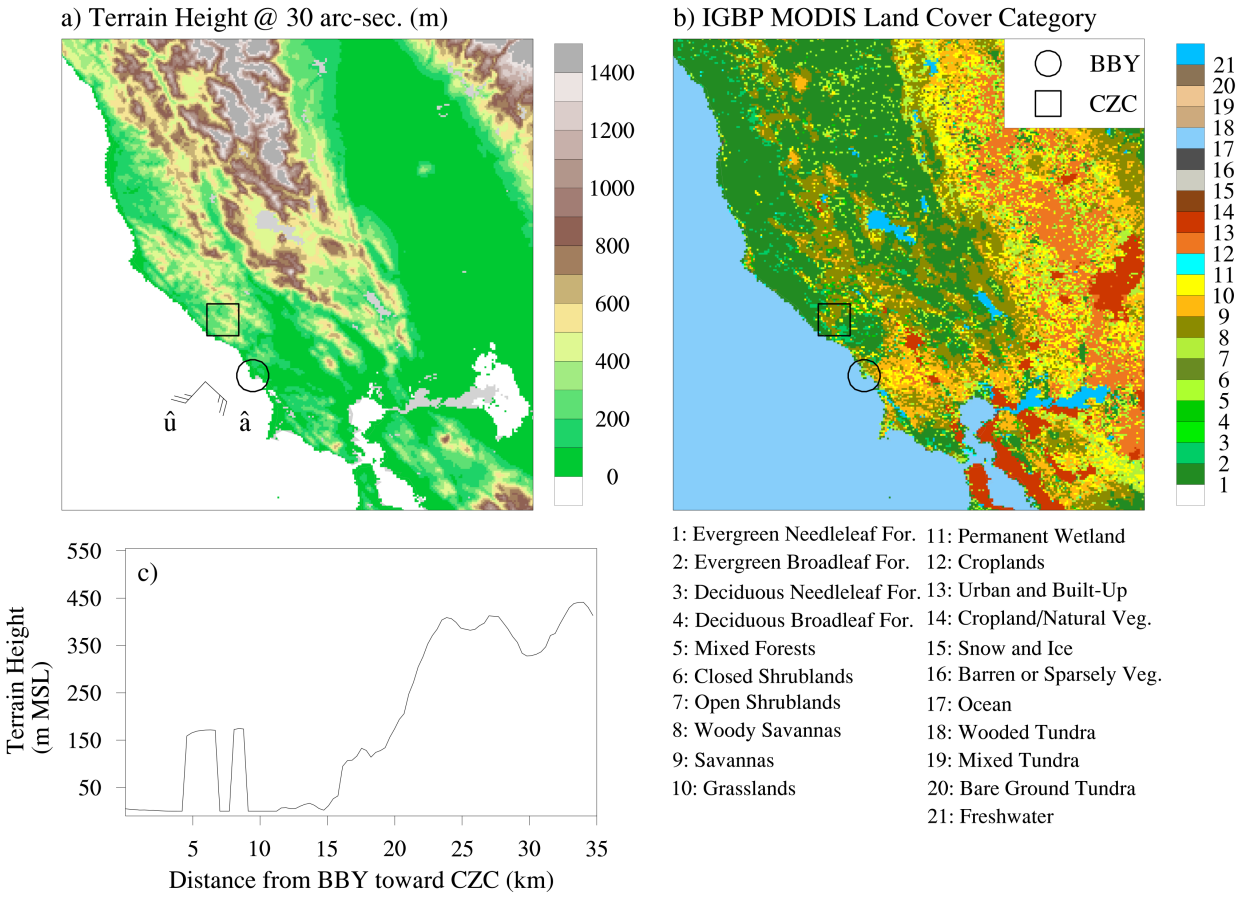

Figure 3.1. a) Plan view of regional terrain height (m - colorfill) from USGS 30 arc-second digital elevation map. Annotations are centered on BBY (circle) and CZC (square) and depict theoretical wind barbs aligned with the upslope (û) and along-slope directions (â). (b) As in a, except the dominant category from the IGBP-MODIS landuse database is depicted (colorfill - see legend for category name). c) Transect of terrain height (m MSL) along a great circle path from BBY to CZC.

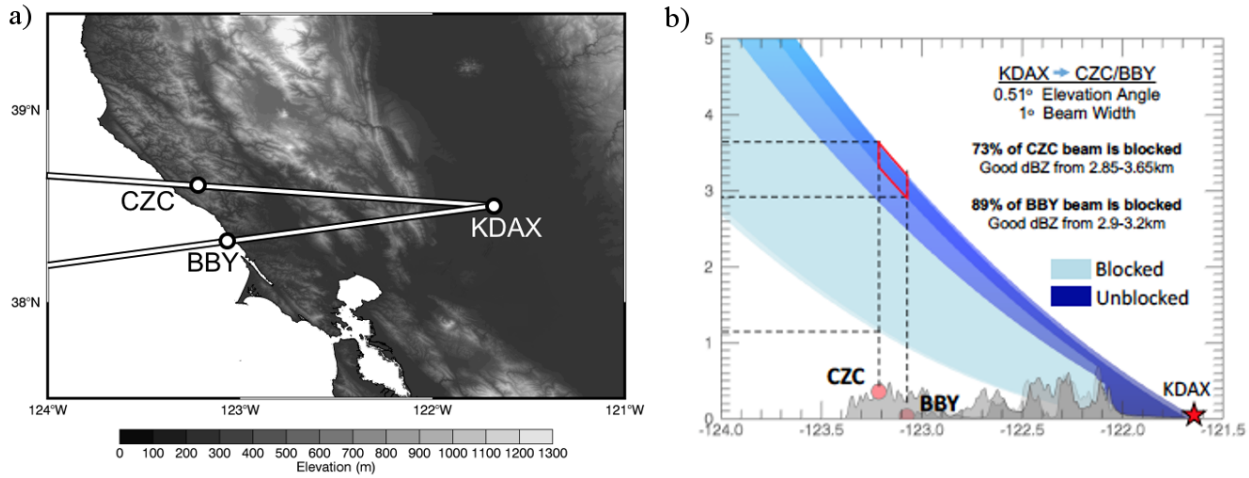

Figure 3.2. a) Plan view of region surrounding the study area with KDAX, BBY and CZC labelled. Beams show path of radar from KDAX to each site (BBY, CZC). White shading indicates relative terrain height (m MSL). b) Height vs. longitude cross-section with KDAX 0.51 degree elevation scan beam blocked (light blue), unblocked over CZC (medium blue) and unblocked over BBY (dark blue) layers. Red trapezoid indicates the volume from BBY azimuths that are unblocked and share the altitudes of the CZC unblocked layer. Location of BBY (CZC) indicated by red dot at respective longitude and height. Terrain profiles along BBY (CZC) azimuths also indicated in gray shading.

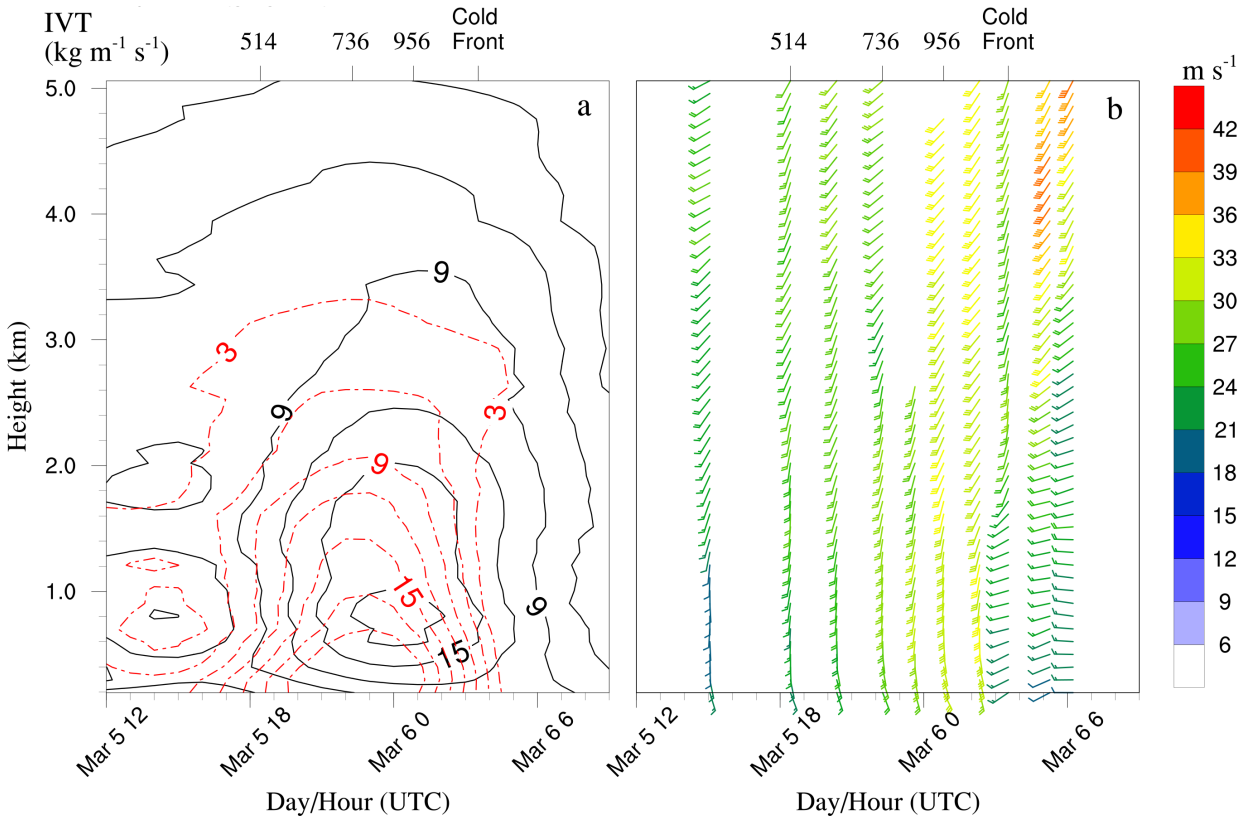

Figure 3.3. a) Upslope (black solid) and along-barrier (red dashed) water vapor flux (g kg^{-1} s^{-1}) derived from rawinsondes during storm period. b) Rawinsonde horizontal wind profiles (m s^{-1}, wind barbs colored by speed) during event. In each a and b, the time of significant sondes are marked along the top axis by their IVT (kg m^{-1} s^{-1}) or by the arrival of the cold front.

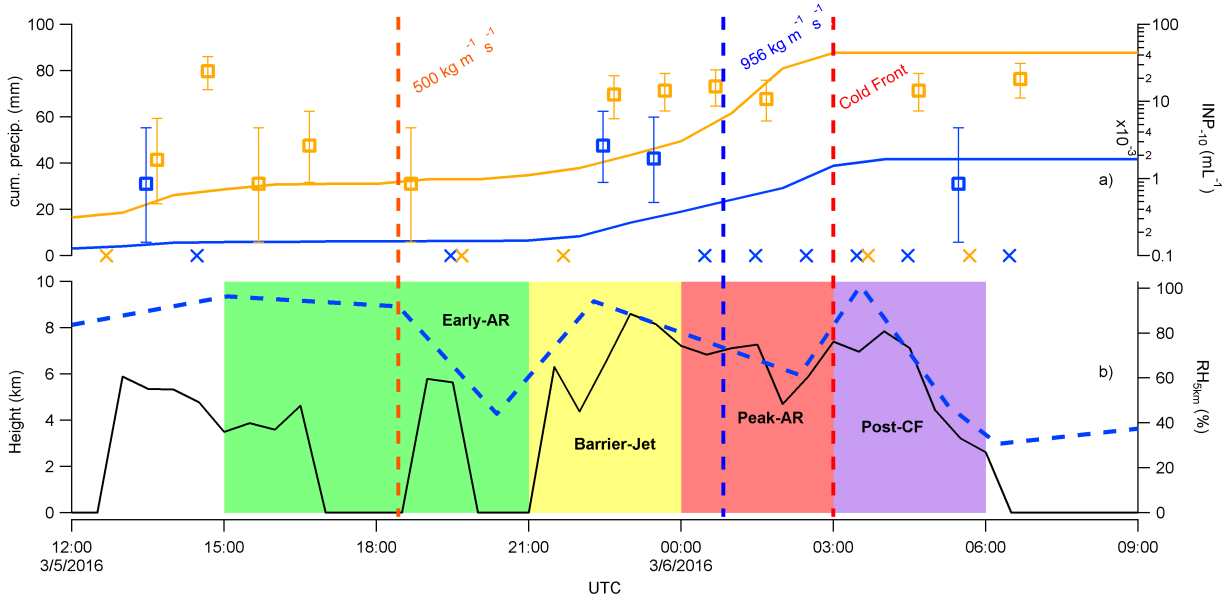

Figure 3.4. a) time series of INP_{-10} (mL^{-1}) at BBY (box-and-whisker - blue), at CZC (box-and-whisker - orange), accum. precip. (mm) at BBY (blue line) and accum. precip. at CZC (orange line). Blue (orange) 'X' on temporal axis indicates precipitation sample with INP_{-10} below AIS detection limit at BBY (CZC). Timing of IVT surpassing 500 kg m^{-1} s^{-1} and cold front transit are annotated in red dashed lines. b) S-band radar derived echo-top (ET - black solid) and brightband (BB - black dashed) height (km MSL) at CZC. Also shown is RH_{5km} (%) from soundings (blue dashed). Shading depicts "Early AR", "Barrier Jet", "Peak AR", and "Post-CF" periods (section 3.5.4), respectively.

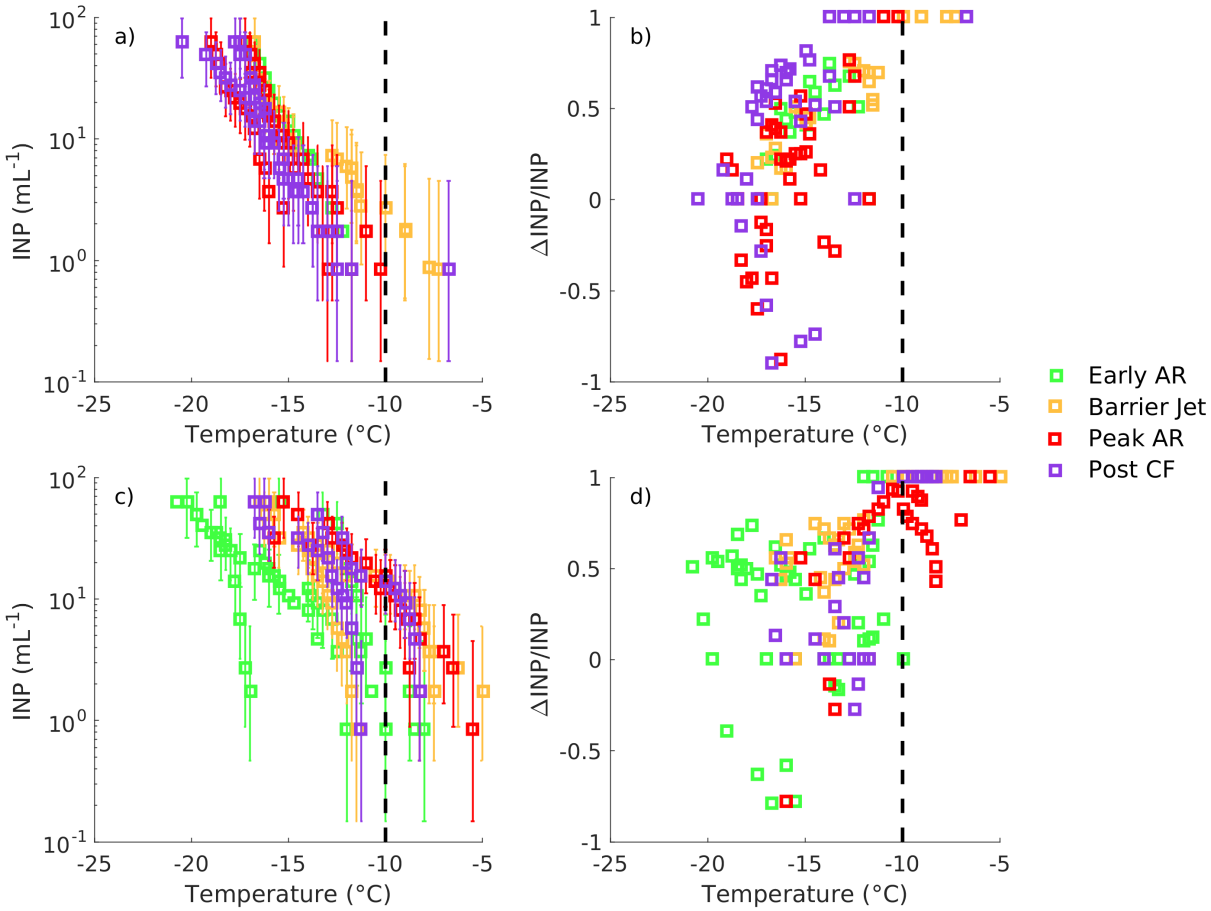

Figure 3.5. a) Un-heated INP(T) (mL^{-1}) from BBY precipitation during "Early AR" (green), "Barrier Jet" (yellow), "Peak AR" (red), and "Post CF" (purple) periods. Whiskers denote technique standard error (mL^{-1}). b) as in a, except for ΔINP(T)/INP(T). c) as in a, except for un-heated precipitation samples from CZC. d) as in c, except for ΔINP(T)/INP(T).

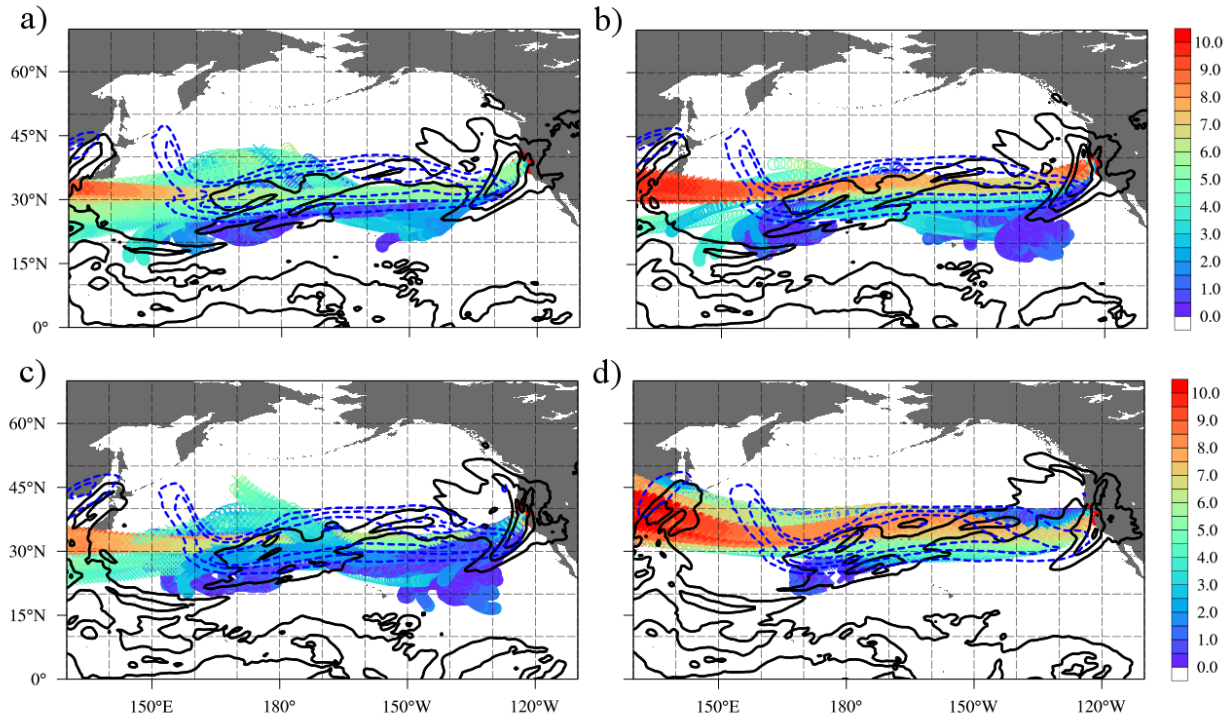

Figure 3.6. a) FLEXPART backward-simulated element position for releases from cloud-top ('X' markers) and mixed-phase ('O' markers) layers over CZC during Early AR period. Marker color denotes element altitude (km MSL). Period average IVT from CFS is shown by black contours from 250 kg m^{-1} s^{-1} to 750 kg m^{-1} s^{-1} every 250 kg m^{-1} s^{-1}. Period average horizontal wind speed in the jet layer (see section 3.4a for layer definition) is shown by blue dashed contours from 50 m s^{-1} to 70 m s^{-1} every 10 m s^{-1}. b) as in a, except for Barrier Jet period. c) as in a, except for Peak AR period. d) as in a, except for Post CF period.

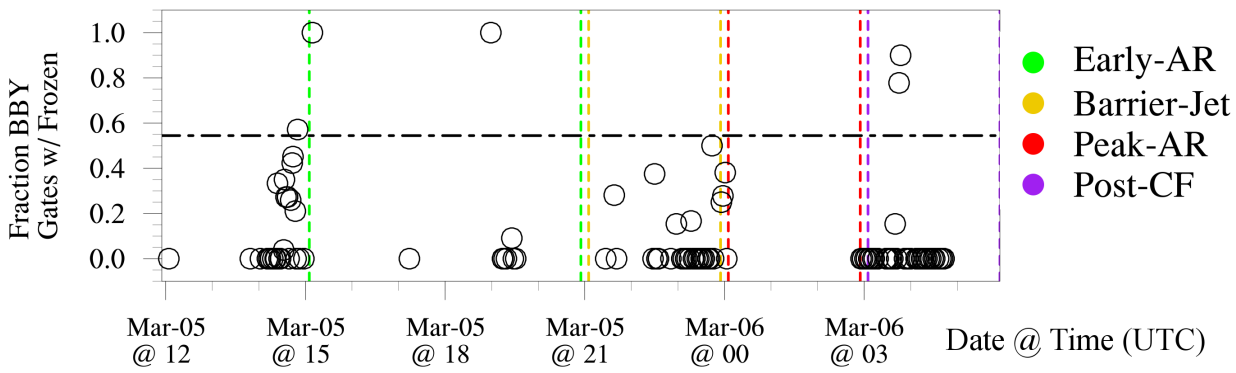

Figure 3.7. a) time series of P_{frz}^{BBY} (black circles) in the unblocked layer from all KDAX scans detecting precipitation at the BBY azimuth. The all-storm mean of P_{frz}^{CZC} is shown by the horizontal dot-dash black line. Vertical dashed lines show the boundaries of kinematic periods, as coded by color in the legend.

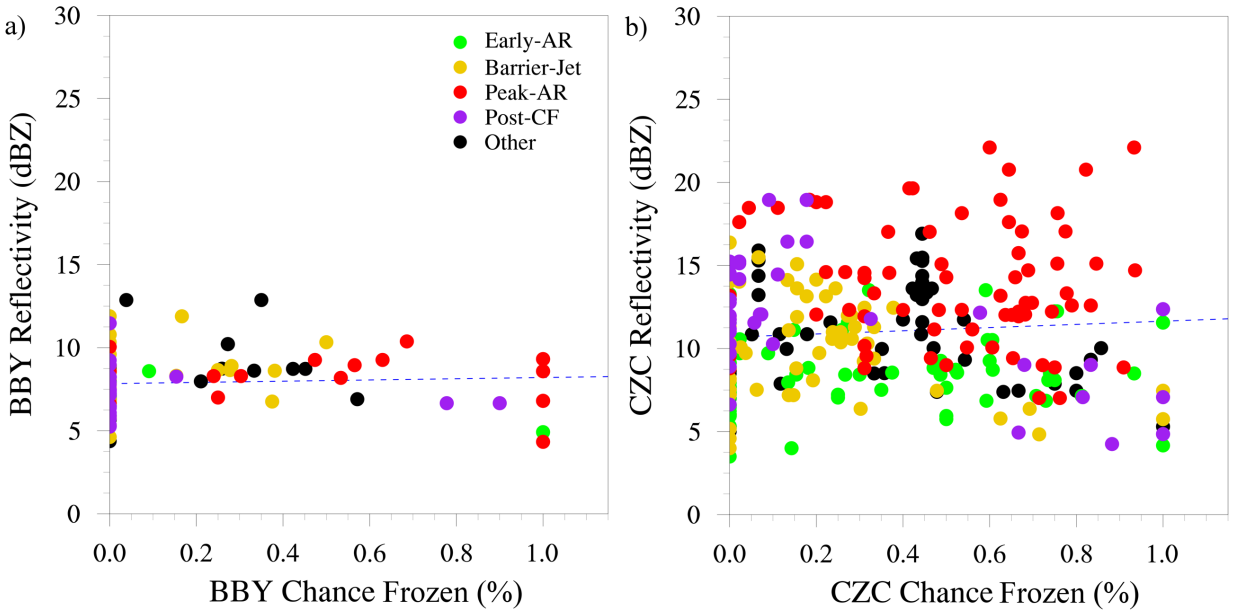

Figure 3.8. a) Relationship between P_{frz}^{BBY} (abscissa) and BBY mean reflectivity (dBZ - ordinate) from all KDAX scans detecting precipitation at the BBY azimuth. Marker color depicts the kinematic period each scan belonged to, as coded by color in the legend. b) as in a, except for P_{frz}^{CZC} and CZC mean reflectivity (dBZ).

3.9 Tables

Table 3.1. ARO Measurements by site (BBY/CZC).

Measurement	BBY	CZC	Reference
449 MHz wind profiling radar	X		White et al., (2013)
S-band profiling precipitation radar		X	White et al., (2013)
GPS-derived Integrated Water Vapor	X	X	White et al., (2013)
Surface weather station (rain gauge, anemometer)	X	X	White et al., (2013)
ISCO 6712 water samplers	X	X	http://www.teledyneisco.com/en-us/

Table 3.2. Balloon-borne soundings launched from BBY and their metadata: IVT, height of freezing isotherm, top (bottom) temperatures of the KDAX radar retrieval layer (see section 3.4.3). Superscripts [M,C] denote maximum AR strength, transit of cold front, respectively.

Sounding time	IVT (kg m^{-1} s^{-1})	$Z_{T=0\,°C}$ (m)	T_{KDAX}^{top} (°C)	T_{KDAX}^{bot} (°C)
1504 UTC, 5 March 2016	416	2562	-4.9	-0.9
1826 UTC, 5 March 2016	514	2613	-5.4	-1.6
2022 UTC, 5 March 2016	560	2666	-4.2	-1.2
2217 UTC, 5 March 2016	736	2560	-4.4	-2.1
0050 UTC, 6 March 2016[M]	956	2944	-4.4	0.5
0220 UTC, 6 March 2016	922	2967	-4.5	0.8
0332 UTC, 6 March 2016[C]	553	2686	-4.9	-1.0
0516 UTC, 6 March 2016	467	2213	-7.5	-3.7
0614 UTC, 6 March 2016	314	2101	-9.2	-5.4

Table 3.3. Kinematic periods, their beginning and end time, maximum sounding-derived IVT, height of cloud layers (see section 3.5.2) used for FLEXPART analysis, mean INP_{-10} at CZC, and accumulated precipitation at each site.

Period name	Start time (UTC)	Max IVT (kg m^{-1} s^{-1})	ZT = 0 ºC / ZT = 0 ºC / ETH (m MSL)	CZC INP_{-10} / CI^{-}-CI^{+}(mL^{-1})	Accum. precip. (mm) (BBY/CZC)
Early AR	15 UTC, 5 Mar	560	2550/4800/5800	0.87/0.23-3.29	4.5/11.2
Barrier jet	21 UTC, 5 Mar	736	2550/4850/8600	8.71/4.5-14.9	7.6/10.4
Peak AR	00 UTC, 6 Mar	956	2950/4850/7800	8.79/4.75-14.82	15.0/37.6
Post CF	03 UTC, 6 Mar	553	2100/4150/8300	4.62/2.52-7.72	6.6/12.5

Table 3.4. Probability of instantaneous element residence in features of interest P_{res}, during FLEXPART backward simulation given a element arrived in the labelled period and layer. Non-zero P_{res} are bold.

Feature	**Period and layer (mixed-phase: MP; cloud-top: CT)**							
	Early AR		Barrier Jet		Peak AR		Post CF	
	MP	CT	MP	CT	MP	CT	MP	CT
P_{UTJ}	0.0	0.003	0.0	**0.194**	0.0	**0.028**	**0.04**	**0.235**
P_{AR}	**0.351**	**0.231**	**0.411**	**0.033**	**0.452**	**0.194**	**0.290**	**0.075**
P_{TBL}	0.0	0.0	**0.062**	0.0	**0.083**	0.0	**0.044**	0.0
P_{MBL}	**0.158**	**0.172**	**0.300**	0.0	**0.398**	**0.182**	**0.313**	**0.028**

3.10 Supplementary methods

3.10.1 Supplemental methods for ATOFMS analysis of precipitation samples

The size-resolved single particle mixing state of precipitation sample residues was measured using an ATOFMS (E. Gard et al., 1997). Samples were aerosolized using a collision-style nebulizer and dried using two silica diffusion driers. Samples were stirred using a magnetic stir bar to ensure that insoluble particles had not settled and were being aerosolized. Temporally adjacent precipitation samples were combined to obtain the requisite sample volume for use with the atomizer (75-100 mL), but samples were not combined across kinematic period boundaries. Single particle spectra and size data were imported into Matlab (The MathWorks, Inc.) and analyzed via the software toolkit FATES (Sultana, et al., 2017). Particles were divided into clusters based on their mass spectral features via an adaptive neural network and recombined based upon their characteristic mass spectra and size distributions (Rebotier & Prather, 2007; Song et al., 1999). Particles were separated into 4 different classes based upon previous ATOFMS lab and field studies: biomass burning (BB), organic carbon (OC), dust, and biological particles (Bio). Table 3.5 below shows the representative peaks and literature references associated with each particle type.

3.11 Supplementary figures

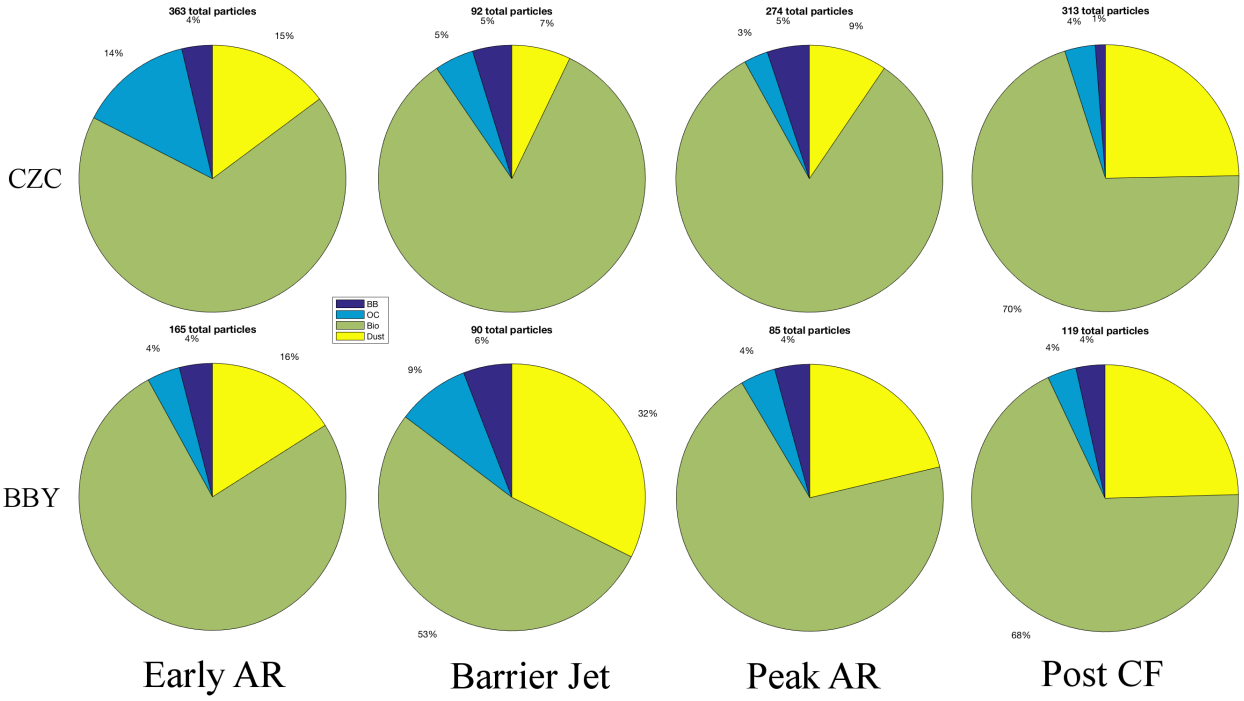

Figure 3.9. Particle fraction by ATOFMS/FATES detected and classified type at CZC (top row) and BBY (bottom row) during precipitation collected during the kinematic periods: Early AR, Barrier Jet, Peak AR, and Post CF.

3.12 Supplementary tables

Table 3.5. Insoluble residue particle types identified using ATOFMS/FATES.

Particle type	Characteristic ion markers
Biomass burning (BB)	Intense $^{39}K^+$ and $^{97}HSO_4^-$, minor contributions from $^{12}C^+$, $^{26}CN^-$, $^{46}NO_2^-$, $^{62}NO_3^-$, $^{125}H(NO_3)_2^-$ (Silva et al., 1999).
Organic carbon (OC)	$^{27}C_2H_3^+$, $^{29}C_2H_5^+$, $^{37}C_3H^+$, $^{43}CH_3CO^+/CHNO^+$ (Qin et al., 2012; Silva & Prather, 2000; Spencer & Prather, 2006).
Dust	$^{7}Li^+$, $^{27}Al^+$, $^{39}K^+$, $^{48,64}Ti$,TiO^+, $^{54,56}Fe^+$, $^{60}SiO_2^-$, $^{76}SiO_3^-$, $^{79}PO_3^-$ (Silva et al., 2000).
Biological (Bio)	Strong $^{39}K^+$ and $^{79}PO_3^-$, minor contributions from organic fragments (Fergenson et al., 2004; Sultana, et al., 2017).

3.13 References

Ault, A. P., Williams, C. R., White, A. B., Neiman, P. J., Creamean, J. M., Gaston, C. J., Ralph, F. M., and Prather, K. A.: Detection of Asian dust in California orographic precipitation, *Journal of Geophysical Research: Atmospheres,* 116, 2011.

Beall, C. M., Dale Stokes, M., Hill, T. C., Demott, P. J., Dewald, J. T., & Prather, K. A. (2017). Automation and heat transfer characterization of immersion mode spectroscopy for analysis of ice nucleating particles. *Atmospheric Measurement Techniques*, *10*(7), 2613–2626. https://doi.org/10.5194/amt-10-2613-2017

Bigg, E. K., Soubeyrand, S., and Morris, C. E.: Persistent after-effects of heavy rain on concentrations of ice nuclei and rainfall suggest a biological cause, *Atmospheric Chemistry and Physics*, 15, 2313–2326, 2015.

Burrows, S. M., Hoose, C., Pöschl, U., and Lawrence, M.: Ice nuclei in marine air: biogenic particles or dust? *Atmospheric Chemistry and Physics*, 13, 245–267, 2013.

Conen, F., Morris, C., Leifeld, J., Yakutin, M., and Alewell, C.: Biological residues define the ice nucleation properties of soil dust, *Atmospheric Chemistry and Physics,* 11, 9643–9648, 2011.

Creamean, J., Ault, A., White, A., Neiman, P., Ralph, F., Minnis, P., and Prather, K.: Impact of interannual variations in sources of insoluble aerosol species on orographic precipitation over California's central Sierra Nevada, *Atmospheric Chemistry and Physics*, 15, 6535–6548, 2015.

Creamean, J. M., Suski, K. J., Rosenfeld, D., Cazorla, A., DeMott, P. J., Sullivan, R. C., White, A. B., Ralph, F. M., Minnis, P., Comstock, J. M., et al.: Dust and biological aerosols from the Sahara and Asia influence precipitation in the western US, science, 339, 1572–1578, 2013.

DeMott, P. J., Prenni, A. J., Liu, X., Kreidenweis, S. M., Petters, M. D., Twohy, C. H., Richardson, M., Eidhammer, T., and Rogers, D.: Predicting global atmospheric ice nuclei distributions and their impacts on climate, Proceedings of the National Academy of Sciences, 107, 11 217–11 222, 2010.

DeMott, P. J., Möhler, O., Stetzer, O., Vali, G., Levin, Z., Petters, M. D., Murakami, M., Leisner, T., Bundke, U., Klein, H., et al.: , Bulletin of the American Meteorological Society, 92, 1623–1635, 2011.

DeMott, P. J., Hill, T. C., McCluskey, C. S., Prather, K. A., Collins, D. B., Sullivan, R. C., Ruppel, M. J., Mason, R. H., Irish, V. E., Lee, T., et al.: Sea spray aerosol as a unique source of ice nucleating particles, Proceedings of the National Academy of Sciences, 113, 5797–5803, 2016.

Dettinger, M. D.: Atmospheric rivers as drought busters on the US West Coast, Journal of Hydrometeorology, 14, 1721–1732, 2013. Dettinger, M. D., Ralph, F. M., Das, T., Neiman, P. J., and Cayan, D. R.: Atmospheric rivers, floods and the water resources of California, Water, 3, 445–478, 2011.

Fan, J., Leung, L., DeMott, P. J., Comstock, J. M., Singh, B., Rosenfeld, D., Tomlinson, J. M., White, A., Prather, K., Minnis, P., et al.: Aerosol impacts on California winter clouds and precipitation during CalWater 2011: local pollution versus long-range transported dust, Atmospheric Chemistry and Physics, 14, 2014.

Fergenson, D. P., Pitesky, M. E., Tobias, H. J., Steele, P. T., Czerwieniec, G. A., Russell, S. C., et al. (2004). Reagentless Detection and Classification of Individual Bioaerosol Particles in Seconds. *Analytical Chemistry*, *76*(2), 373–378. https://doi.org/10.1021/ac034467e

Gard, E., Mayer, J. E., Morrical, B. D., Dienes, T., Fergenson, D. P., & Prather, K. A. (1997). Real-Time Analysis of Individual Atmospheric Aerosol Particles: Design and Performance of a Portable ATOFMS. *Analytical Chemistry*, *69*(20), 4083–4091. https://doi.org/10.1021/ac970540n

Haviland, M. G.: Yates's correction for continuity and the analysis of 2× 2 contingency tables, Statistics in medicine, 9, 363–367, 1990.

Heggli, M. F. and Rauber, R. M.: The characteristics and evolution of supercooled water in wintertime storms over the Sierra Nevada: A summary of microwave radiometric measurements taken during the Sierra Cooperative Pilot Project, Journal of Applied Meteorology, 27, 989–1015, 1988.

Heggli, M. F., Vardiman, L., Stewart, R. E., and Huggins, A.: Supercooled liquid water and ice crystal distributions within Sierra Nevada winter storms, Journal of climate and applied meteorology, 22, 1875–1886, 1983.

Heiss, W. H., McGrew, D. L., and Sirmans, D.: NEXRAD: next generation weather radar (WSR-88D), Microwave Journal, 33, 79–89, 1990.

Hill, T. C., Moffett, B. F., DeMott, P. J., Georgakopoulos, D. G., Stump, W. L., and Franc, G. D.: Measurement of ice nucleation-active bacteria on plants and in precipitation by quantitative PCR, Applied and environmental microbiology, 80, 1256–1267, 2014.

Hill, T. C., DeMott, P. J., Tobo, Y., Fröhlich-Nowoisky, J., Moffett, B. F., Franc, G. D., and Kreidenweis, S. M.: Sources of organic ice nucleating particles in soils, *Atmospheric Chemistry and Physics*, 16, 7195–7211, 2016.

Hoose, C., Kristjánsson, J., and Burrows, S.: How important is biological ice nucleation in clouds on a global scale?, Environmental Research Letters, 5, 024 009, 2010.

Huffman, J. A., Prenni, A., DeMott, P., Pöhlker, C., Mason, R., Robinson, N., Fröhlich-Nowoisky, J., Tobo, Y., Després, V., Garcia, E., et al.: High concentrations of biological aerosol particles and ice nuclei during and after rain, Atmospheric Chemistry and Physics, 13, 6151, 2013.

Kingsmill, D. E., Neiman, P. J., Ralph, F. M., and White, A. B.: Synoptic and topographic variability of northern California precipitation characteristics in landfalling winter storms observed during CALJET, Monthly weather review, 134, 2072–2094, 2006.

Kingsmill, D. E., Neiman, P. J., Moore, B. J., Hughes, M., Yuter, S. E., and Ralph, F. M.: Kinematic and thermodynamic structures of Sierra barrier jets and overrunning atmospheric rivers during a landfalling winter storm in northern California, Monthly Weather Review, 141, 2015–2036, 2013.

Lavers, D. A. and Villarini, G.: The nexus between atmospheric rivers and extreme precipitation across Europe, Geophysical Research Letters, 40, 3259–3264, 2013.

Lavers, D. A. and Villarini, G.: The contribution of atmospheric rivers to precipitation in Europe and the United States, Journal of Hydrology, 522, 382–390, 2015.

Maki, L. R., Galyan, E. L., Chang-Chien, M.-M., and Caldwell, D. R.: Ice nucleation induced by Pseudomonas syringae, Applied microbi- ology, 28, 456–459, 1974.

McCluskey, C. S., Ovadnevaite, J., Rinaldi, M., Atkinson, J., Belosi, F., Ceburnis, D., Marullo, S., Hill, T. C., Lohmann, U., Kanji, Z. A., et al.: Marine and Terrestrial Organic Ice Nucleating Particles in Pristine Marine to Continentally-Influenced Northeast Atlantic Air Masses, Journal of Geophysical Research: Atmospheres, 2018.

Minder, J. R., Durran, D. R., and Roe, G. H.: Mesoscale controls on the mountainside snow line, Journal of the Atmospheric Sciences, 68, 2107–2127, 2011.

Morris, C. E., Conen, F., Alex Huffman, J., Phillips, V., Pöschl, U., and Sands, D. C.: Bioprecipitation: a feedback cycle linking Earth history, ecosystem dynamics and land use through biological ice nucleators in the atmosphere, Global change biology, 20, 341–351, 2014.

Murray, B., O'sullivan, D., Atkinson, J., and Webb, M.: Ice nucleation by particles immersed in supercooled cloud droplets, Chemical Society Reviews, 41, 6519–6554, 2012.

Murray, B., Ross, J., Whale, T., Price, H., Atkinson, J., Umo, N., Webb, M., et al.: The relevance of nanoscale biological fragments for ice nucleation in clouds, Scientific reports, 5, 8082, 2015.

Neiman, P. J., May, P., Stankov, B., and Shapiro, M.: Radio acoustic sounding system observations of an arctic front, Journal of Applied Meteorology, 30, 881–892, 1991.

Neiman, P. J., Ralph, F. M., White, A., Kingsmill, D., and Persson, P.: The statistical relationship between upslope flow and rainfall in California's coastal mountains: Observations during CALJET, Monthly Weather Review, 130, 1468–1492, 2002.

Neiman, P. J., Martin Ralph, F., Persson, P. O. G., White, A. B., Jorgensen, D. P., and Kingsmill, D. E.: Modification of fronts and precipitation by coastal blocking during an intense landfalling winter storm in southern California: Observations during CALJET, Monthly weather review, 132, 242–273, 2004.

Neiman, P. J., Schick, L. J., Ralph, F. M., Hughes, M., and Wick, G. A.: Flooding in western Washington: The connection to atmospheric rivers, Journal of Hydrometeorology, 12, 1337–1358, 2011.

Niemand, M., Möhler, O., Vogel, B., Vogel, H., Hoose, C., Connolly, P., Klein, H., Bingemer, H., DeMott, P., Skrotzki, J., et al.: A particle- surface-area-based parameterization of immersion freezing on desert dust particles, Journal of the Atmospheric Sciences, 69, 3077–3092, 2012.

O'Sullivan, D., Murray, B. J., Ross, J. F., and Webb, M. E.: The adsorption of fungal ice-nucleating proteins on mineral dusts: a terrestrial reservoir of atmospheric ice-nucleating particles, Atmospheric Chemistry and Physics, 16, 7879–7887, 2016.

Park, H. S., Ryzhkov, A., Zrnic´, D., and Kim, K.-E.: The hydrometeor classification algorithm for the polarimetric WSR-88D: Description and application to an MCS, Weather and Forecasting, 24, 730–748, 2009.

Petters, M. and Wright, T.: Revisiting ice nucleation from precipitation samples, Geophysical Research Letters, 42, 8758–8766, 2015. Petters, M. D., Parsons, M. T., Prenni, A. J., DeMott, P. J., Kreidenweis, S. M., Carrico, C. M., Sullivan, A. P., McMeeking, G. R., Levin, E., Wold, C. E., et al.: Ice nuclei emissions from biomass burning, Journal of Geophysical Research: Atmospheres, 114, 2009.

Pitter, R. and Pruppacher, H.: A wind tunnel investigation of freezing of small water drops falling at terminal velocity in air, Quarterly Journal of the Royal Meteorological Society, 99, 540–550, 1973.

Prenni, A., Tobo, Y., Garcia, E., DeMott, P., Huffman, J., McCluskey, C., Kreidenweis, S., Prenni, J., Pöhlker, C., and Pöschl, U.: The impact of rain on ice nuclei populations at a forested site in Colorado, Geophysical Research Letters, 40, 227–231, 2013.

Pruppacher, H. R., Klett, J. D., and Wang, P. K.: Microphysics of clouds and precipitation, 1998.

Qin, X., Pratt, K. a., Shields, L. G., Toner, S. M., & Prather, K. a. (2012). Seasonal comparisons of single-particle chemical mixing state in Riverside, CA. *Atmospheric Environment*, *59*, 587–596. https://doi.org/10.1016/j.atmosenv.2012.05.032

Ralph, F. and Dettinger, M.: Historical and national perspectives on extreme West Coast precipitation associated with atmospheric rivers during December 2010, Bulletin of the American Meteorological Society, 93, 783–790, 2012.

Ralph, F., Coleman, T., Neiman, P., Zamora, R., and Dettinger, M.: Observed impacts of duration and seasonality of atmospheric-river landfalls on soil moisture and runoff in coastal northern California, Journal of Hydrometeorology, 14, 443–459, 2013.

Ralph, F. M., Neiman, P. J., and Rotunno, R.: Dropsonde observations in low-level jets over the northeastern Pacific Ocean from CALJET- 1998 and PACJET-2001: Mean vertical-profile and atmospheric-river characteristics, Monthly weather review, 133, 889–910, 2005.

Ralph, F. M., Neiman, P. J., Wick, G. A., Gutman, S. I., Dettinger, M. D., Cayan, D. R., and White, A. B.: Flooding on California's Russian River: Role of atmospheric rivers, Geophysical Research Letters, 33, 2006.

Ralph, F. M., Wilson, A. M., Shulgina, T., Kawzenuk, B., Sellars, S., Rutz, J. J., Lamjiri, M. A., Barnes, E. A., Gershunov, A., Guan, B., et al.: ARTMIP-early start comparison of atmospheric river detection tools: how many atmospheric rivers hit northern California's Russian River watershed?, Climate Dynamics, pp. 1–22, 2018.

Rebotier, T. P., & Prather, K. A. (2007). Aerosol time-of-flight mass spectrometry data analysis: A benchmark of clustering algorithms. *Analytica Chimica Acta*, *585*, 38–54. https://doi.org/10.1016/j.aca.2006.12.009

Robichaud, A. J. and Austin, G. L.: On the modelling of warm orographic rain by the seeder-feeder mechanism, Quarterly Journal of the Royal Meteorological Society, 114, 967–988, 1988.

Rosenfeld, D., Woodley, W. L., Axisa, D., Freud, E., Hudson, J. G., and Givati, A.: Aircraft measurements of the impacts of pollution aerosols on clouds and precipitation over the Sierra Nevada, Journal of Geophysical Research: Atmospheres, 113, 2008.

Rosenfeld, D., Chemke, R., Prather, K., Suski, K., Comstock, J. M., Schmid, B., Tomlinson, J., and Jonsson, H.: Polluting of winter convective clouds upon transition from ocean inland over central California: Contrasting case studies, Atmospheric research, 135, 112–127, 2014.

Rutz, J. J., Steenburgh, W. J., and Ralph, F. M.: Climatological characteristics of atmospheric rivers and their inland penetration over the western United States, Monthly Weather Review, 142, 905–921, 2014.

Schnell, R. and Vali, G.: World-wide source of leaf-derived freezing nuclei, Nature, 246, 212, 1973.

Schnell, R. and Vali, G.: Biogenic ice nuclei: Part I. Terrestrial and marine sources, Journal of the Atmospheric Sciences, 33, 1554–1564, 1976.

Silva, P., & Prather, K. (2000). Interpretation of mass spectra from organic compounds in aerosol time-of-flight mass spectrometry. *Analytical Chemistry*, *72*(15), 3553–62. Retrieved from å 585–594. https://doi.org/10.1080/02786820600729138

Stohl, A., Forster, C., Frank, A., Seibert, P., and Wotawa, G.: The Lagrangian particle dispersion model FLEXPART version 6.2, Atmospheric Chemistry and Physics, 5, 2461–2474, 2005.

Stopelli, E., Conen, F., Morris, C. E., Herrmann, E., Bukowiecki, N., and Alewell, C.: Ice nucleation active particles are efficiently removed by precipitating clouds, Scientific reports, 5, 16 433, 2015.

Sultana, C. M., Al-Mashat, H., & Prather, K. A. (2017). Expanding Single Particle Mass Spectrometer Analyses for the Identification of Microbe Signatures in Sea Spray Aerosol. *Analytical Chemistry*, *89*(19), 10162–10170. https://doi.org/10.1021/acs.analchem.7b00933

Sultana, C. M., Cornwell, G. C., Rodriguez, P., & Prather, K. A. (2017). FATES: a flexible analysis toolkit for the exploration of single-particle mass spectrometer data. *Atmospheric Measurement Techniques*, *10*(4), 1323–1334. https://doi.org/10.5194/amt-10-1323-2017

Tobo, Y., Prenni, A. J., DeMott, P. J., Huffman, J. A., McCluskey, C. S., Tian, G., Pöhlker, C., Pöschl, U., and Kreidenweis, S. M.: Biological aerosol particles as a key determinant of ice nuclei populations in a forest ecosystem, Journal of Geophysical Research: Atmospheres, 118, 2013.

Tobo, Y., DeMott, P., Hill, T., Prenni, A., Swoboda-Colberg, N., Franc, G., and Kreidenweis, S.: Organic matter matters for ice nuclei of agricultural soil origin, Atmospheric Chemistry and Physics, 14, 8521–8531, 2014.

Vali, G.: Quantitative evaluation of experimental results an the heterogeneous freezing nucleation of supercooled liquids, Journal of the Atmospheric Sciences, 28, 402–409, 1971.

White, A., Anderson, M., Dettinger, M., Ralph, F., Hinojosa, A., Cayan, D., Hartman, R., Reynolds, D., Johnson, L., Schneider, T., et al.: A twenty-first-century California observing network for monitoring extreme weather events, Journal of Atmospheric and Oceanic Technol- ogy, 30, 1585–1603, 2013.

White, A. B., Neiman, P. J., Ralph, F. M., Kingsmill, D. E., and Persson, P. O. G.: Coastal orographic rainfall processes observed by radar during the California Land-Falling Jets Experiment, Journal of Hydrometeorology, 4, 264–282, 2003.

Wilson, T. W., Ladino, L. A., Alpert, P. A., Breckels, M. N., Brooks, I. M., Burrows, S. M., Carslaw, K. S., Huffman, J. A., Judd, C., Kilthau, W. P., et al.: A marine biogenic source of atmospheric ice-nucleating particles, Nature, 525, 234, 2015.

Chapter 4. Improved discrimination between dust and bioaerosol using aerosol time-of-flight mass spectrometry

4.1 Abstract

Ice nucleating particles (INPs) are rare atmospheric particles that can greatly affect clouds and precipitation through their ability to trigger cloud glaciation at warmer temperatures than would occur in their absence. Two particle sources have been shown to be particularly efficient at initiating ice formation in clouds. Dust has modest ice nucleation (IN) activity at temperatures below -15 ºC and is emitted and transported at high altitudes globally in significant quantities. Bioaerosols are less abundant, but certain species possess exceptional IN-activity and may be especially important due to their ability to trigger ice formation at temperatures as warm as -1ºC. Single particle mass spectrometry has become a commonly used method for in-situ measurements of INP composition. However, dust and bioparticles have overlapping mass spectral features, complicating their unambiguous detection. In this work, we present a detailed analysis of standards for dust and bioaerosol. Using insights informed by this analysis, we developed a decision tree for the identification of cellular bioaerosol at a site in coastal California using an aerosol time-of-flight mass spectrometer. These particles showed moderate correlations with a subset of fluorescent particles measured by the wideband integrated bioaerosol sensor and displayed temporal profiles that tracked warm INP concentrations (measured at T = -15 ºC), suggesting that this particle type could serve as a useful proxy for INPs.

4.2 Introduction

Ice nucleating particles (INPs) are a special subclass of aerosol particles that trigger the formation of atmospheric ice at temperatures warmer than the homogeneous freezing point of ~ -38 ºC (DeMott et al., 2010). Despite the fact that only 1 in 10^6 of all particles in the atmosphere

will cause freezing at -20 ºC (Rogers et al., 1998), INPs exert significant influence upon clouds and precipitation by inducing cloud glaciation, though these effects are not easily generalized (DeMott et al., 2010). Dust and bioaerosol (also called primary biological aerosol particles or PBAP) are broadly acknowledged as being effective ice nucleators. Dust has the highest atmospheric loading by mass of any particle class (Andreae and Rosenfeld, 2008; Engelstaedter et al., 2006; Zender, 2004) and they are generally estimated to be the greatest source of INPs at temperatures below -20 ºC (Kanji et al., 2017). While dust particles can activate at warmer temperatures depending upon their mineralogy and organic content (Atkinson et al., 2013; Hill et al., 2016; Tobo et al., 2014), bioaerosol are generally assumed to have higher IN activity than dust at temperatures above -20 ºC. Due to a lack of measurements, however, it is still not well understood whether bioaerosols are abundant enough to impact cloud ice-processes (Fröhlich-Nowoisky et al., 2016). The bioaerosol particle class encompasses whole organisms (e.g. bacteria), spores, pollen, and cell fragments/excretions with particle diameters from nanometers to 100s of microns (Fröhlich-Nowoisky et al., 2016). The breadth and rarity of the bioaerosol class increases the difficulty of detection and analysis and the relative contributions of whole cells vs particles with cell fragments to INP populations is currently not well understood (Kanji et al., 2017).

Many offline techniques have been utilized to measure and identify bioaerosol, including cultures, immunological assays, microscopy, spectroscopy, and mass spectrometry (Després et al., 2012 and references therein). These techniques require bulk sampling, lengthy sampling periods, and specialized handling and preservations techniques which can add uncertainty and bias to the measurements (Després et al., 2012). One of the most poorly understood variables regarding bioaerosol is their concentrations at altitudes where they could affect cloud properties (Fröhlich-Nowoisky et al., 2016; Twohy et al., 2016). Techniques that are reliant upon lengthy sampling

times are unable to provide the temporal and spatial resolution required in aircraft sampling. Thus for the purpose of understanding the abundance of bioaerosol and their ability affect cloud properties, online measurements are preferred.

Single particle mass spectrometers (SPMS), such as the aerosol time-of-flight mass spectrometer (ATOFMS), are uniquely suited to identify potential INPs in clouds because they can measure size-resolved single particle composition in real-time, and have shown the ability to identify both dust (Marsden et al., 2018b; Silva et al., 2000) and bioaerosol (Cahill et al., 2015; Fergenson et al., 2004; Sultana et al., 2017a) and can be made aircraft-capable (Pratt et al., 2009c). Historically, the presence of ion markers $^{26}CN^-$ and $^{42}CNO^-$, considered indicative of organic nitrogen species, and $^{79}PO_3^-$, from phosphates, in dust-like single particle mass spectra have been utilized to distinguish a distinct internally mixed "biological-dust" particle type, where the biological material has been postulated to be bacteria, fungal spores, or plant detritus (Creamean et al., 2013). These ion markers are ubiquitous in cellular (defined as whole cells) single particle mass spectra (e.g. Cahill et al., 2015; Czerwieniec et al., 2005; Fergenson et al., 2004; Steele et al., 2003; Zawadowicz et al., 2017). However, $^{26}CN^-$, $^{42}CNO^-$, and $^{79}PO_3^-$ signals have also been frequently reported in dust mass spectra (Creamean et al., 2014; Marsden et al., 2018a; Schmidt et al., 2017; Silva et al., 2000; Zawadowicz et al., 2017), including mass spectra of mineral dust standards, which would be expected to have little organic material, much less whole or fragmented cells. As summarized by Zawadowicz et al. (2017) it is insufficient to utilize the presence of $^{26}CN^-$, $^{42}CNO^-$, or $^{79}PO_3^-$ ion markers alone as an indicator of cellular material.

To resolve this issue, Zawadowicz et al. (2017) proposed a new methodology to separate "biological" single particle mass spectra from largely inorganic particles. Standards of biological and inorganic particles were sampled by Particle Analysis by Laser Mass Spectrometry (PALMS),

and the data simplified to a two-dimensional space of the ratios of $^{79}PO_3^-/^{63}PO_2^-$ versus $^{26}CN^-/^{42}CNO^-$ ion signals. An approach utilizing a supervised machine learning algorithm was able to distinguish between two particle classes with 97% accuracy within this space. The success of this technique and its utility to the larger SPMS community largely depend upon the natural division of biological and inorganic spectra within this two-dimensional space. Aerosols sampled by SPMS have been shown to exhibit a high degree of mass spectral variation, dependent to varying degrees on factors such as particle size (Reinard and Johnston, 2008), degree of particle desorption (Carson et al., 1997), the wavelength of the desorbing-ionizing laser (Thomson et al., 1997a), and the photon flux experienced by the aerosol within the laser beam (Wenzel and Prather, 2004). Mass spectral signatures generated by aerosolized bacterial cells have been shown to be particularly sensitive to the photon fluence experienced by the particle (Steele et al., 2003, 2005). Given that, SPMS span a wide range of designs and operational conditions. Thus, simple ion signal ratios or thresholds for distinguishing particle types may not be applicable across the field at large.

Given that there is likely high variability in dust and cellular single particle mass spectra both within single data sets and across SPMS designs, it is important for researchers to understand the "landscape" that these mass spectral signatures can occupy in order to more accurately identify them. While methods developed to discriminate the two classes utilizing a few select ion markers with specific ratios or thresholds may be useful for a specific instrument and operating parameters, we show that these techniques may not be easily extended to all single particle datasets. Heterogeneity across the desorbing-ionizing laser beam profile has been shown to account for a huge amount of the variance in spectra (Steele et al., 2005; Wenzel and Prather, 2004), and higher photon fluence generally increases total positive ion intensity (TPII; Steele et al., 2005; Zelenyuk et al., 2008), which can be used to understand the variance non-homogenous laser beams introduce

(Ault et al., 2013; Sultana et al., 2017a, 2017c). For this purpose, we describe the general trends with respect to TPII observed in our dataset as well as highlight cellular ion markers that are likely useful in discriminating the two particle types but that are rarely discussed in studies of externally mixed aerosol samples. This knowledge is used to inform the classification of cellular bioaerosol by a decision tree in an ambient dataset. The measurements determined through this decision tree are validated and compared against co-sampled bioaerosol and INP concentrations made at the same sampling site in order to better understand the contributions of whole cells to INP populations.

4.3 Materials and methods

4.3.1 Aerosol standards

Most of the dust and cellular aerosol standards in this work were analysed with an aircraft aerosol time-of-flight mass spectrometer (A-ATOFMS; Pratt et al., 2009c) at the Aerosol Interaction and Dynamics in the Atmosphere (AIDA) facility at the Karlsruhe Institute of Technology (KIT) during the Fifth International Ice Nucleation Workshop (FIN-1) in November 2014. During this portion of the workshop, a total of 10 single particle mass spectrometers from around the world were gathered to sample a common set of standards and cloud expansion experiments. Additional aerosolized unicellular algal and cyanobacteria standards were analysed at the University of California, San Diego (UCSD) by the A-ATOFMS outfitted with an aerodynamic lens developed for the transmission of large particles (Cahill et al., 2014). Finally, Arizona Test Dust (ATD) was analysed with a nozzle-ATOFMS (Gard et al., 1997) at UCSD.. A summary of the samples is provided in Table 4.1.

4.3.1.1 FIN-1 sampling details

Experiments were conducted in the Aerosol Preparation Chamber (APC) at the AIDA facility. The APC is a stainless-steel cylindrical vessel of controlled pressure and temperature used for characterizing aerosols. Samples of pure dust and pure bacteria were introduced into the APC during separate experiments. A rotation brush generator was used to disperse the dust mineral dust sample into a stream of particle free synthetic air. Larger dust particles were removed using an inertial impactor. For a given bacterial sample, a suspension of 1 g in 200 mL of nanopure water was prepared for dispersion of the bacterial cells into the aerosol phase. The suspension was sprayed using a two-component jet device, which uses a particle free synthetic air to disperse a liquid flow.

4.3.1.2 UCSD sampling details

Details of sample preparation and aerosolization for the algal and cyanobacteria standards analysed at UCSD have been previously published (Cahill, 2014; Cahill et al., 2015). The ATD sample was aerosolized using a flow of filtered air after and then sampled into the nozzle-ATOFMS.

4.3.2 ATOFMS analysis

Single particle mass spectra were collected using an aerosol time-of-flight mass spectrometer (ATOFMS; Gard et al., 1997; D_{va} 0.2-3.0 μm) and an aircraft aerosol time-of-flight mass spectrometer (A-ATOFMS; Pratt et al., 2009; D_{va} 0.1-3.0 μm). For the algal and cyanobacteria standards analysed at UCSD, a specialized lens for the transmission of larger particles (D_{va} 2-10 μm) was used. In brief, particles are introduced into the instrument through either a nozzle and series of skimmers (ATOFMS), or an aerodynamic lens (A-ATOFMS) in order to collimate particles into a tight beam. The particle beam intersects two continuous wave lasers (532 nm; Nd:YAG) 6 cm apart. The scattered light from particles is reflected by ellipsoidal mirrors

onto photomultiplier tubes (PMTs). Particle velocity, calculated from the time between the two PMT signals, is used with external calibration to compute particle vacuum aerodynamic diameter (D_{va}). A pulsed 266 nm laser (Nd:YAG; 1.0-1.3 mJ pulse^{-1}, focused to 700 µm diameter spot size) desorbs and ionizes the particle into a time-of-flight mass spectrometer. For each particle positive and negative mass spectra D_{va}, and time are recorded. This data was imported into Matlab (The MathWorks, Inc.) and analysed using the software toolkit FATES (Sultana et al., 2017b).

Particles measured by the ATOFMS during the CalWater-2015 field campaign were clustered using a neural net algorithm (Rebotier and Prather, 2007; Song et al., 1999) as in Martin et al., (2017). Dust particles (hereafter *Dust* refers to the particles classified as dust during the campaign) were identified based upon their characteristic mass spectra (Schmidt et al., 2017; Silva and Prather, 2000). A total of 65,534 of the 1,220,818 particles measured by the ATOFMS at BML were classified as *Dust* (5.4%). A separate methodology was used to identify biological particles and is described in more detail in Section 4.4.4.

4.3.3 CalWater-2015 field campaign

The CalWater-2015 field campaign was conducted at the Bodega Marine Laboratory (BML) in Bodega Bay, California (38.3 ºN, 123.1 ºW) from January 15 to March 8, 2015. Details of this study have been published elsewhere (Martin et al., 2017), so we provide only a short overview here. Measurements of aerosol size, number, and composition were conducted in a trailer owned by the California Air Resources Board and operated by UCSD researchers. Further details on ATOFMS sampling and analysis can be found in section 4.3.2. Bioparticle concentrations were measured with a wideband integrated bioaerosol sensor (WIBS-4; Droplet Measurement Technologies, Inc.; hereafter WIBS) in the mobile lab operated by Colorado State University

(CSU) and North Carolina State University (NCSU) (Section 4.3.3.1). Ambient aerosol samples were collected and analysed for their INP concentrations (Section 4.3.3.2).

4.3.3.1 Online bioaerosol concentrations

The wideband integrated bioaerosol sensor (WIBS) measures the size, asymmetry factor, and fluorescence signal for particles from 0.5-20 μm optical diameter (Hirst et al., 2004). Fluorescence is measured in three different channels: FL1, excitation 280 nm, emission 310-400 nm; FL2, excitation 280 nm, emission 420-650 nm; FL3, excitation 370 nm, emission 420-650 nm. Due to limited sensitivity to small particles (Gabey et al., 2010, 2011), we limited our analysis to fluorescent particles 0.8-20 μm.

Background fluorescence signal was calculated following Toprak and Schanaiter (2013). Force-triggered sampling of filtered air was conducted for 5 minutes and the background signal, $E_{background,i}$, calculated by the following

$$E_{background,i} = \overline{E_i} + 3\sigma_i \quad (1)$$

where $\overline{E_i}$ is the average signal in channel i, for a force-triggered sample and σ_i is the standard deviation of the force triggered sample signal. $E_{background,i}$ was subtracted from each particle for each channel to yield the final fluorescence signal. Particles were grouped into types based upon their fluorescent signal in each channel using criteria defined in previous studies (Gabey et al., 2010; Perring et al., 2014; Wright et al., 2014a) and summarized in Table 4.3.

4.3.3.2 Offline sample collection for IN analysis

Ambient aerosol was sampled for offline INP measurements using an impinger sampler (Willeke et al. 1998, three-piece 5 mL impinger (SKC Inc. BioSampler®), hereinafter referred to as biosampler. The biosampler was operated by impinging aerosols into 20 mL ultrapure water (HPLC Grade Submicron Filtered Water, Fisher Chemical Cat. No. W5-4). Ambient air was

sampled at a flow rate of 12.5 L min^{-1} for a duration of ~4 h. To avoid reduction in collection efficiency due to evaporation, the sampler was refilled to 20 ml at regular intervals, including the end of the sampling period. At the end of each sampling period, the sample was divided and transferred into 4.5 mL cryogenic vials. Associated background samples (hereafter the field blank), containing only the ultrapure water used to prepare the biosampler, were generated for each sampling period. The ambient and field blank samples were immediately frozen after collection and stored at -80 °C until the end of the campaign. The samples were shipped overnight from BML to NCSU in Raleigh, North Carolina, U.S.A. The samples were kept frozen in transit using dry ice and stored at -80 °C upon arrival, and then individually thawed prior to analysis.

The INP concentrations of these ambient samples were measured using the NCSU Cold Stage (hereafter the cold stage; Hader et al., 2014; Wright and Petters, 2013). Samples were divided into ~200 1 µL volume drops onto a 2 by 2 array of hydrophobic glass cover slides (Siliconized Glass Square Cover Slides, Hampton Research Cat. No. HR3-215), using a single-channel digital pipette. The cover slides were placed on top of the cold stage, a temperature-controlled metal plate that has two embedded thermistors embedded to monitor the temperature during freezing experiments. Droplets were cooled at a rate of 2 K min^{-1} until all drops were frozen. Freezing events were detected using an optical change in the droplets' appearance and were recorded at 0.17K intervals using a digital camera. A flow of 1 L min^{-1} of dry N_2 was used to prevent frosting within the IN cell. To reduce contact freezing amongst the droplets, distance between the droplets was increased beyond the droplets' "sphere of influence". The resolvable temperature-dependent INP spectra ranges from between approximately 5×10^3 and 5×10^6 INP L^{-1} of aqueous sample. Each sample was assayed three times and INP concentrations were binned into 1 K temperature intervals. For each sample and for each temperature bin, the mean concentration

and 95% confidence interval for the three assays are reported. Points where ambient concentrations are less than the background INP concentration are removed from the dataset. Ambient INP concentrations for each temperature bin, $INP_{ambient,T}$, were obtained by the following

$$INP_{ambient,T} = \frac{INP_{aqueous,T} V_{Total}}{Q\ t_{sample}} \quad (2)$$

where $INP_{aqueous,T}$ is the concentration of INPs in the liquid sample for a given temperature, V_{Total} is the total biosampler sample volume, Q is the flow rate into the biosampler, and t_{sample} is the total sampling time. Ambient INP concentration are reported in units of L^{-1} air sampled.

4.4 Results and discussion

This work describes and catalogues mass spectral differences between dust and bioaerosol in SPMS datasets, with the goal of facilitating the discrimination between these two particle types. Section 4.4.1 describes historical descriptions of dust and bioaerosol, while Section 4.4.2 provides the first description of cellular and dust particle spectra as a function of TPII. Section 4.4.3 gives a detailed review of ion markers found in cellular particles, including their likely identity and Section 4.4.4 presents a decision tree for the identification of cellular particles in an ambient dataset collected at a coastal site in California.

4.4.1 Historically "biological" ion markers in dust spectra

Consistent with previous SPMS studies (Creamean et al., 2014; Schmidt et al., 2017; Silva et al., 2000; Zawadowicz et al., 2017), $^{26}CN^-$, $^{42}CNO^-$, and $^{79}PO_3^-$ ion signals were frequently detected for the dust samples analysed in this work (Fig. 4.1). Note that the relative ion signals for Arizona Test Dust (ATD) should not be directly compared to the other dust samples as ATD was analysed by a different ATOFMS. Single particle mass spectra from soil dust samples, especially those collected from noted vegetated areas, generally had higher relative signal from the organic nitrogen ion markers, $^{26}CN^-$ and $^{42}CNO^-$, than the mineral dust samples (Fig. 4.1), in agreement

with previous SPMS dust analyses (Marsden et al., 2018a; Schmidt et al., 2017). Yet, utilizing these organic nitrogen ion markers to confidently identify any single mass spectrum as originating from a relatively "organic-rich" soil dust particle versus an "organic-poor" mineral dust particle is limited due to the variation in mass spectral response within each dust sample. It is highly likely, but in no way certain, that a single dust particle that generates relatively intense organic nitrogen signals is comparatively "organic-rich". Furthermore, as $^{26}CN^-$ and $^{42}CNO^-$ are readily produced from mineral dust, as seen here and in Zawadowicz et al. (2017), implying these signals likely originate from whole or fragmented biological cells as opposed to more decomposed and generic organic material is tenuous. Identification of a number of ion markers more specific to cells is provided in Section 4.4.2.

When plotting the FIN-1 ATOFMS data into the $^{79}PO_3^-/^{63}PO_2^-$ versus $^{26}CN^-/^{42}CNO^-$ coordinate space similar trends are seen for the cellular and dust mass spectra as in Zawadowicz et al. (2017; Fig. 4.2 and Fig. 4.11). Generally, cellular spectra exhibit a wide range of $^{79}PO_3^-/^{63}PO_2^-$ (~10-100) ratios with $^{26}CN^-/^{42}CNO^-$ values limited to relatively low values (~<1). For dust spectra the $^{79}PO_3^-/^{63}PO_2^-$ ratio is relatively narrow and limited to low values (~<10) with a broader $^{26}CN^-/^{42}CNO^-$ distribution when compared to the cellular spectra. However, for the FIN-1 data set there is also clearly a region of high overlap between the cellular and dust particle types (Fig. 4.2). Over 20% of all spectra for the BSD, MSD, KF, and INX dust samples and 14% of the *Ps* cell sample fall within the high overlap region highlighted in Fig. 4.2. The poor separation of ATOFMS-generated dust and cell spectra in $^{79}PO_3^-/^{63}PO_2^-$ versus $^{26}CN^-/^{42}CNO$ space indicates utilization of this technique to distinguish cellular spectra with a SPMS instrument first necessitates a careful examination of data from an array of control samples.

4.4.2 Variance of cellular and dust mass spectra with total positive ion intensity

For particles of similar composition, the TPII of generated spectra has been shown to generally increase with increasing laser pulse energy (Sultana et al., 2017c; Thomson et al., 1997a; Wade et al., 2008; Woods et al., 2002). Therefore, within a sample, TPII may be utilized as a proxy for the photon flux experienced by the particle during desorption/ionization. For SPMS instruments, photon flux is often variable across the ionizing laser beam profile, even if the total energy per laser pulse is relatively consistent due to "hot spots" (Wenzel and Prather, 2004). Across the individual dust and biological particle types in this work, their location in $^{26}CN^-/^{42}CNO^-$ versus $^{79}PO_3^-/^{63}PO_2^-$ space generally shifts towards lower $^{79}PO_3^-/^{63}PO_2^-$ and higher $^{26}CN^-/^{42}CNO^-$ values as a function of TPII (Figs. 4.3 and 4.11), indicating the sensitivity of the mass spectral signatures to ionization conditions. For this purpose, we describe general trends with respect to TPII observed in our dataset. We also highlight cellular ion markers that are likely useful in discriminating the two particle types but are rarely discussed in studies of externally mixed aerosol samples.

4.4.2.1 Dust mass spectra and total positive ion intensity

Consistent with previous descriptions of dust single particle mass spectra, most of the positive spectra for the dust samples analysed here are dominated by a combination of potassium, calcium, sodium, iron, and aluminium ion markers (Figs. 4.4 and 4.12). Describing the full range of signatures generated is outside the scope of this paper. For more general characterizations of mineral and soil dust samples readers are referred to Marsden et al. (2018) Schmidt et al. (2017); Silva et al. (2000); and Zawadowicz et al. (2017). Here we focus on TPII dependent systemic variations within the mass spectra.

While the exact processes governing laser desorption and ionization in SPMS are poorly understood, it is generally considered that both the lattice energy of a compound and the ionization

energy of an atomic species influence the generation of metallic cations (Gross et al., 2000; Thomson et al., 1997b). Higher relative sensitivities are expected for atomic species for which cations can be generated with less energetic input. In this work, the observed trends in relative positive ion signals with total positive ion intensity are consistent with these common paradigms applied to LDI. Within the positive mass spectra, the most consistent trend was the increase in $^{27}Al^+$ and decrease in $^{39}K^+$ relative signal with increasing total positive ion intensity (Figs. 4.5 and 4.12). Within soils and minerals, aluminium content is almost entirely due to the presence of clays where aluminium is organized as sheets of octahedral alumina (Al_2O_3) or in framework silicate minerals where aluminium is bound in tetrahedral alumina (AlO_4) organized into a 3D crystal structure. In contrast, potassium, as well as other elements commonly observed in dust spectra (e.g. sodium, magnesium, calcium) can be present as interstitial cations in clay or framework silicate minerals or as easily soluble compounds in soils. Potassium is the main interstitial ion for both K-feldspar and illite. Releasing aluminium from octahedral or tetrahedral alumina likely requires a high expenditure of energy compared to interstitial potassium consistent with the higher $^{27}Al^+$ relative signal with increasing TPII. Similarly, by utilizing single particle mass spectra ion arrival times from a number of silicate containing minerals, Marsden et al. (2018) suggested that weakly bound interstitial cations between clay sheets desorb and ionize before disintegration of the alumina lattices. For all dust samples presented here it was also observed that the fraction of mass spectra with relatively intense titanium ion signal ($^{48}Ti^+$ and $^{64}TiO^+$) also increased with increasing TPII. Titanium is often found in aluminosilicates as a trace element that substitutes for aluminium within the lattice. We also observed that the relative $^{23}Na^+$ signal decreased with increasing TPII for the KF and BSD samples, similar to the $^{39}K^+$ trend observed across all samples. The KF and BSD samples were the only samples with reported contributions from albite (>20%),

where sodium is the main interstitial ion as opposed to potassium. While we hypothesize that the relationship between TPII and relative signal from metallic cations is a result of their specific microchemical environments, potassium and sodium have lower first ionization energies (4.34 eV and 5.14 eV) than aluminium (5.96 eV) and titanium (6.83 eV) which could also contribute to their preferential detection in mass spectra with lower TPII (Sansonetti and Martin, 2005).

Changes in relative negative ion intensities as a function of TPII were less drastic compared to the positive ion signatures. However, a few consistent but subtle trends were observed across the dust samples analysed. Primarily, signals from a wide range of low m/z ion markers, roughly from *m/z* -12 to -50, increase with increasing TPII, though relative signal from most of these ions remains well below 1% of the total negative ion intensity (Figs. 4.4 and 4.12). Many of the low mass ion peaks, such as $^{24}C_2^-$, $^{25}C_2H^-$, and $^{26}CN^-$, are attributed to fragmentation of organic species, which is expected with increasing deposition of energy into the particle. Signal from $^{16}O^-$ and $^{17}OH^-$, which could be a result of fragmentation of the various oxides within the minerals or adsorbed water on the particles, also generated relatively intense signal at high TPII. While the growth of low *m/z* ions with increasing TPII may be unsurprising to many SPMS users, to our knowledge this relationship is not documented in the current literature. These results highlight the ability of variations in the energy experienced by the particle during the LDI process to influence the relative signal of many markers attributed to the presence of organic species. This is an important consideration when trying to determine the relative content of organic material of an individual particle or a sampled population of dust from single particle mass spectra.

4.4.2.2 Cell mass spectra and total positive ion intensity

Consistent with Steele et al. (2003, 2005), single particle mass spectra for the biological samples analysed in this work showed systematic variations with TPII, generally indicative of

increasing fragmentation of organic species with increasing TPII. A handful of relatively low mass ions, notably $^{26}CN^-$, $^{42}CNO^-$, -66, and -90, increase in relative intensity with increasing TPII (Figs. 4.6 and 4.13). As previously noted, fragmentation of organic species increased with ionization energy, and previous studies have shown an increase in $^{26}CN^-$, $^{42}CNO^-$, -58, and -66, ion markers with increasing laser pulse energy for bacterial cells (Steele et al., 2003, 2005). In the positive spectra, fewer coherent trends were discovered across the biological samples studied. Most consistently signal at *m/z* +59 and +74 decreased with increasing TPII (see section 4.9.1.4 for more details). Increases in inorganic cation response, such as $^{23}Na^+$ and $^{39}K^+$, were also sometimes observed. Steele et al. (2003, 2005) also noted that *m/z* +74 signal decreased markedly with increasing laser pulse energy and was mirrored by a relative increase in $^{39}K^+$ ions. Signal at *m/z* +59 was not noted in these specific laser pulse energy studies but has been frequently reported in cellular single particle mass spectra (Srivastava et al., 2005; Sultana et al., 2017a; Tobias et al., 2005, 2006). For all cell types sampled in the UCSD microalgea studies (2-6 μm D_{va}) as TPII increased there is increasing fragmentation of presumably fatty organic species in the region *m/z* +350 to +625, as indicated by relatively more intense lower *m/z* signal at intervals of 14 *m/z* (Fig. 4.14). Also observed with increasing TPII was decreasing relative intensity for *m/z* -794, -820, which have been attributed previously to the $[M\text{-}H]^-$ ions of sulfoquinovosyldiacylglycerides (Cahill et al., 2015; Plouguerne et al., 2013), a lipid common to chloroplast membranes (Fig. 4.14). These results highlight how fragmentation of organic species with increasing deposition of energy into a particle is especially important to consider in the analysis of cellular particles. Relatively intact ions of organic species specific to cellular material may be fragmented to nonspecific organic ions at lower *m/z* when encountering high photon energy densities, complicating the identification of cellular aerosols within a complex aerosol population.

4.4.3 Key ion markers for identification of cellular spectra

Outside the impact of laser fluence upon ion signatures, cellular single particle mass spectra have also been shown to vary with biological species, growth and nutrient conditions, and the cell life cycle (Cahill et al., 2015; Czerwieniec et al., 2005; Srivastava et al., 2005; Tobias et al., 2006). We have yet to determine any ion marker which can consistently differentiate cells from dust mass spectra and is unique to aerosolized cells. The following discussion details signatures that we hypothesize to be indicative of cellular single particle mass spectra and also likely to be observed across an array of biological species. These ion markers, summarized in Table 4.2, can be grouped into a number of broad classes: nucleobases, amino acids, betaines, negative ion clusters containing phosphate, and positive ion clusters with potassium. By leveraging this information, we propose that researchers should be able to confidently discriminate a fraction of the cellular spectra from a complex data set, if not the entire cellular population. Unless otherwise noted, the "cellular" signatures that will be discussed have not been previously noted for dust mass spectra or other particle types.

4.4.4 Cellular particle in ambient studies

Accurately distinguishing between cellular particles (defined as either whole or fragmented cells) and dust in the ambient atmosphere is important due to their dissimilar ice nucleating potentials (Pratt et al., 2009b; Sun and Ariya, 2006 and references within). Dust particles have a higher atmospheric burden and are broadly acknowledged as the most abundant source of INPs below -20 ºC (Andreae and Rosenfeld, 2008; Kanji et al., 2017). Bioaerosol, while less abundant than dust, can be effective ice nucleators at temperatures ≥ -10 ºC (Alpert et al., 2011; Knopf et al., 2011; Mason et al., 2015), and thus could be more important INPs under at warm temperatures.

In sections 4.4.1-4.4.3, we discussed mass spectral features that may be used to distinguish between dust and cellular particles, the possible identities of those mass spectral features, and the trends associated with variations in laser fluence. In the following sections, we utilize that information for the identification of cellular particles in a complex, ambient SPMS dataset. The particles identified are then compared to bioparticle concentrations measured by the WIBS and INP concentrations measured by droplet freezing assays.

4.4.4.1 *Cell-type* classification

Ion markers with very low signal intensity are likely useful in distinguishing dust and cellular particle types (discussed in more detail in section 4.9.1). Using the information detailed in sections 4.4.2-4.4.3, we developed a decision tree (see section 4.9.2) in order to identify cellular particles (hereafter *Cell-type* particles) during the CalWater-2015 field campaign. Our process highly weights many small ion peaks, outside of those traditionally considered "biological". A total of 2449 *Cell-type* particles were identified out of 1,220,818 particles measured by the ATOFMS at BML (0.2% of particles). It should be noted that many of the steps taken in this process are unique to the context of these measurements and instrumental parameters. While we believe that the decision tree generated can serve as a useful template for future endeavours, it should not be applied to other datasets indiscriminately. Rather, researchers should investigate their data for the presence of characteristic ion markers to identify the cellular population.

Figure 4.7 shows an average spectrum of identified *Cell-type* particles. In addition to intense signal from $^{39}K^+$, $^{79}PO_3^-$, $^{26}CN^-$, and $^{42}CNO^-$, many of the mass spectral features noted in studies of control biological materials were present in *Cell-type* spectra, including nucleobases (66^-, 71^-, 90^-, 117^-, $131\text{-}134^-$), negative phosphates ($^{159}H(PO_3)_2^-$, $^{199}NaH_2P_2O_7^-$), quaternatry amines associated with bacteria ($^{59}N(CH_3)_3^+$, $^{74}N(CH_3)_4^+$), and positive potassium clusters ($^{104}K_2CN^+$,

$^{157}K_2PO_3^+$, $^{175}K_2HSO_4$). These particles also contained ion markers that have been associated with amino acids (86^+, 175^+). It should be noted that while many *Cell-type* particles contained multiple of these markers, none of them contained all of these markers.

Cell-type particles also showed similar trends with regard to increasing TPII (Fig. 4.15) as those observed in the lab studies of aerosolized controls (Fig. 4.13). For instance, signals at +59 and +74 were relatively more intense at lower TPII, while signal from phosphate clusters ($^{159}H(PO_3)_2^-$, $^{199}NaH_2P_2O_7^-$) and potassium clusters ($^{157}K_2PO_3^+$, $^{175}K_2HSO_4$) increased with increasing TPII. These patterns highlight the fact that understanding the full mass spectral space that bioaerosol can occupy is critical to identifying them. Using just one or two of these ion markers to identify potential bioaerosol is limited as very few are consistently found across the entire TPII spectrum.

When translated into CN^-/CNO^- vs PO_3^-/PO_2^- space (Fig. 4.8), *Dust* (more detail on the typing and classification of these particles can be found in section 4.3.2) and *Cell-type* particles exhibited similar trends to the cells sampled during FIN-1 (Fig. 4.2). The PO_3^-/PO_2^- values for *Dust* were primarily located between ~0-20 and the CN^-/CNO^- ratios ranged from ~0-20. *Cell-type* particles ranged broadly, from ~2-50, and the CN^-/CNO ratios were primarily below 2. The distributions of these ion ratios were broader compared to the FIN-1 samples, though whether this can be attributed to differences in particle composition or instrumental differences is unknown. As with the FIN-1 samples, identified *Dust* and *Cell-type* particles are not well separated in CN^-/CNO^- vs PO_3^-/PO_2^- space. A region of particularly high overlap is highlighted by a red box in Fig. 4.8 and contains 17.5% of all *Dust* particles 6.8% of *Cell-type* particles. However, the average spectra for the two types in this overlapping space have numerous distinct ion markers (Fig. 4.16), which allows confident classification as either *Dust* or *Cell-type*.

4.4.4.2 Comparisons of *Cell-type* particles with WIBS and INP concentrations

In recent years the wideband integrated bioaerosol sensor (WIBS) has become one of the standard methods for measuring bioparticle concentrations due to its ease of use, intuitive data processing, quantitative nature, and increasingly deep user base. The WIBS returns the particle size, asymmetry factor, and the excitation-emission spectra for three wavelengths pairs: FL1 280 nm excitation, 310-400 nm emission; FL2 280 nm excitation, 420-650 nm emission; FL3 370 excitation, 420-650 emission. FL1 corresponds to the amino acids tryptophan and tyrosine, FL2 corresponds to riboflavin, and FL3 corresponds to nicotinamide adenine dinucleotide (NADH). Bioparticle classification schemes for fluorescent particles detected by the WIBS-4 (Gabey et al., 2011; Perring et al., 2014; Wright et al., 2014b) are summarized in Table 4.3. Gabey et al., (2010) defined FP as any particle that fluoresces in any channel and the FBAP type as any particle that fluoresces in both FL1 and FL3. Since that work, the FBAP definition has been a popular scheme to quantify a variety of bioaerosol such as bacteria, spores, and pollen (Toprak and Schnaiter, 2013). The FP3 type (Wright et al., 2014a) is defined by very strong signal in the FL1 channel and weak or no fluorescence in either FL2 or FL3. The exact identity of the FP3 class is unknown because it has not been explicitly defined through lab studies. Both the FBAP and FP3 classes have been positively correlated with INP concentrations (Huffman et al., 2013; Suski et al., 2018; Wright et al., 2014a)

Temporal profiles of *Cell-type* particles were compared to the FP, FBAP, and FP3 particle types at BML (Fig. 4.9). The FP and FBAP particle types were poorly correlated with the *Cell-type*, r^2 0.137 and 0.247 respectively. The FP type (a particle with fluorescence signal in any channel) is the broadest class of fluorescent particle and is most likely to contain non-biological aerosol due to the potential interference from weakly fluorescing materials such as polyaromatic

hydrocarbons, soot, and mineral dust (Toprak and Schnaiter, 2013). However, the FP3 class (Wright et al., 2014b) was found to correlate moderately well with the *Cell-type* particle counts (r^2 = 0.525), which suggests that the FP3 class has a large population of whole or fragmented cells.

Measurements of WIBS particle classes and the *Cell-type* counts were compared to INP concentrations measured using offline sampling methods. While the strongest predictor of INP_{-15} concentrations were FP3 concentrations (r^2 of 0.60; Fig. 4.10), the *Cell-type* also correlated well (r^2 of 0.53). While neither dust (r^2 of 0.18), FP (r^2 of 0.09), nor FBAP (r^2 = 0.18) appeared to be strong predictors of INP concentrations, the fact that they follow some of the same general temporal trends indicates that they likely contributed modestly. The relative scarcity of Cell-type particles in the ATOFMS dataset (0.2%) highlights how rare and how important this particle type may be, and thus the need to accurately classify them.

4.5 Conclusions

Laboratory samples for dust and cellular bioaerosol standards were measured and characterized by the ATOFMS in order to better identify cellular bioaerosol in ambient datasets. The mass spectral landscape of these particles was explored as a function of TPII, and supported by an array of previously published control studies, a comprehensive series of characteristic cellular ion markers were identified. How consistently these signals are generated and factors that may contribute to this variance are also considered.

A decision tree was developed in order to identify these particles at a coastal site in California. *Cell-type* particles were defined by elevated markers for many of the mass spectral features identified in the lab studies, including nucleobases (66^-, 71^-, 90^-, 117^-, $131\text{-}134^-$), negative phosphates ($^{159}H(PO_3)_2^-$, $^{199}NaH_2P_2O_7^-$), quaternatry amines associated with bacteria ($^{59}N(CH_3)_3^+$, $^{74}N(CH_3)_4^+$), and positive potassium clusters ($^{104}K_2CN^+$, $^{157}K_2PO_3^+$, $^{175}K_2HSO_4$). *Cell-type*

particles also showed similar trends with regard to increasing TPII as those observed in the lab studies further confirming their identity.

These particles were correlated to bioaerosol concentrations measured by the WIBS. The FP and FBAP showed weak correlations with *Cell-type* particles (r^2 values of 0.137 and 0.247), while the FP3 subclass correlated moderately well with *Cell-type* particles (r^2 of 0.525). The correlation between the Cell the FP3 class may be significant because the FP3 type has been strongly implicated in INP studies (Suski et al., 2018; Wright et al., 2014a). We observed that ambient warm INP (T = -15 ºC) concentrations appear to follow the same general trend as Cell particles at BML (r^2 = 0.533). The sum of this evidence suggests that whole or fragmented cells comprise a significant fraction of the FP3 particle class, and that this population likely contributes significantly to the warm INP population at BML. The work presented in this study presents a new approach to identify biological particles which will be applicable to the SPMS field as a whole.

4.6 Acknowledgements

This research was supported by the CalWater-2015 field campaign, funded by the National Science Foundation. The authors also thank the UC Davis Bodega Marine Laboratory for the use of laboratory and office space and shipping and physical plant support while collecting data, as well as the California Air Resources Board for the trailer used for sampling. The authors also thank the other participants in the FIN-1 workshop, and the staff at the Aerosol Interaction and Dynamics in the Atmosphere (AIDA) facility at the Karlsruhe Institute of Technology for their assistance in sampling. Kylie Hoffman, Mary Hester, Margaret Scott, Hannah Tekleab, Mark Wu, and Seth Goodnight are thanked for their assistance in performing the cold-stage experiments. This research was funded by NSF award number 145147 (GCC, CMS, HA, ACM, KAP) and NSF award number 1450760 (HT, NER, MDP, PJD).

Chapter 4, in full, is currently being prepared for submission for publication to Atmospheric Measurement Techniques. Printed with permission from Cornwell, G. C., Sultana, C. M., Petters, M. D., Al-Mashat, H., Rothfuss, N. E., Taylor, H. P., DeMott, P. J., Martin, A. C., Kreidenweis, S. M., Prather, K. A. Improved discrimination between dust and bioaerosol by aerosol time-of-flight mass spectrometry. Dr. Camille Sultana and the dissertation author are co-first authors of this manuscript.

4.7 Figures

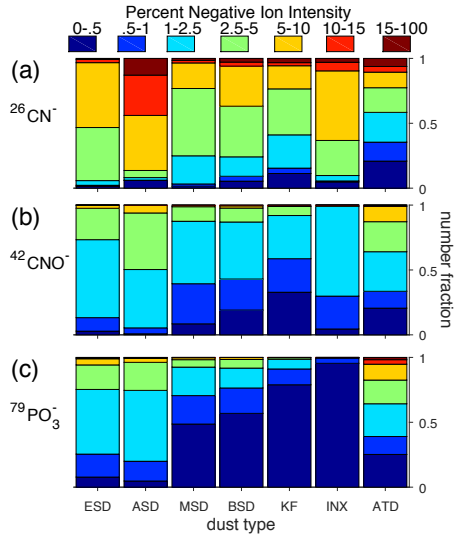

Figure 4.1. Distribution of relative signal for $^{26}CN^-$ (a), $^{42}CNO^-$ (b), and $^{79}PO_3^-$ (c) from a variety of soil and mineral dust samples. Warmer color indicates higher relative intensity. The ATD sample was analysed with a different ATOFMS than all other samples, and thus the relative ion distributions are not directly comparable.

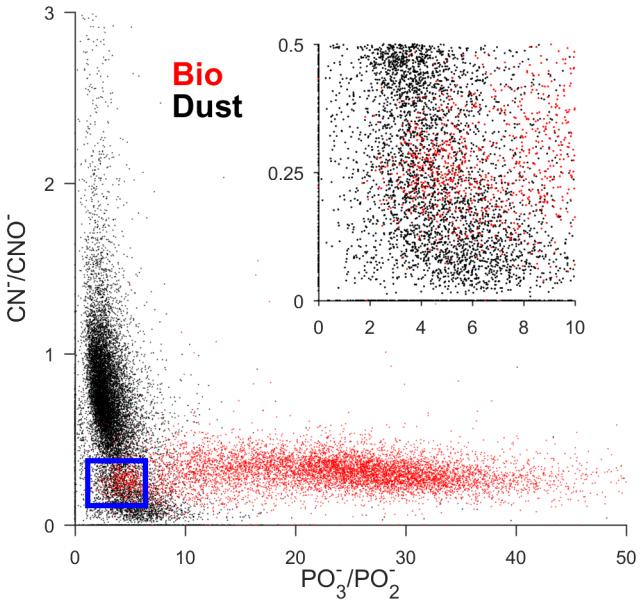

Figure 4.2. Individual mass spectra for all cellular standards (red) and dust standards (black) particles plotted in $^{79}PO_3^-/^{63}PO_2^-$ versus $^{26}CN^-/^{42}CNO^-$ space. The blue box highlights a region of high overlap between the two particle types and is shown in the inset.

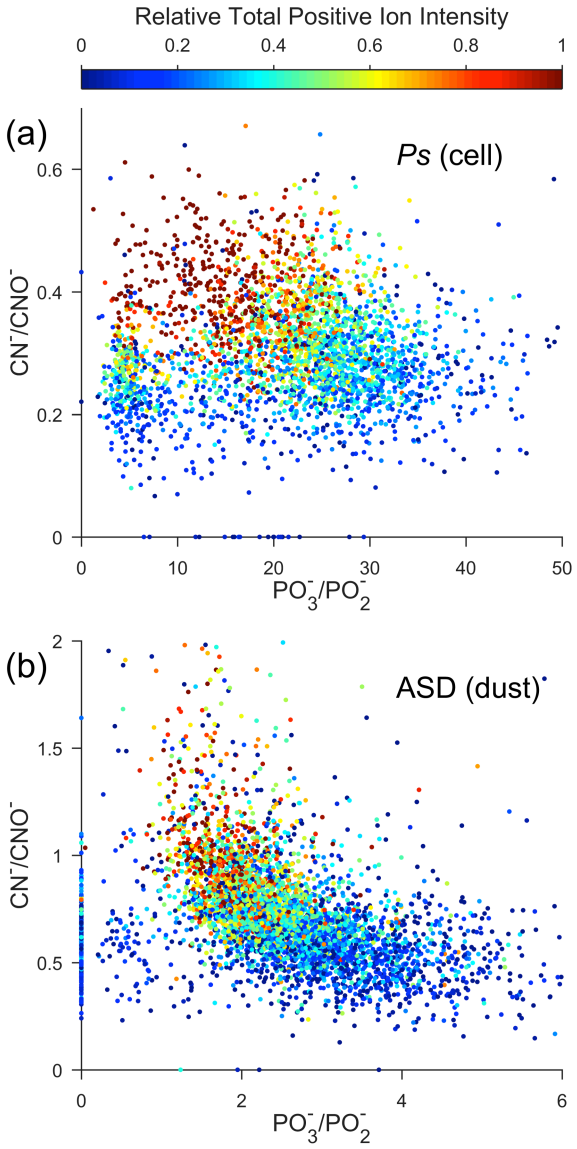

Figure 4.3. Individual (a) *Ps* and (b) ASD mass spectra in $^{79}PO_3^-/^{63}PO_2^-$ versus $^{26}CN^-/^{42}CNO^-$ space. Warmer shades indicate higher total positive ion intensity.

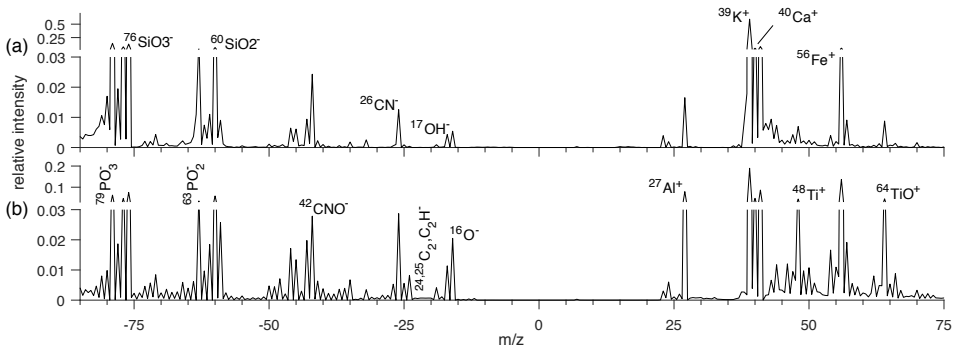

Figure 4.4. Representative mass spectra for ASD (dust) with relatively low (a) and high (b) TPII. The spectra are an average of 52 and 71 individual spectra to reduce noise.

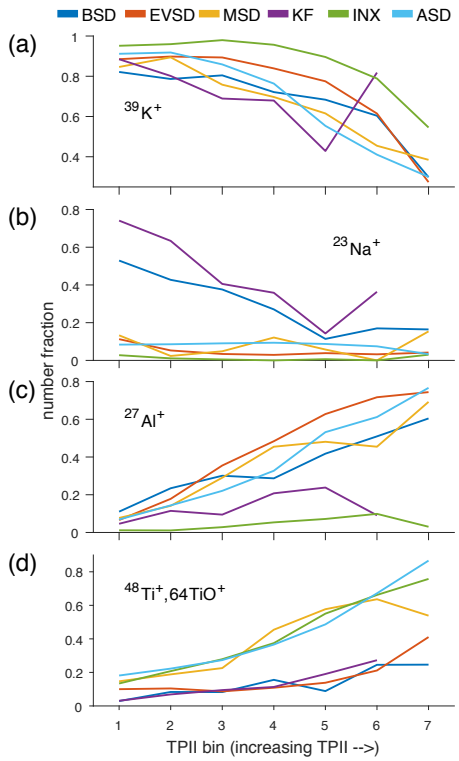

Figure 4.5. For each dust sample analysed, number fraction of mass spectra with relative ion signals for (a) $^{39}K^+ > 0.25$, (b) $^{23}Na^+ > 0.01$, (c) $^{27}Al^+ > 0.05$, (d) and $^{48}Ti^+$,$^{64}TiO^+ > 0.05$.

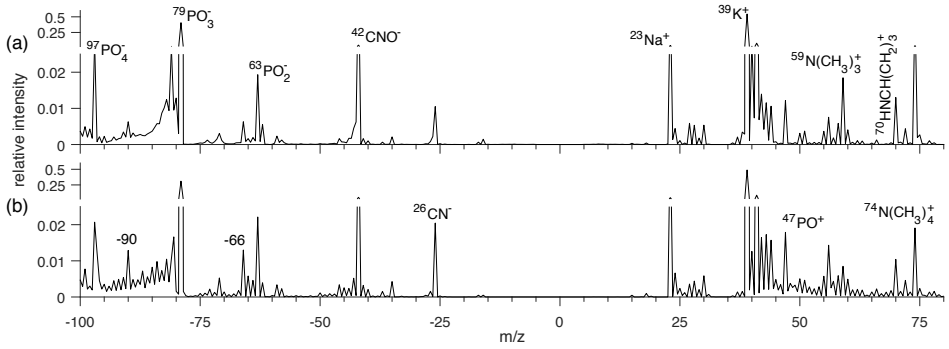

Figure 4.6. Representative mass spectra for *Ps* (cell) with relatively low (a) and high (b) TPII. The spectra are an average of 221 and 228 individual spectra to reduce noise.

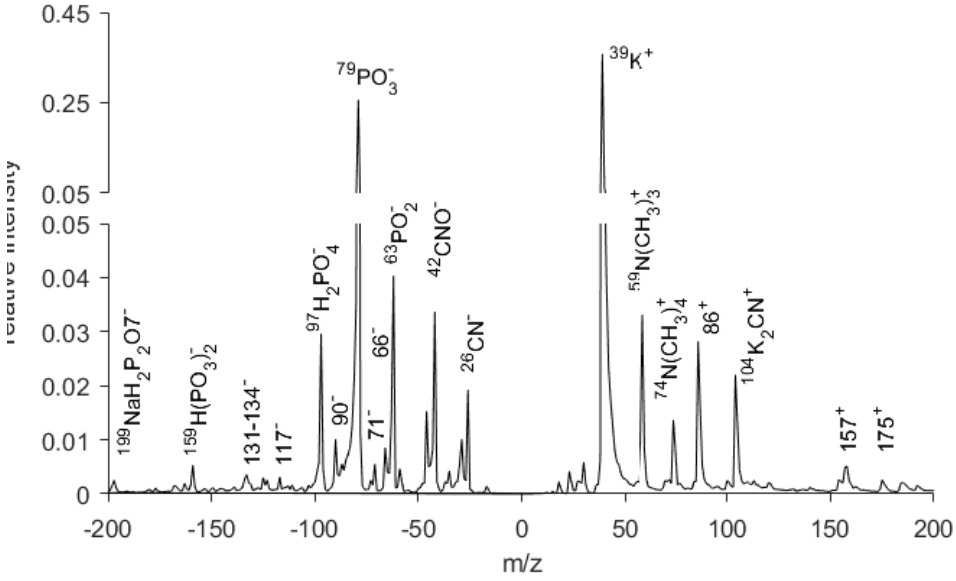

Figure 4.7. Average spectrum for *Cell-type* particles during the CalWater-2015 campaign.

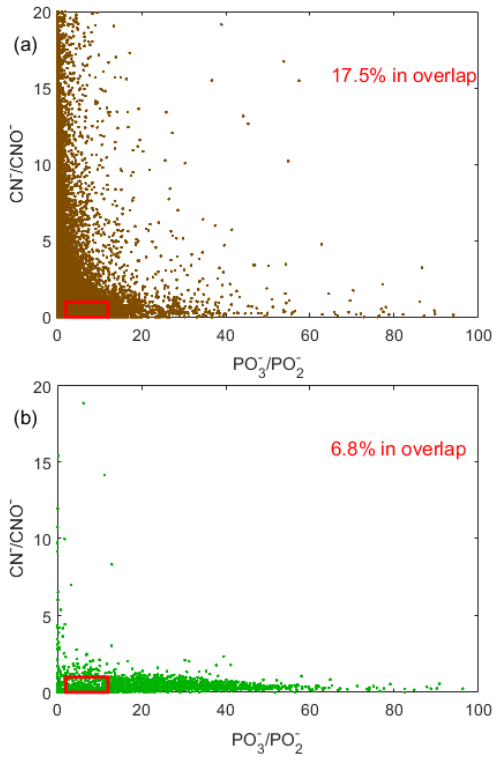

Figure 4.8. Individual mass spectra in $^{79}PO_3^-/^{63}PO_2^-$ versus $^{26}CN^-/^{42}CNO^-$ space for (a) *Dust* and (b) *Cell-type* particles identified at BML. The red box highlights an area of high overlap between the two particle types.

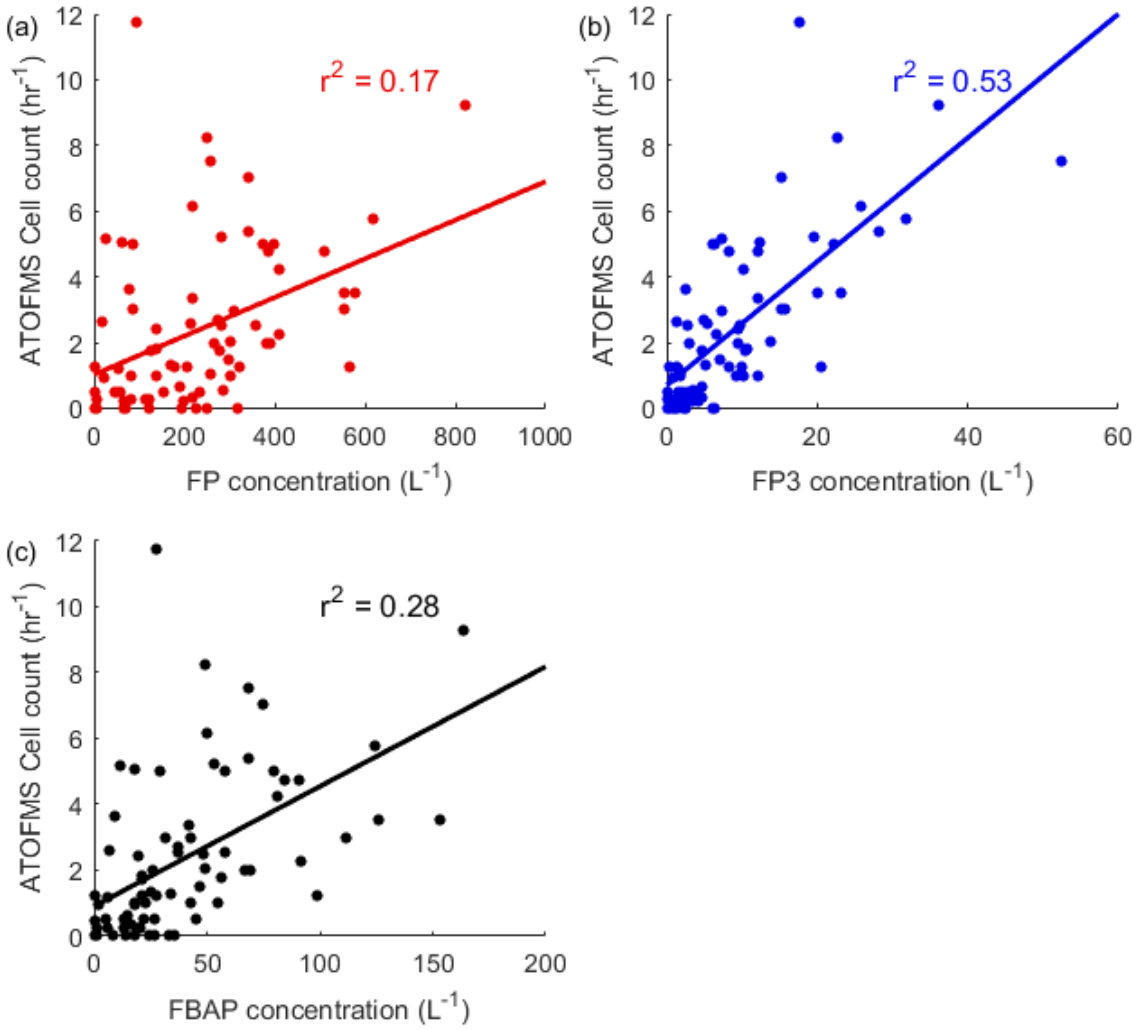

Figure 4.9. Hourly count of ATOFMS *Cell-type* particles versus the concentration (L^{-1}) of WIBS (a) FP, (b), FP3, and (c) FBAP particle types.

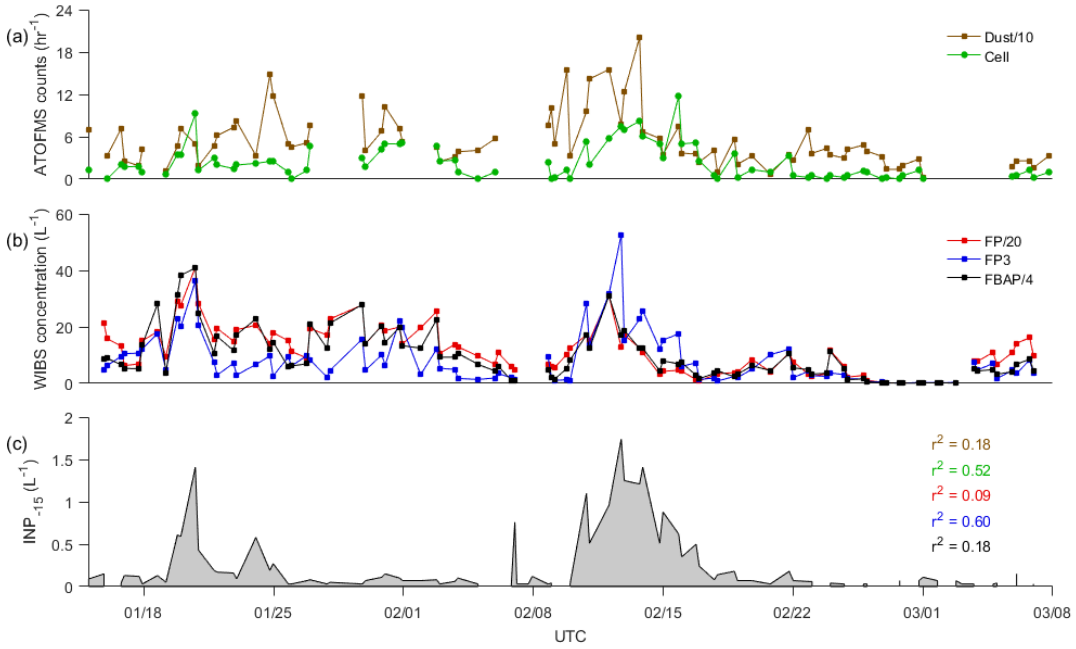

Figure 4.10. Temporal profiles of (a) ATOFMS hourly counts for *Dust* (scaled by 1/10, brown) and *Cell-type* (green), (b) WIBS particle type concentrations for FP (red, scaled by 1/20), FP3 (blue), and FBAP (lavender, scaled by 1/4), and (c) INP_{-15} (L^{-1}). Correlation coefficients (r^2) between INP_{-15} and WIBS or ATOFMS particle types are shown in their respective colors.

4.8 Tables

Table 4.1. Summary of dust and biological samples.

Sample	Name	Description	Study	ATOFMS
Ethiopian soil dust	EVSD	soil from vegetated area	FIN-1	A-ATOFMS
Argentinian soil dust	ASD	top soil from arable area	FIN-1	A-ATOFMS
Morrocan soil dust	MSD	Saharan desert dust	FIN-1	A-ATOFMS
Bachli soil dust	BSD	glacial sediment, no vegetation	FIN-1	A-ATOFMS
KFeldspar	KF	K-rich feldspar sample	FIN-1	A-ATOFMS
Illite NX	INX	Mineral dust standard	FIN-1	A-ATOFMS
Snomax	SX	irradiated, desiccated, ground *Ps*	FIN-1	A-ATOFMS
P. syringae	*Ps*	Gram-negative bacteria	FIN-1	A-ATOFMS
P. fluorescens	*Pf*	Gram-negative bacteria	FIN-1	A-ATOFMS
C. reinhardtii	*Cr*	freshwater microalgae	UCSD	LP-ATOFMS
S. dimorphus	*Sd*	freshwater microalgae	UCSD	LP-ATOFMS
D. tertiolecta	*Dt*	marine microalgae	UCSD	LP-ATOFMS
C. vulgaris	*Cv*	freshwater microalgae	UCSD	LP-ATOFMS
P. purpera	*Pp*	marine microalgae	UCSD	LP-ATOFMS
S. elongates	*Se*	freshwater cyanobacteria	UCSD	LP-ATOFMS
Arizona test dust	ATD	mineral dust standard	UCSD	nozzle-ATOFMS

Table 4.2. Summary of cell mass spectra signatures discussed in the manuscript. References for ion assignments and previous observations are provided as well as samples where signatures were observed in this work.

m/z	Assignment	sample (literature)	sample (this work)
Nucleobase			
-58	potential nucleobase fragments[f]	Ba[a,b,g,h,l], Bt[b], Mt[l], bioSSA[k]	Ps, Pf, Cr, Sd, Dt, Cv, Pp, Se
-66 (smaller -65, -64)	potential nucleobase fragments[g,n]	Ba[a,b,g,h,i,l,m], Bt[b], Bc[l], Mt[l], Ms[l], bioSSA[k]	Ps, Pf, Cr, Sd, Dt, Cv, Pp, Se
-71	potential nucleobase fragments[f]	Ba[a,b,g,h,l], Bt[b], Mt[l], Ms[l], bioSSA[k]	Ps, Pf, Cr, Sd, Dt, Cv, Pp, Se
-90	C_4N_3 (guanine or adenine fragment) [g,n]	Ba[a,b,g,h,i,l,m], Bt[b], Bc[l], Mt[l], Ms[l], bioSSA[k]	Ps, Pf, Cr, Sd, Dt, Cv, Pp, Se
-150,-149, -134-131, -117, -111,-110, -108-106, -95	$^{150}C_5H_4N_5O^-$ (Guanine-H), $^{134}C_5H_4N_5^-$ (Adenine-H), $^{125}C_5H_5N_2O_2^-$ (Thymine-H), $^{111}C_4H_3N_2O_2^-$ (Uracil-H), $^{110}C_4H_4N_3O^-$ (Cytosine-H) [f,g,n]	Ba[a,b,g,h,m], Bt[b], bioSSA[k]	Cr, Sd, Dt, Cv, Pp, Se
+152, +135, +110*	$^{152}C_5H_6N_5O^+$ (Guanine+H), $^{135}C_5H_3N_4O^+$ (Guanine+H-NH_3), $^{110}C_4H_4N_3O^+$ ((Guanine+H)-CH_2N_2)[n]		Cr, Sd, Dt, Cv, Pp, Se
Amino acid			
+70	C_4H_8N (Proline-CO_2H)[a,d]	Ba[a,b,g,l], Bc[l], Ca[b], Mt[l]	Ps, Pf, Cr, Sd, Dt, Cv, Pp, Se
+72	$C_4H_{10}N$ (Valine-CO_2H)[a]	Ba[a,b,g,m], Ca[b]	Ps, Pf, Cr, Sd, Dt, Cv, Pp, Se
+84	$C_5H_{10}N$[a]	Ba[a,b,g,m], Ca[b]	Ps, Pf, Cr, Sd, Dt, Cv, Pp, Se
+86	$C_5H_{12}N$ (Leucine-CO_2H, isoleucine-CO_2H)[a,d]	Ba[a,b,g,m], Ca[b]	Ps, Pf, Cr, Sd, Dt, Cv, Pp, Se
+88	$C_3H_6NO_2$ (Aspartic acid- CO_2H)[g]	Ba[g]	Ps, Pf
+104*	Unknown	Ba[a,g,l,m], Mt[l], Ms[l], bioSSA[k]	Ps, Pf, Cr, Cv, Pp, Se
+110*	$C_5H_8N_3$ (Histidine-CO_2H)[a]	Ba[a,m]	Ps, Pf, Cr, Sd, Dt, Cv, Pp, Se

Table 4.2. Summary of cell mass spectra signatures discussed in the manuscript (continued).

m/z	Assignment	sample (literature)	sample (this work)
Amino acid			
+120*	$C_8H_{10}N$ (Phenylalanine-CO_2H)[a]	Ba[a,l,m], Mt[l], Ms[l], bioSSA[k]	Ps, Pf, Cr, Sd, Dt, Cv, Pp, Se
+175*	$C_6H_{15}N_4O_2$ (Arginine+H)[a]	Ba[a,c,g,l], Mt[l], Ms[l], bioSSA[k]	Ps, Pf, Cr
-173	$C_6H_{13}N_4O_2$ (Arginine-H)[a]	Ba[a,b,g]	
-146	$C_5H_8NO_4$ (Glutamic acid-H)[a,d]	Ba[a,b,g], bioSSA[k]	
Organophosphate			
-97	H_2PO_4[a,j]	Ba[a,b,c,l,m], Bt[b], Bc[l], Ts[b], Ca[b], Mt[l], Ms[l], bioSSA[k], vegetative detritus[e]	Ps, Pf, Cr, Sd, Dt, Cv, Pp, Se
-159	$HPO_3)_2$[a,j]	Ba[a,m,c], Ca[b]	Ps, Pf, Cr, Sd, Dt, Cv, Pp, Se
-177	$H_3(PO_3)(PO_4)$[a,j]	Ba[a]	Cv, Pp
-199	$NaH_2PO_3PO_4$[a]	Ba[a,c]	Ps, Pf, Cr, Cv, Pp, Se
-215	$NaH_2(PO_4)_2$[a]	Ba[a,c]	
-239	$H_2(PO_3)_3$[j]		Cr, Pp, Se
-261	$NaH(PO_3)_3$[a]	Ba[a,c,l]	Ps, Pf, Sd, Cr, Cv, Pp, Se
-277	$Na_2H(PO_3)_2(PO_4)$[a]	Ba[a,c]	Ps, Pf, Cr, Dt, Cv
-301	$H(PO_3)_3PO_2$		Ps, Pf, Cr, Pp
-381	$H_2(PO_3)_4PO_2$	Ba[l]	Ps, Pf, Cr, Se
Quaternary amine			
+59	$N(CH_3)_3$[g]	Ba[g,l,m], Mt[l], bioSSA[k]	Ps, Pf, Cr, Sd, Dt, Cv, Pp
+74	$N(CH_3)_4$[g]	Ba[a,b,g,h,i,l,m], Mt[l], bioSSA[k]	Ps, Pf, Cr
Potassium-cluster[&]			
+104*	K_2CN[e]	bioSSA[k], vegetative detritus[e]	Ps, Pf, Cr
+120*	K_2CNO[e]	bioSSA[k], vegetative detritus[e]	Ps, Pf, Cr
+141	K_2PO_2[e]	bioSSA[k], vegetative detritus[e]	Ps, Pf, Cr
+157	K_2PO_3[e]	Ba[l,m], Bt[l], Mt[l], Ms[l], bioSSA[k], vegetative detritus[e]	Ps, Pf, Cr

Table 4.2. Summary of cell mass spectra signatures discussed in the manuscript (continued).

m/z	Assignment	sample (literature)	sample (this work)
***Potassium-cluster*[&]**			
+175*	K_2HSO_4[e]	Mt[l], bioSSA[k], vegetative detritus[e]	Ps, Pf, Cr
+197	K_3SO_3[e]	bioSSA[k], , vegetative detritus[e]	Ps, Pf, Cr
+213	K_3SO_4[e]	Mt[l], Ms[l], bioSSA[k], vegetative detritus[e]	Ps, Pf, Cr

[a](Czerwieniec et al., 2005) [b](Fergenson et al., 2004) [c](Gieray et al., 1997) [d](Schmidt et al., 2017) [e](Silva, 2000) [f](Smith et al., 1983) [g](Srivastava et al., 2005) [h](Steele et al., 2003) [i](Steele et al., 2005) [j](Strzelecka et al., 2017) [k](Sultana et al., 2017a) [l](Tobias et al., 2005) [m](Tobias et al., 2006) [n](Varmuza et al., 1999) [*]Signal at specific *m/z* could be isobars or generated from ionization of different organic species, see rest of table [&]Only listing spectra from the literature where the X+2 isotope is evident or samples in this work where some spectra have the X+2 isotope evident.

4.9 Supplementary information

4.9.1 Extended discussion of key ion markers for identification of cellular spectra

The following discussion details signatures that we hypothesize to be indicative of cellular single particle mass spectra and also likely to be observed across an array of biological species. These ion markers, summarized in Table 4.2, can be grouped into a number of broad classes: nucleobases, amino acids, betaines, negative ion clusters containing phosphate, and positive ion clusters with potassium. Unless otherwise noted, the "cellular" signatures that will be discussed have not been previously noted for dust mass spectra or other particle types.

4.9.1.1 Nucleobase signatures

Here we describe mass spectral details of nucleobases, focusing on ion markers previously reported in cellular single particle mass spectra or observed in this study. Negative mass spectra of nucleobases are characterized by the $[M\text{-}H]^-$ ion, such as ^{150}[Guanine-H]$^-$, ^{134}[Adenine-H]$^-$, ^{125}[Thymine-H]$^-$, ^{110}[Cytosize-H]$^-$, with further fragmentation of these species potentially yielding additional ion markers at *m/z* -58, -71, -64 to -67, -90, -95, -106 - -108, -117, -131 to -133, -149 (Smith et al., 1983; Srivastava et al., 2005; Varmuza et al., 1999). Cooccuring nucleobase ion markers at -90, -95, -111, -117, -134, -150 were reported in single particle mass spectra of *Bacillus atrophaeus* cells (Czerwieniec et al., 2005; Steele et al., 2003; Tobias et al., 2006). SSA particles concluded to contain cellular material also generated signal at *m/z* -117 and -107, and -90 (Sultana et al., 2017a), characteristic of adenine fragmentation (Srivastava et al., 2005). For the UCSD microalgae studies, nucleobase signatures were frequently observed, characterized by peaks at *m/z* -90, -106 to -107, -117, -131 to -134, -149, and -150 (Figs. 4.13 and 4.17a). With strong negative nucleobase ion signatures, positive ion signal was also commonly detected at *m/z* +110, +135, and +152 (Fig. 4.17b), likely a result of guanine ionization (Varmuza et al., 1999), and +185, not

assigned at this time. In the FIN-1 bacteria studies weak signal at -90 was sometimes observed, however nucleobase ion markers above -90 were rare. Relatively high *m/z* (-90 to -150 *m/z*) nucleotide signatures have never been detailed for single particle dust mass spectra and were also not observed in the dust samples discussed herein, making them good candidates to enable the separation of cellular and dust spectra.

Ion markers, potentially a result of extensive nucleoside fragmentation, at *m/z* -58, -64 to -66, and -71, have been reported in studies of *Bacillus* cells (Czerwieniec et al., 2005; Fergenson et al., 2004; Srivastava et al., 2005; Steele et al., 2003; Tobias et al., 2005) and were observed in all the the cellular samples examined here as well. In cellular mass spectra a very specific ion signature within the -67-64 range is pervasive, where signal at *m/z* -66 > -65 ~>= -64 and signal at -67 is very low relative to all these three (Fig. 4.17c). With increasing laser pulse energy (Steele et al., 2003, 2005) or TPII, as examined here, the relative intensity of these markers generally increases, with signal at *m/z* -65 and -64 approaching the relative intensity at -66 (Fig. 4.17d). Approxiamtely 70% of all bacterial FIN-1 and microalgea negative spectra had relative signal at *m/z* -66 above 0.005. The homogeneity of the signature in the region from *m/z* -58 to -71 across cellular mass spectra suggests a common source, however confidently attributing these ions to nucleosides rather than other organic species is less certain. Furthermore, the mere prescence of ion signal at these *m/z* values can not be used to distinguish cellular from dust spectra. Signal at *m/z* -71 is relatively common in dust spectra. In addition, at very high TPII dust frequently generate very low intensity signals at integer *m/z* in broad regions of the spectra, from roughly *m/z* -24 to -100 (Fig. 4.4b), likely a result of extensitve fragmentation and reorganization of organic species. However, in these instances the low intensity ion markers at integer locations all have very similar

relative intensities. Therefore the characteristic cellular signature from *m/z* -64 to -67, with the relatively strong peak at -66 can still be informative in identifying cellular spectra.

4.9.1.2 Amino acid signatures

Ion markers which have been assigned to an array of amino acids (Czerwieniec et al., 2005; Schneider et al., 2011; Srivastava et al., 2005) have been widely noted in cellular single particle mass spectra, including *Bacillus*, *Mycobacterium*, and *Clostridium acetobutylicum* cells (Fergenson et al., 2004; Srivastava et al., 2005; Tobias et al., 2005, 2006). As noted in the literature and observed for all biological species analysed in this work, peaks which can be attributed to amino acid $[M\text{-}CO_2]^+$ ions (e.g. $^{70}[Proline\text{-}CO_2]^+$, $^{86}[Leucine\text{-}CO_2]^+$, $^{110}[Histidine\text{-}CO_2]^+$, $^{120}[Phenylalanine\text{-}CO_2]^+$) frequently cooccur in cellular single particle mass spectra (Figure 4.17e). In spectra with a relativley intense $^{86}[Leucine\text{-}CO_2]^+$ peak, signal at *m/z* +84 at a similar relative intensity is almost always observed for the samples analysed herein and has also been previously noted (Czerwieniec et al., 2005). The amino acid markers $^{173}[Arginine\text{-}H]^-$, $^{175}[Arginine+H]^+$, and $^{146}[Glutamic\ acid\text{-}H]^-$ have also been noted in single particle mass spectra of *Bacillus* cells (Czerwieniec et al., 2005; Srivastava et al., 2005). Strong ion signal at *m/z* -146 was also noted for low TPII spectra of cell containing SSA particles (Sultana et al., 2017a). For the cellular spectra examined in this study, signal at *m/z* 175 was detected in ~32% of the bacterial FIN-1 mass spectra, but no other ion markers indicative of arginine or glutamic acid were noted in the FIN-1 or microalgea studies.

4.9.1.3 Negative phosphate-derived ions

Signal from characteristic ion fragments of organophosphate species (Strzelecka et al., 2017) has been frequently noted in cellular single particle mass spectra (Fergenson et al., 2004; Srivastava et al., 2005; Tobias et al., 2005, 2006). Unfortunately, the two most common

organophosphate ion markers in cellular spectra, $^{79}PO_3^-$ and $^{63}PO_2^-$, which have been utilized to identify potential biological particles in ambient aerosol populations (Creamean et al., 2013, 2014; Pratt et al., 2009a), are also readily generated by inorganic phosphates (Silva, 2000; Zawadowicz et al., 2017). Signal from $^{97}H_2PO_4^-$ has been noted in nearly every published SPMS cell analysis and was also ubiquitous in the cellular particle types sampled here, but utilizing *m/z* -97 as an identifier for cellular spectra in ambient data sets is problematic. The production of sulphates during aerosol atmospheric processing commonly results in the detection of $^{97}HSO_4^-$. Even in unprocessed dust particles significant signal from $^{97}H_2PO_4^-$ has been shown to be relatively rare, but not completely absent. However, a series of higher *m/z* phosphate-derived signals ($^{159}H(PO_3)_2^-$, $^{199}NaH_2PO_3PO_4^-$, $^{215}NaH_2(PO_4)^2$, $^{261}NaH(PO_3)_3^-$, $^{277}Na_2H(PO_3)_2(PO_4)^-$, $^{381}H_2(PO_3)_4PO_2$), characteristic of organophosphate species such as DNA (Strzelecka et al., 2017), has been reported for *Bacillus* species (Czerwieniec et al., 2005; Tobias et al., 2005) . For both the bacterial FIN-1 and UCSD microalgae mass spectra a similar series of phosphate-derived ions are repeatedly observed, with signal at some combination of -*m/z* 159, 199, 239, (proposed to be $^{239}H_2(PO_3)_3^-$), 261, 277, 301 (proposed to be $^{301}H(PO_3)_3PO_2^-$), and 381 (Fig. 4.17f). Out of these markers, relatively intense signal at *m/z* -159 is most frequently detected; 44% of bacterial FIN-1 and 59% of microalgea negative spectra had relative signal above 0.01. This series of high mass (>= -159 *m/z*) phosphate-derived negative ions has never been noted in dust spectra, and thus this organophosphate signature is an excellent candidate for distinguishing cellular spectra.

4.9.1.4 Positive signal at *m/z* 59 and 74

A number of SPMS *Bacillus* and *Tuberculosis* cell studies have noted signal at *m/z* +74, often accompanied by signal at *m/z* +59 (Czerwieniec et al., 2005; Fergenson et al., 2004; Srivastava et al., 2005; Tobias et al., 2005, 2006). These markers have been attributed to the

fragmentation of organic species with quaternary amines, such as trimethylglycine, generating $^{74}N(CH_3)_4^+$ and $^{59}N(CH_3)_3^+$ (Srivastava et al., 2005). In this work, for all the species studied the relative intensity of *m/z* +59 and +74 generally decreased with increasing TPII (Fig. 4.12), consistent with previous SPMS *Bacillus* studies (Steele et al., 2003, 2005) and descriptions of likely cell-containing SSA (Sultana et al., 2017a). Mass spectra with relatively intense signal at *m/z* +59 and +74 (Fig. 4.17g) were common in the *Ps*, *Pf*, and *Cr* data sets, but were relatively rare in the UCSD microalgae dataset. This betaine signature has never been noted in dust mass spectra though isobaric contributions from $^{59}Co^+$ as well as $^{59}Na(H_2O)_2^+$, common to SSA spectra, could complicate identification of cell particles in complex atmospheric samples.

4.9.1.5 Positive potassium-cluster ions

A series of relatively low intensity signals above *m/z* +100, including +104, +120, +157, +141, +175, +197, and +213, have been noted in some SPMS studies of cells (Tobias et al., 2005), vegetative detritus (Silva, 2000), and likely cell-containing SSA (Sultana et al., 2017a). Silva (2000) attributed these signals to potassium-cluster ions ($^{104}K_2CN^+$, $^{120}K_2CNO^+$, $^{141}K_2PO_2^+$, $^{157}K_2PO_3^+$, $^{175}K_2HSO_4^+$, $^{197}K_3SO_3^+$, and $^{213}K_3SO_4^+$) though we don't treat these assignments as definitive. As previously mentioned the ionization of amino acids arginine and phenylalanine can generate ^{175}[Arginine+H]$^+$ (Srivastava et al., 2005) and ^{120}[Phenylalanine-CO_2]$^+$ (Czerwieniec et al., 2005). Also isotopic labeling of *Bacillus* cells indicated that signal at *m/z* 104 was generated by an ion species containing two carbons and one nitrogen atom which is incompatible with an assignment of $^{104}K_2CN^+$. All of the potassium-cluster ions described by Silva (2000) have distinctive isotopic signatures with a X:X+2 ratio (e.g. $^{157}K_2PO_3^+$:$^{159}K_2PO_3^+$) within the range of 7:1 to 4:1. Isotopic signal at *m/z* X+2 is apparent in the provided mass spectra within Sultana et al. (2017) and Silva (2000), indicating contributions from potassium-cluster ions, though many

cellular spectra with signal reported at *m/z* +175 show no significant signal at +177. In the cellular datasets examined in this work only *Ps*, *Pf*, and *Cr* generated spectra with at least some obvious contributions from potassium-cluster ions, as evidenced by ion signal at *m/z* X+2 (Fig. 4.17h). For these samples, relative intensity at *m/z* 104, 120, 141, 157, 175, 197, and 213 generally increased with increasing TPII, consistent with results from Sultana et al. (2017). The ratio of X:X+2 for the entire *Ps* dataset at these *m/z* is 9.8, 9.3, 5, 5.5, 7.2, 5.1, and 4.4. The high X:X+2 ratio for X = 104, 120, and 175, 9.8, 9.3, and 7.2 respectively, is indicative of contributions from ion species without potassium atoms.

The aforementioned potassium-cluster ions are a potential tool to identify cellular spectra from complex data sets but should be done with care. While the authors know of no published SPMS dust study that notes this specific signature, Silva (2000) readily detected $^{141}K_2PO_2^+$ and $^{157}K_2PO_3^+$ ions from potassium phosphate standards and biomass burning particles can also generate $^{104}K_2CN^+$, $^{120}K_2CNO^+$, $^{197}K_3SO_3^+$, and $^{213}K_3SO_4^+$ ions (Silva et al., 1999).

4.9.2 Flow process of *Cell-type* identification

This section details the steps used to define *Cell-type* particles. Peaks are discriminated based off of their relative peak areas, which range from 0 to 1 and have arbitrary units. "&" denotes boolean AND, while "|" denotes boolean OR.

<u>Group 1—Meets one of the following</u>
(1) $39^+ \geq 0.1$ & $79^- \geq 0.05$
(2) $59^+ > 0.1$ & $39^+ > 0.025$ & $77^+ < 0.05$
(3) $104^+ > 0.05$ & $39^+ > 0.01$
(4) $90^- > 0.01$ & $39^+ > 0.01$
(5) $66^- > 0.01$ & $39^+ > 0.01$
(6) $74^+ > 0.05$ & $39^+ > 0.01$ & $77^+ < 0.01$
(7) $86^+ > 0.05$ & $39^+ > 0.01$ & $77^+ < 0.01$

<u>Group 2:</u>
Group 1: $81^+ >= 0.015$

Group 3
Group 1: $12^{+} >= 0.005$

Group 6
Group 1: $37^{+} >= 0.01$ | $51^{+} >= 0.01$

Group 5
Group 1: $23^{+} >= 0.175$ | ...

Group 4
Group 1: $117^{-} > 0$ | $159^{-} > 0$

Group 7
Group 1: if (-) spectra exists, $79^{-} < 0.1$

Group 8
Group 3: $39^{+} \geq 0.2$ & $79^{-} > 0.1$

Group 9
Group 6: $79^{-} \geq 0.075$

Group 1
Combine groups 1, 8, and 9

Group 10
Group 1 & 4: $76^{-} > 0.01$ | $56^{+} > 0.005$ | $64^{+} > 0.01$

Group 11
Group 10: $59^{+} > 0.01$ | $74^{+} > 0.01$ | $86^{+} > 0.01$

Group 1
Combine groups 1 and 11

Group 13
Group 1 & 4: $27^{+} > .01$ | $62^{+} > 0.02$

Group 14
Group 13: $59^{+} > 0.01$ | $74^{+} > 0.01$ | $86^{+} > 0.01$ | $104^{+} > 0.01$

Group 1
Combine groups 1 and 14

Group 15
Group 1: $46 > 0.01$ | $-62 > 0.015$

Group 10
Combine group 10 and group 15

Group 11
Group 4: $59^{+} > 0.025$ | $74^{+} > 0.025$| $86^{+} > 0.025$ | $104^{+} > 0.025$ | $66^{-} > 0.01$ | $90^{-} > 0.01$ | $157^{+} > 0.005$ | $159^{-} > 0.005$

Group 1
Combine groups 1 and 11

Group 11
Group 7 or group 10: $74^{+} > 0.015$| $86^{+} > 0.015$ | $104^{+} > 0.015$

Group 1
Combine groups 1 and 11

Group 16:
Group 1: $46^{-} > 0.05$ | $62^{-} > 0.05$

Group 13
Combine groups 13 and 16

Group 11
Group 13: 79- > 0.2

Group 1
Combine groups 1 and 11

Group 11
Group 13: $59^{+} > 0.01$ | $74^{+} > 0.01$ | $86^{+} > 0.01$ | $104^{+} > 0.01$

Group 1
Combine groups 1 and 11

Group 10
Group 1: 56+ > 0.01

Group 11:
Group 10: 157+ > 0.01

Group 1
Combine groups 1 and 11

Group 17:
Group 1: $23^{+} > 0.05$ | $24^{+} > 0.05$ | $27^{+} > 0.05$

Cell-type particles are anything left as Group 1.

4.10 Supplementary figures

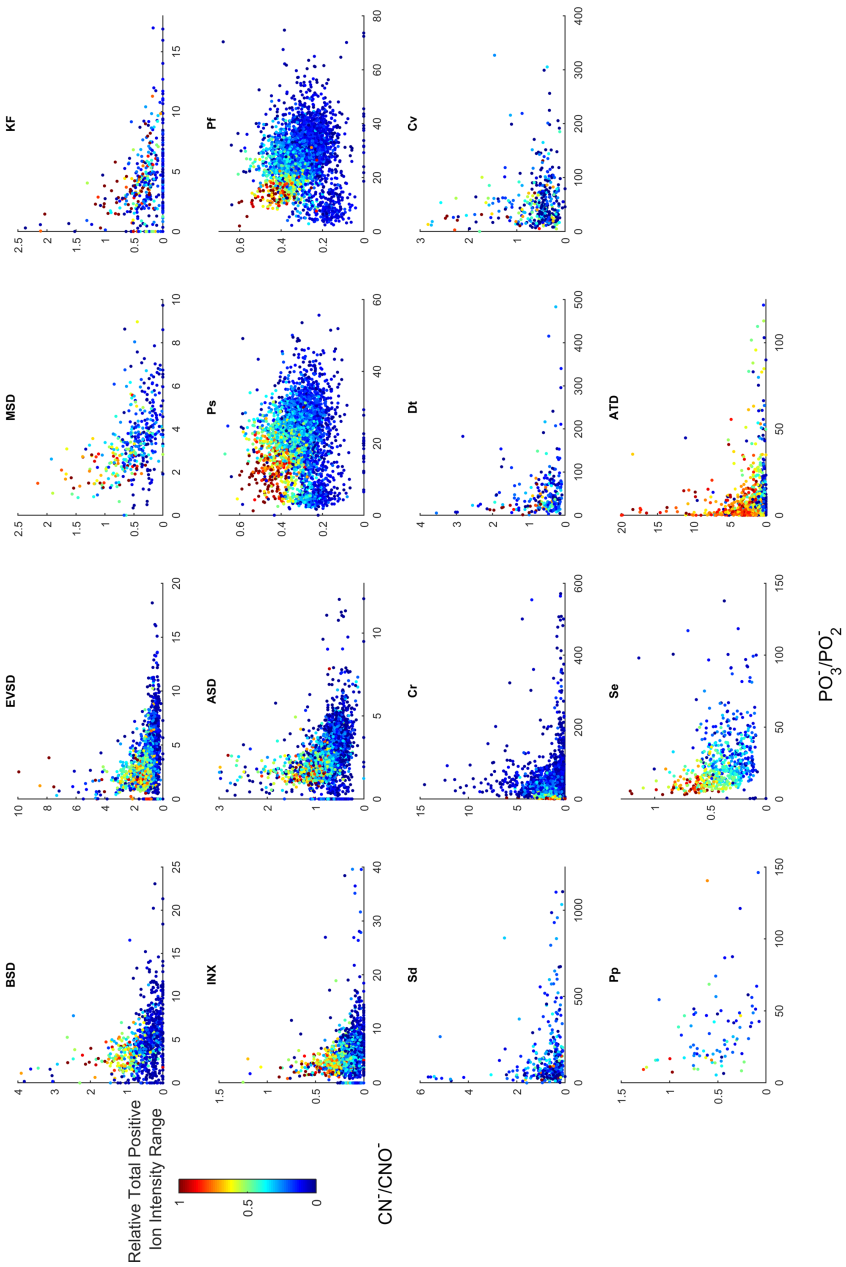

Figure 4.11. Each point represents an individual mass spectrum in $^{79}PO_3^-/^{63}PO_2^-$ vs $^{26}CN^-/^{42}CNO^-$ space, for each sample analysed by ATOFMS. Warmer shades indicate higher TPII. TPII was normalized within each sample data set.

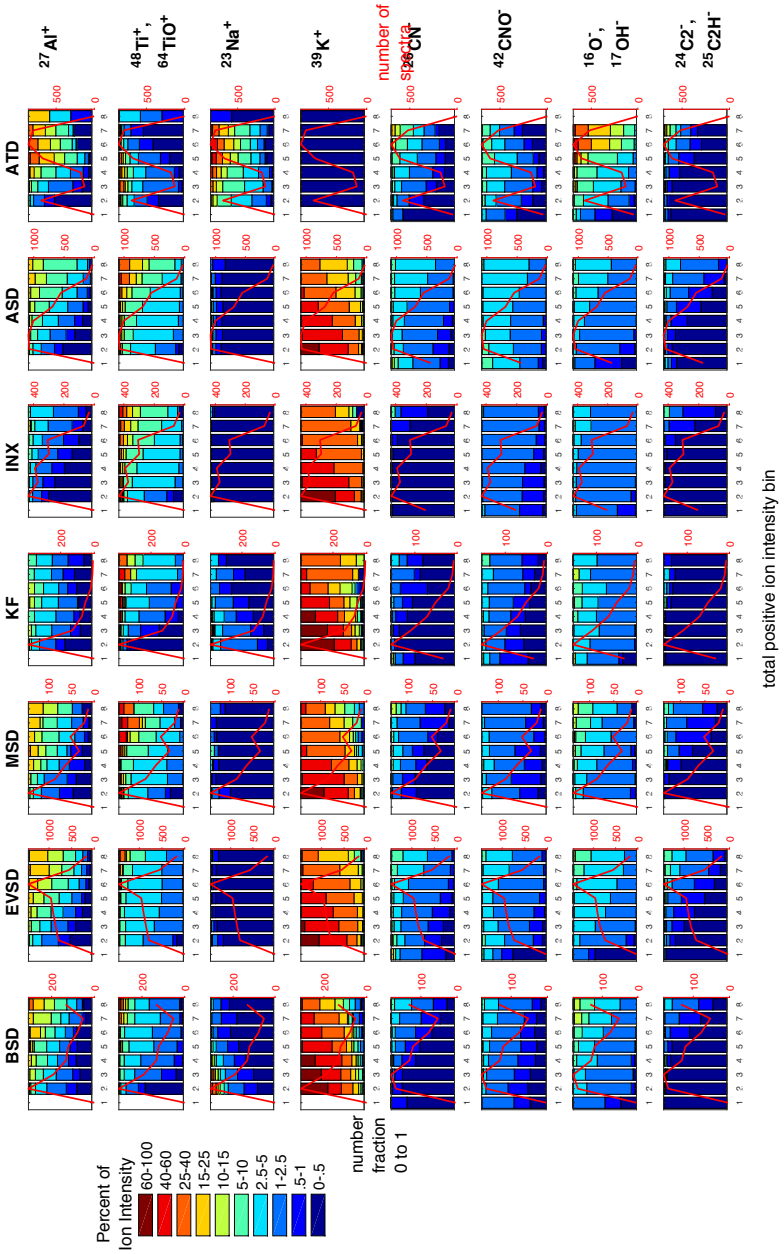

Figure 4.12. Distribution of relative signal for various ion markers with spectra grouped by TPII, for dust samples analysed by ATOFMS. Warmer colors indicate higher relative ion intensity. TPII increases moving to the right for each plot. The red trace indicates the number of spectra within each TPII bin.

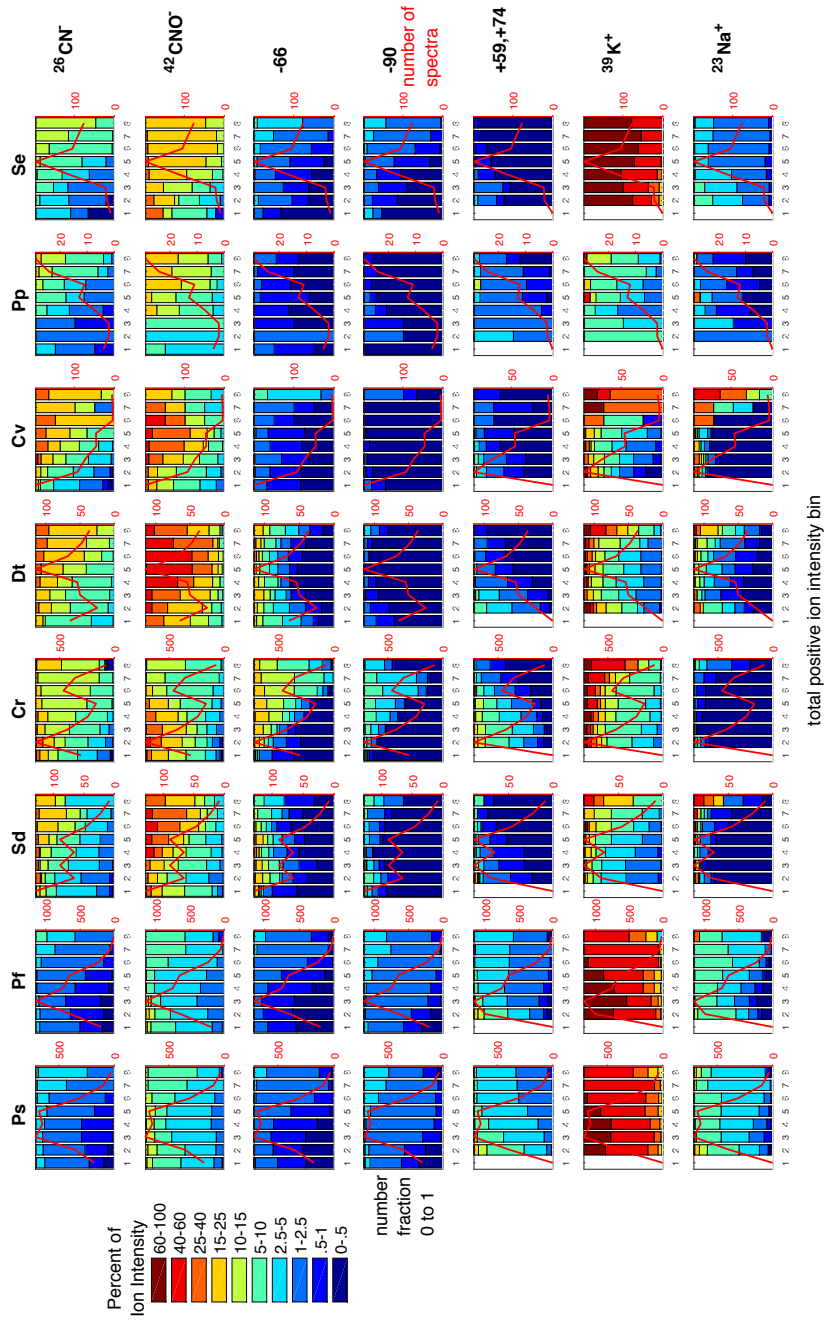

Figure 4.13. Distribution of relative signal for various ion markers with spectra grouped by TPII, for cell samples analysed by ATOFMS. Warmer colors indicate higher relative ion intensity. TPII increases moving to the right for each plot. The red trace indicates the number of spectra within each TPII bin.

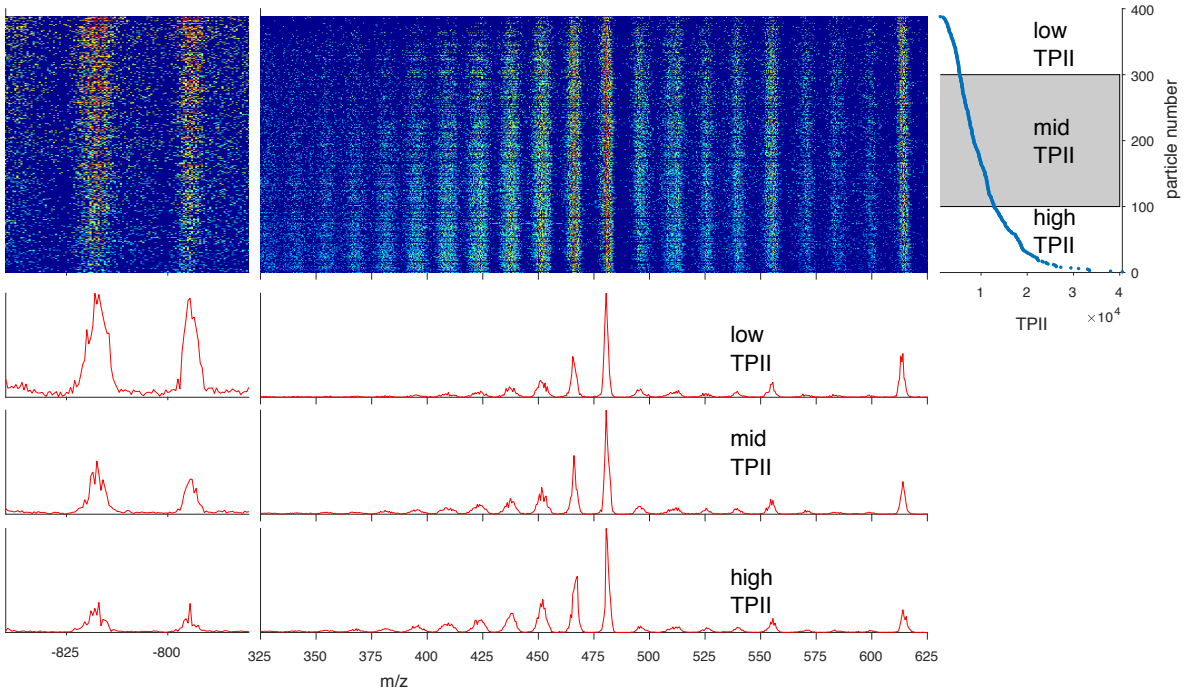

Figure 4.14. Examination of high *m/z* regions of *Sd* mass spectra. The top row is a heat map where each row is mass spectral data from an individual particle and warmer colors indicate higher relative ion signal. The mass spectra are ordered by TPII, with increasing TPII moving down (far right). Average signal for spectra grouped by low, mid, and high TPII (bottom rows) are also shown, with arbitrary units on the y-axis.

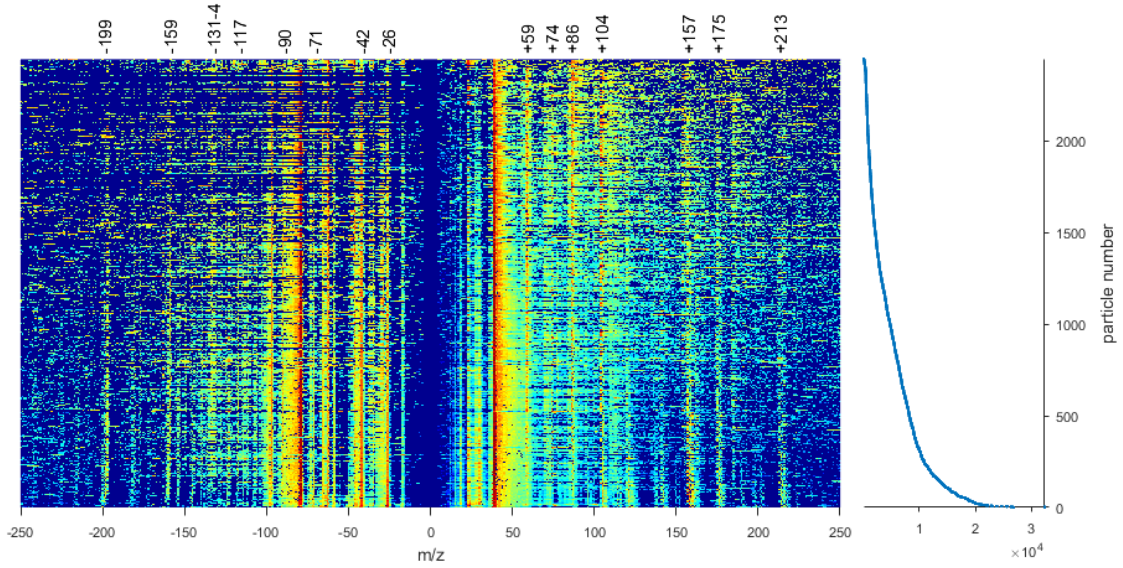

Figure 4.15. Mass spectral heat map for *Cell-type* particles identified at BML. Right panel shows the TPII.

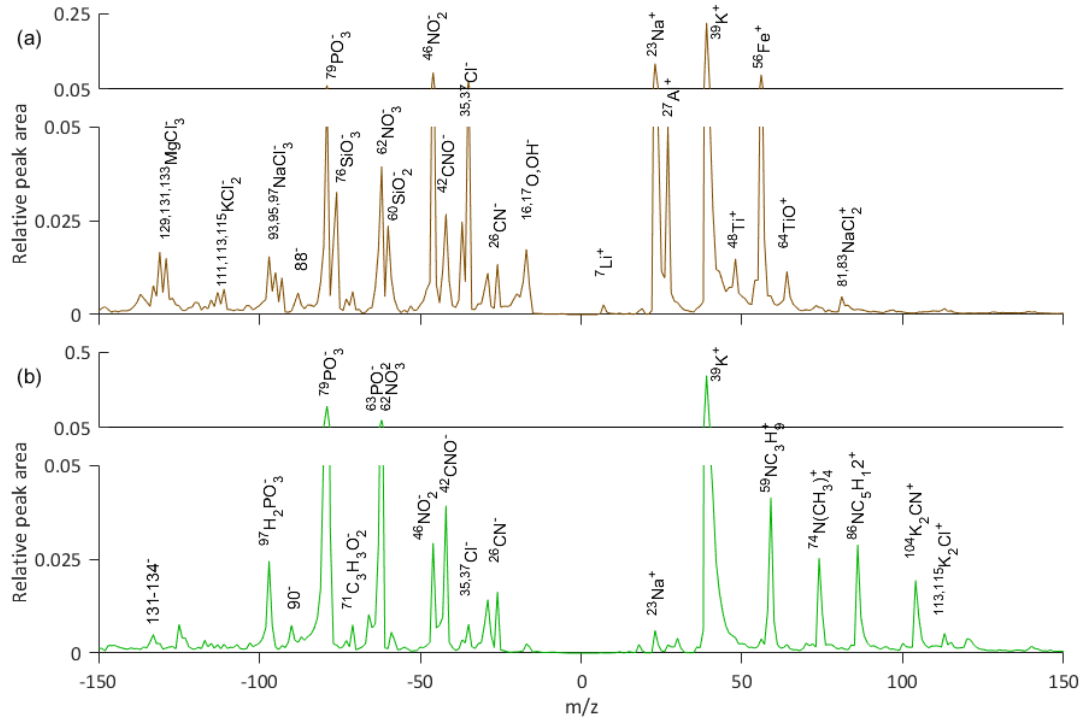

Figure 4.16. Average spectra from overlap regions for (a) *Dust* and (b) *Cell-type* particles.

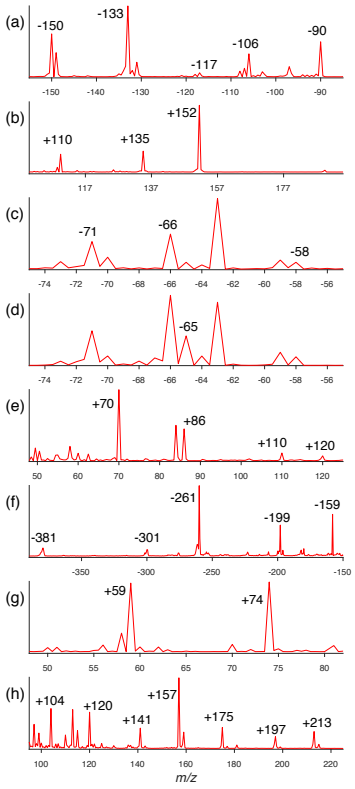

Figure 4.17. Representative cellular standard mass spectra illustrating signatures indicative of ionization of (a & b) nucleobases, (e) amino acids, (f) organophosphates, and (g) quarternary amines. The cellular signature in the region between *m/z* -56 and -74 for relatively (c) low and (d) high TPII mass spectra is also shown. A characteristic signature from *m/z* +100 to +220 is also shown which could partially be attributed to amino acid ions or potassium-cluster ions. The spectra are an average of 154 *Cr*, 47 *Se*, 36 *Se*, 66 *Dt*, 240 *Ps*, 177 *Ps*, and 298 *Ps* individual spectra to minimize noise.

4.11 Supplementary tables

Table 4.3. Bioparticle classification types for the WIBS. FL1, FL2, and FL3 refer to fluorescent channels 1, 2, and 3 respectively. Reference denotes the study where the particle type was originally described.

Particle type	Particle definitions	Reference
FP	FL1 > 0 | FL2 > 0 | FL3 > 0	Gabey et al., (2011)
FP3	FL1 > 1900 & FL2 ≤ 500 & FL3 ≤ 500	Wright et al., (2014)
FBAP	FL1 > 0.0 | FL2 > 0.0 | FL3 > 0.0	Gabey et al., (2011)

4.12 References

Alpert, P. A., Aller, J. Y. and Knopf, D. a.: Ice nucleation from aqueous NaCl droplets with and without marine diatoms, Atmos. Chem. Phys. Discuss., 11(3), 8291–8336, doi:10.5194/acpd-11-8291-2011, 2011.

Andreae, M. O. and Rosenfeld, D.: Aerosol-cloud-precipitation interactions. Part 1. The nature and sources of cloud-active aerosols, Earth-Science Rev., 89(1–2), 13–41, doi:10.1016/j.earscirev.2008.03.001, 2008.

Atkinson, J. D., Murray, B. J., Woodhouse, M. T., Whale, T. F., Baustian, K. J., Carslaw, K. S., Dobbie, S., O'Sullivan, D. and Malkin, T. L.: The importance of feldspar for ice nucleation by mineral dust in mixed-phase clouds, Nature, 500(7463), 490–490, doi:10.1038/nature12384, 2013.

Ault, A. P., Guasco, T. L., Ryder, O. S., Baltrusaitis, J., Cuadra-rodriguez, L. A., Collins, D. B., Ruppel, M. J., Bertram, T. H., Prather, K. A. and Grassian, V. H.: Inside versus Outside: Ion Redistribution in Nitric Acid Reacted Sea Spray Aerosol Particles as Determined by Single Particle Analysis, , doi:10.1021/ja407117x, 2013.

Cahill, J. F.: Novel techniques and applications in single particle mass spectrometry, University of California, San Diego., 2014.

Cahill, J. F., Darlington, T. K., Wang, X., Mayer, J., Spencer, M. T., Holecek, J. C., Reed, B. E. and Prather, K. A.: Development of a high-pressure aerodynamic lens for focusing large particles (4-10 μm) into the aerosol time-of-flight mass spectrometer, Aerosol Sci. Technol., 48(9), 948–956, doi:10.1080/02786826.2014.947400, 2014.

Cahill, J. F., Darlington, T. K., Fitzgerald, C., Schoepp, N. G., Beld, J., Burkart, M. D. and Prather, K. A.: Online Analysis of Single Cyanobacteria and Algae Cells under Nitrogen-Limited Conditions Using Aerosol Time-of-Flight Mass Spectrometry, Anal. Chem., 87(16), 8039–8046, doi:10.1021/acs.analchem.5b02326, 2015.

Carson, P. G., Johnston, M. V. and Wexler, A. S.: Real-Time Monitoring of the Surface and Total Composition of Aerosol Particles, Aerosol Sci. Technol., 26(4), 291–300, doi:10.1080/02786829708965431, 1997.

Creamean, J. M., Suski, K. J., Rosenfeld, D., Cazorla, A., DeMott, P. J., Sullivan, R. C., White, A. B., Ralph, F. M., Minnis, P., Comstock, J. M., Tomlinson, J. M. and Prather, K. a: Dust and biological aerosols from the Sahara and Asia influence precipitation in the western U.S., Science, 339(2013), 1572–8, doi:10.1126/science.1227279, 2013.

Creamean, J. M., Lee, C., Hill, T. C., Ault, A. P., DeMott, P. J., White, A. B., Ralph, F. M. and Prather, K. a.: Chemical properties of insoluble precipitation residue particles, J. Aerosol Sci., 76, 13–27, doi:10.1016/j.jaerosci.2014.05.005, 2014.

Czerwieniec, G. A., Russell, S. C., Tobias, H. J., Pitesky, M. E., Fergenson, D. P., Steele, P., Srivastava, A., Horn, J. M., Frank, M., Gard, E. E. and Lebrilla, C. B.: Stable Isotope Labeling of Entire Bacillus atrophaeus Spores and Vegetative Cells Using Bioaerosol Mass Spectrometry, Anal. Chem., 77(4), 1081–1087, doi:10.1021/ac0488098, 2005.

DeMott, P. J., Prenni, A. J., Liu, X., Kreidenweis, S. M., Petters, M. D., Twohy, C. H., Richardson, M. S., Eidhammer, T. and Rogers, D. C.: Predicting global atmospheric ice nuclei distributions and their impacts on climate, Proc. Natl. Acad. Sci., 107(25), 11217–11222, doi:10.1073/pnas.0910818107, 2010.

Després, V. R., Alex Huffman, J., Burrows, S. M., Hoose, C., Safatov, A. S., Buryak, G., Fröhlich-Nowoisky, J., Elbert, W., Andreae, M. O., Pöschl, U. and Jaenicke, R.: Primary biological aerosol particles in the atmosphere: A review, Tellus, Ser. B Chem. Phys. Meteorol., 64(1), doi:10.3402/tellusb.v64i0.15598, 2012.

Engelstaedter, S., Tegen, I. and Washington, R.: North African dust emissions and transport, Earth-Science Rev., 79(1–2), 73–100, doi:10.1016/j.earscirev.2006.06.004, 2006.

Fergenson, D. P., Pitesky, M. E., Tobias, H. J., Steele, P. T., Czerwieniec, G. A., Russell, S. C., Lebrilla, C. B., Horn, J. M., Coffee, K. R., Srivastava, A., Pillai, S. P., Shih, M. T. P., Hall, H. L., Ramponi, A. J., Chang, J. T., Langlois, R. G., Estacio, P. L., Hadley, R. T., Frank, M. and Gard, E. E.: Reagentless Detection and Classification of Individual Bioaerosol Particles in Seconds, Anal. Chem., 76(2), 373–378, doi:10.1021/ac034467e, 2004.

Fröhlich-Nowoisky, J., Kampf, C. J., Weber, B., Huffman, J. A., Pöhlker, C., Andreae, M. O., Lang-Yona, N., Burrows, S. M., Gunthe, S. S., Elbert, W., Su, H., Hoor, P., Thines, E., Hoffmann, T., Després, V. R. and Pöschl, U.: Bioaerosols in the Earth system: Climate, health, and ecosystem interactions, Atmos. Res., 182, 346–376, doi:10.1016/j.atmosres.2016.07.018, 2016.

Gabey, A. M., Gallagher, M. W., Whitehead, J., Dorsey, J. R., Kaye, P. H. and Stanley, W. R.: Measurements and comparison of primary biological aerosol above and below a tropical forest canopy using a dual channel fluorescence spectrometer, Atmos. Chem. Phys., 10(10), 4453–4466, doi:10.5194/acp-10-4453-2010, 2010.

Gabey, A. M., Stanley, W. R., Gallagher, M. W. and Kaye, P. H.: The fluorescence properties of aerosol larger than 0.8 μ in urban and tropical rainforest locations, Atmos. Chem. Phys., 11(11), 5491–5504, doi:10.5194/acp-11-5491-2011, 2011.

Gard, E., Mayer, J. E., Morrical, B. D., Dienes, T., Fergenson, D. P. and Prather, K. A.: Real-Time Analysis of Individual Atmospheric Aerosol Particles: Design and Performance of a Portable ATOFMS, Anal. Chem., 69(20), 4083–4091, doi:10.1021/ac970540n, 1997.

Gieray, R. A., Reilly, P. T. A., Yang, M., Whitten, W. B. and Ramsey, J. M.: Real-time detection of individual airborne bacteria, J. Microbiol. Methods, 29(3), 191–199, doi:10.1016/S0167-7012(97)00049-3, 1997.

Gross, D. S., Gälli, M. E., Silva, P. J. and Prather, K. A.: Relative sensitivity factors for alkali metal and ammonium cations in single-particle aerosol time-of-flight mass spectra, Anal. Chem., 72(2), 416–422, doi:10.1021/ac990434g, 2000.

Hader, J. D., Wright, T. P. and Petters, M. D.: Contribution of pollen to atmospheric ice nuclei concentrations, Atmos. Chem. Phys., 14(11), 5433–5449, doi:10.5194/acp-14-5433-2014, 2014.

Hill, T. C. J., Demott, P. J., Tobo, Y., Fröhlich-Nowoisky, J., Moffett, B. F., Franc, G. D. and Kreidenweis, S. M.: Sources of organic ice nucleating particles in soils, Atmos. Chem. Phys., 16(11), 7195–7211, doi:10.5194/acp-16-7195-2016, 2016.

Hirst, E., Kaye, P. H., Foot, V., Clark, J. M. and Withers, P. B.: An instrument for the simultaneous acquisition of size, shape, and spectral fluorescence data from single aerosol particles, Proc. SPIE, 5617, 416–423, doi:10.1117/12.578269, 2004.

Huffman, J. A., Prenni, A. J., Demott, P. J., Pöhlker, C., Mason, R. H., Robinson, N. H., Fröhlich-Nowoisky, J., Tobo, Y., Després, V. R., Garcia, E., Gochis, D. J., Harris, E., Müller-Germann, I., Ruzene, C., Schmer, B., Sinha, B., Day, D. A., Andreae, M. O., Jimenez, J. L., Gallagher, M., Kreidenweis, S. M., Bertram, A. K. and Pöschl, U.: High concentrations of biological aerosol particles and ice nuclei during and after rain, Atmos. Chem. Phys., 13(13), 6151–6164, doi:10.5194/acp-13-6151-2013, 2013.

Kanji, Z. A., Ladino, L. A., Wex, H., Boose, Y., Burkert-Kohn, M., Cziczo, D. J. and Krämer, M.: Overview of Ice Nucleating Particles, Meteorol. Monogr., 58, 1.1-1.33, doi:10.1175/AMSMONOGRAPHS-D-16-0006.1, 2017.

Knopf, D. A., Alpert, P. A., Wang, B. and Aller, J. Y.: Stimulation of ice nucleation by marine diatoms, Nat. Geosci., 4(2), 88–90, doi:10.1038/ngeo1037, 2011.

Marsden, N. A., Ullrich, R., Möhler, O., Eriksen Hammer, S., Kandler, K., Cui, Z., Williams, P. I., Flynn, M. J., Liu, D., Allan, J. D. and Coe, H.: Mineralogy and mixing state of North African mineral dust by on-line single-particle mass spectrometry, Atmos. Chem. Phys. Discuss., (August), 1–41, doi:10.5194/acp-2018-725, 2018a.

Marsden, N. A., Flynn, M. J., Allan, J. D. and Coe, H.: Online differentiation of mineral phase in aerosol particles by ion formation mechanism using a LAAP-TOF single-particle mass spectrometer, Atmos. Meas. Tech., 11(1), 195–213, doi:10.5194/amt-11-195-2018, 2018b.

Martin, A. C., Cornwell, G. C., Atwood, S. A., Moore, K. A., Rothfuss, N. E., Taylor, H., DeMott, P. J., Kreidenweis, S. M., Petters, M. D. and Prather, K. A.: Transport of pollution to a remote coastal site during gap flow from California's interior: impacts on aerosol composition, clouds, and radiative balance, Atmos. Chem. Phys., 17(2), 1491–1509, doi:10.5194/acp-17-1491-2017, 2017.

Mason, R. H., Si, M., Li, J., Chou, C., Dickie, R., Toom-Sauntry, D., Pöhlker, C., Yakobi-Hancock, J. D., Ladino, L. A., Jones, K., Leaitch, W. R., Schiller, C. L., Abbatt, J. P. D., Huffman, J. A. and Bertram, A. K.: Ice nucleating particles at a coastal marine boundary layer site: Correlations with aerosol type and meteorological conditions, Atmos. Chem. Phys., 15(21), 12547–12566, doi:10.5194/acp-15-12547-2015, 2015.

Perring, A. E., Schwarz, J. P., Baumgardner, D. G., Hernandez, M. T., Spracklen, D. V., Heald, C. L., Gao, R. S., Kok, G., McMeeking, G. R., McQuaid, J. B. and Fahey, D. W.: Airborne observations of regional variation in fluorescent aerosol across the United States, J. Geophys. Res. Atmos., 120, 1153–1170, doi:10.1002/2013JD020225.Received, 2014.

Plouguerne, E., de Souza, L. M., Sassaki, G. L., Figueiredo Cavalcanti, J., Villela Romanos, M. T., Gama, B. A. P., Pereira, R. C. and Barreto-Bergter, E.: Antiviral Sulfoquinovosyldiacylglycerols (SQDGs) from the Brazilian Brown Seaweed Sargassum vulgare, Mar. Drugs, 11, 4628–4640, doi:10.3390/md11114628, 2013.

Pratt, K. A., Demott, P. J., French, J. R., Wang, Z., Westphal, D. L., Heymsfield, A. J., Twohy, C. H., Prenni, A. J. and Prather, K. A.: In situ detection of biological particles in cloud ice-crystals, Nat. Geosci., 2(6), 398–401, doi:10.1038/ngeo521, 2009b.

Pratt, K. A., DeMott, P. J., French, J. R., Wang, Z., Westphal, D. L., Heymsfield, A. J., Twohy, C. H., Prenni, A. J. and Prather, K. A.: In situ detection of biological particles in cloud ice-crystals, Nat. Geosci., 2(6), 398–401, doi:10.1038/ngeo521, 2009a.

Pratt, K. a, Mayer, J. E., Holecek, J. C., Moffet, R. C., Sanchez, R. O., Rebotier, T. P., Furutani, H., Gonin, M., Fuhrer, K., Su, Y., Guazzotti, S., Prather, K. a, Fuhrer, X. K. and Su, X. Y.: Development and Characterization of an Aircraft Aerosol Time-of-Flight Mass Spectrometer Development and Characterization of an Aircraft Aerosol Time-of-Flight Mass Spectrometer, Anal. Chem., 81(5), 1792–1800, doi:10.1021/ac801942r, 2009c.

Rebotier, T. P. and Prather, K. A.: Aerosol time-of-flight mass spectrometry data analysis: A benchmark of clustering algorithms, Anal. Chim. Acta, 585, 38–54, doi:10.1016/j.aca.2006.12.009, 2007.

Reinard, M. S. and Johnston, M. V.: Ion Formation Mechanism in Laser Desorption Ionization of Individual Nanoparticles, J. Am. Soc. Mass Spectrom., 19(3), 389–399, doi:10.1016/j.jasms.2007.11.017, 2008.

Rogers, D. C., DeMott, P. J., Kreidenweis, S. M. and Chen, Y.: Measurements of ice nucleating aerosols during SUCCESS, Geophys. Res. Lett., 25(9), 1383–1386, doi:10.1029/97GL03478, 1998.

Sansonetti, J. E. and Martin, W. C.: Handbook of basic atomic spectroscopic data, J. Phys. Chem. Ref. Data, 34(4), 1559–2259, doi:10.1063/1.1800011, 2005.

Schmidt, S., Schneider, J., Klimach, T., Mertes, S., Schenk, L. P., Kupiszewski, P., Curtius, J. and Borrmann, S.: Online single particle analysis of ice particle residuals from mountain-top mixed-phase clouds using laboratory derived particle type assignment, Atmos. Chem. Phys., 17(1), 575–594, doi:10.5194/acp-17-575-2017, 2017.

Schneider, J., Freutel, F., Zorn, S. R., Chen, Q., Farmer, D. K., Jimenez, J. L., Martin, S. T., Artaxo, P., Wiedensohler, A. and Borrmann, S.: Mass-spectrometric identification of primary biological particle markers and application to pristine submicron aerosol measurements in Amazonia, Atmos. Chem. Phys., 11, 11415–11429, doi:10.5194/acp-11-11415-2011, 2011.

Silva, P. and Prather, K.: Interpretation of mass spectra from organic compounds in aerosol time-of-flight mass spectrometry, Anal. Chem., 72(15), 3553–62 [online] Available from: http://www.ncbi.nlm.nih.gov/pubmed/10952542, 2000.

Silva, P. J.: Source Profiling and Apportionment of Airborne Particles: A New Approach Using Aerosol Time-of-Flight Mass Spectrometry, University of California, Riverside., 2000.

Silva, P. J., Prather, K. A. and Noble, C. A.: Size and Chemical Characterization of Individual Particles Resulting from Biomass Burning of Local Southern California Species Size and Chemical Characterization of Individual Particles Resulting from Biomass Burning of Local Southern California Species, Environ. Sci. Technol., 33(18), 3068–3076, doi:10.1021/es980544p, 1999.

Silva, P. J., Carlin, R. a and Prather, K. a: Single particle analysis of suspended soil dust from Southern California, Atmos. Environ., 34(11), 1811–1820, doi:10.1016/S1352-2310(99)00338-6, 2000.

Smith, D. L., Schram, K. H. and Mccloskey, J. A.: The Negative Ion Mass Spectra of Selected Nucleosides, Biomed. Mass Spectrom., 10(4), 269–275, doi:10.1002/bms.1200100407, 1983.

Song, X. H., Hopke, P. K., Fergenson, D. P. and Prather, K. a.: Classification of single particles analyzed by ATOFMS using an artificial neural network, ART-2A, Anal. Chem., 71(4), 860–865, doi:10.1021/ac9809682, 1999.

Srivastava, A., Pitesky, M. E., Steele, P. T., Tobias, H. J., Fergenson, D. P., Horn, J. M., Russell, S. C., Czerwieniec, G. A., Lebrilla, C. B., Gard, E. E. and Frank, M.: Comprehensive assignment of mass spectral signatures from individual Bacilluss atrophaeus spores in matrix-free laser desorption/ionization bioaerosol mass spectrometry, Anal. Chem., 77(10), 3315–3323, doi:10.1021/ac048298p, 2005.

Steele, P. T., Tobias, H. J., Fergenson, D. P., Pitesky, M. E., Horn, J. M., Czerwieniec, G. a, Russell, S. C., Lebrilla, C. B., Gard, E. E. and Frank, M.: Laser power dependence of mass spectral signatures from individual bacterial spores in bioaerosol mass spectrometry, Anal. Chem., 75(20), 5480–5487, doi:10.1021/ac034419u, 2003.

Steele, P. T., Srivastava, A., Pitesky, M. E., Fergenson, D. P., Tobias, H. J., Gard, E. E. and Frank, M.: Desorption/ionization fluence thresholds and improved mass spectral consistency measured using a flattop laser profile in the bioaerosol mass spectrometry of single Bacillus endospores, Anal. Chem., 77(22), 7448–7454, doi:10.1021/ac051329b, 2005.

Strzelecka, D., Chmielinski, S., Bednarek, S. and Jemielity, J.: Analysis of mononucleotides by tandem mass spectrometry : investigation of fragmentation pathways for phosphate- and ribose-modified nucleotide analogues, Sci. Rep., (May), 17–23, doi:10.1038/s41598-017-09416-6, 2017.

Sultana, C. M., Al-Mashat, H. and Prather, K. A.: Expanding Single Particle Mass Spectrometer Analyses for the Identification of Microbe Signatures in Sea Spray Aerosol, Anal. Chem., 89(19), 10162–10170, doi:10.1021/acs.analchem.7b00933, 2017a.

Sultana, C. M., Cornwell, G. C., Rodriguez, P. and Prather, K. A.: FATES: a flexible analysis toolkit for the exploration of single-particle mass spectrometer data, Atmos. Meas. Tech., 10(4), 1323–1334, doi:10.5194/amt-10-1323-2017, 2017b.

Sultana, C. M., Collins, D. B. and Prather, K. A.: The Effect of Structural Heterogeneity in Chemical Composition on Online Single Particle Mass Spectrometry Analysis of Sea Spray Aerosol Particles, Environ. Sci. Technol., doi:10.1021/acs.est.6b06399, 2017c.

Sun, J. and Ariya, P. A.: Atmospheric organic and bio-aerosols as cloud condensation nuclei (CCN): A review, Atmos. Environ., 40(5), 795–820, doi:10.1016/j.atmosenv.2005.05.052, 2006.

Suski, K. J., Hill, T. C. J., Levin, E. J. T., Miller, A., DeMott, P. J. and Kreidenweis, S. M.: Agricultural harvesting emissions of ice-nucleating particles, Atmos. Chem. Phys., 18(18), 13755–13771, doi:10.5194/acp-18-13755-2018, 2018.

Thomson, D. S., Middlebrook, A. M. and Murphy, D. M.: Thresholds for laser-induced ion formation from aerosols in a vacuum using ultraviolet and vacuum-ultraviolet laser wavelengths, Aerosol Sci. Technol., 26(6), 544–559, doi:10.1080/02786829708965452, 1997a.

Thomson, D. S., Middlebrook, A. M. and Murphy, D. M.: Thresholds for Laser-Induced Ion Formation from Aerosols in a Vacuum Using Ultraviolet and Vacuum-Ultraviolet Laser Wavelengths, Aerosol Sci. Technol., 26(6), 544–559, doi:10.1080/02786829708965452, 1997b.

Tobias, H. J., Schafer, M. P., Pitesky, M., Fergenson, P., Horn, J., Frank, M., Eric, E., Fergenson, D. P. and Gard, E. E.: Bioaerosol Mass Spectrometry for Rapid Detection of Individual Airborne Mycobacterium tuberculosis H37Ra Particles Bioaerosol Mass Spectrometry for Rapid Detection of Individual Airborne Mycobacterium tuberculosis H37Ra Particles, Appl. Environ. Microbiol., 71, 6086–6095, doi:10.1128/AEM.71.10.6086, 2005.

Tobias, H. J., Pitesky, M. E., Fergenson, D. P., Steele, P. T., Horn, J., Frank, M. and Gard, E. E.: Following the biochemical and morphological changes of Bacillus atrophaeus cells during the sporulation process using Bioaerosol Mass Spectrometry, J. Microbiol. Methods, 67, 56–63, doi:10.1016/j.mimet.2006.03.001, 2006.

Tobo, Y., Demott, P. J., Hill, T. C. J., Prenni, A. J., Swoboda-Colberg, N. G., Franc, G. D. and Kreidenweis, S. M.: Organic matter matters for ice nuclei of agricultural soil origin, Atmos. Chem. Phys., 14(16), 8521–8531, doi:10.5194/acp-14-8521-2014, 2014.

Toprak, E. and Schnaiter, M.: Fluorescent biological aerosol particles measured with the Waveband Integrated Bioaerosol Sensor WIBS-4: Laboratory tests combined with a one year field study, Atmos. Chem. Phys., 13(1), 225–243, doi:10.5194/acp-13-225-2013, 2013.

Twohy, C. H., McMeeking, G. R., DeMott, P. J., McCluskey, C. S., Hill, T. C. J., Burrows, S. M., Kulkarni, G. R., Tanarhte, M., Kafle, D. N. and Toohey, D. W.: Abundance of fluorescent biological aerosol particles at temperatures conducive to the formation of mixed-phase and cirrus clouds, Atmos. Chem. Phys., 16(13), 8205–8225, doi:10.5194/acp-16-8205-2016, 2016.

Varmuza, K., Werther, W., Krueger, F. R., Kissel, J. and Schmid, E. R.: Organic substances in cometary grains : comparison of secondary ion mass spectral data and californium-252 plasma desorption data from reference compounds, Int. J. Mass Spectrom., 189, 79–92, 1999.

Wade, E. E., Farquar, G. R., Steele, P. T., McJimpsey, E. L., Lebrilla, C. B. and Fergenson, D. P.: Wavelength and size dependence in single particle laser aerosol mass spectra, J. Aerosol Sci., 39(8), 657–666, doi:10.1016/j.jaerosci.2008.03.007, 2008.

Wenzel, R. J. and Prather, K. A.: Improvements in ion signal reproducibility obtained using a homogeneous laser beam for on-line laser desorption/ionization of single particles, Rapid Commun. Mass Spectrom., 18, 1525–1533, doi:10.1002/rcm.1509, 2004.

Woods, E. I., Smith, G. D., Miller, R. E. and Baer, T.: Depth Profiling of Heterogeneously Mixed Aerosol Particles Using Single-Particle Mass Spectrometry, Anal. Chem., 74(7), 1642–1649, 2002.

Wright, T. P. and Petters, M. D.: The role of time in heterogeneous freezing nucleation, J. Geophys. Res. Atmos., 118(9), 3731–3743, doi:10.1002/jgrd.503652013, 2013.

Wright, T. P., Hader, J. D., McMeeking, G. R. and Petters, M. D.: High relative humidity as a trigger for widespread release of ice nuclei, Aerosol Sci. Technol., 48(11), i–v, doi:10.1080/02786826.2014.968244, 2014a.

Wright, T. P., Hader, J. D., McMeeking, G. R. and Petters, M. D.: High Relative Humidity as a Trigger for Widespread Release of Ice Nuclei, Aerosol Sci. Technol., 48(11), i–v, doi:10.1080/02786826.2014.968244, 2014b.

Zawadowicz, M. A., Froyd, K. D., Murphy, D. M. and Cziczo, D. J.: Improved identification of primary biological aerosol particles using single particle mass spectrometry, Atmos. Chem. Phys., 17, 7193–7212, doi:10.5194/acp-2016-1119, 2017.

Zelenyuk, A., Juan, Y., Chen, S., Zaveri, R. A., Imre, D., Yang, J., Song, C., Zaveri, R. A. and Imre, D.: "Depth-profiling" and quantitative characterization of the size, composition, shape, density, and morphology of fine particles with SPLAT, a single-particle mass spectrometer, J. Phys. Chem. A, 112(4), 669–671, doi:10.1021/jp077308y, 2008.

Zender, C. S.: Quantifying Mineral Dust Mass Budgets: Terminology, Constraints, and Current Estimates, Eos (Washington. DC)., 85(48), 509–512, doi:10.1029/2003JD003483, 2004.

Chapter 5. Direct on-line mass spectrometry measurements of ice nucleating particles at a coastal site

5.1 Abstract

The formation of ice in clouds can strongly impact cloud properties and precipitation processes occurring in storms, including atmospheric rivers. Sea spray aerosol (SSA) particles are relatively inefficient as ice nucleating particles (INPs) compared to mineral dust. However, due to the vast coverage of the Earth's surface by the oceans, a number of recent studies have focused on identifying sources of marine INPs, particularly in regions lacking a strong influence from dust aerosol. This study describes the integration, validation and application of a system coupling a continuous flow diffusion chamber with a single particle mass spectrometer using a pumped counterfow virtual impactor to remove un-activated particles. In-situ measurements of immersion freeing INP composition were made at a coastal site in California using the integrated system. Mineral dust particles were the most abundant ice crystal residual type during the sampling period. SSA were more abundant in ambient measurements but represented only a minor portion of the ice crystal residual population at -30 °C. Notably, the SSA particles that activated were enriched with organic-nitrogen species that were likely transferred from the ocean. Calculations of ice nucleation active site densities were within good agreement with previous studies of mineral dust and SSA.

5.2 Introduction

Atmospheric aerosol particles capable of initiating heterogeneous ice nucleation, ice nucleating particles (INPs), are rare but play an important role in affecting the amount, type, and spatial distribution of precipitation (Fan et al., 2014; Fan et al., 2017; Ralph et al., 2016). Atmospheric rivers (ARs) are long and narrow storm systems which are typified by strong

horizontal vapor transport (Zhu & Newell, 1998). ARs are particularly important in California, because two or three ARs can account for half of the state's annual water budget (Dettinger et al., 2011) in addition to being responsible for flooding events on the west coast of the U.S (Dettinger et al., 2011). INP formation and subsequent cloud microphysical processes are possible factors that have been hypothesized to positively affect precipitation totals in ARs (Ault et al., 2011). While local and long-range transported aerosols can be important sources of INPs, landfalling ARs also bring in marine and coastal airmasses with their own distinct aerosol populations (Creamean et al., 2013). This study investigates the INP populations present in marine and coastal air masses that may influence ARs.

Previous studies of INPs in marine environments suggest that elevated INP concentrations could be correlated to regions of ocean water upwelling and high biological activity (Bigg, 1973; Schnell & Vali, 1976). These findings have been supported in laboratory studies of nascent marine INPs, in which increases in INP activity were observed during phytoplankton blooms (DeMott et al., 2016; McCluskey et al., 2017; McCluskey et al., 2018a) and in measurements of marine phytoplankton and exudates (Knopf et al., 2011; Wilson et al., 2015). Sea spray aerosol (SSA) composition is a complex mixture of inorganic salts, particulate organics (including bacteria and viruses), and organic matter found in the ocean (Cochran et al., 2017a; Cochran et al., 2017b). An observed increase in SSA ice nucleation (IN) activity has been attributed to either microbes (McCluskey et al., 2018a) or surface-active molecules such as proteins or long-chain fatty acids (DeMott et al., 2018; McCluskey et al., 2018a; Wilson et al., 2015). McCluskey et al. (2018b) identified a period of elevated heat-labile INP concentrations in pristine marine air associated with elevated marine organic aerosol arising from the North Atlantic Ocean. Other measurements of INPs at coastal sites concluded that local terrestrial bioaerosol and dust were the major sources of

INPs with little evidence for marine sources of INPs (Mason et al., 2015). INP measurements collected at a coastal site in the Arctic suggested that the major source of INPs were dust and primary marine aerosol (Creamean et al., 2018). However, all of these studies lacked direct measurements that conclusively identified the composition of individual INPs.

Typically, 1 in 10^5 atmospheric particles in the free troposphere acts as an INP at -30 ºC (DeMott et al., 2010). Therefore, bulk aerosol chemistry measurements are insensitive to INP composition. In this work, we follow from previous studies that have devised a methodology to measure INP composition using single particle mass spectrometry (Cziczo et al., 2003; DeMott et al., 2003). An aerosol time-of-flight mass spectrometer (ATOFMS), which provides real-time, size-resolved chemical composition of individual particles (Gard et al., 1997), was coupled to a continuous flow diffusion chamber (CFDC) which measures INP concentrations in real-time by creating a cold, humid environment where INPs can nucleate into ice crystals (Rogers, 1988). In a CFDC, ice crystals are grown to exceed the sizes of other aerosols as the means of differentiating the numbers of INPs in a volume of air. Connecting the CFDC and ATOFMS with a pumped counterflow virtual impactor (PCVI), which separates particles on the basis of inertia (Boulter et al., 2006; Kulkarni et al., 2011), allows for the selective measurement of ice crystal residuals (the INPs) without interference from non-INPs. Coupling a CFDC to a single particle mass spectrometer such as the ATOFMS to sample INP composition has never been done in a marine or coastal environment (Corbin et al., 2012; Cziczo et al., 2003; DeMott et al., 2003; Gallavardin et al., 2008; Murphy et al., 2007; Richardson et al., 2007).

This paper describes the development and characterization of this integrated instrumental configuration for the real-time characterization of INPs. This technique was subsequently applied to INP composition at the University of California, Davis Bodega Marine Laboratory from

February 12-19, 2015. The CFDC was operated in order to nucleate INPs through the immersion/condensation freezing mode, which is the most relevant ice nucleation mechanism for mixed-phase clouds such as those found in winter orographic storms in California. Instrument configurations, validation experiments, and the field campaign are detailed in Section 5.3. Results from the validation experiments and field measurements are presented and discussed in Section 5.4, while Section 5.5 provides a short summary.

5.3 Materials and methods

This work focuses upon integrating a CFDC with an ATOFMS and a PCVI to characterize INPs in both lab and field experiments. Here we provide a short overview of the materials and methods to clarify what was done. The operation and data analysis of the CFDC and the ATOFMS will be described in Sections 5.3.1 and 5.3.2 respectively, while a description of the integration of the two instruments using a PCVI to separate out un-activated particles, and an overview of validation experiments are given in Section 5.3.3 (results for these experiments are in Section 5.4.1). Section 5.3.4 details the measurements taken at a coastal site in California during February 2015. Finally, Section 5.3.5 describes ice nucleation active site densities for dust and SSA using the integrated CFDC-PCVI-ATOFMS and an APS.

5.3.1 CFDC operation

The Colorado State University (CSU) CFDC (Rogers, 1988; Eidhammer et al., 2010) was used to make real-time INP concentration measurements. The CSU-CFDC is a vertically mounted system with cylindrical walls 1.1 cm apart. The walls are chemically treated to be wettable by water, and each cylindrical column is independently temperature controlled. To form a thin layer of ice on each wall, the annular gap is flooded with water while each wall is held at approximately -27 °C. After icing, aerosols are introduced into the annular gap via flow through a cylindrical

knife edge inlet, which is surrounded by a dry, particle-free sheath flow. Both the knife edge and the sheath flow focus the minor aerosol flow into a lamina, where the temperature and relative humidity with respect to water (RH_w) can be controlled by controlling the temperature of each cylindrical column. For immersion-mode freezing experiments, the wall temperatures were set to sample RH_w of nominally 105% to ensure that aerosol activate into droplets. Those droplets that contain INPs at the aerosol lamina temperature or warmer nucleate to form ice. The bottom third of the CSU-CFDC is the droplet-evaporation section, where the ice-coated walls are held at the same temperature. Here, the aerosol lamina adjusts toward ice saturation, and is therefore water subsaturated. Thus, droplets will evaporate in this section and ice crystals will persist. All particles larger than ~500 nm are detected by an optical particle counter at the bottom of the evaporation section. Under the conditions in these experiments, ice crystals are assumed to be larger than 3.0 μm based on expected growth rates of ice particles and previous observations of the ice crystal size mode. The CFDC was operated for this study with a 1.5 μm impactor in front of the inlet in order to ensure that large aerosol particles were not erroneously counted as INPs.

Methods for accounting for CFDC measurement uncertainty and background follow previous work (Schill et al., 2016) and are summarized here. Number concentrations of INPs (N_{INPs}) and particles larger than 500 nm (N_{500}) were determined for 3-5 minute subsampling period within a given sampling period. Standard error associated with N_{INPs} and N_{500} were determined following Poisson counting statistics (Taylor, 1997). Periods between sampling were dedicated to measuring background concentrations by measuring filtered air. Background N_{INPs} and N_{500} were determined by calculating a time-weighted average of the filter periods before and after the sampling period. This value was subtracted from the sample N_{INPs} and N_{500} and the standard errors

were added in quadrature. Statistically significant N_{INPs} were defined herein as those that were higher than the background concentration plus two times the standard deviation.

An aerosol concentrator (Model 4240, MSP Corporation; Romay et al., 2002) was placed upstream of the CFDC to improve INP sampling statistics, as described in Tobo et al. (2013). Enhancements in aerosol concentrations are obtained in this concentrator using virtual impactors which affect only particles with diameters larger than 0.5 μm. In previous studies, the enhancement factor for aerosol particles varied from 10 at 0.5 microns up to about 140 at diameters above 1 μm (Tobo et al., 2013). Following Tobo et al. (2013), the INP concentration factor (ICF) for INPs was defined using the ratio of N_{INP} sampling with versus without the concentrator, as measured within 15 minutes before or after the 3-5 minute subsampling period. N_{INPs} measured without the concentrator were often not statistically significantly different from background concentrations and the calculated ICFs were highly variable from day to day with an average and standard deviation of 7.7±10.2. Therefore, an ICF was calculated for each subsampling period when possible (i.e., when N_{INP} were statistically significant) and a daily mean and standard deviation of ICF was used for other subsampling periods. Daily ICFs ranged from 1.2 to 22.9, lower than previous studies (e.g., 90±3, Suski et al., 2018) due to changes in the concentrator performance experienced during this study. Standard error associated with the ICF was propagated in the final N_{INP}, calculated by dividing the subsample N_{INP} by the ICF.

5.3.2 ATOFMS operation and analysis

Size-resolved single particle mixing state was measured using an ATOFMS (Gard et al., 1997). Single particle mass spectra and size data were imported into Matlab (The MathWorks, Inc.) and analyzed via the software toolkit FATES (Sultana et al., 2017). Particles were divided into clusters based on their mass spectral features via an adaptive neural network and recombined

based upon their characteristic mass spectra and size distributions (Rebotier & Prather, 2007; Song et al., 1999). Similar to previous field studies using ATOFMS analysis (Cahill et al., 2012; Pratt & Prather, 2010; Sullivan et al., 2007), particle types were manually re-grouped upon inspection of the clusters based on spectral similarities. Particle type number, fraction, and standard error of measurement for each particle type are shown in Table 5.1, while representative spectra of the 8 particle types detected in this study are shown in Figure 5.1. The characteristic ion markers for all types and assignments from the literature are given in Table 5.1.

5.3.3 PCVI integration with the coupled CFDC-ATOFMS

Prior to the field study, initial optimization experiments integrating the CFDC and the ATOFMS with the PCVI were conducted prior to the field study at CSU in Fort Collins, CO. Block diagrams for the instrumental setup and the flow configuration are shown in Figure 5.2. The flows of the PCVI (Brechtel Manufacturing Inc., Model 8100) were optimized in order to eliminate transmission of particles with aerodynamic diameters (D_a) below 3 μm. The pull flow of the PCVI was set to 12 vlpm while the chilled counterflow was set to 6 vlpm. The transmission efficiency (TE) of the PCVI (Figure 5.3), was determined by atomizing ammonium sulfate ($(NH_4)_2SO_4$) particles through the PCVI into an Aerodynamic Particle Sizer (APS; TSI 3321). Transmission efficiencies were calculated for particles with diameters larger than 500 nm by determining the ratio of number of particles detected over a five minute period without the PCVI to the number of particles detected over a five minute period with the PCVI. The TE of particles larger than 3 μm was $5x10^{-3} \pm 11\%$. Particles smaller than 500 nm were not measured due to the lower size limit of the ATOFMS. The ATOFMS-specific TE, (described more in Section 5.3.2) is also shown in Fig. 5.3 (green line). Diameters for the 10th, 25th, and 50th percentile (D_{10}, D_{25}, and D_{50}) were calculated using the maximal measured TE (0.05 at 5 μm). Additional validation experiments were

conducted using Arizona Test Dust (ATD) suspended from a fluidized bed, and atomized $(NH_4)_2SO_4$. For some of these experiments, aerosol size distributions were measured using an APS. The results of these experiments are detailed in Section 5.4.1.

5.3.4 Sampling location and selection of control periods

The CalWater-2015 field campaign was conducted in order to better understand how aerosols interact with landfalling ARs in the western United States and influence precipitation amount, phase, and spatial distributions (Ralph et al., 2016). As part of this effort, ground-based measurements and air samples were collected from January 14, 2015 to March 9, 2015 at Bodega Marine Laboratory (BML, 38° 19'N, 123° 4') in Bodega Bay, California (Martin et al., 2017). The sampling site at BML included two instrumented trailers located ~100 m ENE of the seashore. Aerosol composition, INP concentrations, and APS size distributions were measured in a trailer operated by the University of California, San Diego (UCSD).

The TE for the ATOFMS was determined via comparison with an APS during ambient sampling at BML. Distributions of ambient aerosol aerodynamic diameter are measured by the APS and the average number of particles per bin, per unit volume are calculated ($N_{APS,i}$). ATOFMS, size-resolved data is binned using the APS size bins and the average number of particles per bin, per unit volume are calculated ($N_{ATOFMS,i}$). The TE of a given size bin (TE_i) is thus given by

$$TE_i = \frac{N_{ATOFMS,i}}{N_{APS,i}} \quad (1)$$

Wind speed and direction were determined using a 10m surface meteorology tower was located ~100 m North of the two trailers and operated by the Earth System Research Laboratory, National Oceanic and Atmospheric Administration.

The CFDC-PCVI-ATOFMS system was used to measure the composition of INPs. The CFDC was operated at approximately -30 ºC. This temperature is typical of the upper levels (6-10 km) of deep orographic clouds that form over the Sierra Mountains in California (Creamean et al., 2016). Additionally, due to the low sampling efficiency of this system, the CFDC was operated in order to maximize the number of ice crystals created (i.e., at a lower temperature to favor higher INP concentrations). INP composition was measured for a few hours each day, from February 12-19, 2015 (hereafter referred to as the INP_{-30} sampling period). Time periods immediately before and after INP_{-30} sampling were selected for comparison based upon the wind directions and speeds during INP_{-30} sampling, indicating they were of the same airmass (hereafter ambient). Ambient periods totaled 30 hours and 6 minutes, during which the composition of 39,314 individual particles were measured with the ATOFMS. A complete listing of sampling periods can be found in Table 5.2. Figure 5.4a shows the time series of wind direction and wind speeds during the INP_{-30} sampling periods (red boxes) and the ambient sampling periods (black boxes). Wind rose plots for the composite sampling periods also show that the conditions were very similar for ambient (Fig. 5.4b) and INP_{-30} (Fig. 5.4c) sampling. It should be noted that from Feb-12 to Feb-17, BML experienced a persistent land/sea breeze pattern and while the airmasses measured here were primarily onshore, they likely contained a moderate influence from terrestrial particles.

5.3.5 Calculation of active site density

The active site density (n_s, expressed here as m^{-2}) for INPs can be expressed as the number concentration of INPs (N_{INP}) per particle surface area per unit volume (S):

$$n_s = \frac{N_{INP}}{S} \quad (2)$$

This calculation is typically applied to single INP species and this approach requires either laboratory studies in which a single particle type can be characterized (Niemand et al., 2012) or

ambient airmasses dominated by a single particle type such that the n_s can be attributed to one particle type (McCluskey et al., 2018b; Price et al., 2018). Neither of these conditions apply to this dataset, so we use the integrated CFDC-PCVI-ATOFMS to separate the n_s for dust and SSA. $n_{s,dust}$ and $n_{s,SSA}$ can be defined as the following:

$$n_{s,dust} = \frac{N_{INP,dust}}{S_{dust}} \qquad n_{s,SSA} = \frac{N_{INP,SSA}}{S_{SSA}} \tag{3}$$

In this case, we assume that the number of dust INPs ($N_{INP,dust}$) and SSA INPs ($N_{INP,SSA}$) can be described via the following

$$N_{INP,dust} = N_{INP}\, f_{dust} \qquad N_{INP,SSA} = N_{INP}\, f_{SSA} \tag{4}$$

where N_{INP} is the number concentrations of INPs measured by the CFDC as discussed in Section 5.3.1 and f_{dust} and f_{SSA} are the fraction of INP_{-30} particles measured by the ATOFMS determined to be dust and SSA (see Table 5.3).

The total surface area (per unit volume) for a given particle class, S_x (i.e. S_{dust} or S_{SSA}), calculated from tandem measurements of the ATOFMS and APS, can be expressed as

$$S_x = \sum_{i=1}^{51} D_{p,x,i}^2\, \pi\, n_i f_{x,i} \tag{5}$$

where $D_{p,x,i}$ is the particle physical (spherical equivalent) diameter for that bin for particle class x, n_i is the number concentration of particles in that size bin (from measurements made by the APS during INP_{-30} sampling), and $f_{x,i}$ is the fraction of particles of a given particle class (from ambient measurements made by the ATOFMS) for that same size bin. $D_{p,x}$ can be calculated from the aerodynamic diameter, D_a, using the following

$$D_{p,x} = D_a \sqrt{\frac{\rho_o \chi_x}{\rho_x}} \tag{6}$$

where χ is the dynamic shape factor, and ρ_0 is the reference density (1 in this case), and ρ_x is the particle density. For our calculations we assumed that dust had a χ_x of 1.9 (Chou et al., 2008) and

a ρ_x of 2.65 g cm^{-3} (Kanji et al., 2013), SSA had a χ_x of 1.25 and a ρ_x of 2.2 g cm^{-3} (King et al., 2012).

While the ATOFMS can have composition-based biases due to matrix effects, these biases are unlikely to affect the calculation of n_s because the comparisons are within individual particle classes. In other words, because the ATOFMS's sensitivity to a specific particle type, x, would affect the calculation of both $N_{INP,x}$ and S_x, this sensitivity can effectively be discounted.

5.4 Results and discussion

5.4.1 Validation of CFDC and ATOFMS integration

The CFDC-PCVI system was validated by measuring transmission characteristics of a non-INP, $(NH_4)_2SO_4$, and a known ice nucleation active material, ATD particles, with an APS (Figure 5.5). The first set of experiments were conducted using $(NH_4)_2SO_4$ without the CFDC being iced in order to determine transmission of different sized particles through the PCVI as a function of flow parameters. This was done to optimize flows for assuring PCVI selection of only larger ice particles. Fig. 5.5a shows that for counterflows (CF) less than 6.0 vlpm, substantial numbers of $(NH_4)_2SO_4$ particles were measured by the APS at sizes below the desired PCVI cut-point diameter (3 μm). However, at a CF of 6.0 vlpm virtually no particles are transmitted, a sign that the system was working as intended. A second set of experiments using ATD particles were conducted to demonstrate proper transmission of known (activated) INPs with the CFDC set to operational temperature and water supersaturated conditions. The expected reduction or loss of INP activity of ATD at water subsaturation was also examined in proof of concept experiments. Fig. 5.5b shows that no particles were detected under subsaturated conditions (T = -32.8 ± 0.1 ºC, SS_w = -18.7 ± 0.2%) while under supersaturated conditions (T = -32.6 ± 0.1 ºC, SS_w = 8.4 ± 0.4%), particles were transmitted through to the APS. It should be noted that particles larger than the upstream impactor

(50% cutoff diameter of 1.5 μm) were transmitted through the PCVI under supersaturated conditions. These could be particles that still retained water as the APS was situated immediately after the PCVI with no active method applied to evaporate residual ice. It is unlikely to be large particles not being removed by the upstream impactor because no particles of these sizes were observed under subsaturated conditions.

This second experiment was repeated using the ATOFMS instead of the APS in order to ensure that particle composition could be measured with this instrumental configuration. Figure 5.6 shows the number of particles detected by the ATOFMS, as well as the number concentrations of total particles greater than 500 nm (N_{500}) and INPs measured by the CFDC (N_{INP}). During this experiment, CFDC chamber temperature was maintained between -27 and -28 °C while water supersaturation was maintained between 3-7% and then later reduced to <0%. Particles were observed by the ATOFMS only when the CFDC was supersaturated (early period in Fig. 5.5) and ice crystals were detected, indicating that the PCVI only transmitted ice crystal residues. A total of 12 particles were measured by the ATOFMS, while the CFDC detected 38,682 INPs during that same time interval, a detection efficiency of 3.10×10^{-4}.

A small percentage of particles below the PCVI cutpoint can get through the counterflow, which is known as breakthrough. Due to the scarcity of INPs in the atmosphere, this small amount of breakthrough particles can overwhelm the true INP signal and necessitates an aggressive approach for filtering out particles that are not INPs. A conservative counterflow for the PCVI was used to ensure that non-INPs were eliminated and only ice crystals were transmitted through the PCVI and into the ATOFMS. This conservative approach reduces the probability of false positives from breakthrough of smaller particles, but likely contributed to a poor transmission of INPs. Another contributing factor in the poor TE is the transmission efficiency of the ATOFMS which

at its peak is roughly ~1-5 for hit particles% (seen in Figure 5.3). As a result of these factors impacting the transmission and detection of INPs, the system is limited to measuring the composition of 1 INP for approximately every 2,000 INPs detected (INP detection efficiency of ~ $5x10^{-4}$).

5.4.2 Ambient and INP_{-30} composition at Bodega Marine Laboratory

The compositions of ambient particles and ice crystal residuals from the CFDC were measured using ATOFMS at BML (Figure 5.7). Sampling consisted of a total time of 16 hours and 28 minutes, during which the composition of 107 ice crystal residuals were measured. During this same time period 277,734 INPs were detected by the CFDC corresponding to a total detection efficiency of $3.85x10^{-4}$, comparable to the detection efficiency from the validation experiments ($3.10x10^{-4}$, see section 5.4.1 above). This detection efficiency is lower than the capture efficiency of the PCVI because of the total detection efficiency is also dependent upon the transmission efficiency of the ATOFMS, which at its peak is approximately 1-5% (Fig. 5.3). Approximately 85% of the ambient particles were classified as SSA (Figure 5.7a), which was unsurprising due the site's close proximity to the Pacific Ocean and on-shore flow observed during most of these sampling periods (Figure 5.4b). The other particle types measured during ambient sampling were dust (4.4%), elemental carbon (EC, 1.9%), Na/K (1.8%), biomass burning (BB, 1.8%), elemental carbon/organic carbon (ECOC, 0.8%), organic carbon (OC, 0.4%), and primary biological (Bio, 0.3%). These results are summarized in Table 5.3. It should be noted that the particle type percentage is partially a reflection of the ATOFMS transmission efficiency bias towards measuring larger particles (≥0.5 μm) and does not accurately provide the distribution of sources without proper scaling with auxiliary measurements of particle size and mass (Bhave et al., 2002; Qin et al., 2006).

The compositions of ice crystal residuals detected by the ATOFMS from all INP_{-30} periods were distinct from the dominant ambient particle types (Figure 5.7b). The most abundant INP particle type was dust which comprised 71% of all INP_{-30} particles while SSA was the second most abundant type at 15%. The Na/K (7%), Bio (5%), EC (2%), and OC (1%) particle types were minor contributors. Once again it should be noted that these results are biased towards types in the larger sizes due to the transmission efficiency of the ATOFMS. However, the size range of particles measured in this study (0.5-5.0 μm) overlaps well with the typical size range reported for previous INP size measurements (Kanji et al., 2017) and thus the resultant bias may be relatively minimal. BB and ECOC were not detected during INP_{-30} sampling periods. The efficiency with which particles nucleate ice can be determined by comparing the prevalence of a particle type in the ice residuals to their abundance during ambient periods. Here, we define the ice nucleation enrichment factor (EF) for a particle type using the following relationship:

$$EF = \frac{f_{INP}}{f_{ambient}} \quad (7)$$

where f_{INP} is the fraction of particles for a given type out of all INP particles and $f_{ambient}$ is the fraction of particles for a given type out of all ambient particles. The particle types with the highest EFs were the dust and biological types, with 14.2±0.7 and 13.7±1.3, respectively, while SSA was depleted with an EF of 0.2±0.0 (Figure 5.5c). The high EF values for dust and biological particles is consistent with previous reports of these particle types serving as effective INPs across a range of different temperatures (Atkinson et al., 2013; Boose et al., 2016b; Garcia et al., 2012; Huffman et al., 2013; Niemand et al., 2012; Knopf et al., 2011; Pratt et al., 2009; Stopelli et al., 2017). The depletion of SSA in ice crystal residuals is also consistent with reports showing that SSA particles have active site densities two to three orders of magnitude lower than mineral and soil dust (DeMott et al., 2016; McCluskey et al., 2018b). In general, the major source of INP_{-30} were

identified as mineral dust particles while the major source in ambient particles were identified as SSA.

While SSA may have been a relatively minor source of INPs during this study relative to dust, the ocean may indeed be an important source of INPs, particularly over the remote ocean (Burrows et al., 2013; Vergara-Temprado et al., 2017). SSA are mixtures of inorganic salts, particulate organics (including bacteria and viruses), and organic matter found in the ocean (Cochran et al., 2017a; Cochran et al., 2017b). ATOFMS ion markers for organic nitrogen and phosphate ($^{26}CN^-$, $^{42}CNO^-$, and $^{79}PO_3^-$) are elevated in SSA with higher amounts of bio-organic species (Lee et al., 2015). For particles of the same type, the relative peak area (RPA) for an ion marker qualitatively reflects the amount of that species within a given particle (Cahill et al., 2012). The colorstack plots in Figure 5.8 show the fraction of SSA particles (both ambient and INP_{-30}) with RPAs for these organic markers. These peaks were significantly elevated in SSA particles detected in ice crystal residuals when compared to ambient SSA. While some caution should be exercised when interpreting these results due to the low number of SSA particles measured during INP_{-30}, these results suggest that the organic species in SSA play an important role in their ability to act as INPs. The enrichment of organic markers in SSA measured by the ATOFMS is also consistent with field measurements collected at Mace Head Research Station (McCluskey et al., 2018b) which found elevated organic INPs during a marine-transport event. However, we found no evidence (such as mixing with salt species) that the primary biological particles detected in INP_{-30} were oceanic in origin. Interestingly, nearly 12% of dust particles detected in INP_{-30} contained markers indicative of sea salt ($^{81}Na_2Cl^+$ and $^{93}NaCl_2^-$). While we do not currently have a methodology or the capability to distinguish between dust resuspended from the ocean and dust

that becomes internally mixed with sea salt through in-cloud processing in the marine boundary layer, this warrants future study.

5.4.3 Atmospheric Implications

The most striking finding in this study is the prevalence of dust particles serving as INP_{-30}, despite the fact that the majority of ambient aerosols measured by the ATOFMS were SSA. Active site density (n_s) has previously been determined for a number of different particle sources, including mineral dust (Niemand et al., 2012; Ullrich et al., 2017) and SSA (DeMott et al., 2016; McCluskey et al., 2018b). While n_s has also been determined for ambient aerosol (Price et al., 2018) and in a few cases above where it was deemed that evidence strongly supported a dominance of one particle type, decomposing the relative contributions to the n_s from different particle sources in an externally mixed aerosol scenario has not been attempted previously. Figure 5.9 shows the n_s value calculated from the integrated CFDC-PCVI-ATOFMS results (see Section 5.3.5 for more details) for mineral dust (~10^{10} m^{-2}) and SSA (~$5x10^{8}$ m^{-2}). Also shown in Fig. 5.9 are parameterizations for dust (N12; Niemand et al., 2012) and SSA (M18; McCluskey et al., 2018b), as well as an exponential fit of n_s values for desert dust dominated airmasses (P18; Price et al., 2018). Our results for SSA, $n_{s,SSA}$, are in relatively good agreement with M18, within a factor of 3.8 (evaluated at -31.5 ºC, the median temperature for all INP measurements). Our results for dust active site density were within a factor of 6.8 of the N12 parameterization (also evaluated at -31.5 ºC). However, N12 was determined in a laboratory setting from a limited selection of dust types and may not accurately represent the ambient dust at Bodega Bay in 2015 due to the importance of both atmospheric aging (Boose et al., 2016a; Sullivan et al., 2010) and mineralogy (Atkinson et al., 2013; Boose, et al., 2016b) for the IN-activity of dust. Fig. 5.9 also shows an exponential fit of n_s of desert-dominated airmasses from Price et al. (P18; 2018). The CFDC-PCVI-ATOFMS

derived $n_{s,dust}$ (evaluated at -31.5 ºC) is within a factor of 1.4 of the P18 fit. This difference in activity could be due to mineralogy, atmospheric aging, or some combination thereof. We have not applied the correction factor noted by DeMott et al. (2015) when sampling mineral dust INPs, to account for the fact that the CFDC may not fully activate these INPs until instrument lamina RH values of up to 109% are used (105% nominal used in this study). DeMott et al. (2015) expressed that it was unclear if similar correction factors would apply to other INP types or to ambient INPs in general. The application of the DeMott et al. (2015) correction factor is indicated in Fig. 5.9 by an upper bar on the data point for mineral dust and shows that the N12 parameterization may describe the IN-activity of dust better than otherwise expected. This decomposition of active site densities to their sources highlight the importance of dust in the coastal boundary layer INP population at Bodega Bay during the period of observations in February 2015.

5.5 Conclusions

The Colorado State University CFDC was integrated with an ATOFMS using a PCVI to directly measure INP composition. Validation experiments confirmed that the ATOFMS only detected particles when the CFDC chamber was producing ice crystals, and the typical detection efficiency was 3.10×10^{-4}. The integrated system was deployed to measure INP_{-30} composition at a coastal site in Bodega Bay, California. Ice crystal residuals were enriched with dust particles compared to ambient measurements, which were dominated by SSA. Ice crystal residuals were also comprised of SSA and bioparticles, though in much lower abundance than dust. However, primary bioparticles were also enriched in INP_{-30} relative to ambient while SSA was not. The SSA particles found in the ice residual samples were found to be enriched in organic species relative to ambient SSA. While the IN-activity of SSA has previously been tied to organic species produced

by biological activity in lab (DeMott et al., 2016; McCluskey et al., 2018a) and field experiments (McCluskey et al., 2018b; Creamean et al., 2018) this is the first time that it has been directly measured in ambient particles. Finally, the active site density (n_s) for all, dust, and SSA particles were calculated using the combined data from the CFDC and ATOFMS. The SSA n_s agreed well with the ambient SSA parameterization from McCluskey et al. (2018a). The dust n_s may agree better with values estimated from ambient data on dust off of Africa (Price et al., 2018), compared to a laboratory-based parameterization (Niemand et al., 2012). The CFDC-PCVI-ATOFMS technique developed and validated in this study illustrates promise for determining the composition and sources of INPs in ambient environments due to its ability to classify individual particles as well as its ability to probe particle mixing state.

5.6 Acknowledgements

This research was supported by the Center for Aerosol Impacts on Chemistry of the Environment (CAICE), a National Science Foundation Center for Chemical Innovation, and the CalWater-2015 field campaign, funded by the National Science Foundation. The authors would also like to thank the UC Davis Bodega Marine Laboratory for the use of laboratory and office space and shipping and physical plant support while collecting data, as well as the California Air Resources Board for the trailer used for sampling. This research was funded by NSF award number 145147 (GC, KP) and NSF award number (1450760, CSM, SMK, PJD.

Chapter 5, in full, has been submitted for publication to Journal of Geophysical Research: Atmospheres. Printed with permission from Cornwell, G. C., M., McCluskey, C. S., Levin, E. J. T., Suski, K. J., DeMott, P. J., Kreidenweis, S. M., Prather, K. A. Direct on-line mass spectrometry measurements of ice nucleating particles at a California coastal site. The dissertation author was the primary investigator and author of this paper.

5.7 Figures

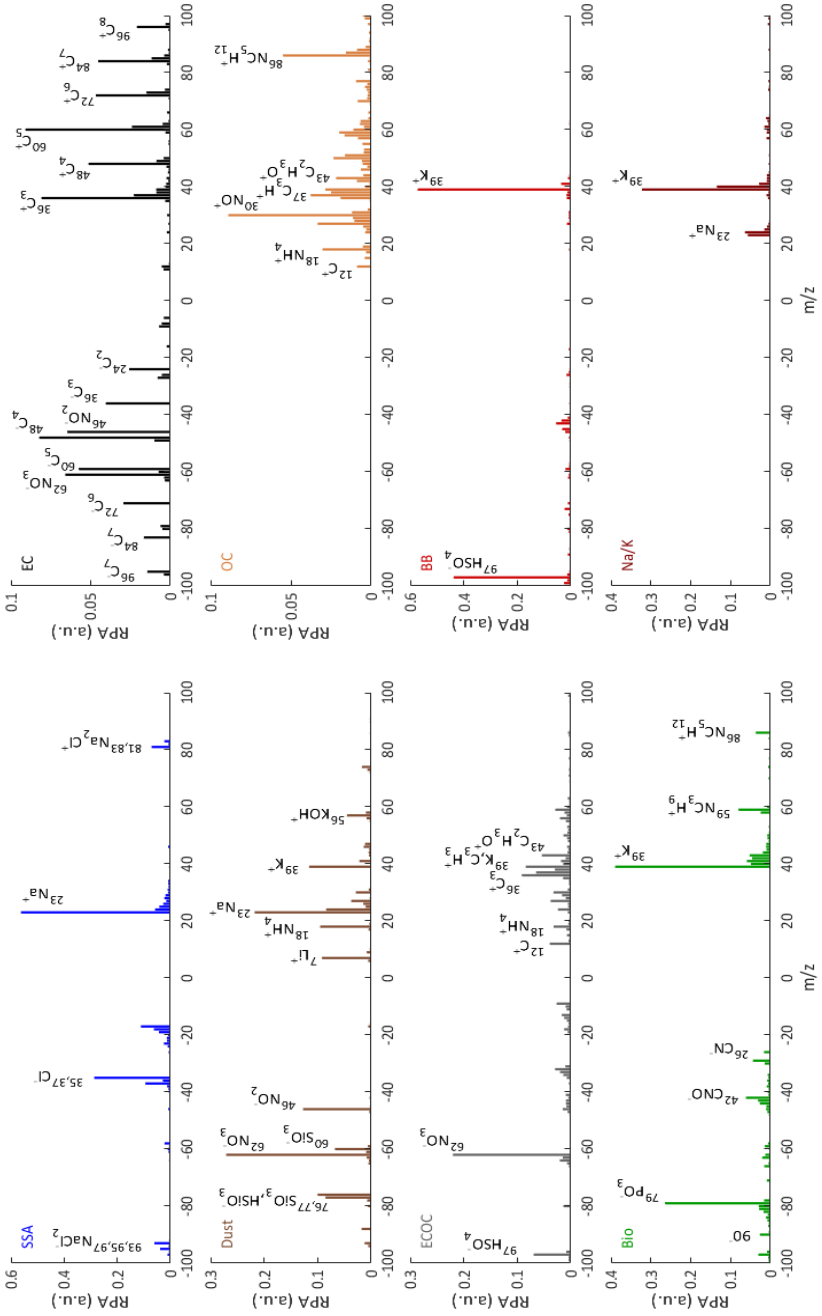

Figure 5.1. Representative spectra for the ATOFMS particle types observed during this study given in relative peak area (RPA): sea spray aerosol (SSA), dust, elemental carbon organic carbon (ECOC), primary biological (Bio), elemental carbon (EC), organic carbon (OC), biomass burning (BB), and Na/K.

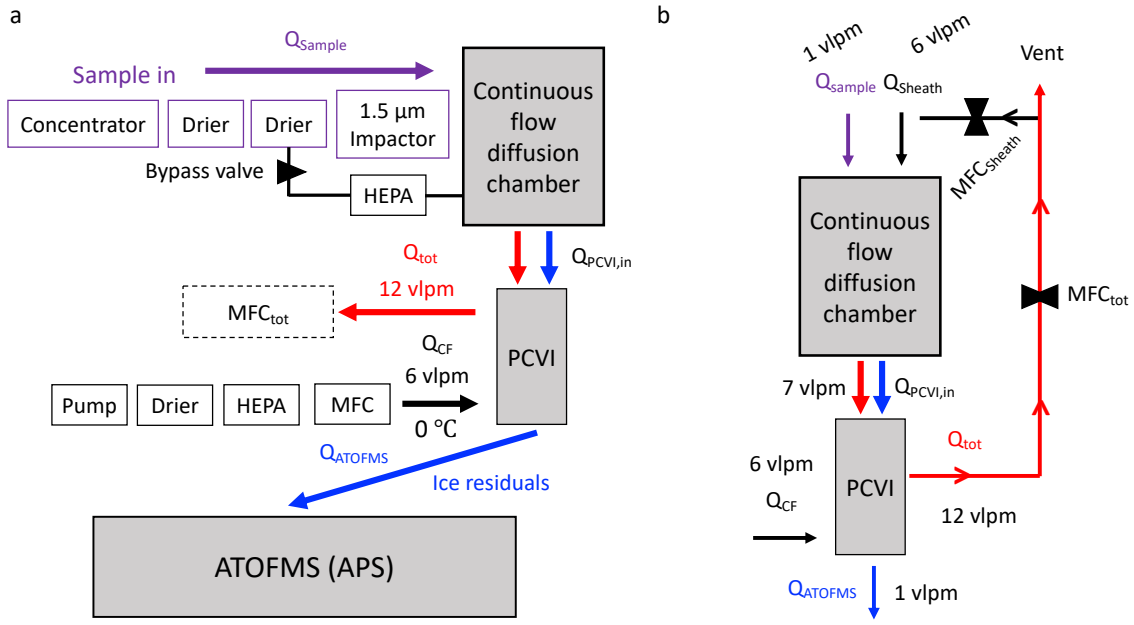

Figure 5.2. (a) Instrumental setup for the integrated CFDC-PCVI-ATOFMS system. Purple marks samples with both INPs and non-INPs in it. Blue denotes ice crystals while red marks ambient non-INPs. PCVI stands for pumped counterflow virtual impactor. ATOFMS stands for aerosol time-of-flight mass spectrometer, APS stands for aerodynamic particle sizer. MFC stands for mass flow controller, and HEPA stands for high efficiency particulate air filter. Q_{Sample}, Q_{Sheath}, $Q_{PCVI,in}$, Q_{tot}, Q_{CF}, and Q_{ATOFMS} are the flow rates of the sample, sheath, air into the PCVI, total CFDC flow, PCVI counterflow, and ATOFMS flow rate. (b) Detailed schematic of how flows were controlled during the integrated experiments.

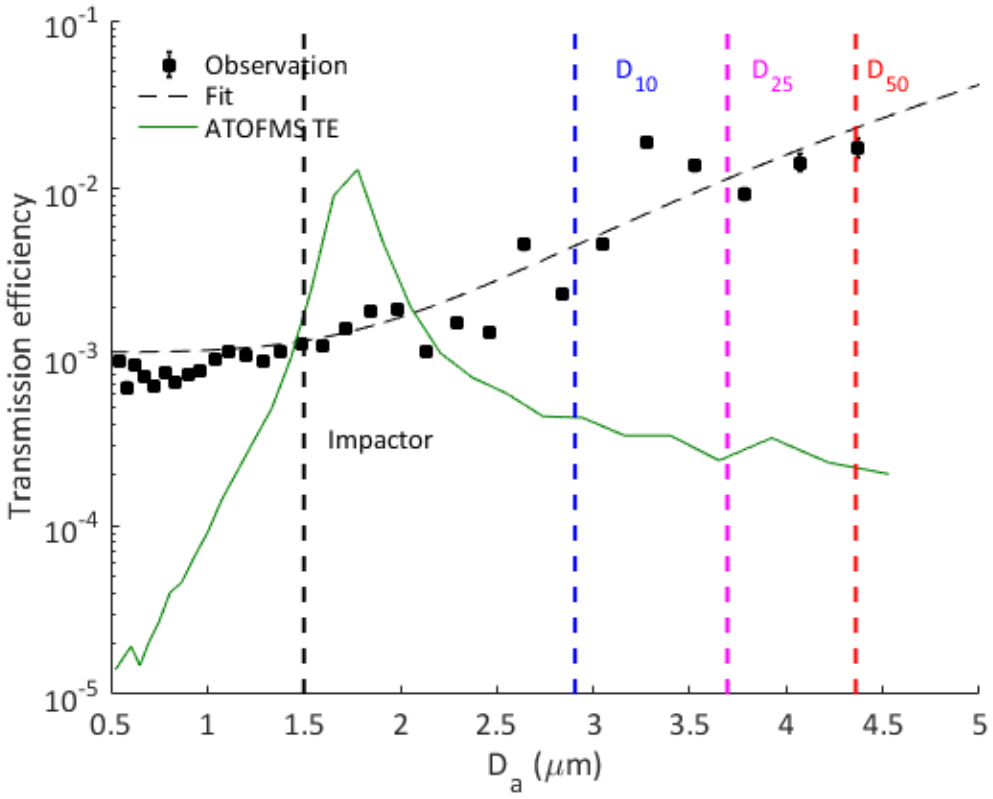

Figure 5.3. Transmission efficiency curve for the PCVI as a function of aerodynamic diameter (D_a). The green line shows the transmission efficiency for the ATOFMS. Observations are shown in the square markers, while the dashed black line shows the power law fit. The blue, purple, and red dashed lines show the diameters for the 10th, 25th, and 50th percentiles (D_{10}, D_{25}, and D_{50}) of the PCVI transmission efficiency. The dark grey dashed line shows the 1.5 µm impactor upstream of the continuous flow diffusion chamber (CFDC).

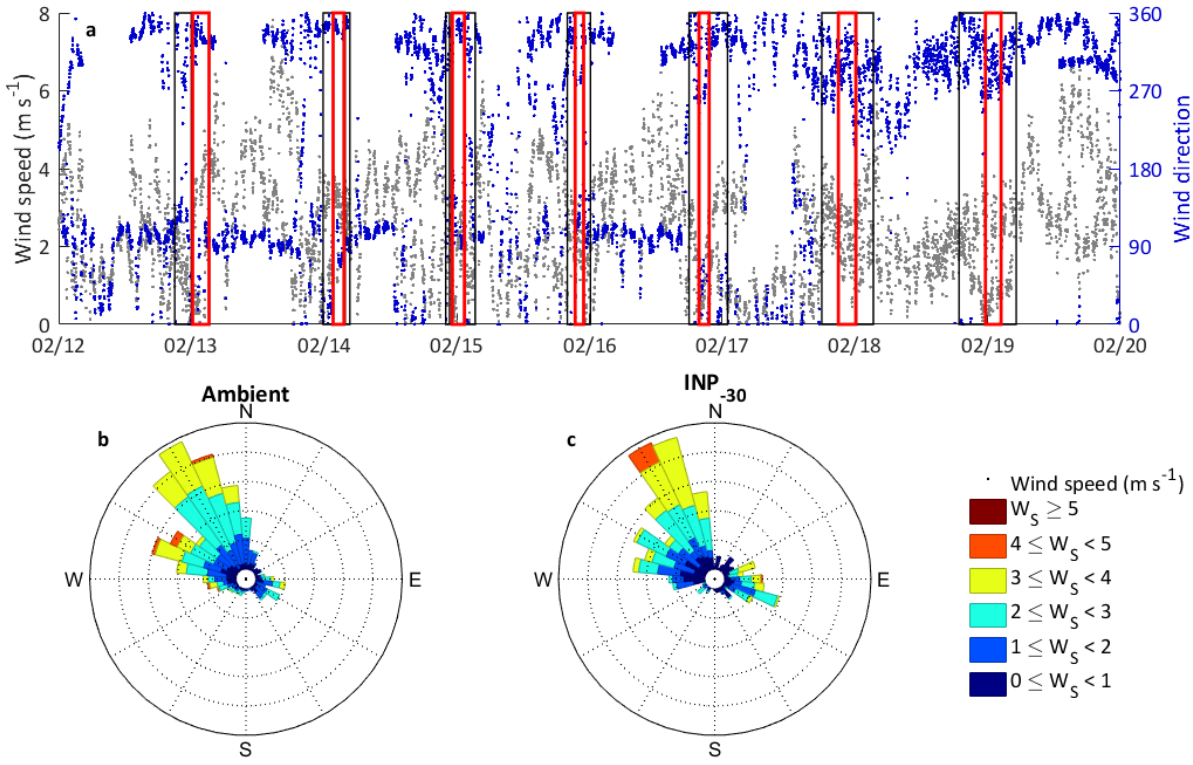

Figure 5.4. (a) Timeline of wind direction and speed from NOAA/ESRL surface meteorology station. Black boxes indicate ambient sampling periods while red boxes indicate INP_{-30} sampling periods. Wind rose for (b) ambient and (c) INP_{-30} sampling periods.

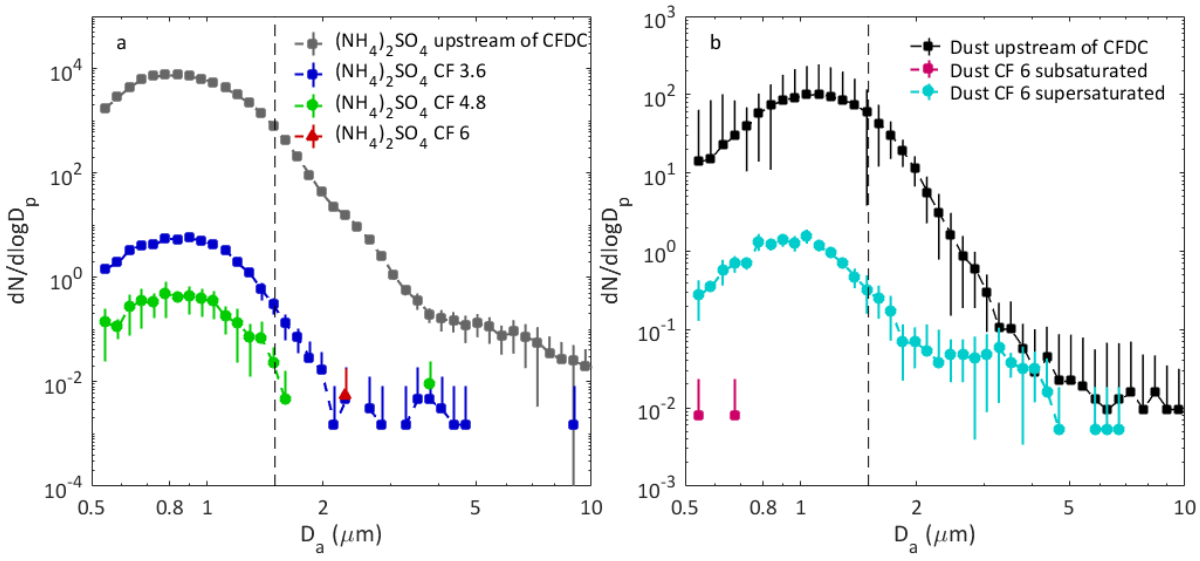

Figure 5.5. APS number size distributions ($dN/dlogD_p$) measured through the CFDC and PCVI during validation experiments: (a) testing transmission of particles with different counterflows (CF) with $(NH_4)_2SO_4$ and (b) testing transmission of ice crystals formed from ATD in subsaturated and supersaturation conditions. Measurements of controls for both experiments were collected upstream of the CFDC (and its 1.5 µm 50% cut-size impactor, indicated by the dashed line). Error bars indicate the standard deviation.

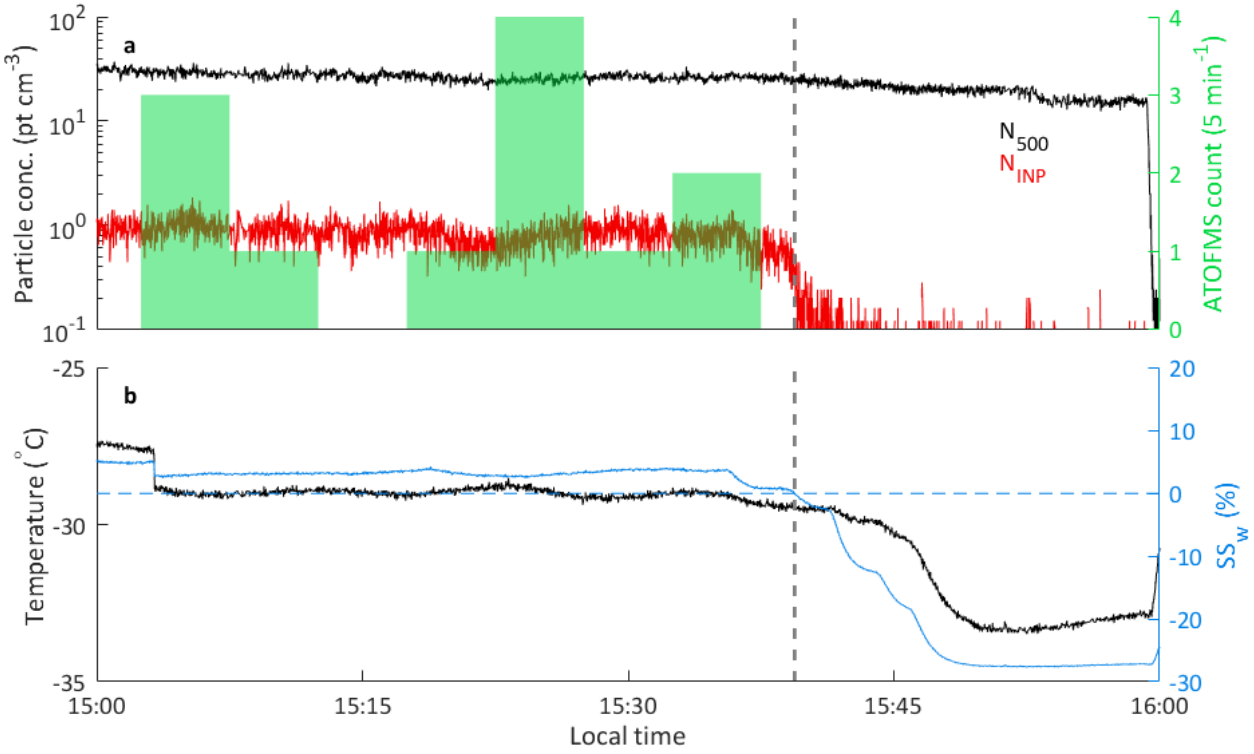

Figure 5.6. Validation experiment for the integrated CFDC-PCVI-ATOFMS system. (a) Timeline of CFDC-derived concentrations for N_{500} (black) and N_{INP} (red), calculated at 1 Hz, as well as the number of particles detected by the ATOFMS every five minutes (green bars). (b) shows the CFDC chamber temperature (black) and supersaturation with respect to water (SS_w; blue). The grey dashed lines correspond to the time when $SS_w = 0$. The blue dashed line shows $SS_w = 0$.

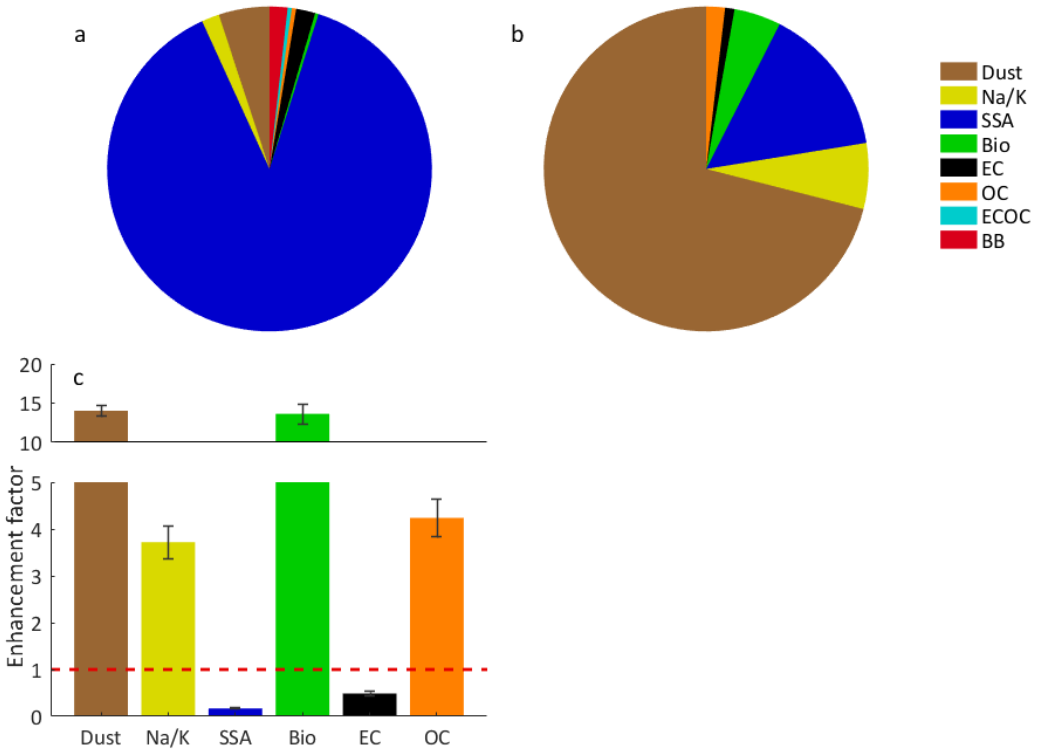

Figure 5.7. ATOFMS particle type fraction for (a) ambient and (b) INP_{-30}. (c) shows the enhancement factor for each particle type detected during INP_{-30} (see Table 5.3). The dashed red line shows the 1:1 line corresponding to no enrichment.

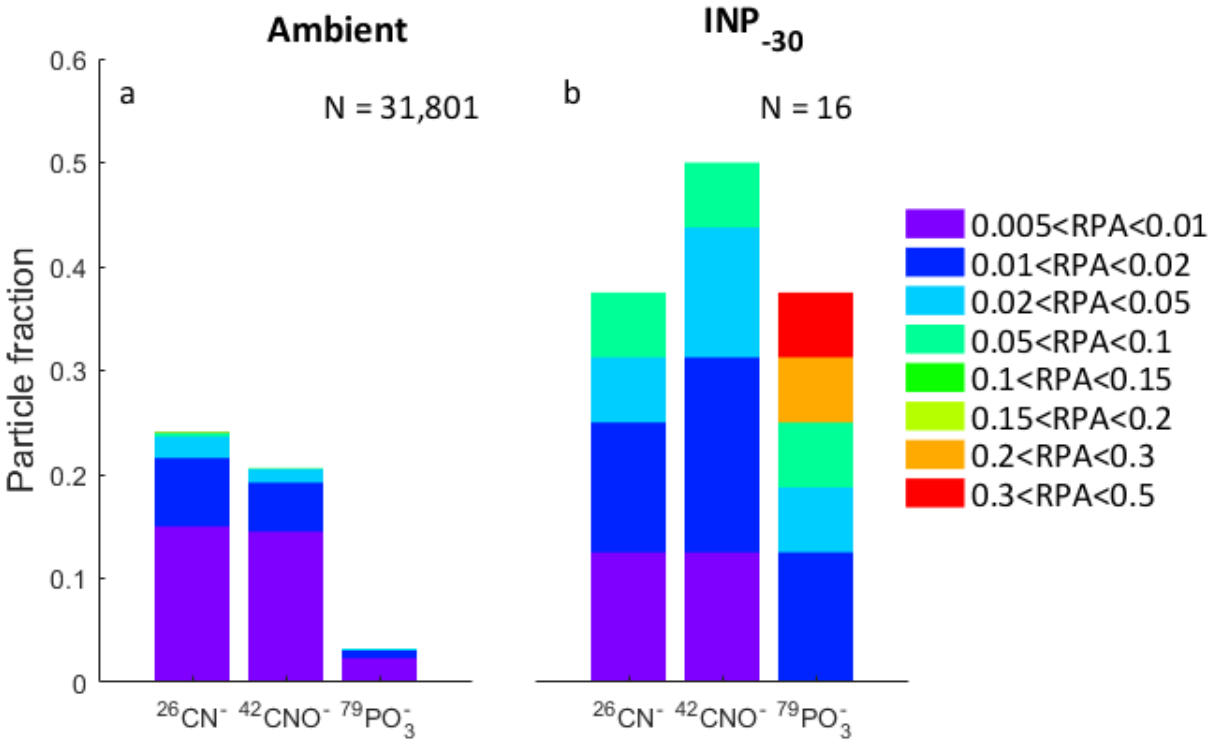

Figure 5.8. Colorstack plots of organic ion markers for SSA particles for (a) ambient and (b) INP_{-30}. Colored bars indicate the fraction of particles that have a relative peak area (RPA) within the corresponding bounds.

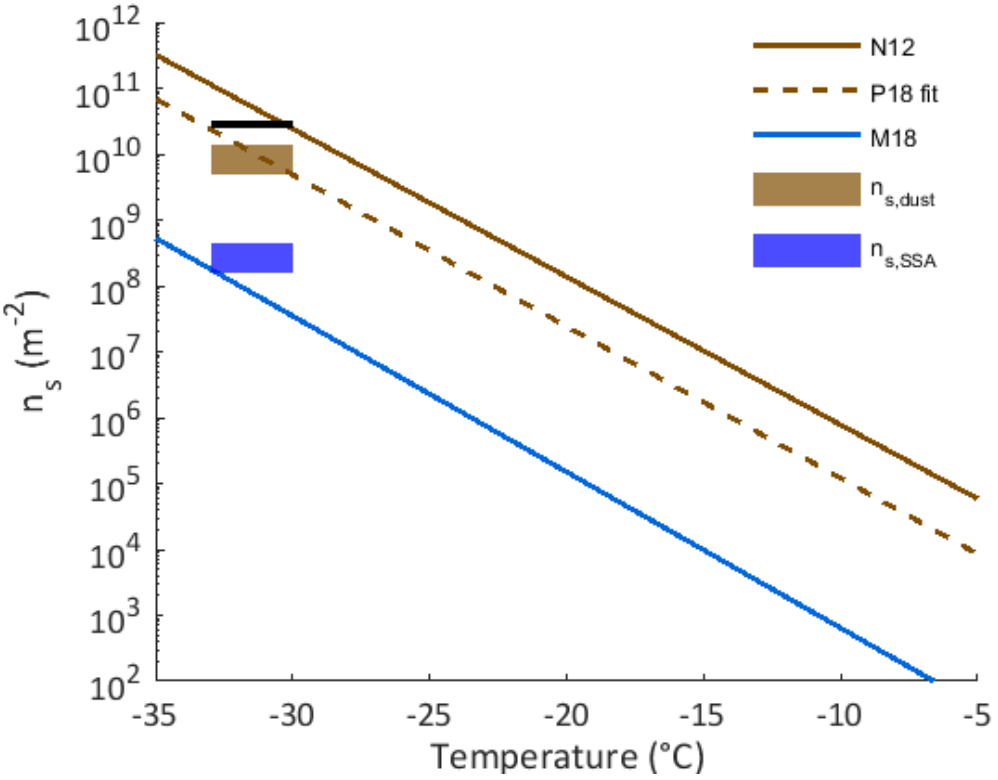

Figure 5.9. Active site density (n_s) vs temperature for dust (brown) and SSA (blue) as determined by the CFDC-PCVI-ATOFMS. Also shown are n_s parameterizations for dust (N12, brown; Niemand et al., 2012), SSA (M18, blue; McCluskey et al., 2018), and an exponential fit of dust-dominated airmasses (P18, brown dashed line; Price et al., 2018). The application of the DeMott et al. (2015) correction factor is indicated by the black bar above the $n_{s,dust}$ value.

5.8 Tables

Table 5.1. Description of ATOFMS particle types, including common ion marker assignments and literature references.

Particle type	Characteristic ion markers
Dust	$^{7}Li^{+}$, $^{27}Al^{+}$, $^{39}K^{+}$, $^{48,64}Ti,TiO^{+}$, $^{54,56}Fe^{+}$, $^{60}SiO_2^{-}$ $^{76}SiO_3^{-}$, $^{79}PO_3^{-}$ (Silva et al., 2000).
Na/K	$^{23}Na^{+}$, $^{39}K^{+}$ (Pratt & Prather, 2010).
Sea spray aerosol (SSA)	$^{23}Na^{+}$, $^{24}Mg^{+}$, $^{39}K^{+}$, $^{46}Na_2^{+}$, $^{81,83}Na_2Cl^{+}$, $^{35,37}Cl^{-}$, $^{46}NO_2^{-}$, $^{58}NaCl^{-}$, $^{62}NO_3^{-}$, $^{93,95,97}NaCl_2^{-}$(Gard et al., 1998).
Primary biological (Bio)	Strong $^{39}K^{+}$ and $^{79}PO_3^{-}$, minor contributions from 59^{+}, 74^{+}, nucleoside fragment peaks at 66^{-}, 71^{-}, 90^{-} (Fergenson et al., 2004; Sultana et al., 2017).
Elemental Carbon (EC)	Clusters every 12 m/z at C_n^{+} and C_n^{-} (Moffet & Prather, 2009; Spencer & Prather, 2006).
Organic Carbon (OC)	$^{27}C_2H_3^{+}$, $^{29}C_2H5$, $^{37}C_3H^{+}$, $^{43}CH_3CO^{+}/CHNO^{+}$ (Qin et al., 2012; P. Silva & Prather, 2000; Spencer & Prather, 2006).
Elemental carbon organic carbon (ECOC)	$^{12}C^{+}$, $^{24}C_2^{+}$, $^{27}C_2H_3^{+}$, $^{36}C_3^{+}$, $^{37}C_3H^{+}$, $^{43}CH_3CO^{+}/CHNO^{+}$ (Moffet & Prather, 2009; Qin et al., 2012).
Biomass burning (BB)	Intense $^{39}K^{+}$ and $^{97}HSO_4^{-}$, minor contributions from $^{12}C^{+}$, $^{26}CN^{-}$, $^{46}NO_2^{-}$, $^{62}NO_3^{-}$, $^{125}H(NO_3)_2^{-}$ (Silva et al., 1999).

Table 5.2. Times for ambient (AMB) and ice nucleating particle sampling (INP_{-30}) periods during operation of the integrated CFDC-PCVI-ATOFMS system, as well as the number of particles observed by the ATOFMS and CFDC. All times are in UTC.

Date	Start time	End time	Sampling type	ATOFMS particles	INP detected by CFDC	Total detection efficiency
12-Feb-2015	21:00:00	23:59:59	AMB	4730	N/A	N/A
13-Feb-2015	00:14:30	03:12:32	INP_{-30}	30	49,730	$6.0x10^{-4}$
13-Feb-2015	21:20:54	01:14:02	AMB	2079	N/A	N/A
14-Feb-2015	01:38:13	03:35:51	INP_{-30}	24	44,379	$5.4x10^{-4}$
14-Feb-2015	03:48:52	05:20:00	AMB	1376	N/A	N/A
14-Feb-2015	22:00:00	22:41:18	AMB	995	N/A	N/A
14-Feb-2015	23:11:32	01:23:25	INP_{-30}	12	40,469	$3.0x10^{-4}$
15-Feb-2015	01:31:57	03:20:00	AMB	2114	N/A	N/A
15-Feb-2015	20:00:00	21:21:22	AMB	1632	N/A	N/A
15-Feb-2015	21:24:15	22:56:30	INP_{-30}	4	12,011	$3.3x10^{-4}$
15-Feb-2015	22:56:30	02:00:00	AMB	1086	N/A	N/A
16-Feb-2015	18:00:00	19:48:15	AMB	393	N/A	N/A
16-Feb-2015	19:48:16	21:38:12	INP_{-30}	3	20,060	$1.5x10^{-4}$
16-Feb-2015	21:44:36	00:58:12	AMB	1169	N/A	N/A
17-Feb-2015	18:00:00	21:00:09	AMB	8856	N/A	N/A
17-Feb-2015	21:00:00	00:09:47	INP_{-30}	26	43,619	$6.0x10^{-4}$
18-Feb-2015	00:19:21	03:20:00	AMB	6060	N/A	N/A
18-Feb-2015	18:50:00	23:36:10	AMB	5816	N/A	N/A
18-Feb-2015	23:36:10	02:26:29	INP_{-30}	22	67,466	$3.3x10^{-4}$
19-Feb-2015	2:26:29	05:10:00	AMB	3008	N/A	N/A

Table 5.3. Particle type number, fraction, and INP enrichment factor (EF). Ambient indicates particles measured during control time periods, and INP_{-30} indicates time periods when ice crystal residuals were measured. Error for EFs indicate standard error of measured number.

Particle type	Ambient number	Ambient fraction	INP_{-30} number	INP_{-30} fraction	INP EF
Dust	1904	0.050	76	0.71	14.2±0.7
Na/K	662	0.018	7	0.07	3.7±0.4
SSA	31,801	0.88	16	0.15	0.2±0.0
Bio	129	0.0030	5	0.05	13.7±1.3
EC	720	0.019	1	0.01	0.5±0.1
OC	166	0.0040	2	0.02	4.3±0.5
BB	671	0.018	0	0	N/A
ECOC	151	0.0080	0	0	N/A

5.9 References

Atkinson, J. D., Murray, B. J., Woodhouse, M. T., Whale, T. F., Baustian, K. J., Carslaw, K. S., … Malkin, T. L. (2013). The importance of feldspar for ice nucleation by mineral dust in mixed-phase clouds. *Nature*, *500*(7463), 490–490. https://doi.org/10.1038/nature12384

Ault, A. P., Williams, C. R., White, A. B., Neiman, P. J., Creamean, J. M., Gaston, C. J., … Prather, K. a. (2011). Detection of Asian dust in California orographic precipitation. *Journal of Geophysical Research*, *116*(D16205), 1–15. https://doi.org/10.1029/2010JD015351

Bhave, P. V., Allen, J. O., Morrical, B. D., Fergenson, D. P., Cass, G. R., & Prather, K. a. (2002). A field-based approach for determining ATOFMS instrument sensitivities to ammonium and nitrate. *Environmental Science and Technology*, *36*(22), 4868–4879. https://doi.org/10.1021/es015823i

Bigg, E. K. E. (1973). Ice Nucleus Concentrations in Remote Areas. *Journal of Atmospheric Sciences*, *30*(6), 1153–1157. https://doi.org/10.1016/0169-8095(90)90025-8

Boose, Y., Sierau, B., Isabel García, M., Rodríguez, S., Alastuey, A., Linke, C., … Lohmann, U. (2016a). Ice nucleating particles in the Saharan Air Layer. *Atmospheric Chemistry and Physics*, *16*, 9067–9087. https://doi.org/10.5194/acp-16-9067-2016

Boose, Y., Welti, A., Atkinson, J., Ramelli, F., Danielczok, A., Bingemer, H. G., … Lohmann, U. (2016b). Heterogeneous ice nucleation on dust particles sourced from nine deserts worldwide - Part 1: Immersion freezing. *Atmospheric Chemistry and Physics*, *16*, 15075–15095. https://doi.org/10.5194/acp-16-15075-2016

Boulter, J. E., Cziczo, D. J., Middlebrook, a. M., Thomson, D. S., & Murphy, D. M. (2006). Design and Performance of a Pumped Counterflow Virtual Impactor. *Aerosol Science and Technology*, *40*, 969–976. https://doi.org/10.1080/02786820600840984

Burrows, S. M., Hoose, C., Poschl, U., & Lawrence, M. G. (2013). Ice nuclei in marine air: Biogenic particles or dust? *Atmospheric Chemistry and Physics*, *13*, 245–267. https://doi.org/10.5194/acp-13-245-2013

Cahill, J. F., Suski, K., Seinfeld, J. H., Zaveri, R. a., & Prather, K. a. (2012). The mixing state of carbonaceous aerosol particles in northern and southern California measured during CARES and CalNex 2010. *Atmospheric Chemistry and Physics*, *12*, 10989–11002. https://doi.org/10.5194/acp-12-10989-2012

Chou, C., Formenti, P., Maille, M., Ausset, P., Helas, G., Harrison, M., & Osborne, S. (2008). Size distribution, shape, and composition of mineral dust aerosols collected during the African Monsoon Multidisciplinary Analysis Special Observation Period 0: Dust and Biomass-Burning Experiment field campaign in Niger, January 2006. *Journal of Geophysical Research Atmospheres*, *113*(23), 1–17. https://doi.org/10.1029/2008JD009897

Cochran, R. E., Laskina, O., Trueblood, J. V., Estillore, A. D., Morris, H. S., Jayarathne, T., … Grassian, V. H. (2017a). Molecular Diversity of Sea Spray Aerosol Particles: Impact of Ocean Biology on Particle Composition and Hygroscopicity. *Chem*, *2*(5), 655–667. https://doi.org/10.1016/j.chempr.2017.03.007

Cochran, R. E., Ryder, O. S., Grassian, V. H., & Prather, K. A. (2017b). Sea Spray Aerosol: The Chemical Link between the Oceans, Atmosphere, and Climate. *Accounts of Chemical Research*, *50*(3), 599–604. https://doi.org/10.1021/acs.accounts.6b00603

Corbin, J. C., Rehbein, P. J. G., Evans, G. J., & Abbatt, J. P. D. (2012). Combustion particles as ice nuclei in an urban environment: Evidence from single-particle mass spectrometry. *Atmospheric Environment*, *51*, 286–292. https://doi.org/10.1016/j.atmosenv.2012.01.007

Creamean, J. M., Suski, K. J., Rosenfeld, D., Cazorla, A., DeMott, P. J., Sullivan, R. C., … Prather, K. a. (2013). Dust and biological aerosols from the Sahara and Asia influence precipitation in the western U.S. *Science (New York, N.Y.)*, *339*(2013), 1572–8. https://doi.org/10.1126/science.1227279

Creamean, J. M., White, A. B., Minnis, P., Palikonda, R., Spangenberg, D. A., & Prather, K. A. (2016). The relationships between insoluble precipitation residues, clouds, and precipitation over California's southern Sierra Nevada during winter storms. *Atmospheric Environment*, *140*, 298–310. https://doi.org/10.1016/j.atmosenv.2016.06.016

Creamean, J. M., Kirpes, R. M., Pratt, K. A., Spada, N. J., Maahn, M., de Boer, G., … China, S. (2018). Marine and terrestrial influences on ice nucleating particles during continuous springtime measurements in an Arctic oilfield location. *Atmospheric Chemistry and Physics*, *18*, 18023–18042. https://doi.org/10.5194/acp-2018-545

Cziczo, D. J., DeMott, P. J., Brock, C., Hudson, P. K., Jesse, B., Kreidenweis, S. M., … Murphy, D. M. (2003). A Method for Single Particle Mass Spectrometry of Ice Nuclei. *Aerosol Science and Technology*, *37*(5), 460–470. https://doi.org/10.1080/02786820300976

DeMott, P. J., Cziczo, D. J., Prenni, A. J., Murphy, D. M., Kreidenweis, S. M., Thomson, D. S., … Rogers, D. C. (2003). Measurements of the concentration and composition of nuclei for cirrus formation. *Proceedings of the National Academy of Sciences*, *100*(25), 14655–14660. https://doi.org/10.1073/pnas.2532677100

DeMott, P. J., Prenni, A. J., Liu, X., Kreidenweis, S. M., Petters, M. D., Twohy, C. H., … Rogers, D. C. (2010). Predicting global atmospheric ice nuclei distributions and their impacts on climate. *Proceedings of the National Academy of Sciences*, *107*(25), 11217–11222. https://doi.org/10.1073/pnas.0910818107

Demott, P. J., Prenni, A. J., McMeeking, G. R., Sullivan, R. C., Petters, M. D., Tobo, Y., … Kreidenweis, S. M. (2015). Integrating laboratory and field data to quantify the immersion freezing ice nucleation activity of mineral dust particles. *Atmospheric Chemistry and Physics*, *15*(1), 393–409. https://doi.org/10.5194/acp-15-393-2015

DeMott, P. J., Hill, T. C. J., McCluskey, C. S., Prather, K. A., Collins, D. B., Sullivan, R. C., … Franc, G. D. (2016). Sea spray aerosol as a unique source of ice nucleating particles. *Proceedings of the National Academy of Sciences*, *113*(21), 5797–5803. https://doi.org/10.1073/pnas.1514034112

DeMott, P. J., Mason, R. H., McCluskey, C. S., Hill, T. C. J., Perkins, R. J., Desyaterik, Y., … Prather, K. A. (2018). Ice nucleation by particles containing long-chain fatty acids of relevance to freezing by sea spray aerosols. *Environmental Science: Processes and Impacts*, *20*(11), 1559–1569. https://doi.org/10.1039/c8em00386f

Dettinger, M. D., Ralph, F. M., Das, T., Neiman, P. J., & Cayan, D. R. (2011). Atmospheric Rivers, Floods and the Water Resources of California. *Water*, *3*(4), 445–478. https://doi.org/10.3390/w3020445

Eidhammer, T., DeMott, P. J., Prenni, A. J., Petters, M. D., Twohy, C. H., Rogers, D. C., … Kreidenweis, S. M. (2010). Ice Initiation by Aerosol Particles: Measured and Predicted Ice Nuclei Concentrations versus Measured Ice Crystal Concentrations in an Orographic Wave Cloud. *Journal of the Atmospheric Sciences*, *67*(8), 2417–2436. https://doi.org/10.1175/2010JAS3266.1

Fan, J., Leung, L. R., Demott, P. J., Comstock, J. M., Singh, B., Rosenfeld, D., … Min, Q. (2014). Aerosol impacts on California winter clouds and precipitation during calwater 2011: Local pollution versus long-range transported dust. *Atmospheric Chemistry and Physics*, *14*, 81–101. https://doi.org/10.5194/acp-14-81-2014

Fan, J., Leung, L. R., Rosenfeld, D., Demott, P. J., Ruby Leung, L., Rosenfeld, D., & Demott, P. J. (2017). Effects of cloud condensation nuclei and ice nucleating particles on precipitation processes and supercooled liquid in mixed-phase orographic clouds. *Atmospheric Chemistry and Physics*, *17*, 1017–1035. https://doi.org/10.5194/acp-17-1017-2017

Fergenson, D. P., Pitesky, M. E., Tobias, H. J., Steele, P. T., Czerwieniec, G. A., Russell, S. C., … Gard, E. E. (2004). Reagentless Detection and Classification of Individual Bioaerosol Particles in Seconds. *Analytical Chemistry*, *76*(2), 373–378. https://doi.org/10.1021/ac034467e

Gallavardin, S. J., Froyd, K. D., Lohmann, U., Moehler, O., Murphy, D. M., & Cziczo, D. J. (2008). Single Particle Laser Mass Spectrometry Applied to Differential Ice Nucleation Experiments at the AIDA Chamber. *Aerosol Science and Technology*, *42*(March 2015), 773–791. https://doi.org/10.1080/02786820802339538

Garcia, E., Hill, T. C. J., Prenni, A. J., DeMott, P. J., Franc, G. D., & Kreidenweis, S. M. (2012). Biogenic ice nuclei in boundary layer air over two U.S. high plains agricultural regions. *Journal of Geophysical Research Atmospheres*, *117*(17), 1–12. https://doi.org/10.1029/2012JD018343

Gard, E. E., Kleeman, M. J., Gross, D. S., Hughes, L. S., Allen, J. O., Morrical, B. D., … Prather, K. A. (1998). Direct Observation of Heterogeneous Chemistry in the Atmosphere. *Science*, *279*(5354), 1184–1187. https://doi.org/10.1126/science.279.5354.1184

Gard, E., Mayer, J. E., Morrical, B. D., Dienes, T., Fergenson, D. P., & Prather, K. A. (1997). Real-Time Analysis of Individual Atmospheric Aerosol Particles: Design and Performance of a Portable ATOFMS. *Analytical Chemistry*, *69*(20), 4083–4091. https://doi.org/10.1021/ac970540n

Huffman, J. A., Prenni, A. J., Demott, P. J., Pöhlker, C., Mason, R. H., Robinson, N. H., … Pöschl, U. (2013). High concentrations of biological aerosol particles and ice nuclei during and after rain. *Atmospheric Chemistry and Physics*, *13*, 6151–6164. https://doi.org/10.5194/acp-13-6151-2013

Kanji, Z. A., Welti, A., Chou, C., Stetzer, O., & Lohmann, U. (2013). Laboratory studies of immersion and deposition mode ice nucleation of ozone aged mineral dust particles. *Atmospheric Chemistry and Physics*, *13*, 9097–9118. https://doi.org/10.5194/acp-13-9097-2013

Kanji, Z. A., Ladino, L. A., Wex, H., Boose, Y., Burkert-Kohn, M., Cziczo, D. J., & Krämer, M. (2017). Overview of Ice Nucleating Particles. *Meteorological Monographs*, *58*, 1.1-1.33. https://doi.org/10.1175/AMSMONOGRAPHS-D-16-0006.1

King, S. M., Butcher, A. C., Rosenoern, T., Coz, E., Lieke, K. I., De Leeuw, G., … Bilde, M. (2012). Investigating primary marine aerosol properties: CCN activity of sea salt and mixed inorganic-organic particles. *Environmental Science and Technology*, *46*(19), 10405–10412. https://doi.org/10.1021/es300574u

Knopf, D. A., P. A. Alpert, B. Wang, J. Y. Aller. 2011. Stimulation of ice nucleation by marine diatoms. *Nature Geoscience* 4:88–90

Kulkarni, G., Pekour, M., Afchine, A., Murphy, D. M., & Cziczo, D. J. (2011). Comparison of Experimental and Numerical Studies of the Performance Characteristics of a Pumped Counterflow Virtual Impactor. *Aerosol Science and Technology*, *45*, 382–392. https://doi.org/10.1080/02786826.2010.539291

Lee, C., Sultana, C. M., Collins, D. B., Santander, M. V., Axson, J. L., Malfatti, F., … Prather, K. A. (2015). Advancing Model Systems for Fundamental Laboratory Studies of Sea Spray Aerosol Using the Microbial Loop. *Journal of Physical Chemistry A*, *119*(33), 8860–8870. https://doi.org/10.1021/acs.jpca.5b03488

Martin, A. C., Cornwell, G. C., Atwood, S. A., Moore, K. A., Rothfuss, N. E., Taylor, H., … Prather, K. A. (2017). Transport of pollution to a remote coastal site during gap flow from California's interior: impacts on aerosol composition, clouds, and radiative balance. *Atmospheric Chemistry and Physics*, *17*, 1491–1509. https://doi.org/10.5194/acp-17-1491-2017

Mason, R. H., Si, M., Li, J., Chou, C., Dickie, R., Toom-Sauntry, D., … Bertram, A. K. (2015). Ice nucleating particles at a coastal marine boundary layer site: Correlations with aerosol type and meteorological conditions. *Atmospheric Chemistry and Physics*, *15*, 12547–12566. https://doi.org/10.5194/acp-15-12547-2015

McCluskey, C. S., Hill, T. C. J., Malfatti, F., Sultana, C. M., Lee, C., Santander, M. V., … DeMott, P. J. (2017). A dynamic link between ice nucleating particles released in nascent sea spray aerosol and oceanic biological activity during two mesocosm experiments. *Journal of the Atmospheric Sciences*, *74*(2017), JAS-D-16-0087.1. https://doi.org/10.1175/JAS-D-16-0087.1

McCluskey, C. S., Hill, T. C. J., Sultana, C. M., Laskina, O., Trueblood, J., Santander, M. V., … DeMott, P. J. (2018a). A mesocosm double feature: Insights into the chemical make-up of marine ice nucleating particles. *Journal of the Atmospheric Sciences*. https://doi.org/10.1175/JAS-D-15-0370.1

McCluskey, C. S., Ovadnevaite, J., Rinaldi, M., Atkinson, J., Franco, B., Ceburnis, D., … Demott, P. J. (2018b). Marine and Terrestrial Organic Ice Nucleating Particles in Pristine Marine to Continentally-Influenced Northeast Atlantic Air Masses. *Journal of Geophysical Research: Atmospheres*, *123*, 1–17. https://doi.org/10.1029/2017JD028033

Moffet, R. C., & Prather, K. A. (2009). In-situ measurements of the mixing state and optical properties of soot with implications for radiative forcing estimates. *Proceedings of the National Academy of Sciences*, *106*(29), 11872–11877. https://doi.org/10.1073/pnas.0900040106

Murphy, D. M., Hudson, P. K., Cziczo, D. J., Gallavardin, S., Froyd, K. D., Johnston, M. V., … Wexler, A. S. (2007). Distribution of lead in single atmospheric particles. *Atmospheric Chemistry and Physics*, *7*, 3195–3210. https://doi.org/10.5194/acpd-7-3763-2007

Niemand, M., Möhler, O., Vogel, B., Vogel, H., Hoose, C., Connolly, P., … Leisner, T. (2012). A Particle-Surface-Area-Based Parameterization of Immersion Freezing on Desert Dust Particles. *Journal of the Atmospheric Sciences*, *69*(10), 3077–3092. https://doi.org/10.1175/JAS-D-11-0249.1

O'Sullivan, D., Murray, B. J., Malkin, T. L., Whale, T. F., Umo, N. S., Atkinson, J. D., … Webb, M. E. (2014). Ice nucleation by fertile soil dusts: Relative importance of mineral and biogenic components. *Atmospheric Chemistry and Physics*, *14*, 1853–1867. https://doi.org/10.5194/acp-14-1853-2014

O'Sullivan, D., Murray, B. J., Ross, J. F., Whale, T. F., Price, H. C., Atkinson, J. D., … Webb, M. E. (2015). The relevance of nanoscale biological fragments for ice nucleation in clouds. *Scientific Reports*, *5*, 1–7. https://doi.org/10.1038/srep08082

Pratt, K. A., DeMott, P. J., French, J. R., Wang, Z., Westphal, D. L., Heymsfield, A. J., … Prather, K. A. (2009). In situ detection of biological particles in cloud ice-crystals. *Nature Geoscience*, *2*(6), 398–401. https://doi.org/10.1038/ngeo521

Pratt, K. A., & Prather, K. A. (2010). Aircraft measurements of vertical profiles of aerosol mixing states. *Journal of Geophysical Research*, *115*(D11305), 1–10. https://doi.org/10.1029/2009JD013150

Price, H. C., Baustian, K. J., McQuaid, J. B., Blyth, A., Bower, K. N., Choularton, T., … Murray, B. J. (2018). Atmospheric Ice-Nucleating Particles in the Dusty Tropical Atlantic. *Journal of Geophysical Research: Atmospheres*, *123*(4), 2175–2193. https://doi.org/10.1002/2017JD027560

Qin, X., Bhave, P. V, & Prather, K. A. (2006). Comparison of Two Methods for Obtaining Quantitative Mass Concentrations from Aerosol Time-of-Flight Mass Spectrometry Measurements. *Analytical Chemistry*, *78*(17), 6169–6178.

Qin, X., Pratt, K. a., Shields, L. G., Toner, S. M., & Prather, K. a. (2012). Seasonal comparisons of single-particle chemical mixing state in Riverside, CA. *Atmospheric Environment*, *59*, 587–596. https://doi.org/10.1016/j.atmosenv.2012.05.032

Ralph, F. M., Prather, K. A., Cayan, D., Spackman, J. R., Demott, P., Dettinger, M., … Intrieri, J. (2016). Calwater field studies designed to quantify the roles of atmospheric rivers and aerosols in modulating U.S. West Coast Precipitation in a changing climate. *Bulletin of the American Meteorological Society*, *97*(7), 1209–1228. https://doi.org/10.1175/BAMS-D-14-00043.1

Rebotier, T. P., & Prather, K. A. (2007). Aerosol time-of-flight mass spectrometry data analysis: A benchmark of clustering algorithms. *Analytica Chimica Acta*, *585*, 38–54. https://doi.org/10.1016/j.aca.2006.12.009

Richardson, M. S., DeMott, P. J., Kreidenweis, S. M., Cziczo, D. J., Dunlea, E. J., Jimenez, J. L., … Lersch, T. L. (2007). Measurements of heterogeneous ice nuclei in the western United States in springtime and their relation to aerosol characteristics. *Journal of Geophysical Research Atmospheres*, *112*(2), 1–16. https://doi.org/10.1029/2006JD007500

Rogers, D. C. (1988). Development of a continuous flow thermal gradient diffusion chamber for ice nucleation studies. *Atmospheric Research*, *22*(2), 149–181. https://doi.org/10.1016/0169-8095(88)90005-1

Romay, F. J., Roberts, D. L., Marple, V. A., Liu, B. Y. H., & Olson, B. A. (2002). A high-performance aerosol concentrator for biological agent detection. *Aerosol Science and Technology*, *36*(2), 217–226. https://doi.org/10.1080/027868202753504074

Schill, G. P., Jathar, S. H., Kodros, J. K., Levin, E. J. T., Galang, A. M., Friedman, B., … DeMott, P. J. (2016). Ice-nucleating particle emissions from photochemically aged diesel and

biodiesel exhaust. *Geophysical Research Letters*, *43*(10), 5524–5531. https://doi.org/10.1002/2016GL069529

Schnell, R. C., & Vali, G. (1976). Biogenic Ice Nuclei: Part I. Terrestrial and Marine Sources. *Journal of the Atmospheric Sciences*. https://doi.org/10.1175/1520-0469(1976)033<1554:BINPIT>2.0.CO;2

Silva, P. J., Liu, D., Noble, C. A., & Prather, K. A. (1999). Size and Chemical Characterization of Individual Particles Resulting from Biomass Burning of Local Southern California Species. *Environmental Science & Technology*, *33*(18), 3068–3076.

Silva, P. J., Carlin, R. a, & Prather, K. a. (2000a). Single particle analysis of suspended soil dust from Southern California. *Atmospheric Environment*, *34*(11), 1811–1820. https://doi.org/10.1016/S1352-2310(99)00338-6

Silva, P., & Prather, K. (2000b). Interpretation of mass spectra from organic compounds in aerosol time-of-flight mass spectrometry. *Analytical Chemistry*, *72*(15), 3553–62.

Song, X. H., Hopke, P. K., Fergenson, D. P., & Prather, K. a. (1999). Classification of single particles analyzed by ATOFMS using an artificial neural network, ART-2A. *Analytical Chemistry*, *71*(4), 860–865. https://doi.org/10.1021/ac9809682

Spencer, M. T., & Prather, K. a. (2006). Using ATOFMS to Determine OC/EC Mass Fractions in Particles. *Aerosol Science and Technology*, *40*, 585–594. https://doi.org/10.1080/02786820600729138

Stopelli, E., Conen, F., Guilbaud, C., Zopfi, J., Alewell, C., & Morris, C. E. (2017). Ice nucleators, bacterial cells and Pseudomonas syringae in precipitation at Jungfraujoch. *Biogeosciences*, *14*(5), 1189–1196. https://doi.org/10.5194/bg-14-1189-2017

Sullivan, R. C., Guazzotti, S. A., Sodeman, D. A., Tang, Y., Carmichael, G. R., & Prather, K. A. (2007). Mineral dust is a sink for chlorine in the marine boundary layer. *Atmospheric Environment*, *41*(34), 7166–7179. https://doi.org/10.1016/j.atmosenv.2007.05.047

Sullivan, R. C., Miñambres, L., Demott, P. J., Prenni, A. J., Carrico, C. M., Levin, E. J. T., & Kreidenweis, S. M. (2010). Chemical processing does not always impair heterogeneous ice nucleation of mineral dust particles. *Geophysical Research Letters*, *37*(24), 1–5. https://doi.org/10.1029/2010GL045540

Suski, K. J., Hill, T. C. J., Levin, E. J. T., Miller, A., DeMott, P. J., & Kreidenweis, S. M. (2018). Agricultural harvesting emissions of ice-nucleating particles. *Atmospheric Chemistry and Physics*, *18*(18), 13755–13771. https://doi.org/10.5194/acp-18-13755-2018

Sultana, C. M., Al-Mashat, H., & Prather, K. A. (2017). Expanding Single Particle Mass Spectrometer Analyses for the Identification of Microbe Signatures in Sea Spray Aerosol.

Analytical Chemistry, *89*(19), 10162–10170. https://doi.org/10.1021/acs.analchem.7b00933

Sultana, C. M., Cornwell, G. C., Rodriguez, P., & Prather, K. A. (2017). FATES: a flexible analysis toolkit for the exploration of single-particle mass spectrometer data. *Atmospheric Measurement Techniques*, *10*(4), 1323–1334. https://doi.org/10.5194/amt-10-1323-2017

Taylor, J. R. (1997). *An introduction to error analysis : the study of uncertainties in physical measurements* (2nd editio). Sausalito, CA: University Science Books.

Tobo, Y., A. J. Prenni, P. J. DeMott, J. A. Huffman, C. S. McCluskey, G. Tian, C. Po¨ hlker, U. Po¨ schl, and S. M. Kreidenweis (2013), Biological aerosol particles as a key determinant of ice nuclei populations in a forest ecosystem, J. Geophys. Res. Atmos., 118, 10,100–10,110, doi:10.1002/jgrd.50801

Ullrich, R., Hoose, C., Möhler, O., Niemand, M., Wagner, R., Höhler, K., … Leisner, T. (2017). A New Ice Nucleation Active Site Parameterization for Desert Dust and Soot. *Journal of the Atmospheric Sciences*, *74*(3), 699–717. https://doi.org/10.1175/JAS-D-16-0074.1

Vergara-Temprado, J., Murray, B. J., Wilson, T. W., O'Sullivan, D., Browse, J., Pringle, K. J., … Carslaw, K. S. (2017). Contribution of feldspar and marine organic aerosols to global ice nucleating particle concentrations. *Atmospheric Chemistry and Physics*, *17*(5), 3637–3658. https://doi.org/10.5194/acp-17-3637-2017

Wilson, T. W., Ladino, L. A., Alpert, P. A., Breckels, M. N., Brooks, I. M., Browse, J., … Murray, B. J. (2015). A marine biogenic source of atmospheric ice-nucleating particles. *Nature*, *525*(7568), 234–238. https://doi.org/10.1038/nature14986

Zhu, Y., & Newell, R. E. (1998). A Proposed Algorithm for Moisture Fluxes from Atmospheric Rivers. *Monthly Weather Review*, *126*, 725–735. https://doi.org/10.1175/1520-0493(1998)126<0725:APAFMF>2.0.CO;2

Chapter 6. Assessing contributions to ice nucleating particle concentrations at a coastal site in California using single particle measurements

6.1 Abstract

Ice nucleating particles (INPs) can affect the amount, type, and spatial distribution of precipitation, and therefore understanding the source, chemical characteristics, activation temperature of INPs is of significant interest. Bulk aerosol chemistry measurements are insensitive to INP composition due to their rarity, presenting a unique analytical challenge. This work details the development of a method to estimate the contributions of different particle sources to INP populations without direct measurements of INP composition. Tandem measurements of particle composition, number, and size are used to calculate the total surface areas. INP concentrations for dust and SSA are estimated using ice nucleation active site densities. Biological particle concentrations are measured using a wideband integrated bioaerosol sensor and used to infer INP concentrations from biological particles. The total estimated concentrations from these three types are constrained with INP concentration measurements determined through droplet freezing assays. This methodology is then used to assess relative abundances of INP sources in a coastal environment for the duration of the entire study. INP_{-20} concentrations are determined to be driven primarily by biological particles. Dust particles also contributed to INP_{-20} concentrations, while SSA was found to be an unimportant source.

6.2 Introduction

Ice nucleating particles (INPs) can play an important role in affecting the amount, type, and spatial distribution of precipitation (Fan et al., 2014, 2017; Ralph et al., 2016). They are estimated to represent only 1 in 10^5-10^6 atmospheric particles (DeMott et al. 2010). In the absence of INPs, ice will not form in the atmosphere at temperatures below the homogeneous freezing

point (approximately -38 ºC; DeMott et al., 2010). The formation of ice crystals and subsequent cloud microphysical processes can potentially affect precipitation totals (Ault et al., 2011; Fan et al., 2014, 2017). Therefore, understanding the source, chemical characteristics, activation temperature of aerosols that act as INP is an area of significant current interest.

Bulk aerosol chemistry measurements are insensitive to INP composition due to their rarity, presenting a unique analytical challenge. Attempts to address this problem have been made by correlating INP concentrations to complementary measurements such as particle concentrations or chemical tracers (Huffman et al., 2013; Mason et al., 2015). Generally, INP concentrations are measured before and after subjecting samples to heat or chemical tests, and inferring the particle source from the difference in IN-activity (Hill et al., 2016; Suski et al., 2018; Tobo et al., 2014; Chapter 3 of this thesis). This approach can be useful for identifying relatively warm INP-containing biogenic components as those are particularly sensitive to thermal/chemical changes. Alternately, isolated ice crystals are collected, melted with their composition measured directly (Cziczo et al., 2017; DeMott et al., 2003; Richardson et al., 2007; Chapter 5 of this dissertation). This direct measurement is preferable because it directly measures single INP composition. However, this approach is limited by collection ability, which can be complicated due to in-cloud sampling or requiring instrumentation to generate ice crystals such as a cloud chamber or continuous flow diffusion chamber. Additionally, sampling time can be lengthy and collection efficiencies low, as shown in Chapter 5 of this thesis in which 20 hours of ambient air was sampled resulting in 100 ice crystal residuals. Thus, alternative methods of apportioning INP concentrations are desirable.

The aerosol time-of-flight mass spectrometer (ATOFMS; Gard et al., 1997) measures the size-resolved single particle composition of particles in the range shown to be important for ice

nucleation (0.5-5.0 μm). However, obtaining quantitative concentrations and masses from the ATOFMS is complicated by the fact that the sensitivity of ATOFMS to different chemical species can vary considerably (Gross et al., 2000; Reilly et al., 2000) and requires transmission efficiency correction with co-located measurements of aerosol size distributions (Bhave et al., 2002; Moffet et al., 2004; Qin et al., 2006). Scaling ATOFMS measurements with a co-located aerodynamic particle sizer (APS) allows for the quantitative characterization of mass by chemical species (Qin et al., 2006). Chapter 5 of this thesis extends this methodology to calculate particle-class based surface area and derive ice nucleation active site densities (n_s) for dust and sea spray. A continuous flow diffusion chamber (CFDC) was connected to an ATOFMS so that direct measurements of ice crystal residual composition could be performed. The CFDC-ATOFMS method of calculating n_s agreed well with previous results, though this approach has a naturally low collection efficiency and necessitated both extensive sampling times and the need to measure INP concentrations at T = -30 ºC in order to detect a sufficient number of particles. Thus alternative approaches are required in order to apportion INP source at warmer temperatures.

This paper details the development of a method to estimate the contributions of different particle sources to INP populations without direct measurements of INP composition. Tandem measurements of particle composition, number, and size are used to calculate the total surface areas for dust and SSA. Particle surface areas are used to estimate contributions of SSA and dust to ambient INP concentrations at a coastal site in California. Additionally, a wideband integrated bioaerosol sensor (WIBS) is used to measure bioaerosol concentrations, and this information is used to infer the contribution of biological particles to INP concentrations. The total estimated concentrations from these three types are constrained with INP concentration measurements

determined through droplet freezing assays. This methodology is then used to assess relative abundances of INP sources in a coastal environment for the duration of the entire study.

6.3 Materials and methods

6.3.1 Field measurements site

Field measurements of aerosol size, number, composition, and microphysical properties were collected at Bodega Marine Lab (BML), in Bodega Bay, CA (38.3 ºN, 123.1 ºW) as part of the CalWater-2015 field campaign. Measurements were collected from January 14 to March 8, 2015. These measurements have been described before (Martin et al., 2017), so we provide only a short overview. Two mobile sampling labs were deployed to the site with instruments for the measurement of aerosol number, size, composition, and microphysical properties. Bioaerosol concentrations, black carbon mass and gas-phase tracer concentrations were also measured. A meteorology station owned and operated by the National Oceanic and Atmospheric Administration's Earth System Research Laboratory was located ~100 m north of the site. Offline samples for droplet freezing assays were collected using impingers and are described in more detail in Section 6.3.4.

6.3.2 Single particle composition

Single particle mass spectra were collected using an aerosol time-of-flight mass spectrometer (ATOFMS; Gard et al., 1997). In brief, particles are introduced into the instrument and collimated and focused by a series of skimmers. The particle beam is oriented through the path of two continuous wave lasers (532 nm; Nd:YAG) 6 cm apart. Upon traversing the laser path, particles scatter light from the two lasers. This scattered light is reflected by ellipsoidal mirrors onto photomultiplier tubes (PMTs) and the duration between signal at the two PMTs is used to calculate the particle velocity. Through external calibration with spheres of known size and

density, the particle velocity can be used to determine the particle vacuum aerodynamic diameter (D_{va}). The particle velocity also triggers a pulsed 266 nm laser (Nd:YAG; 1.0-1.3 mJ $pulse^{-1}$) to desorb and ionize particles into a dual polarity time-of-flight mass spectrometer. Both positive and negative ions are generated by the laser desorption process. For each particle, the dual polarity mass spectrum, D_{va}, and timestamp are recorded. This data was imported into Matlab (The MathWorks, Inc.) and analysed using the software toolkit FATES (Sultana et al., 2017). Particles were clustered based upon their mass spectral features via an adaptive neural network (Rebotier and Prather, 2007; Song et al., 1999). Similar to previous field studies using ATOFMS analysis, particle types were manually re-grouped upon inspection of the clusters based on spectral similarities. In this work, we focus only upon those particles identified as dust or SSA. Representative spectra of these particle types are shown in Figure 6.7.

6.3.3 Bioaerosol concentration

The wideband integrated bioaerosol sensor (WIBS) measures the size, asymmetry factor, and fluorescence signal for particles from 0.5-20 μm. Fluorescence is measured in three different channels: FL1, excitation 280 nm, emission 310-400 nm; FL2, excitation 280 nm, emission 420-650 nm; FL3, excitation 370 nm, emission 420-650 nm. These excitation-emission bands were chosen to overlap with the signal of common fluorescent markers such as tryptophan, tyrosine, NADH, and riboflavin. The detection of fluorescent particles from 0.5-0.8 μm is limited by the sensitivity of the instrument's detectors (Gabey et al., 2010, 2011), therefore we limit fluorescent particles to the size range of 0.8-20 μm.

Background fluorescence signal was calculated following (Toprak and Schnaiter, 2013). Force-triggered sampling of filtered air was conducted for 5 minutes and the background signal, $E_{background,i}$, calculated by the following:

$$E_{background,i} = \overline{E_i} + 3\sigma_i \quad (1)$$

Where $\overline{E_i}$ is the average signal in channel i, for a force-triggered sample and σ_i is the standard deviation of the force triggered sample signal. $E_{background,i}$ was subtracted from each particle for each channel to yield the final fluorescence signal. Particles were classified into types based upon their fluorescent signal in each channel using criteria (summarized in Table 6.1) defined in previous studies (Gabey et al., 2010; Wright et al., 2014).

6.3.4 INP methods

Ambient aerosol was sampled for offline INP measurements using an impinger sampler (Willeke et al. 1998, three-piece 5 mL impinger (SKC Inc. BioSampler®), hereinafter referred to as biosampler. The biosampler was operated by impinging aerosols into 20 mL ultrapure water (HPLC Grade Submicron Filtered Water, Fisher Chemical Cat. No. W5-4). Ambient air was sampled at a flow rate of 12.5 L min^{-1} for a duration of ~4 h. To avoid reduction in collection efficiency due to evaporation, the sampler was refilled to 20 ml at regular intervals, including the end of the sampling period. At the end of each sampling period, the sample was divided and transferred into 4.5 mL cryogenic vials. Associated background samples (hereafter the field blank), containing only the ultrapure water used to prepare the biosampler, were generated for each sampling period. The ambient and field blank samples were immediately frozen after collection and stored at -80 °C until the end of the campaign. The samples were shipped overnight from BML to NCSU in Raleigh, North Carolina, U.S.A. The samples were kept frozen in transit using dry ice and stored at -80 °C upon arrival, and then individually thawed prior to analysis.

The INP concentrations of these ambient samples were measured using the NCSU Cold Stage (hereafter the cold stage (Hader et al., 2014; Wright and Petters, 2013). Prior studies using this technique suspended water droplets into squalene in a dish before freezing. This method was

changed in order to decrease the distance between water droplets and the cold stage and thus monitor freezing temperatures more accurately. Instead, samples were divided into ~200 1 μL volume drops onto a 2 by 2 array of hydrophobic glass cover slides (Siliconized Glass Square Cover Slides, Hampton Research Cat. No. HR3-215), using a single-channel digital pipette. The cover slides were placed on top of the cold stage, a temperature-controlled metal plate that has two embedded thermistors embedded to monitor the temperature during freezing experiments. Droplets were cooled at a rate of 2 K min^{-1} until all drops were frozen. Freezing events were detected using an optical change in the droplets' appearance and were recorded at 0.17 K intervals using a digital camera. A flow of 1 L min^{-1} of dry N_2 was used to prevent frosting with the IN cell. To reduce contact freezing amongst the droplets, distance between the droplets was increased beyond the droplets' "sphere of influence". The resolvable temperature-dependent INP spectra ranges from between approximately 5×10^3 and 5×10^6 INP L^{-1} of aqueous sample. Each sample was assayed three times and INP concentrations were binned into 1 K temperature intervals. For each sample and for each temperature bin, the mean concentration and 95% confidence interval for the three assays are reported. Points where ambient concentrations are less than the background INP concentration were removed from the dataset. Ambient INP concentrations for each temperature bin, $INP_{ambient,T}$, were obtained by the following

$$INP_{ambient,T} = \frac{INP_{aqueous,T} V_{Total}}{Q\ t_{sample}} \quad (2)$$

where $INP_{aqueous,T}$ is the concentration of INPs in the liquid sample for a given temperature, V_{Total} is the total biosampler sample volume, Q is the flow rate into the biosampler, and t_{sample} is the total sampling time. Ambient INP concentration are reported in units of L^{-1} air sampled.

6.3.5 Calculating expected contributions of INP concentrations from dust and SSA using combined ATOFMS and APS measurements

INP concentrations for particle type x, $N_{INP,x}$, can be estimated via surface-area based parameterizations using the following

$$N_{INP,x} = n_{s,x} A_x \quad (3)$$

where $n_{s,x}$ is the ice nucleation active site density for a particle class (i.e. $n_{s,dust}$ or $n_{s,SSA}$) and A_x is the total surface area for a particle class (i.e. A_{dust} or A_{SSA}). $n_{s,x}$ has been parameterized for a number of particle types including mineral dust (Niemand et al., 2012), soil dust (Tobo et al., 2014), agricultural dust (Steinke et al., 2016), and SSA (McCluskey et al., 2018b), while A_x can be calculated from tandem measurements of the ATOFMS and APS (Chapter 5 of this dissertation) by the following

$$A_x = \sum_{i=1}^{51} D_{p,x,i}^2 \, \pi \, n_i f_{x,i} \quad (4)$$

where $D_{p,x,i}$ is the particle physical (spherical equivalent) diameter for that bin for particle class x, n_i is the number of particles in that size bin (from the APS), and $f_{x,i}$ is the fraction of particles of a given particle class (from the ATOFMS) for that same size bin. $D_{p,x}$ can be calculated from the aerodynamic diameter, D_a, using the following

$$D_{p,x} = D_a \sqrt{\frac{\rho_o \chi_x}{\rho_x}} \quad (5)$$

where χ is the dynamic shape factor, and ρ_0 is the reference density (1 in this case), and ρ_x is the particle density. For our calculations we assumed that dust had a χ_x of 1.9 (Chou et al., 2008) and a ρ_x of 2.65 g cm^{-3} (Kanji et al., 2013), SSA had a χ_x of 1.25 and a ρ_x of 2.2 g cm^{-3} (King et al., 2012).

6.4 Results and discussion

6.4.1 Relative contributions of dust and sea spray to INP populations

The particle type-specific surface areas for dust and sea spray at BML were calculated via combined measurements of the APS and ATOFMS. Through the majority of the study, the particle

surface area for sea spray (A_{SSA}; see section 6.3.5 for details on calculation) was higher than that calculated for dust (A_{dust}; Figure 6.1). There were a few exceptions to this, mainly when the site was under gap flow conditions in which terrestrial aerosol particles from the Central Valley were transported to the site, as described previously (Martin et al., 2017).

The A_{SSA}, in tandem with the parameterization of ambient SSA from McCluskey et al., (2018; hereafter referred to as M18) was used to estimate the contribution of SSA to INP populations. For all measured temperatures, the predicted contributions to INP populations from SSA (INP_{SSA}) are significantly below observations (Figure 6.2), indicating that SSA is not one of the major sources of INPs at BML.

Dust INP (INP_{dust}) concentrations can likewise be estimated using the APS-ATOFMS derived surface area (A_{dust}) and n_s parameterizations. However, "dust" is a broad and inclusive categorization, with IN-activities that span an extensive range. For example, Niemand et al (2012) developed an n_s parameterization using lab studies of selected mineral dusts (hereafter N12) with an n_s of 1.37 x 10^8 m^{-2} at a temperature of -20 ºC, while the parameterization developed for agricultural dust by Steinke et al (2016, hereafter S16) had an n_s of 2.70 x 10^9 m^{-2} at that same temperature. While the difference in IN-activity is likely attributable at least in part to samples in S16 being externally mixed with cells and other bioparticles, this illustrates the potential range in n_s due to presence of organics on the particles. Applying each parameterization to the A_{dust} the predicted vs measured INP_{-20} concentrations for dust using N12, S16, and an exponential fit of n_s from desert dust dominated airmasses (Price et al., 2018; hereafter P18) the variability in dust is highlighted (Figure 6.3).

Of the dust parameterizations applied to INP calculations, N12 most closely aligns with observations, S16 consistently overpredicts by an order of magnitude, and P18 under-predicts.

However, it should be noted that the observational data are not segregated by particle type and due to the strong relationship between FP3 and INP concentrations, bioaerosol are likely the significant source of INPs (Chapter 4 of this dissertation). Thus, by accurately predicting INP concentrations, N12 is in fact over-predicting INP contributions from dust due to the strong influence/contribution from bioaerosol INPs. Single particle measurements of INP composition were made at BML (described in detail in Chapter 5 of this dissertation) and from those measurements the n_s for dust was calculated and the parameterization that best described those data was P18. Hereafter we will use P18 to estimate the IN-activity of dust.

6.4.2 Estimating bioaerosol contribution to INP populations

The WIBS-measured FP3 and FBAP particle types have both been correlated to INP concentrations. Huffman et al., (2013) observed an increase in both INP_{-25} and FBAP particle concentrations during and shortly after precipitation. Strong relationships between INP_{-20} and FP3 concentrations were observed by Wright et al., (2014) in what was presumed to be a fungal spore release event and Suski et al., (2018) from measurements made at farm fields in Kansas and Wyoming. However, a strong relationship between FBAP and INP concentrations was not observed. For this study, we observed that the correlation between FP3 and INP_{-20} were much stronger than between FBAP and INP_{-20} (Figure 6.8) and was confirmed through visual examination of the temporal profiles for FP3, FBAP, and INP_{-20} (Figure 6.9). On the basis of this evidence, FP3 particles will be used as a proxy for ice-active bioaerosol concentrations.

Strictly using FP3 concentrations will lead to an overestimation of INP concentrations (Figure 6.8). Wright et al., (2014) observed that INP_{-20} and FP3 concentrations were 1:1 during some sampling periods, while Suski et al., (2018) observed INP_{-20}/FP3 ratios ranging from 0.14-0.93. However, they measured agricultural emissions, which in addition to ice-active bioaerosol

would have contained dust particles that would also be ice-active, and thus the ratio of bioaerosol INP_{-20} to FP3 should actually be lower.

To assess the fraction of FP3 particles that may be ice-active at a given temperature, we assume that all INPs at BML can be attributed to either dust, bioaerosol, or SSA. We derive an expected contribution of bioaerosol INPs, $INP_{Bio,exp}$, from the following:

$$INP_{Bio,exp} = INP_{total} - (INP_{SSA} + INP_{Dust}) \quad (5)$$

where INP_{total} is the measured INP concentrations. We define a scaling factor, α, to estimate the fraction of FP3 particles that may serve as INPs at a given temperature by the following:

$$\alpha = \frac{INP_{Bio,exp}}{FP3} \quad (6)$$

α would be the slope from a linear fit of correlation plot between FP3 and INP if bioaerosol were the only source of INPs. In the case where there are other sources of INPs, α should be lower than this slope. For each temperature of INP evaluated here, the median value of α for each temperature (Figure 6.10) was used to estimate the concentration of INPs from bioaerosol, INP_{Bio}. Using this methodology to estimate total INPs from INP_{dust}, INP_{SSA}, and INP_{Bio} returns relatively good agreement with measured values (Figure 6.4).

6.4.3 Relative abundance of particle types acting as INPs

Using the results detailed in sections 6.4.1 and 6.4.2, normalized probability distributions of the fraction of INP_{-20} due to each particle type were calculated (Figure 6.5). Bioaerosol were the primary contributor, while dust particles were a relatively minor source of INPs, and SSA determined to be insignificant. While we observed that the particle surface area for SSA was greater than dust by a factor of ~5, expected contributions from SSA across all temperatures were ultimately concluded to be negligible due to the fact that dust particles typically have n_s values 2-3 order of magnitude greater than SSA (McCluskey et al., 2018b; Niemand et al., 2012). While

SSA are thought to be a potentially important source of INPs over remote ocean regions (Burrows et al., 2013; Vergara-Temprado et al., 2017, 2018), this study highlights the large impact even small concentrations of efficient ice nucleators can have on INP concentrations and the more specifically the importance of bioaerosols to warm INP populations.

Temporal profiles of particle types show that there were two periods with elevated INP_{-20} concentrations and these were mostly due to spikes in bioaerosol INPs (Figure 6.6). The first occurred on January 20th, a couple days after a small storm. Concentrations were elevated for about a day before decreasing. The second period of elevated bioaerosol INPs occurred February 11th and lasted for several days. This event occurred a couple days after an atmospheric river (AR) storm made landfall at BML and deposited >100 mm of precipitation at the site. Precipitation can lead to increased production of bioaerosol and INPs during and shortly after rainfall (Huffman et al., 2013; Morris et al., 2014; Chapter 3 of this thesis), though that does not appear to be the case for these results as INP_{Bio} actually decreased during rainfall. Elevated warm INP concentrations have been observed up to 20 days after heavy precipitation due to rainfall-induced spore germination and subsequent release (Bigg et al., 2015). Rainfall-induced spore release triggered by rain could also lead to recurrent maxima and may partially explain the spike in warm INP_{Bio} observed 2/20-2/22. After this maxima, there was an extended drying out period in which the relative humidity (RH) at the site dropped below 40% for several days. Following this period, bioaerosol production decreased significantly. An increase in wind speed and direction shift to the N/NW (i.e. from the Pacific Ocean) resulting in dust becoming the primary aerosol type of INPs. After the winds shifted, bioaerosol once again became the primary source of INP_{-20} for the rest of the study.

While recent research has implicated that the emission of bioaerosol from the ocean may contribute to INP populations (Burrows et al., 2013; DeMott et al., 2016; McCluskey et al., 2018a), it appears that the source of bioaerosols during this study were primarily terrestrial. To date there has been no published evidence that rainfall leads to increased emission of bioparticles from the ocean, while there is ample evidence that terrestrial bioaerosol are increased after rainfall (Bigg et al., 2015; Huffman et al., 2013; Morris et al., 2014). This conclusion is supported through examination of the single particle mass spectra of *Cell-type* particles identified by the ATOFMS (see Chapter 4 of this dissertation). Only 1-2% of these particles contained ion markers associated with sea spray thus suggesting that the ocean was not a major source of these particles.

Direct measurements of INP concentrations at this site were described during Chapter 5 of this dissertation and dust was found to be the primary source of INP_{-30}. During the time periods measured during that study (2/12-2/19), the primary source of estimated INP_{-20} in this work were actually biological particles. This is not surprising, as Mason et al., (2015) also observed that coastal INPs were dominated by biological particles -20 ºC and dust at -30 ºC, it does highlight the importance of considering temperature when describing sources of INPs.

6.5 Conclusions

Single particle ATOFMS measurements of aerosol composition were combined with particle size distributions to estimate contributions of dust, SSA, and bioaerosol to INP concentrations at a coastal site in California. Particle surface areas were calculated for dust and SSA using combined measurements from the ATOFMS and APS. The surface area of dust used to estimate INP_{dust} concentrations using a fit of desert dust-dominated n_s from Price et al., (2018) while the surface area of SSA was used to estimate INP_{SSA} using the n_s parameterization from

McCluskey et al., (2018). Bioaerosol INP concentrations were estimated using the FP3 particle class concentrations measured by the WIBS.

Over the course of the entire study, bioaerosols were determined to be the major source of INP at this site across all temperatures monitored here. Dust was determined to be a relatively minor source overall, while SSA contributions to INP concentrations were negligible. The greatest increase in INP concentrations was observed a few days after precipitation events, and was attributed to increases in bioaerosol production. We hypothesize that the increase in both bioaerosol and INP concentrations during these time periods is due to increased spore germination and subsequent release as previously described in Bigg et al., (2015). This study presents a novel new way to estimate INP sources without using direct measurements of their composition and could be useful for future studies to estimate INP sources in the absence of direct measurements of INP composition.

6.6 Acknowledgements

Louise Kristensen is acknowledged for assisting in the editing of this chapter. This research was supported by the CalWater-2015 field campaign, funded by the National Science Foundation. The authors would also like to thank the UC Davis Bodega Marine Laboratory for the use of laboratory and office space and shipping and physical plant support while collecting data, as well as the California Air Resources Board for the trailer used for sampling. This research was funded by NSF award number 145147 (GC, KP) and NSF award number (1450760, CSM, SMK, PJD.

Chapter 6, in full, is currently being prepared for submission for publication to Atmospheric Chemistry and Physics. Printed with permission from Cornwell, G. C., Rothfuss, N. E., Taylor, H. P., Petters, M. D., DeMott, P. J., Prather, K. A. Assessing contributions to ice

nucleating particle concentrations at a coastal site in California using single particle measurements. The dissertation author was the primary investigator and author of this paper.

6.7 Figures

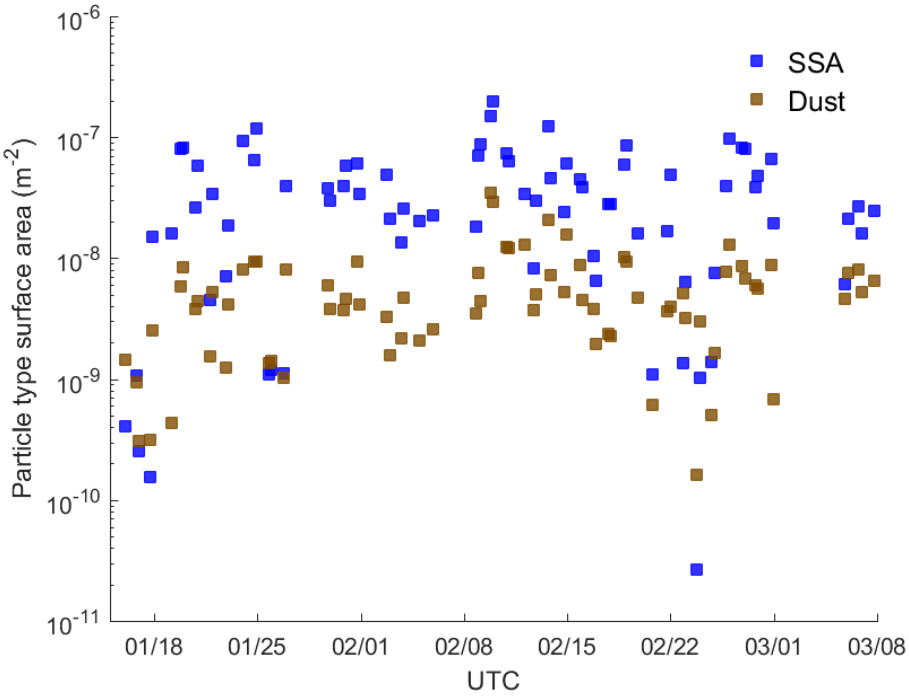

Figure 6.1. Particle type surface areas for SSA (blue) and dust (brown).

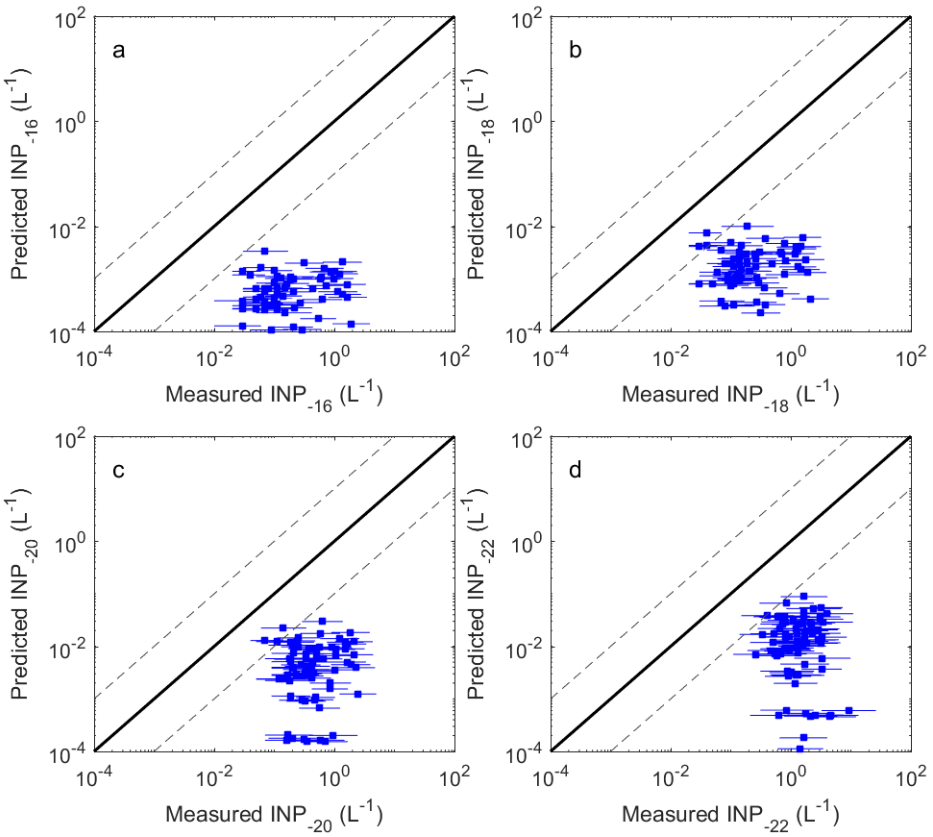

Figure 6.2. Predicted concentrations from SSA as determined by the APS and ATOFMS vs measured concentrations for (a) INP_{-18}, (b) INP_{-20}, and (c) INP_{-22}. Markers indicate mean values while lines indicate the 95% confidence intervals. Straight line shows 1:1, while dashed lines show one order of magnitude above and below the one line.

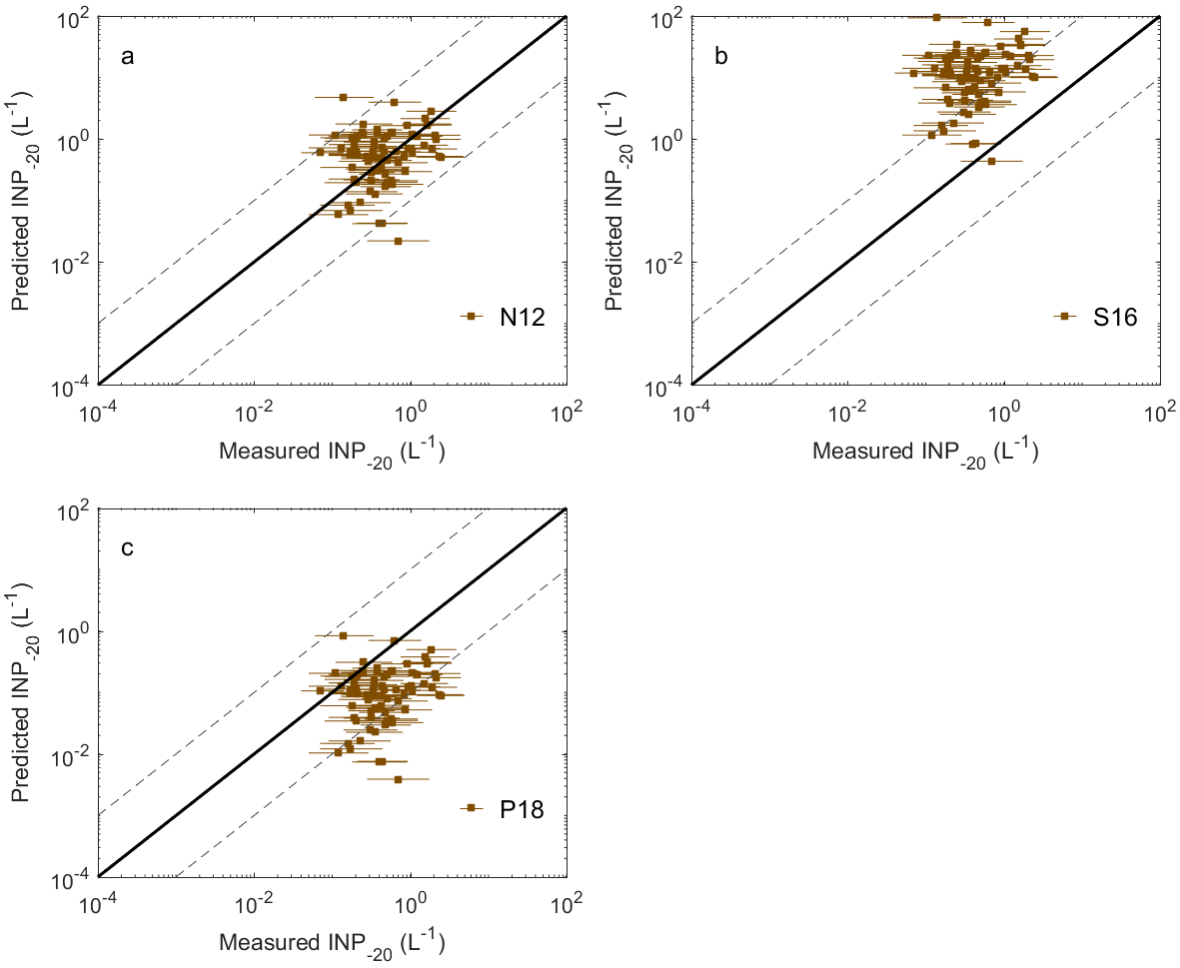

Figure 6.3. Predicted concentrations from dust as determined by the APS and ATOFMS vs measured concentrations using the n_s parameterizations (a) N12 (Niemand et al., 2012), (b) S16 (Steinke et al., 2016), and (c) P18 (an exponential fit of desert-dust dominated airmasses from Price et al., 2018). Markers indicate mean values while lines indicate the 95% confidence intervals. Straight line shows 1:1, while dashed lines show one order of magnitude above and below the 1:1 line.

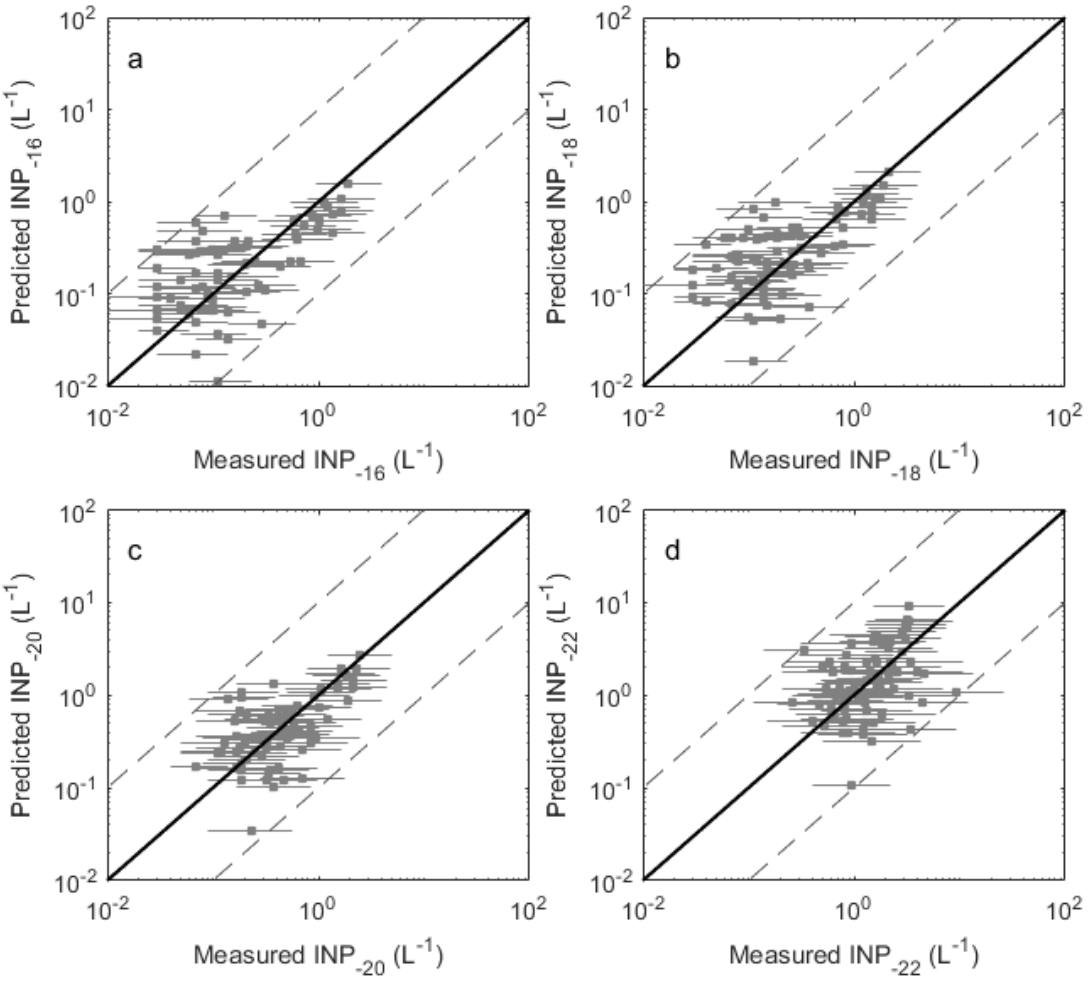

Figure 6.4. Total INP concentrations estimated vs measured for (a) -16 ºC, (b) -18 ºC, (c) -20 ºC, and (c) -22 ºC.

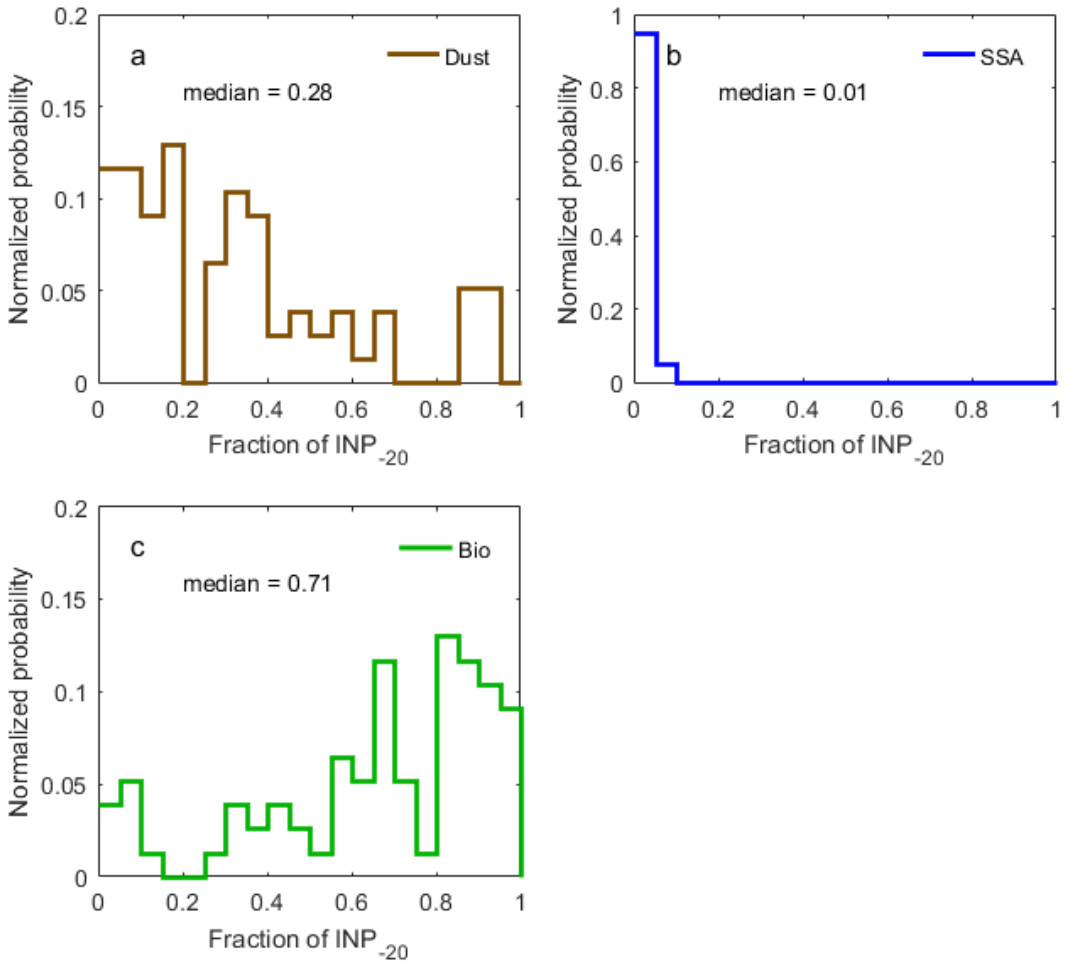

Figure 6.5. Normalized probability distributions of the fraction of INP_{-20} attributed to (a) dust, (b) SSA, and (c) bioaerosol.

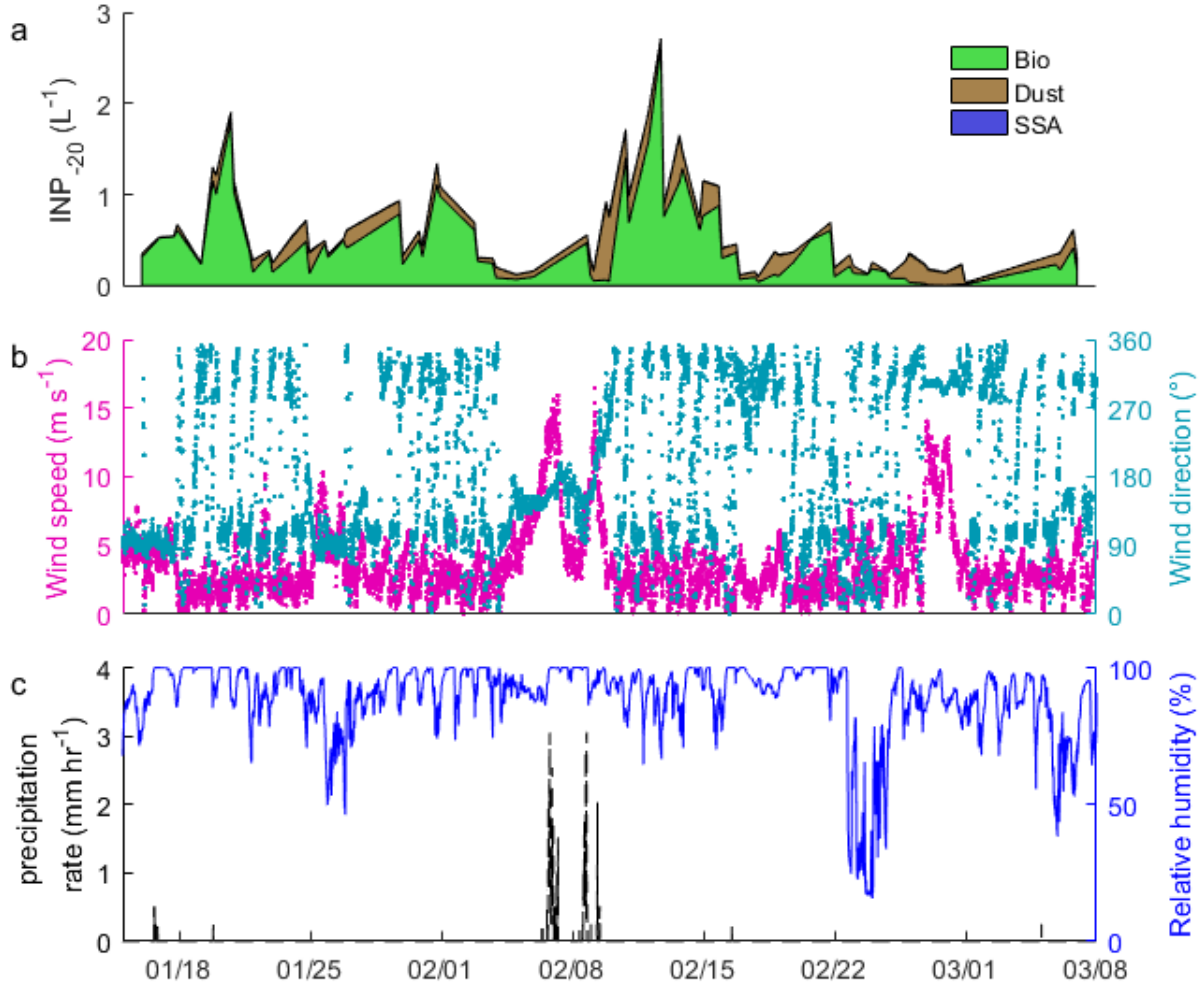

Figure 6.6. Temporal profiles for (a) INP_{-20} segregated by particle type for Bio (green), Dust (brown), and SSA (blue), (b) wind speed (magenta; m s^{-1}) and wind direction (blue-green; º from north), and (c) precipitation rate (black; mm hr^{-1}) and relative humidity (blue; %).

6.8 Supplementary figures

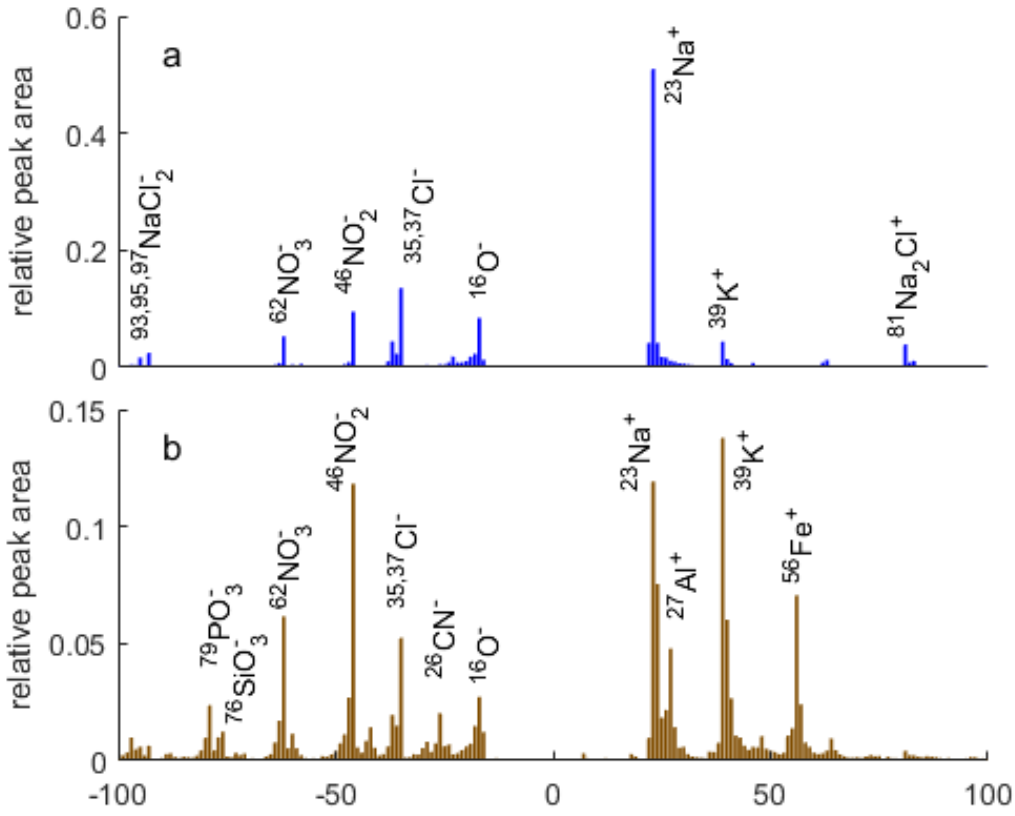

Figure 6.7. Representative spectra for (a) SSA and (b) dust.

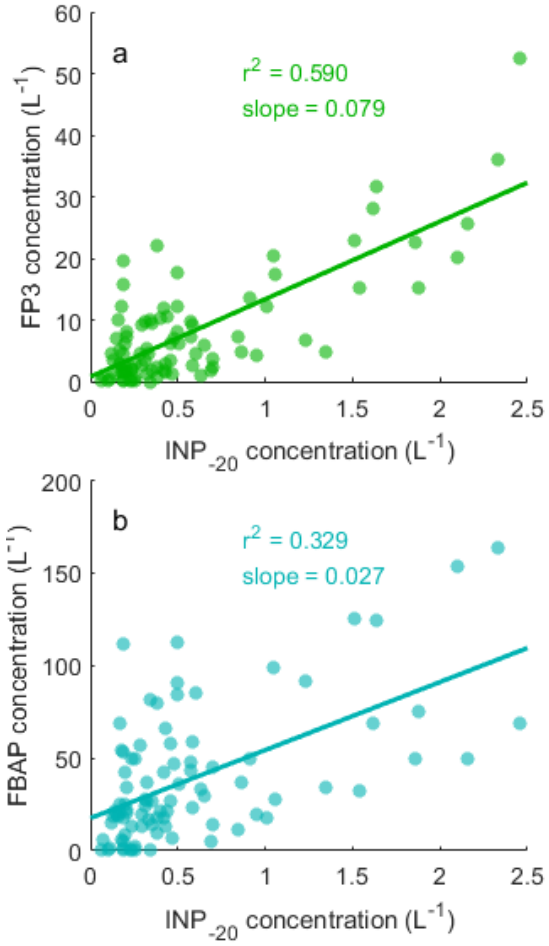

Figure 6.8. Correlation plots between INP_{-20} and (a) FP3 and (b) FBAP particle concentrations measured by the WIBS.

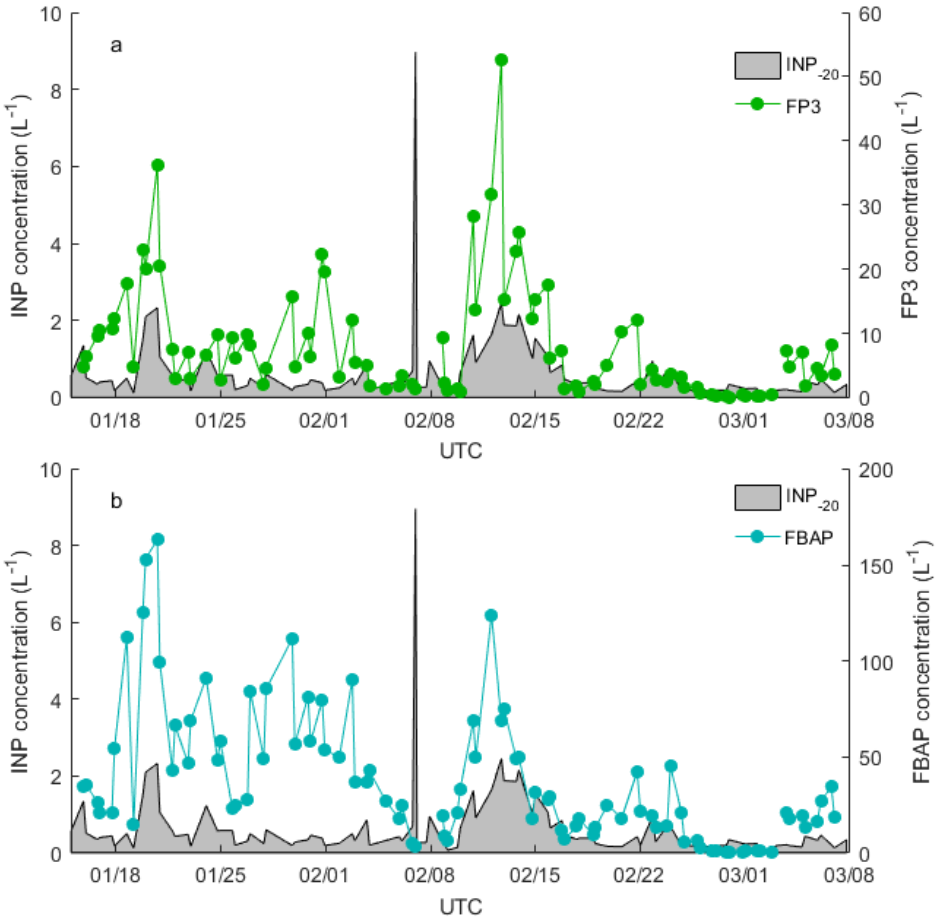

Figure 6.9. Temporal profiles for (a) FP3 particle concentrations (green) and (b) FBAP particle concentrations (turquoise). For both plots, the grey shaded area represents INP_{-20} concentrations.

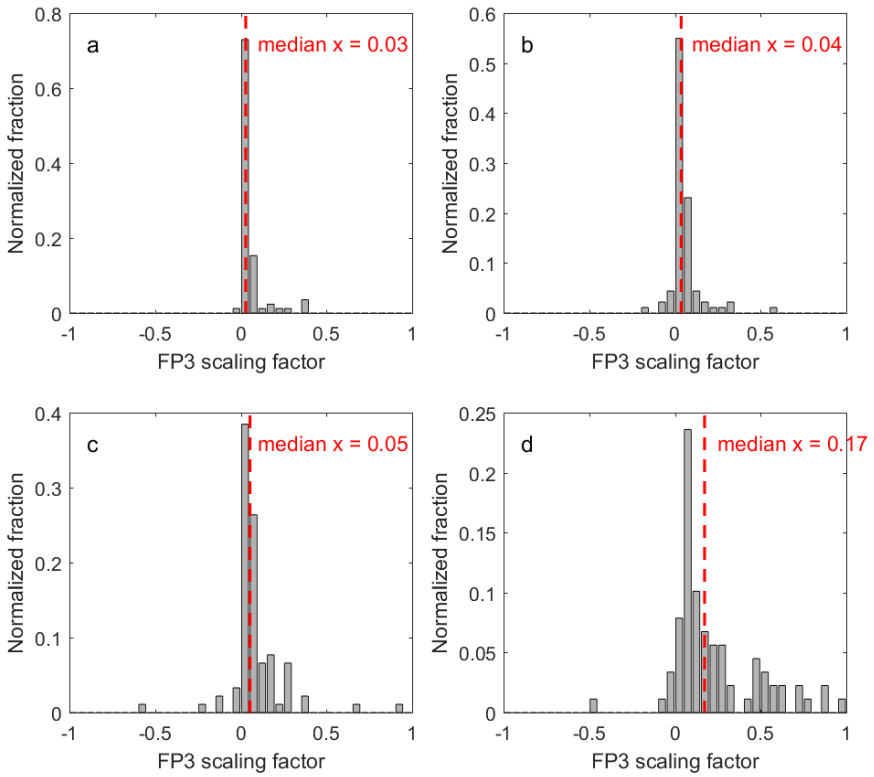

Figure 6.10. Normalized fraction of the FP3 scaling factor, α for (a) -16 ºC, (b) -18 ºC, (c) -20 ºC, and (d) -22 ºC. The red dashed lines show median values.

6.9 Supplementary tables

Table 6.1. Bioparticle classification types for the WIBS. FL1, FL2, and FL3 refer to fluorescent channels 1, 2, and 3 respectively. Reference denotes the study where the particle type was originally described.

Particle type	Particle definitions	Reference
FP	FL1 > 0.0 | FL2 > 0.0 | FL3 > 0	Gabey et al., (2011)
FP3	FL1 ≥ 1900 & FL2 ≤ 500 & FL3 ≤ 500	Wright et al., (2014)
FBAP	FL1 > 0.0 & FL2 ≥ 0.0 & FL3 > 0	Gabey et al., (2011)

6.10 References

Ault, A. P., Williams, C. R., White, A. B., Neiman, P. J., Creamean, J. M., Gaston, C. J., Ralph, F. M. and Prather, K. a.: Detection of Asian dust in California orographic precipitation, J. Geophys. Res., 116(D16205), 1–15, doi:10.1029/2010JD015351, 2011.

Bhave, P. V., Allen, J. O., Morrical, B. D., Fergenson, D. P., Cass, G. R. and Prather, K. a.: A field-based approach for determining ATOFMS instrument sensitivities to ammonium and nitrate, Environ. Sci. Technol., 36(22), 4868–4879, doi:10.1021/es015823i, 2002.

Bigg, E. K., Soubeyrand, S., Morris, C. E. C. E. and Morris, C. E. C. E.: Persistent after-effects of heavy rain on concentrations of ice nuclei, , (2001), 2313–2326, doi:10.5194/acp-15-2313-2015, 2015.

Burrows, S. M., Hoose, C., Poschl, U. and Lawrence, M. G.: Ice nuclei in marine air: Biogenic particles or dust?, Atmos. Chem. Phys., 13(1), 245–267, doi:10.5194/acp-13-245-2013, 2013.

Cziczo, D. J., Ladino, L., Boose, Y., Kanji, Z. A., Kupiszewski, P., Lance, S., Mertes, S. and Wex, H.: Measurements of Ice Nucleating Particles and Ice Residuals, Meteorol. Monogr., 58(April), 8.1-8.13, doi:10.1175/AMSMONOGRAPHS-D-16-0008.1, 2017.

DeMott, P. J., Cziczo, D. J., Prenni, A. J., Murphy, D. M., Kreidenweis, S. M., Thomson, D. S., Borys, R. and Rogers, D. C.: Measurements of the concentration and composition of nuclei for cirrus formation, Proc. Natl. Acad. Sci., 100(25), 14655–14660, doi:10.1073/pnas.2532677100, 2003.

DeMott, P. J., Prenni, A. J., Liu, X., Kreidenweis, S. M., Petters, M. D., Twohy, C. H., Richardson, M. S., Eidhammer, T. and Rogers, D. C.: Predicting global atmospheric ice nuclei distributions and their impacts on climate, Proc. Natl. Acad. Sci., 107(25), 11217–11222, doi:10.1073/pnas.0910818107, 2010.

DeMott, P. J., Hill, T. C. J., McCluskey, C. S., Prather, K. A., Collins, D. B., Sullivan, R. C., Ruppel, M. J., Mason, R. H., Irish, V. E., Lee, T., Hwang, C. Y., Rhee, T. S., Snider, J. R., McMeeking, G. R., Dhaniyala, S., Lewis, E. R., Wentzell, J. J. B., Abbatt, J., Lee, C., Sultana, C. M., Ault, A. P., Axson, J. L., Diaz Martinez, M., Venero, I., Santos-Figueroa, G., Stokes, M. D., Deane, G. B., Mayol-Bracero, O. L., Grassian, V. H., Bertram, T. H., Bertram, A. K., Moffett, B. F. and Franc, G. D.: Sea spray aerosol as a unique source of ice nucleating particles, Proc. Natl. Acad. Sci., 113(21), 5797–5803, doi:10.1073/pnas.1514034112, 2016.

Fan, J., Leung, L. R., Demott, P. J., Comstock, J. M., Singh, B., Rosenfeld, D., Tomlinson, J. M., White, A., Prather, K. A., Minnis, P., Ayers, J. K. and Min, Q.: Aerosol impacts on California winter clouds and precipitation during calwater 2011: Local pollution versus long-range transported dust, Atmos. Chem. Phys., 14(1), 81–101, doi:10.5194/acp-14-81-2014, 2014.

Fan, J., Leung, L. R., Rosenfeld, D., Demott, P. J., Ruby Leung, L., Rosenfeld, D. and Demott, P. J.: Effects of cloud condensation nuclei and ice nucleating particles on precipitation processes and supercooled liquid in mixed-phase orographic clouds, Atmos. Chem. Phys., 17(2), 1017–1035, doi:10.5194/acp-17-1017-2017, 2017.

Gabey, A. M., Gallagher, M. W., Whitehead, J., Dorsey, J. R., Kaye, P. H. and Stanley, W. R.: Measurements and comparison of primary biological aerosol above and below a tropical forest canopy using a dual channel fluorescence spectrometer, Atmos. Chem. Phys., 10(10), 4453–4466, doi:10.5194/acp-10-4453-2010, 2010.

Gabey, A. M., Stanley, W. R., Gallagher, M. W. and Kaye, P. H.: The fluorescence properties of aerosol larger than 0.8 μ in urban and tropical rainforest locations, Atmos. Chem. Phys., 11(11), 5491–5504, doi:10.5194/acp-11-5491-2011, 2011.

Gard, E., Mayer, J. E., Morrical, B. D., Dienes, T., Fergenson, D. P. and Prather, K. A.: Real-Time Analysis of Individual Atmospheric Aerosol Particles: Design and Performance of a Portable ATOFMS, Anal. Chem., 69(20), 4083–4091, doi:10.1021/ac970540n, 1997.

Gross, D. S., Gälli, M. E., Silva, P. J. and Prather, K. A.: Relative sensitivity factors for alkali metal and ammonium cations in single-particle aerosol time-of-flight mass spectra, Anal. Chem., 72(2), 416–422, doi:10.1021/ac990434g, 2000.

Hader, J. D., Wright, T. P. and Petters, M. D.: Contribution of pollen to atmospheric ice nuclei concentrations, Atmos. Chem. Phys., 14(11), 5433–5449, doi:10.5194/acp-14-5433-2014, 2014.

Hill, T. C. J., Demott, P. J., Tobo, Y., Fröhlich-Nowoisky, J., Moffett, B. F., Franc, G. D. and Kreidenweis, S. M.: Sources of organic ice nucleating particles in soils, Atmos. Chem. Phys., 16(11), 7195–7211, doi:10.5194/acp-16-7195-2016, 2016.

Huffman, J. A., Prenni, A. J., Demott, P. J., Pöhlker, C., Mason, R. H., Robinson, N. H., Fröhlich-Nowoisky, J., Tobo, Y., Després, V. R., Garcia, E., Gochis, D. J., Harris, E., Müller-Germann, I., Ruzene, C., Schmer, B., Sinha, B., Day, D. A., Andreae, M. O., Jimenez, J. L., Gallagher, M., Kreidenweis, S. M., Bertram, A. K. and Pöschl, U.: High concentrations of biological aerosol particles and ice nuclei during and after rain, Atmos. Chem. Phys., 13(13), 6151–6164, doi:10.5194/acp-13-6151-2013, 2013.

King, S. M., Butcher, A. C., Rosenoern, T., Coz, E., Lieke, K. I., De Leeuw, G., Nilsson, E. D. and Bilde, M.: Investigating primary marine aerosol properties: CCN activity of sea salt and mixed inorganic-organic particles, Environ. Sci. Technol., 46(19), 10405–10412, doi:10.1021/es300574u, 2012.

Martin, A. C., Cornwell, G. C., Atwood, S. A., Moore, K. A., Rothfuss, N. E., Taylor, H., DeMott, P. J., Kreidenweis, S. M., Petters, M. D. and Prather, K. A.: Transport of pollution to a remote coastal site during gap flow from California's interior: impacts on aerosol

composition, clouds, and radiative balance, Atmos. Chem. Phys., 17(2), 1491–1509, doi:10.5194/acp-17-1491-2017, 2017.

Mason, R. H., Si, M., Li, J., Chou, C., Dickie, R., Toom-Sauntry, D., Pöhlker, C., Yakobi-Hancock, J. D., Ladino, L. A., Jones, K., Leaitch, W. R., Schiller, C. L., Abbatt, J. P. D., Huffman, J. A. and Bertram, A. K.: Ice nucleating particles at a coastal marine boundary layer site: Correlations with aerosol type and meteorological conditions, Atmos. Chem. Phys., 15(21), 12547–12566, doi:10.5194/acp-15-12547-2015, 2015.

McCluskey, C. S., Hill, T. C. J., Sultana, C. M., Laskina, O., Trueblood, J., Santander, M. V., Beall, C. M., Michaud, J. M., Kreidenweis, S. M., Prather, K. A., Grassian, V. and DeMott, P. J.: A Mesocosm Double Feature: Insights into the Chemical Makeup of Marine Ice Nucleating Particles, J. Atmos. Sci., 75(7), 2405–2423, doi:10.1175/JAS-D-17-0155.1, 2018a.

McCluskey, C. S., Jurgita, O., Matteo, R., James, A., Franco, B., Darius, C., Salvatore, M., J., H. T. C., Ulrike, L., A., K. Z., Colin, O., M., K. S. and J., D. P.: Marine and Terrestrial Organic Ice Nucleating Particles in Pristine Marine to Continentally-Influenced Northeast Atlantic Air Masses, J. Geophys. Res. Atmos., 0(ja), doi:10.1029/2017JD028033, 2018b.

Moffet, R. C., Shields, L. G., Berntsen, J., Devlin, R. B. and Prather, K. a.: Characterization of an Ambient Coarse Particle Concentrator Used for Human Exposure Studies: Aerosol Size Distributions, Chemical Composition, and Concentration Enrichment, Aerosol Sci. Technol., 38(March 2015), 1123–1137, doi:10.1080/027868290890344, 2004.

Morris, C. E., Conen, F., Alex Huffman, J., Phillips, V., Pöschl, U. and Sands, D. C.: Bioprecipitation: A feedback cycle linking Earth history, ecosystem dynamics and land use through biological ice nucleators in the atmosphere, Glob. Chang. Biol., 20(2), 341–351, doi:10.1111/gcb.12447, 2014.

Niemand, M., Möhler, O., Vogel, B., Vogel, H., Hoose, C., Connolly, P., Klein, H., Bingemer, H., DeMott, P., Skrotzki, J. and Leisner, T.: A Particle-Surface-Area-Based Parameterization of Immersion Freezing on Desert Dust Particles, J. Atmos. Sci., 69(10), 3077–3092, doi:10.1175/JAS-D-11-0249.1, 2012.

Qin, X., Bhave, P. V and Prather, K. A.: Comparison of Two Methods for Obtaining Quantitative Mass Concentrations from Aerosol Time-of-Flight Mass Spectrometry Measurements, Anal. Chem., 78(17), 6169–6178, 2006.

Ralph, F. M., Prather, K. A., Cayan, D., Spackman, J. R., Demott, P., Dettinger, M., Fairall, C., Leung, R., Rosenfeld, D., Rutledge, S., Waliser, D., White, A. B., Cordeira, J., Martin, A., Helly, J. and Intrieri, J.: Calwater field studies designed to quantify the roles of atmospheric rivers and aerosols in modulating U.S. West Coast Precipitation in a changing climate, Bull. Am. Meteorol. Soc., 97(7), 1209–1228, doi:10.1175/BAMS-D-14-00043.1, 2016.

Rebotier, T. P. and Prather, K. A.: Aerosol time-of-flight mass spectrometry data analysis: A benchmark of clustering algorithms, Anal. Chim. Acta, 585, 38–54, doi:10.1016/j.aca.2006.12.009, 2007.

Reilly, P. T. A., Lazar, A. C., Gieray, R. A., Whitten, W. B. and Ramsey, J. M.: The elucidation of charge-transfer-induced matrix effects in environmental aerosols via real-time aerosol mass spectral analysis of individual airborne particles, Aerosol Sci. Technol., 33(1–2), 135–152, doi:10.1080/027868200410895, 2000.

Richardson, M. S., DeMott, P. J., Kreidenweis, S. M., Cziczo, D. J., Dunlea, E. J., Jimenez, J. L., Thomson, D. S., Ashbaugh, L. L., Borys, R. D., Westphal, D. L., Casuccio, G. S. and Lersch, T. L.: Measurements of heterogeneous ice nuclei in the western United States in springtime and their relation to aerosol characteristics, J. Geophys. Res. Atmos., 112(2), 1–16, doi:10.1029/2006JD007500, 2007.

Song, X. H., Hopke, P. K., Fergenson, D. P. and Prather, K. a.: Classification of single particles analyzed by ATOFMS using an artificial neural network, ART-2A, Anal. Chem., 71(4), 860–865, doi:10.1021/ac9809682, 1999.

Steinke, I., Funk, R., Busse, J., Iturri, A., Kirchen, S., Leue, M., Möhler, O., Schwartz, T., Schnaiter, M., Sierau, B., Toprak, E., Ullrich, R., Ulrich, A., Hoose, C. and Leisner, T.: Ice nucleation activity of agricultural soil dust aerosols from Mongolia, Argentina, and Germany, J. Geophys. Res., 121(22), 13,559-13,576, doi:10.1002/2016JD025160, 2016.

Sultana, C. M., Cornwell, G. C., Rodriguez, P. and Prather, K. A.: FATES: a flexible analysis toolkit for the exploration of single-particle mass spectrometer data, Atmos. Meas. Tech., 10(4), 1323–1334, doi:10.5194/amt-10-1323-2017, 2017.

Suski, K. J., Hill, T. C. J., Levin, E. J. T., Miller, A., DeMott, P. J. and Kreidenweis, S. M.: Agricultural harvesting emissions of ice-nucleating particles, Atmos. Chem. Phys., 18(18), 13755–13771, doi:10.5194/acp-18-13755-2018, 2018.

Tobo, Y., Demott, P. J., Hill, T. C. J., Prenni, A. J., Swoboda-Colberg, N. G., Franc, G. D. and Kreidenweis, S. M.: Organic matter matters for ice nuclei of agricultural soil origin, Atmos. Chem. Phys., 14(16), 8521–8531, doi:10.5194/acp-14-8521-2014, 2014.

Toprak, E. and Schnaiter, M.: Fluorescent biological aerosol particles measured with the Waveband Integrated Bioaerosol Sensor WIBS-4: Laboratory tests combined with a one year field study, Atmos. Chem. Phys., 13(1), 225–243, doi:10.5194/acp-13-225-2013, 2013.

Vergara-Temprado, J., Murray, B. J., Wilson, T. W., O'Sullivan, D., Browse, J., Pringle, K. J., Ardon-Dryer, K., Bertram, A. K., Burrows, S. M., Ceburnis, D., Demott, P. J., Mason, R. H., O'Dowd, C. D., Rinaldi, M. and Carslaw, K. S.: Contribution of feldspar and marine organic aerosols to global ice nucleating particle concentrations, Atmos. Chem. Phys., 17(5), 3637–3658, doi:10.5194/acp-17-3637-2017, 2017.

Vergara-Temprado, J., Miltenberger, A. K., Furtado, K., Grosvenor, D. P., Shipway, B. J., Hill, A. A., Wilkinson, J. M., Field, P. R., Murray, B. J. and Carslaw, K. S.: Strong control of Southern Ocean cloud reflectivity by ice-nucleating particles, Proc. Natl. Acad. Sci., 201721627, doi:10.1073/pnas.1721627115, 2018.

Wright, T. P. and Petters, M. D.: The role of time in heterogeneous freezing nucleation, J. Geophys. Res. Atmos., 118(9), 3731–3743, doi:10.1002/jgrd.503652013, 2013.

Wright, T. P., Hader, J. D., McMeeking, G. R. and Petters, M. D.: High relative humidity as a trigger for widespread release of ice nuclei, Aerosol Sci. Technol., 48(11), i–v, doi:10.1080/02786826.2014.968244, 2014.

Chapter 7. Resuspension of dust as a novel source of ice nucleating particles

7.1 Abstract

The ocean has long been believed to be a relatively weak source of ice nucleating particles (INPs). Thus, dust transported from terrestrial regions can dominate atmospheric INP numbers even in remote marine regions. Studies of ocean-emitted INPs have focused upon sea spray aerosols containing biogenic species produced during phytoplankton blooms. Even though large concentrations of dust are transported over marine regions, resuspended dust has never been explicitly considered as a possible source of oceanic INPs because models assume that deposited dust is not re-emitted from the ocean. We show through laboratory studies of aerosol particles produced from synthetic seawater doped with dust and natural coastal seawater that dust can indeed be ejected from water during bubble bursting. Measurements of INP concentrations show that these ejected dust particles retain their IN activity. Simulating a strong dust deposition event leads to the production of INPs active at temperatures colder than -12 ºC, one to two orders of magnitude greater than both lab sea spray and ambient marine boundary layer measurements. The relevance of these findings is shown in single particle composition measurements along the Californian coast which show that at least 9.0% of dust particles were mixed with sea salt. Additionally, aerosol transport simulations show that resuspension of dust from the ocean will be most impactful over the Southern Ocean, where oceanic INP are thought to dominate atmospheric INP populations.

7.2 Introduction

Atmospheric aerosols are small particles suspended in the atmosphere, onto which water vapor can condense and thus form clouds. Certain aerosols can act as ice nucleating particles (INPs) to trigger the freezing of cloud droplets. Without INPs, ice will not form in the atmosphere at temperatures above -38 ºC (Pruppacher & Klett, 2010). On average, only 1 in 10^5 aerosol

particles in the atmosphere can act as INPs (DeMott et al., 2010), though this is strongly dependent upon particle size, composition, morphology, and temperature (DeMott et al., 2010; Kanji et al., 2017). Despite their rarity, INPs can exert a disproportionate effect upon climate and precipitation dynamics because ice crystals have different lifetimes, growth dynamics, and optical properties compared to liquid water droplets (DeMott et al., 2010).

Dust is considered to be the dominant source of INPs globally (Boose et al., 2016; DeMott et al., 2010). The importance of both predominantly mineral (Atkinson et al., 2013; DeMott et al., 2003, 2010) and mixed organic/mineral soil dust (O'Sullivan et al., 2014; Tobo et al., 2014) as INPs has been confirmed through multiple field studies. Modelling has confirmed the prevalence of dust as INPs, even in marine regions far from major dust sources (Burrows et al., 2013; Vergara-Temprado et al., 2017). Early field studies suggested that ocean sources and transport of continental aerosol particles explained the INP concentrations found over remote marine regions (Bigg, 1973), although it was also noted that regions of elevated INP concentrations were aligned over ocean regions with significant upwelling and thus presumably high phytoplankton populations (Schnell & Vali, 1976). Recent measurements confirm that nascent sea spray aerosol (SSA) emissions are a source of INPs and that these emissions are reasonably consistent with INP concentrations found over some ocean regions (DeMott et al., 2016). To date, most research of oceanic INP populations, has focused upon biogenic species, such as phytoplankton, bacteria, and large biomolecules (DeMott et al., 2016; McCluskey et al., 2017; Wilson et al., 2015). However, when dust is deposited to the sea surface, insoluble particulate metals have been shown to concentrate in surface waters due to bubble-scavenging (Wallace & Duce, 1975, 1978), and be ejected through bubble-bursting (Arimoto et al., 2003) generated by breaking waves (Lewis &

Schwartz, 2004). Sea spray aerosols containing insoluble dust residues could thus represent a previously unrecognized source of ocean-derived INPs.

Bubble bursting at the ocean's surface produces droplets that contain both dissolved and particulate species from seawater (Wang et al., 2017). Through this process, dust particles suspended in the ocean could be ejected from the ocean into the atmosphere. Upon drying, this aerosol would contain an insoluble dust particle, in addition to other constituents in seawater such as dissolved salts and organic species (Figure 7.1). Field measurements have shown that dust is frequently mixed with sea salt in marine and coastal aerosol particles (Andreae et al., 1986; Fan et al., 1996; Sullivan et al., 2007). However, these studies also suggested that the internally mixed dust-sea spray particles were formed by coalescence of cloud droplets containing dust and sea spray and subsequent evaporation, also known as in-cloud processing, and not through ocean ejection of deposited dust (Andreae et al., 1986). To our knowledge, no previous laboratory studies have attempted to determine whether dust may be ejected directly during bubble bursting processes such as in oceanic wave-breaking.

To determine whether sea spray containing dust may contribute significantly to INP populations in marine regions, we utilized a diverse approach that includes laboratory, field, and modeling experiments. Realistic SSA generation methods were used to aerosolize dust from NaCl solutions and natural seawater. The number, size, composition, and IN-activity of these particles were measured, and through these experiments a framework for identifying ocean-ejected dust was determined and compared to previous field studies. Finally, we used a chemical transport model to estimate the global importance of this process.

7.3 Materials and methods

7.3.1 Natural seawater studies overview

SSA were generated from natural seawater via a plunging waterfall mechanism using a Marine Aerosol Reference Tank (MART) The MART replicates the bubble production of breaking waves and the number concentrations and chemical mixing state of SSA generated during wave-breaking processes (Collins et al., 2014; Stokes et al., 2016).

A total of six experiments with natural seawater were conducted in the MART tanks. Each MART was filled with seawater collected at the end of Scripps Pier (La Jolla, CA, 32° 52' N, 117° 15' W, 275 m offshore). Seawater was collected from approximately the top meter of the ocean's surface and a table of collection dates can be found in Table 7.5. Seawater was filtered through 50 μm Nitex mesh (Sefar Nitex 03-100/32) to remove grazers and large debris. Within 24 hours, SSA was generated and mass spectra collected using ATOFMS. More details of these experiments can be found in Lee et al. (2015).

7.3.2 Synthetic seawater studies overview

Sodium chloride (NaCl) aerosols, a simple proxy for SSA, were generated using a miniature Marine Aerosol Reference Tank (Stokes et al., 2016). Synthetic seawater solutions made from typical sea salt mixtures contain trace concentrations of elements also commonly found in dust, making discerning dust particles more difficult. Thus, these experiments were conducted using 35 g NaCl (Fisher Scientific, Certified ACS grade) L-1 milliQ water solution as an inorganic seawater proxy in order to facilitate the unambiguous identification of ejected dust particles during bubble bursting.

For all experiments, 7 L of NaCl solution was doped with 0.5 g of A1 Ultrafine Arizona Test Dust (ATD; Powder Technology Inc., ISO12103-1), equivalent to a 9 g m^{-2} deposition event. Deposition events up to 22 g m^{-2} have been measured, so the amounts used in this study are very large but still atmospherically relevant (Ternon et al., 2010). For each experiment, much of the

seeded dust appeared to sink to the bottom of the tank where it remained during the experiment. However, the NaCl solution grew cloudy indicating that some of the dust particles had become suspended in the solution. Measurements of aerosol particle size, single-particle composition, bulk aerosol composition, and IN activity were made for aerosols generated from both the NaCl and dust-doped NaCl solutions. Experiments measuring aerosol composition and size were performed at University of California, San Diego (UCSD), while the experiments measuring INP concentrations were performed at Colorado State University (CSU) using identical tanks.

7.3.3 CalWater2 Field Campaign

Marine boundary layer aerosol measurements were conducted at the Bodega Marine Laboratory (BML; 38° 190' N, 123° 40' W) in Bodega Bay, California from January 14 to March 9 in 2015 as part of the CalWater2 field campaign. These measurements have been summarized elsewhere (Martin et al., 2017) so we provide only a short overview here. The sampling site at BML was located 100 m ENE of the seashore, and 30 m north of the northernmost BML permanent building. Single particle aerosol composition was measured via ATOFMS in a mobile laboratory.

7.3.4 Ice nucleation measurements

The Colorado State University (CSU) continuous flow diffusion chamber (CFDC; Demott et al., 2015; Rogers et al., 2001) measured INPs in real-time. The CSU-CFDC is a vertically mounted CFDC with cylindrical walls 1.1 cm apart. The walls are chemically treated to be wettable by water, and each cylindrical column is independently temperature controlled. To form a thin layer of ice on each wall, the annular gap is flooded with room temperature water while each wall is held at approximately -27 °C. After icing, aerosols are introduced into the annular gap via a cylindrical knife edge, which is surrounded by a dry, particle-free sheath flow that makes up 85% of the total flow. Both the knife edge and the sheath flow focus the aerosol into a tight lamina,

where the temperature and RH can be precisely controlled by controlling the temperature of each cylindrical column. For immersion-mode freezing experiments, the RH with respect to water was set to a nominal value of 105% to ensure that most aerosol activate into droplets prior to full cooling. Those droplets that contain INP at the aerosol lamina temperature or warmer nucleate into ice. The bottom third of the CSU-CFDC consists of a droplet-evaporation section, where the cylindrical walls are held at the same temperature. Here, the aerosol lamina adjusts toward ice saturation, and is therefore water subsaturated. Thus, droplets will evaporate in this section and ice crystals will persist. All particles >500nm are detected by an OPC at the bottom of the evaporation section, and ice crystals are assumed to be larger than 3.0 μm. The CFDC was operated with a 1.5 μm impactor in front of the inlet in order to ensure that large particles were not erroneously counted as INP.

Aerosol was also collected for offline IN measurements. Aerosol particles were collected on a 0.2 μm pore diameter, 47 mm-diameter Nuclepore track-etched polycarbonate filter (Whatman, GE Healthcare Life Sciences) fitted within an inline filter unit (Pall). Aerosol was filtered with a flow starting at 2.55 L min-1 and reducing to 2.2 L min-1 over a 19 h sampling period. The details of filter and filter unit pre-cleaning procedures are the same as given in McCluskey et al. (McCluskey et al., 2017), except that 0.1 μm filtered deionized water was used for final rinses and all steps were carried out in a laminar flow cabinet.

The filter was placed in a sterile 50 mL Falcon polypropylene tube (Corning Life Sciences), 6 mL of 0.1 um filtered deionized water added and particles re-suspended by tumbling at 1 cycle s-1 on a Roto-Torque (Cole-Palmer) for 20 min. Twenty- and forty-fold dilutions of the suspension were also made, and then 32×50 μL aliquots of each suspension were dispensed into 96 well PCR trays (μCycler). Immersion freezing temperature spectra and 95% confidence intervals were

obtained using the Colorado State University Ice Spectrometer (IS), as described in Hiranuma et al. (2015) but with the headspace purged with 1.0-0.25 L min-1 of cooled nitrogen, with flow decreasing as temperatures were lowered.

7.3.5 ATOFMS measurements and particle type identification

The ATOFMS measures size-resolved single particle chemical composition (E. Gard et al., 1997). The instrument was calibrated for D_{va} with an external calibration of the sizing region using polystyrene latex sphere standards. A 266 nm pulsed Nd:YAG laser (1.0-1.3 mJ/pulse, 8 ns pulse, 700 μm spot size) was used to desorb and ionize particles into a bipolar time-of-flight mass spectrometer. Positive and negative mass spectra were collected and, along with particle size, used to identify particle types.

Particles from 0.5 to 4.5 μm (D_{va}) were utilized for analysis in this work. A total of 102,685, 2,811,330, and 1,207,617 single particle mass spectra were acquired by the ATOFMS during the NaCl solution, natural seawater, and CalWater-2 field campaign, respectively. All particles were dried prior to measurements using two silicate diffusion drier (RH~15-30%) in order to improve the quality of the spectra. Particle data were imported into Matlab (Mathworks Inc., www.mathworks.com) and analyzed using the single-particle mass spectrometer analysis toolkit FATES (Sultana et al., 2017). For the natural and synthetic seawater experiments, peak area filters were created to identify NaCl-Dust (Table 7.1) and SSA-Dust particles (Table 7.2) through mass spectral features associated with dust (Guazzotti et al., 2001; Sullivan et al., 2007). A list of common mass spectral features for both dust and sea spray are also provided (Table 7.3). Due to the chemical complexity of the CalWater-2 dataset, clustering techniques were employed in order to identify particle types. Relative mass spectra were initially grouped by the ART-2a neural net algorithm (Song et al., 1999). The algorithmically generated clusters were refined and grouped

into particle types using expert knowledge utilizing particle size, mass spectral similarity, and referencing particle types in previously published lab and field studies on dust (Silva et al., 2000; Sullivan et al., 2007) and sea spray (Gard et al., 1998; Sultana et al., 2017).

7.3.6 Simulations of Dust Resuspension and Effects upon INP Concentrations

The Community Atmospheric Model, version 5. (CAM5), which is the atmospheric component of the Community Earth System Model (CESM 1.2.2), was used to investigate the global relevance of the ejection of dust in sea spray (Hurrell et al., 2013; Neale et al., 2012). The meteorological model was nudged with Modern-Era Retrospective analysis for Research and Applications (MERRA) reanalysis fields for the year 2015. Aerosol processes, including the emission, transport, and deposition of mineral dust and sea salt, were computed with the modal aerosol module (MAM3) aerosol scheme (Albani et al., 2014; Liu et al., 2012). Extra tracer species were added to distinguish the fresh and re-aerosolized dust particles.

Ejection of the deposited dust was computed from sea spray emission and dust concentrations in the ocean surface layer (OSL) analogous to the method used to Mayol et al. (2014). CAM5 includes an emission model for sea spray aerosol based on Monahan et al. (1986) and Martensson et al. (2003), which provides the emitted dry mass of SSA. Sea salt emission flux was converted to ejected volume of ocean water and the dust concentration in the OSL multiplied by the EF was used to compute the dust aerosolization flux. The factors governing EF are not well understood, and highly variable. Two EF were simulated in order to determine the upper and lower bounds of this process, an EF of 100 (Aller et al., 2005) and 10000 (Weisel et al., 1984).

Dust concentrations in the OSL were determined from the mass of dust particles deposited onto the sea surface by both dry and wet deposition. Large uncertainties are present in the estimates of the surface lifetime of dust because not much is known about how dust interacts with the

organic-enriched SSML or with bubbles created by breaking waves. Dust lifetime was determined using a range of particle sedimentation velocities from 0.2 to 10 m day-1 (Dammshäuser et al., 2013; Ohnemus & Lam, 2015), and assuming that the depth of the OSL was 1 m. Dust lifetimes in the OSL were kept constant for all atmospheric conditions and the same lifetimes were applied for wet and dry deposited dust. Due to the fact that dust particles are ejected inside of sea spray droplets there is an upper limit on the size of dust particles that can be resuspended by breaking waves. As such, re-emitted dust particles were assigned to a size bin with 3 μm geometric mean diameter with a 1.5 μm standard deviation. INP emissions from dust resuspension were calculated using total particle surface area and the Niemand parameterization (2012) to estimate the number of active sites. INP concentrations were assumed to be equal to the number of active sites. Model simulation parameters and outputs are summarized in Table 7.6.

7.4 Results and discussion

7.4.1 Aerosolization of dust via bubble bursting

Aerosols were generated utilizing realistic bubble bursting techniques from two systems: NaCl solutions doped with Arizona Test Dust (ATD, a heterogeneous dust standard) and natural surface seawater collected from a coastal location. A population of the single particle mass spectra from both aerosols, measured with an aerosol time-of-flight mass spectrometer (ATOFMS), contained ion signatures indicative of dust, showing that dust was ejected into the aerosol phase (Figure 7.2 and Figure 7.6). These mass spectra with dust signatures (NaCl-Dust and SSA-Dust for the NaCl solution and natural seawater experiments, respectively) also frequently contained sodium chloride ion markers ($^{81,83}Na_2Cl^+$, $^{93,95,97}NaCl_2^-$), indicating the presence of sodium chloride internally mixed with dust within the same aerosol particle, as depicted in Figure 7.1.

Internally mixed dust with sea salt has been previously observed in field studies using ATOFMS, though its presence was attributed to in-cloud processing (Sullivan et al., 2007).

Dust ion signatures observed in the NaCl-Dust and SSA-Dust mass spectra could have resulted from the dissolution of dust chemical species into the seawater rather than the ejection of particulate dust in an SSA droplet. If the detected dust signatures were the result of the transfer of dissolved species from the water to aerosol, then the NaCl-Dust and SSA-Dust fractions would likely contain no clear trend across the aerosol size range whereas the likelihood of particulate dust transfer in an SSA droplet should increase with aerosol particle size. Figure 7.3 shows that the number fraction of NaCl-Dust and SSA-Dust particles increased with increasing vacuum aerodynamic particle diameter (D_{va}), suggesting that these aerosols indeed contained particulate dust. The number fraction of NaCl-Dust in the synthetic seawater experiments increased from ~6 to 33 % and the number fraction of SSA-Dust in the natural seawater experiments increased from ~2 to 6% from 0.5 to 4.5 μm (D_{va}). However, these values do not represent the true number fraction of dust-containing aerosols due to the semi-quantitative nature of the ATOFMS (Allen et al., 2000; Gross, Gälli, Silva, & Prather, 2000). The number fraction of SSA particles containing dust in the natural seawater experiments was estimated through a combination of sizing, ICP-MS, and ATOFMS measurements to range from 0.04-1.23% (see section 7.8 for more details). Although our results indicate that dust can be emitted through bubble-bursting, dust-containing aerosols are unlikely to make up a large number fraction of the aerosol particles generated. However, INP concentrations are extremely low over oceans in comparison to land regions (DeMott et al., 2016; McCluskey, et al., 2018). Over the Southern Ocean (SO), this may result in a cloud regime that is ultra-sensitive to any additional sources of INP, so even modest increases in INP number concentrations could have a large effect upon cloud glaciation (Vergara-Temprado et al., 2018).

7.4.2 Identification of SSA-Dust in marine environments

Aerosols were generated utilizing realistic bubble bursting techniques from two systems: NaCl solutions doped with Arizona Test Dust (ATD, a heterogeneous dust standard) and natural surface seawater collected from a coastal location. A population of the single particle mass spectra from both aerosols, measured with an aerosol time-of-flight mass spectrometer (ATOFMS), contained ion signatures indicative of dust, showing that dust was ejected into the aerosol phase (Figure 7.2 and Figure 7.7). These mass spectra with dust signatures (NaCl-Dust and SSA-Dust for the NaCl solution and natural seawater experiments, respectively) also frequently contained sodium chloride ion markers ($^{81,83}Na_2Cl^+$, $^{93,95,97}NaCl_2^-$), indicating the presence of sodium chloride internally mixed with dust within the same aerosol particle, as depicted in Figure 7.1. Internally mixed dust with sea salt has been previously observed in field studies using ATOFMS, though its presence was attributed to in-cloud processing (Sullivan et al., 2007).

Dust ion signatures observed in the NaCl-Dust and SSA-Dust mass spectra could have resulted from the dissolution of dust chemical species into the seawater rather than the ejection of particulate dust in an SSA droplet. If the detected dust signatures were the result of the transfer of dissolved species from the water to aerosol, then the NaCl-Dust and SSA-Dust fractions would likely contain no clear trend across the aerosol size range whereas the likelihood of particulate dust transfer in an SSA droplet should increase with aerosol particle size. Figure 7.3 shows that the number fraction of NaCl-Dust and SSA-Dust particles increased with increasing vacuum aerodynamic particle diameter (D_{va}), suggesting that these aerosols indeed contained particulate dust. The number fraction of NaCl-Dust in the synthetic seawater experiments increased from ~6 to 33 % and the number fraction of SSA-Dust in the natural seawater experiments increased from ~2 to 6% from 0.5 to 4.5 μm (D_{va}). However, these values do not represent the true number fraction

of dust-containing aerosols due to the semi-quantitative nature of the ATOFMS (Allen et al., 2000; Gross et al., 2000). The number fraction of SSA particles containing dust in the natural seawater experiments was estimated through a combination of sizing, ICP-MS, and ATOFMS measurements to range from 0.04-1.23% (see section 7.8 for more details). Although our results indicate that dust can be emitted through bubble-bursting, dust-containing aerosols are unlikely to make up a large number fraction of the aerosol particles generated. However, INP concentrations are extremely low over oceans in comparison to land regions (DeMott et al., 2016; McCluskey et al., 2018). Over the Southern Ocean (SO), this may result in a cloud regime that is ultra-sensitive to any additional sources of INP, so even modest increases in INP number concentrations could have a large effect upon cloud glaciation (Vergara-Temprado et al., 2018).

7.4.3 Ice nucleating activity of ocean-ejected dust

The modest IN activity of SSA has been attributed to biogenic components in sea spray (DeMott et al., 2016; McCluskey et al., 2017) The re-suspension of dust in SSA has never been explicitly considered as a source of enhanced IN activity in marine aerosols. However, our model experiments show that sea spray containing dust particles can act as INPs. INP measurements of the aerosols generated from the dust-doped NaCl solutions were normalized to 150 pt cm^{-3} for direct comparison to prior laboratory and field data, and yielded INP concentrations of over 100 L^{-1} at -30 °C (Figure 7.4a) and IN activity was detectable at temperatures as warm as -13 °C. Pure NaCl droplets do not undergo immersion/condensation heterogeneous freezing (Alpert et al., 2011), which indicates that the measured IN activity is a result of dust ejected in the NaCl water droplet.

The magnitude, nucleation temperature, and the temporal evolution of marine biological INPs represent active areas of research and, as yet, it is difficult to compare their relative

importance with dust INPs ejected from the ocean in sea spray. McCluskey et al. (2017) measured IN activity of lab-generated SSA during the course of an ocean-relevant phytoplankton bloom and reported INP concentrations up to 1 L^{-1} at temperatures colder than -25 ºC. In contrast, the dust INP concentrations were between 30 and 40 L^{-1} at -26 ºC, when total aerosol concentration is normalized to 150 pt cm^{-3}. These INP values reported here are for an extremely large, though still atmospherically relevant (see Ternon et al., 2010 for more info) dust deposition event (9 g m^{-2}) and may represent an upper limit for contributions from resuspended dust (Lawrence & Neff, 2009). Assuming that INP concentrations scale proportionately with dust deposition, a more realistic dust deposition event of 0.3 g m^{-2} would result in INP concentrations of 1 L^{-1} at -26 ºC. Under these conditions, the ejection of dust in sea spray would contribute as much or more to INP populations than what has been observed for freshly produced SSA.

The active site density (n_s), a parameter commonly used to compare relative IN-activity between different sources in a deterministic manner (Niemand et al., 2012), was calculated in order to facilitate comparison with other studies. The n_s for the dust-doped NaCl aerosols was at least one order of magnitude greater than that measured for the lab-generated SSA across all temperatures (Figure 7.4b), and greater than two orders of magnitude for temperatures colder than -18 ºC. The difference is not as great when compared to the ambient marine boundary layer (MBL) measurements shown which may include INP from non-marine sources, though a trend in increased IN activity at temperatures below -18 ºC was also observed. Notably, the measurements for the dust-doped NaCl aerosols approach the mineral dust parameterization developed by Niemand et al. (Niemand et al., 2012), though it should be reiterated that the assumed atmospheric dust concentrations were relatively high.

The IN measurements presented in this study show that dust particles remain effective as INP after ejection from the ocean. Our measurements were collected within a few hours of the dust addition, but longer ocean residence times could potentially alter the structure and/or composition of the dust through dissolution and thus disrupt active sites. However, seawater also contains small (<0.2 μm) organic ice nucleating entities (INE) from diatom or bacterial exudates that freeze at temperatures >-8 ºC (McCluskey, et al., 2018; Wilson et al., 2015). These INE could adsorb onto dust conferring their IN activity in an analogous processed observed for organic species mixing and increasing the freezing temperature of mineral soil dusts (Augustin-Bauditz et al., 2016; O'Sullivan et al., 2016; Tobo et al., 2014).

7.4.4 Atmospheric implications

The Community Atmospheric Model (CAM5.0), the atmospheric component of the Community Earth System Model (CESM 1.2.2), was used to investigate the global relevance of the ejection of dust in sea spray (Hurrell et al., 2013; Neale et al., 2012). While additional sources of dust to the ocean such as terrestrial run-off or riverine inputs will contribute to potential dust concentrations we focus only upon atmospheric deposition processes in this study, based on model studies modifying the existing dust and sea salt parameterizations within the model (Albani et al., 2014; Liu et al., 2012).

The spatial distribution of ejected dust was similar across all simulations, while the total magnitude changed based upon the input parameters. As such we show the results of a single simulation to highlight the key spatial trends and regions most affected by these processes. The fraction of dust particles that get resuspended was highest in regions with high sea spray emissions such as the SO and south of Greenland (Figure 7.5a). The calculated INP_{-25} concentration in the surface layer of the model is highest in regions downwind of major dust sources including the

Caribbean and the Arabian sea (Figure 7.5c). However, resuspended dust particles make up the greatest fraction of relative to all dust in the atmosphere in the SO (Figure 7.5b). Coupled with the fact that the SO is predicted to have low INP contributions from other sources, the effect of dust resuspension on atmospheric INPs is expected to be the greatest in the SO (Vergara-Temprado et al., 2017, 2018).

While the SO is the location where this newly-discovered dust resuspension process will likely be most important, the total magnitude of this effect remains to be determined. The factors driving the ejection of dust from the ocean are (1) the lifetime of dust in the upper surface of the ocean, (2) the enrichment factor (EF) of dust transfer from seawater to the aerosol phase, and (3) the total amount of sea spray emitted. The lifetime of suspended particles in the surface ocean is complex and depends upon a wide range of intertangled processes. Dust size and density will dictate how long particles remain suspended at a depth where they may be aerosolized, while their size and composition will affect their dissolution rates (Mackey et al., 2015). In addition, suspended particles can be removed through vertical convection (Migon et al., 2002) and through aggregation with organic species (Bressac et al., 2014; Deuser et al., 2018). Field studies have measured particle settling velocities ranging over a considerable range, from 0.1 to 55 m day^{-1} (Dammshäuser et al., 2013; Ohnemus & Lam, 2015). To address the range of settling velocities within the model we used particle lifetimes of 0.1, 1, 5 days, and 50 days within the upper 1 meter of the ocean.

Ejection of dust from seawater is also driven by the EF of particulate dust from the surface ocean to the aerosol phase. The EF will likely vary by dust size, density and composition, while variables such as particle depth, bubble size, and organic content of the water will also affect transfer. As such, we use lower (100) and upper (10,000) estimates for the EF to show the extent

to which this process might vary (Aller et al., 2005; Hunter, 1980). A single grid cell (52 ºS, 80 ºE) was chosen to compare how particle lifetime and EF affect dust resuspension (Figure 7.5d). For a simulation with a dust particle lifetime of 0.1 day in the ocean and a 100 EF simulation, there is virtually no resuspended dust, while for a simulation with a dust particle lifetime of 5 days and an EF of 10000, nearly 90% of the dust at the surface came from the ocean. The corresponding range of additional INP_{-25} produced by resuspended dust can vary by over three orders of magnitude. Comparisons of INP_{-20} simulated here to measurements conducted at Cabo Verde Observatory (Figure 7.10) show that the combination of an EF of 10000 and a particle lifetime of greater than 1 day produces unrealistically high INP concentrations though most of the other simulations do not (Welti et al., 2018). This demonstrates that determining the true impact of this process requires that the parameters controlling resuspension be better constrained. It should also be noted that the results reported here are annual emissions so it is also possible that contributions of resuspended dust to INP populations could be significant at times following a major dust transport event. Due to the uncertainty in marine INP identity and the magnitude of their effects upon climate, if dust resuspension contributes significantly to their emission then it is critical that this process be accounted for in future studies.

7.5 Conclusions

A series of lab experiments conducted using realistic sea spray generation methodologies showed that dust can be resuspended during wave breaking. Dust deposition events 9 g m^{-2} were simulated and their single-particle composition monitored with an ATOFMS. Dust was shown to be aerosolized during all of these experiments. The strong relationship between sea spray particle size and the likelihood that it contained dust indicated that these whole dust particles and not dissolved elements. Online and offline measurements of INP concentrations showed that this

resuspended dust was still IN-active at concentrations significantly higher than lab-generated SSA or ambient measurements. The relatively weak IN-activity of sea spray and the well-documented IN-activity of dust means that even modest amounts of dust ejected from the ocean may significantly affect INP concentrations over remote marine regions.

The global prevalence of this process was modelled using the Community Earth System Model (CESM 1.2.2) and effects upon INP concentrations were estimated using an active site density parameterization for dust (Niemand et al., 2012). The spatial distribution of ejected dust was similar across all simulations, while the total magnitude changed based upon the input parameters. The fraction of dust particles that get resuspended was highest in regions with high sea spray emissions such as the SO and south of Greenland. The calculated INP_{-25} concentration in the surface layer of the model is highest in regions downwind of major dust sources including the Caribbean and the Arabian sea. However, resuspended dust particles make up the greatest fraction of relative to all dust in the atmosphere in the SO. Coupled with the fact that the SO is predicted to have low INP contributions from other sources, the effect of dust resuspension on atmospheric INPs is expected to be the greatest in the SO (Vergara-Temprado et al., 2017, 2018). Due to the uncertainty in marine INP identity and the magnitude of their effects upon climate, if dust resuspension contributes significantly to their emission then it is critical that this process be accounted for in future studies.

7.6 Acknowledgements

This work was supported by the National Science Foundation through the Centers of Chemical Innovation Program via the Center for Aerosol Impacts on Chemistry of the Environment (CHE-1305427) and the CalWater2 field campaign (NSF AGS-1451347). The authors thank the UC Davis Bodega Marine Laboratory for the use of laboratory and office space

and shipping and physical plant support during the CalWater2 field campaign. NM and MP acknowledge support from the Atkinson Center for a Sustainable Future at Cornell University.

Chapter 7, in full, is currently being prepared for submission for publication to Journal of Geophysical Research: Atmospheres. Printed with permission from Cornwell, G. C., Sultana, C. M., Prank, M., Cochran, R. E., Hill, T. C. J., Schill, G. P., DeMott, P. J., Mahowald, N., Prather, K. A. Resuspension of dust as a novel source of ice nucleating particles. The dissertation author was the primary investigator and author of this paper.

7.7 Figures

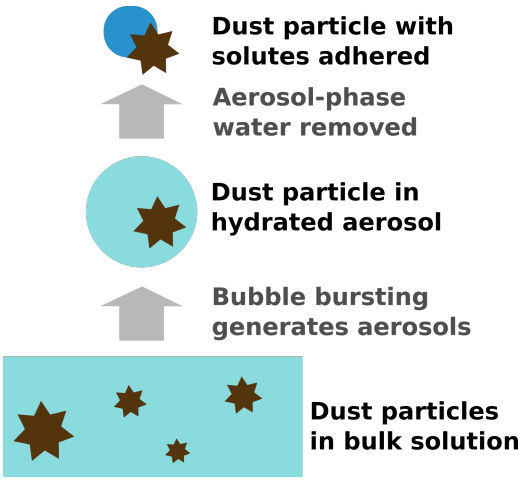

Figure 7.1. Schematic representation of the process through which dust gets ejected during bubble bursting and becomes incorporated into the aerosol phase.

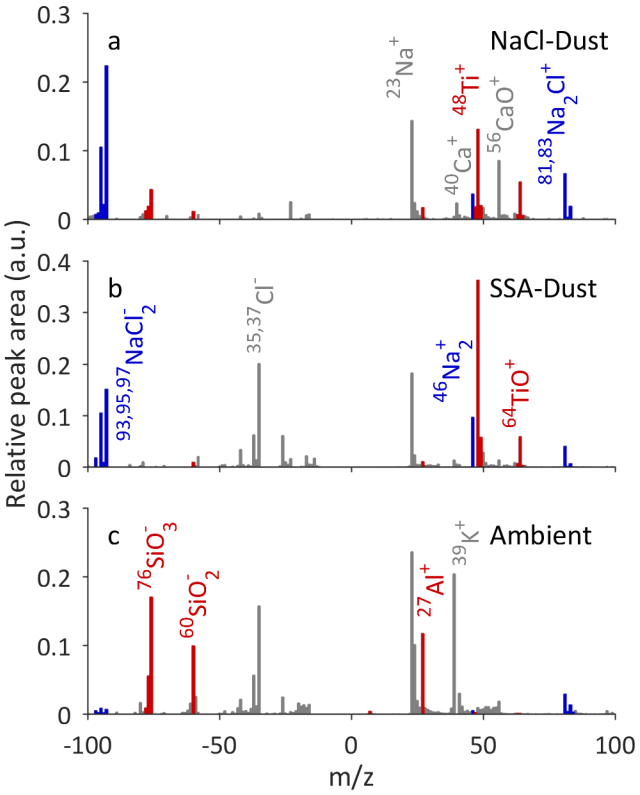

Figure 7.2. Representative mass spectra with dust ion signatures observed during (a) the dust-doped NaCl solution experiments, (b) natural seawater experiments, and (c) the CalWater2 field campaign. Peaks associated with sea salt and dust are shown in blue and red, respectively. Peaks shown in grey are commonly found in mass spectra of both sea spray and dust particles. Peak areas are in arbitrary units (a.u.).

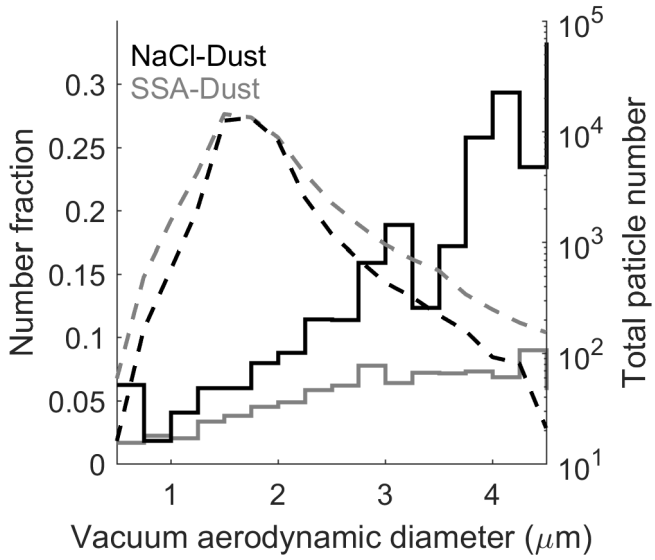

Figure 7.3. The size resolved fraction of single particle mass spectra classified as NaCl-Dust (black) and SSA-Dust (grey) (solid lines, left axis). The total number of mass spectra within each bin is also indicated (dashed lines, right axis).

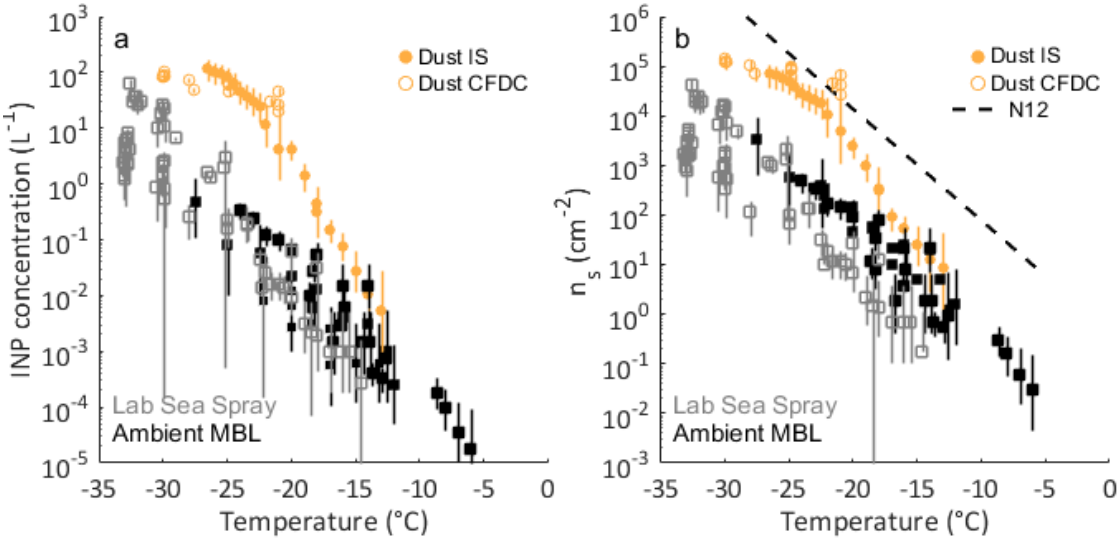

Figure 7.4. Temperature profile of (a) INP concentrations and (b) surface active site density, ns, for the dust-doped NaCl experiments described here (yellow), previously published laboratory sea spray (grey), and ambient marine boundary layer (black) measurements. Lab sea spray INP concentrations, including the dust-doped NaCl experiments, are normalized to 150 pt cm-3. The dashed black line shows the mineral dust parameterization from Niemand et al. (2012).

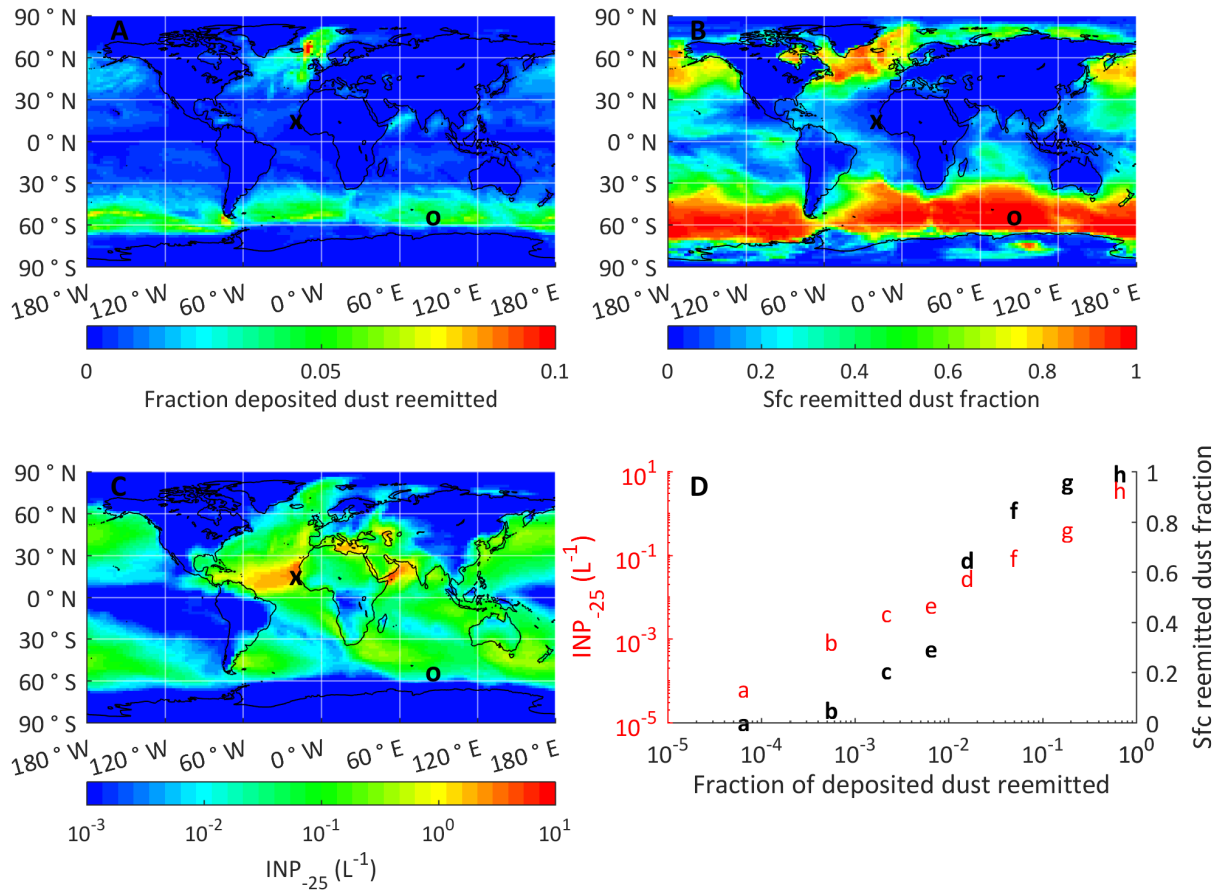

Figure 7.5. Spatial distribution of the annual average for (a) the fraction of deposited dust that is reemitted (b) the fraction of dust at the lowest model layer (sfc) that has been resuspended from the ocean (c) INP-25 concentrations. Panels (a), (b), and (c) are shown for simulation case c. Panel (d) shows the dependence of INP-25 and resuspended dust fraction on different parameters at the grid box in the Southern Ocean (marked with an o). Cabo Verde Observatory is marked with an x. Each of the simulation cases (a, b, c, d, e, f, g, h) has a different assumption for the lifetime in the top 1m layer (0.1, 1, 5, 50, 0.1, 1, 5 and 50 days, respectively) and water to aerosol enrichment factor (100, 100, 100, 100, 10000, 10000, 10000, and 10000 respectively).

7.8 Supplementary materials

7.8.1 Identification of dust particles via ATOFMS

Figure 7.6 shows representative mass spectra for NaCl, sea spray aerosol, dust, and NaCl-Dust and SSA-Dust. Particle mass spectra were normalized to the total peak area for each spectrum. Peak area filters were determined to identify NaCl-Dust from NaCl (Table 7.1) and SSA-Dust from SSA (Table 7.2) particles through mass spectral features associated with dust (Guazzotti et al., 2001; Ryan C. Sullivan et al., 2007). Mass spectral peaks commonly found in dust and sea spray, along with their assignments, are shown in Table 7.3.

7.8.2 Aerosol sizing

Particle size distributions were collected alongside ATOFMS in order to determine if the ejection of dust via bubble-bursting caused a change in the size or number of particles emitted (Figure 7.7). There was no significant difference between the size distributions of the control and dust-doped experiments.

Synthetic sea spray aerosol particle size was measured using a Scanning Mobility Particle Sizer 3938 (SMPS, TSI Inc.) and an Aerodynamic Particle Sizer 3321 (APS, TSI Inc.). Aerosol particles were dried to an RH of approximately 15-30% prior to measurement using two silicate diffusion driers. The SMPS was operated with a pump flow of 0.6 L min^{-1} and a sheath flow of 3.0 L min^{-1}, measuring the mobility diameter from 13.6 to 736.5 nm. Assuming that particles are spherical, mobility diameter corresponds to physical diameter (D_p). Standard corrections provided by the software, diffusion and multiple charge corrections, were applied to the SMPS data. The APS was operated with a sample flow rate of 1.0 L min^{-1} and a sheath flow of 4.0 L min^{-1} and measured aerodynamic diameter from 0.6 to 20 μm. Aerodynamic diameter was converted to

physical diameter assuming spherical particles and an effective density of 1.8 g cm^{-3} as in previous studies of SSA (Wang et al., 2015).

7.9 Supplementary figures

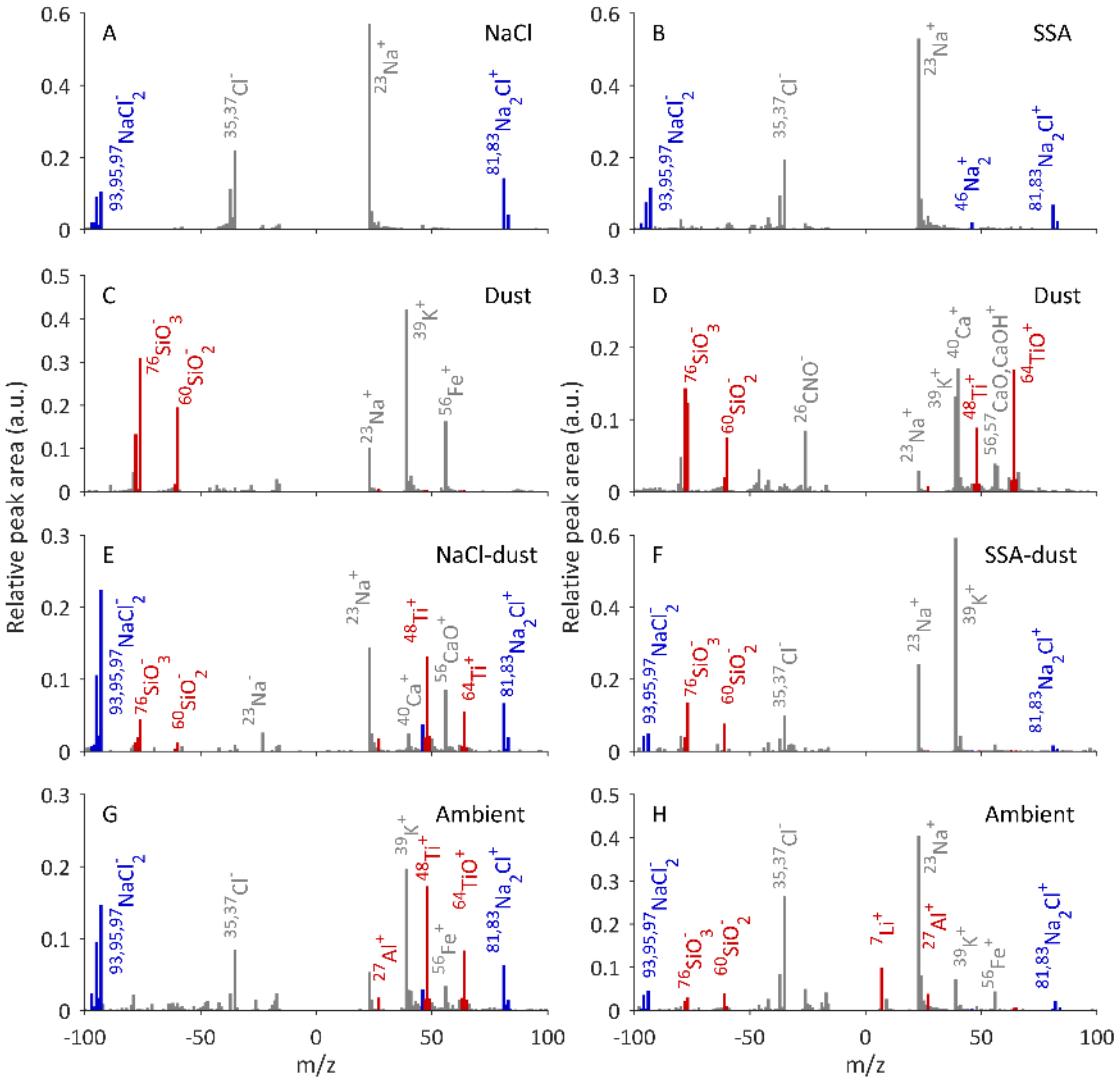

Figure 7.6. Representative mass spectra for particles detected by the ATOFMS for (a) NaCl (NaCl solution experiment), (b) SSA (natural seawater experiment), (c) Dust (dry aerosolized ATD) (d) Dust (dry aerosolized ATD), (e) NaCl-Dust (dust-doped NaCl solution experiment), (f) SSA-Dust (natural seawater experiment), (g) SSA-Dust (CalWater2), and (h) SSA-Dust (CalWater2). Peaks only associated with salt are shown in blue, peaks only associated with dust are shown in red, and peaks common to both are shown in gray.

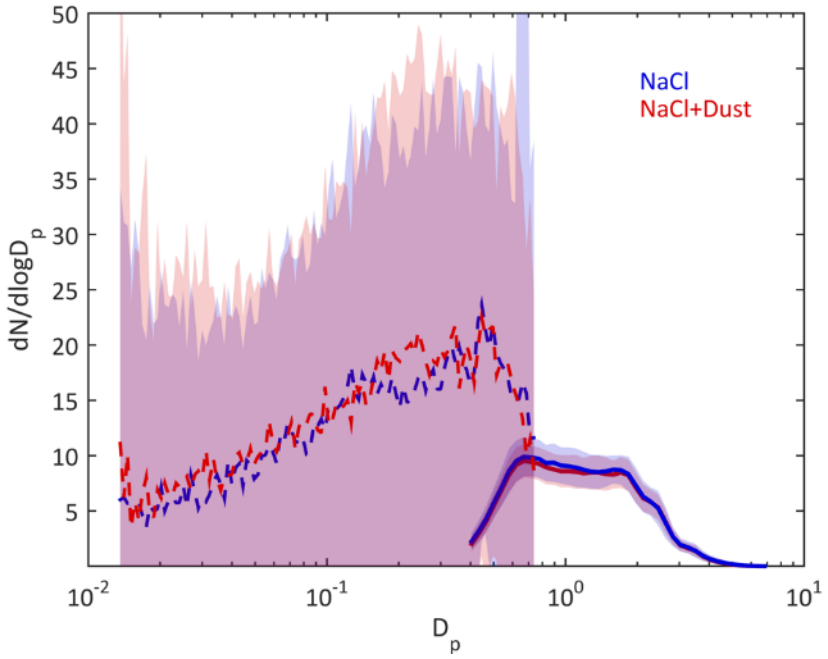

Figure 7.7. Merged particle size distribution for NaCl solution experiments (blue) and dust doped NaCl solution experiments (red). SMPS measurements are shown in the dashed lines, while the APS is shown in regular lines. Shaded areas indicate 2 standard deviations.

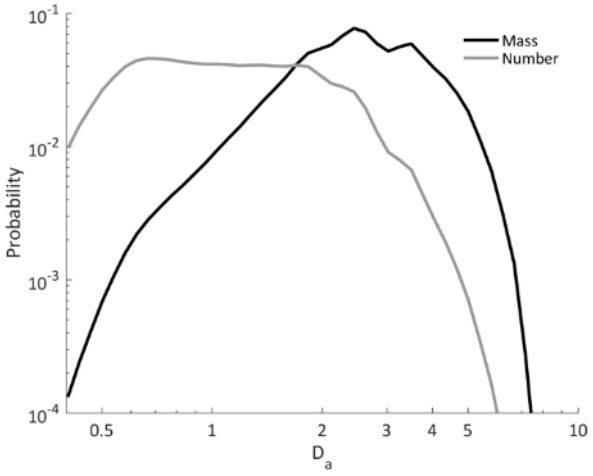

Figure 7.8. Probability distribution functions for all aerosols for the dust-doped NaCl system for mass concentration (black) and number concentration (grey).

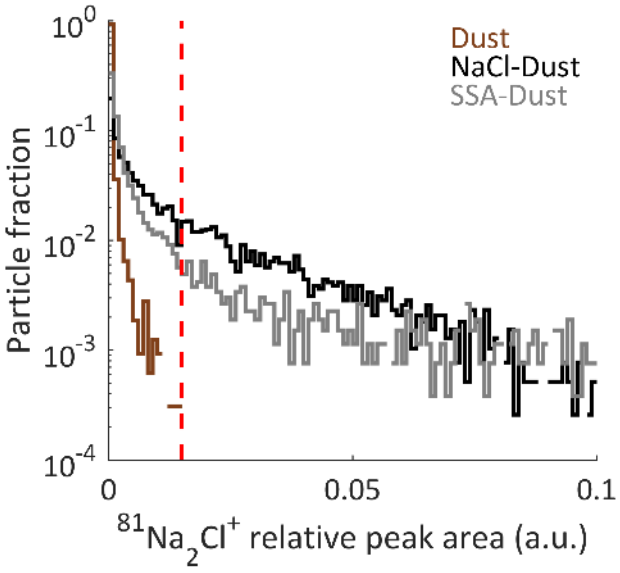

Figure 7.9. The relative peak area distributions of $^{81}Na_2Cl^+$ for Arizona Test Dust (brown), NaCl-Dust (black), and SSA-Dust (grey). The red dashed line shows the threshold value of 0.015 used to distinguish between dust and dust mixed with sea salt for particles observed during CalWater2. Relative peak area is listed in arbitrary units (a.u.).

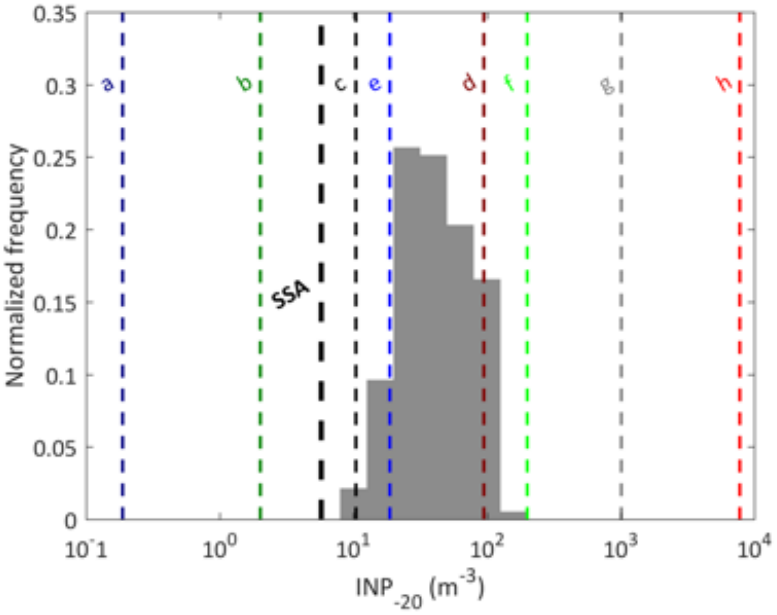

Figure 7.10. Normalized frequency distribution for INP_{-20} concentrations from measurements conducted from 2009-2013 at Cabo Verde Observatory (Welti et al., 2018). Dotted lines show INP_{-20} concentrations from the simulations here. Each of the cases (a, b, c, d, e, f, g, h) has a different assumption for the lifetime in the top 1m layer (0.1, 1, 5, 50, 0.1, 1, 5 and 50 days, respectively) and water to aerosol enrichment factor (100, 100, 100, 100, 10000, 10000, 10000, and 10000 respectively). Thick dashed line shows the INP-20 contribution from SSA, calculated using the parameterization from McCluskey et al., (2018).

7.10 Supplementary tables

Table 7.1. Definition rules to select NaCl-Dust mass spectra. If any of the below conditions were met then the particle was deemed to contain dust. RPA stands for relative peak area and varies from zero to one.

Identification Rules for NaCl-Dust
$^{27}Al^{+}$ RPA $\geq$ 0.125
$^{76}SiO_3^{-}$ RPA $\geq$ 0.05
$^{48}Ti^{+}$ OR $^{64}TiO^{+}$ RPA $\geq$ 0.1
$^{39}K^{+}$ RPA > 0.05
$^{56}Fe^{+}$ RPA > 0.15

Table 7.2. Definition rules to select SSA-Dust spectra. If either of these conditions were met then the particle was deemed to contain dust. RPA stands for relative peak area and varies from zero to one. There was a small population of particles containing black carbon in this experiment. Mass spectra for black carbon particles also commonly contain a peak at an M/Z of 48 ($^{48}C_4^+$) and these particles could be mistakenly categorized as dust if the selection rule is only based upon the peak at M/Z +48.

Identification Rules for SSA-Dust

$^{76}SiO_3^-$ RPA $\geq$ 0.01
$^{12}C^+$ RPA$<$ 0.005 AND $^{36}C_3^+ <$ 0.025 AND $^{73}C_6H^- <$ 0.025 AND ($^{48}Ti^+$ AND/OR $^{64}TiO^+$ $\geq$ 0.1)

Table 7.3. Mass-to-charge of ions and their ion marker assignments.

M/z	Ion marker assignments	Particle type
7	$^{7}Li^{+}$	Dust
23	$^{23}Na^{+}$	dust and sea spray
27	$^{27}Al^{+}$	dust
39	$^{39}K^{+}$	dust and sea spray
46	$^{46}Na_2^{+}$	sea spray
48, 64	$^{48}Ti^{+}$, $^{64}TiO^{+}$	dust
56	$^{56}Fe^{+}$, $^{56}CaOH^{+}$	dust and sea spray
81, 83	$^{81, 83}Na_2Cl^{+}$	sea spray
139, 141, 143	$^{139, 141, 143}Na_3Cl_2^{+}$	sea spray
35, 37	$^{35, 37}Cl^{-}$	dust and sea spray
60	$^{60}SiO_2^{-}$	dust
76, 77	$^{76}SiO_3^{-}$, $HSiO_3^{-}$	Dust
93, 95, 97	$^{93, 95, 97}NaCl_2^{-}$	sea spray
119	$^{119}AlSiO_4^{-}$	Dust
136	$^{136}Si_2O_5^{-}$	Dust

Table 7.4. Measured and derived mass and number fractions from APS, ATOFMS, and ICP-MS measurements. R_{max} is the maximum radius of dust that can be incorporated into a sea spray droplet. MF_{AA} is the APS/ATOFMS-derived mass fraction. Ø is the calculated scaling factor, and NF is the total number fraction of dust-containing aerosol derived from the scaling factor.

$R_{max\ (\mu m)}$	MF_{AA}	Ø	NF
0.25	$9.25*10^{-4}$	0.1408	0.0123
0.5	$6.60*10^{-3}$	0.1379	0.0120
1.0	0.0410	0.0221	$1.90*10^{-3}$
1.5	0.0958	0.0095	$8.27*10^{-4}$
2.5	0.163	0.0056	$4.87*10^{-4}$
5.0	0.177	0.0051	$4.44*10^{-4}$

Table 7.5. Select metrics of the coastal Pacific Ocean at the time of seawater collection from the Scripps Pier for each MART experiment. Data was provided by the Southern California Coastal Ocean Observing System (www.sccoos.org). Data from SCCOOS were not available for the 12/1/13 collection. Two separate tanks were run using the water collected on 1/5/14.

Date	Chlorophyll-A (mg m^{-3})	Water Temp (°C)	Salinity (PSU)
6/11/13 16:00	0.04	19.4	33.6
7/11/13 12:00	0.84	21.1	33.4
9/10/13 18:00	2.03	17.3	33.4
12/1/13 12:00	n/a	n/a	n/a
1/5/14 16:30	1.35	15.1	33.5

Table 7.6. Summary of dust transport simulation input parameters and outputs. Sfc denotes the lowest model layer (up to 100 m).

Enrichment Factor (EF)	Particle lifetime in OSL (days)	Average re-emitted dust fraction (sfc)	Median re-emitted dust fraction (sfc)	Max re-emitted dust fraction (sfc)	Fraction dust re-emitted (mean)
100	0.1	0.0001	0.0000	0.0066	$1.442*10^{-5}$
100	1	0.0011	0.0001	0.0533	$1.162*10^{-4}$
100	5	0.0043	0.0004	0.2100	$4.809*10^{-4}$
10000	0.1	0.0101	0.0006	0.3982	0.0014
10000	1	0.0623	0.0087	0.8487	0.0113
10000	5	0.1424	0.0360	0.9467	0.0433

7.11 References

Albani, S., Mahowald, N. M., Perry, A. T., Scanza, R. A., Zender, C. S., Heavens, N. G., … Ott-Bliesner, B. L. (2014). Improved dust representation in the Community Atmosphere Model. *Journal of Advances …*, *6*, 547–570. https://doi.org/10.1002/2013MS000279.

Allen, J. O., Fergenson, D. P., Gard, E. E., Hughes, L. S., Morrical, B. D., Kleeman, M. J., … Cass, G. R. (2000). Particle detection efficiencies of aerosol time of flight mass spectrometers under ambient sampling conditions. *Environmental Science and Technology*, *34*(1), 211–217. https://doi.org/10.1021/es9904179

Aller, J. Y., Kuznetsova, M. R., Jahns, C. J., & Kemp, P. F. (2005). The sea surface microlayer as a source of viral and bacterial enrichment in marine aerosols. *Journal of Aerosol Science*, *36*(5–6), 801–812. https://doi.org/10.1016/j.jaerosci.2004.10.012

Alpert, P. A., Aller, J. Y., & Knopf, D. a. (2011). Ice nucleation from aqueous NaCl droplets with and without marine diatoms. *Atmospheric Chemistry and Physics Discussions*, *11*(3), 8291–8336. https://doi.org/10.5194/acpd-11-8291-2011

Andreae, M. O., Charlson, R. J., Bruynseels, F., Storms, H., Van Grieken, R., & Maenhaut, W. (1986). Internal Mixture of Sea Salt, Silicates, and Excess Sulfate in Marine Aerosols. *Science*, *232*(4758), 9–12. https://doi.org/10.1126/science.232.4758.1620

Arimoto, R., Duce, R. A., Ray, B. J., & Tomza, U. (2003). Dry deposition of trace elements to the western North Atlantic. *Global Biogeochemical Cycles*, *17*(1). https://doi.org/10.1029/2001GB001406

Atkinson, J. D., Murray, B. J., Woodhouse, M. T., Whale, T. F., Baustian, K. J., Carslaw, K. S., … Malkin, T. L. (2013). The importance of feldspar for ice nucleation by mineral dust in mixed-phase clouds. *Nature*, *500*(7463), 490–490. https://doi.org/10.1038/nature12384

Augustin-Bauditz, S., Wex, H., Denjean, C., Hartmann, S., Schneider, J., Schmidt, S., … Stratmann, F. (2016). Laboratory-generated mixtures of mineral dust particles with biological substances: Characterization of the particle mixing state and immersion freezing behavior. *Atmospheric Chemistry and Physics*, *16*(9), 5531–5543. https://doi.org/10.5194/acp-16-5531-2016

Bigg, E. K. E. (1973). Ice Nucleus Concentrations in Remote Areas. *Journal of Atmospheric Sciences*, *30*(6), 1153–1157. https://doi.org/10.1016/0169-8095(90)90025-8

Boose, Y., Sierau, B., Isabel García, M., Rodríguez, S., Alastuey, A., Linke, C., … Lohmann, U. (2016). Ice nucleating particles in the Saharan Air Layer. *Atmospheric Chemistry and Physics*, *16*(14), 9067–9087. https://doi.org/10.5194/acp-16-9067-2016

Bressac, M., Guieu, C., Doxaran, D., Bourrin, F., Desboeufs, K., Leblond, N., & Ridame, C.

(2014). Quantification of the lithogenic carbon pump following a simulated dust-deposition event in large mesocosms. *Biogeosciences*, *11*(4), 1007–1020. https://doi.org/10.5194/bg-11-1007-2014

Burrows, S. M., Hoose, C., Poschl, U., & Lawrence, M. G. (2013). Ice nuclei in marine air: Biogenic particles or dust? *Atmospheric Chemistry and Physics*, *13*(1), 245–267. https://doi.org/10.5194/acp-13-245-2013

Collins, D. B., Zhao, D. F., Ruppel, M. J., Laskina, O., Grandquist, J. R., Modini, R. L., … Prather, K. a. (2014). Direct aerosol chemical composition measurements to evaluate the physicochemical differences between controlled sea spray aerosol generation schemes. *Atmospheric Measurement Techniques*, *7*(11), 3667–3683. https://doi.org/10.5194/amt-7-3667-2014

Dammshäuser, A., Wagener, T., Garbe-Schönberg, D., & Croot, P. (2013). Particulate and dissolved aluminum and titanium in the upper water column of the Atlantic Ocean. *Deep-Sea Research Part I: Oceanographic Research Papers*, *73*, 127–139. https://doi.org/10.1016/j.dsr.2012.12.002

DeMott, P. J., Cziczo, D. J., Prenni, A. J., Murphy, D. M., Kreidenweis, S. M., Thomson, D. S., … Rogers, D. C. (2003). Measurements of the concentration and composition of nuclei for cirrus formation. *Proceedings of the National Academy of Sciences*, *100*(25), 14655–14660. https://doi.org/10.1073/pnas.2532677100

DeMott, P. J., Hill, T. C. J., McCluskey, C. S., Prather, K. A., Collins, D. B., Sullivan, R. C., … Franc, G. D. (2016). Sea spray aerosol as a unique source of ice nucleating particles. *Proceedings of the National Academy of Sciences*, *113*(21), 5797–5803. https://doi.org/10.1073/pnas.1514034112

DeMott, P. J., Prenni, A. J., Liu, X., Kreidenweis, S. M., Petters, M. D., Twohy, C. H., … Rogers, D. C. (2010). Predicting global atmospheric ice nuclei distributions and their impacts on climate. *Proceedings of the National Academy of Sciences*, *107*(25), 11217–11222. https://doi.org/10.1073/pnas.0910818107

Demott, P. J., Prenni, A. J., McMeeking, G. R., Sullivan, R. C., Petters, M. D., Tobo, Y., … Kreidenweis, S. M. (2015). Integrating laboratory and field data to quantify the immersion freezing ice nucleation activity of mineral dust particles. *Atmospheric Chemistry and Physics*, *15*(1), 393–409. https://doi.org/10.5194/acp-15-393-2015

Deuser, A. W. G., Brewer, P. G., Jickells, T. D., & Commeau, R. F. (2018). Biological Control of the Removal of Abiogenic Particles from the Surface Ocean Publish. *Science*, *219*(4583), 388–391.

Fan, X. B., Okada, K., Niimura, N., Kai, K., Arao, K., Shi, G. Y., … Mitsuta, Y. (1996). Mineral particles collected in China and Japan during the same Asian dust-storm event. *Atmospheric Environment*, *30*(2), 347–351. https://doi.org/10.1016/1352-2310(95)00271-

Y

Gard, E. E., Kleeman, M. J., Gross, D. S., Hughes, L. S., Allen, J. O., Morrical, B. D., … Prather, K. A. (1998). Direct Observation of Heterogeneous Chemistry in the Atmosphere. *Science*, *279*(5354), 1184–1187. https://doi.org/10.1126/science.279.5354.1184

Gard, E., Mayer, J. E., Morrical, B. D., Dienes, T., Fergenson, D. P., & Prather, K. A. (1997). Real-Time Analysis of Individual Atmospheric Aerosol Particles: Design and Performance of a Portable ATOFMS. *Analytical Chemistry*, *69*(20), 4083–4091. https://doi.org/10.1021/ac970540n

Gross, D. S., Gälli, M. E., Silva, P. J., & Prather, K. A. (2000). Relative sensitivity factors for alkali metal and ammonium cations in single-particle aerosol time-of-flight mass spectra. *Analytical Chemistry*, *72*(2), 416–422. https://doi.org/10.1021/ac990434g

Guazzotti, S. a, Whiteaker, J. R., Suess, D., Coffee, K. R., & Prather, K. a. (2001). Real-time measurements of the chemical composition of size- resolved particles during a Santa Ana wind episode, California USA. *Atmospheric Environment*, *35*(December 1998), 3229–3240.

Hiranuma, N., Augustin-Bauditz, S., Bingemer, H., Budke, C., Curtius, J., Danielczok, A., … Yamashita, K. (2015). A comprehensive laboratory study on the immersion freezing behavior of illite NX particles: A comparison of 17 ice nucleation measurement techniques. *Atmospheric Chemistry and Physics*, *15*(5), 2489–2518. https://doi.org/10.5194/acp-15-2489-2015

Hunter, K. A. (1980). Processes affecting particulate trace metals in the sea surface microlayer. *Marine Chemistry*, *9*(1), 49–70. https://doi.org/10.1016/0304-4203(80)90006-7

Hurrell, J. W., M., H. M., Gent, P. R., S., G., Kay, J. E., Kushner, P. J., … Long, M. C. (2013). The Community Earth System Model. *Bulletin of the American Meteorological Society*, (September), 1339–1360. https://doi.org/10.1175/BAMS-D-12-00121.1

Kanji, Z. A., Ladino, L. A., Wex, H., Boose, Y., Burkert-Kohn, M., Cziczo, D. J., & Krämer, M. (2017). Overview of Ice Nucleating Particles. *Meteorological Monographs*, *58*, 1.1-1.33. https://doi.org/10.1175/AMSMONOGRAPHS-D-16-0006.1

Lawrence, C. R., & Neff, J. C. (2009). The contemporary physical and chemical flux of aeolian dust: A synthesis of direct measurements of dust deposition. *Chemical Geology*, *267*(1–2), 46–63. https://doi.org/10.1016/j.chemgeo.2009.02.005

Lee, C., Sultana, C. M., Collins, D. B., Santander, M. V., Axson, J. L., Malfatti, F., … Prather, K. A. (2015). Advancing Model Systems for Fundamental Laboratory Studies of Sea Spray Aerosol Using the Microbial Loop. *Journal of Physical Chemistry A*, *119*(33), 8860–8870. https://doi.org/10.1021/acs.jpca.5b03488

Liu, X., Easter, R. C., Ghan, S. J., Zaveri, R., Rasch, P., Shi, X., … Mitchell, D. (2012). Toward a minimal representation of aerosols in climate models: Description and evaluation in the Community Atmosphere Model CAM5. *Geoscientific Model Development*, *5*(3), 709–739. https://doi.org/10.5194/gmd-5-709-2012

Mackey, K. R. M. M., Chien, C. Te, Post, A. F., Saito, M. A., & Paytan, A. (2015). Rapid and gradual modes of aerosol trace metal dissolution in seawater. *Frontiers in Microbiology*, *6*(JAN), 1–11. https://doi.org/10.3389/fmicb.2014.00794

Mårtensson, E. M., Nilsson, E. D., de Leeuw, G., Cohen, L. H., & Hansson, H.-C. (2003). Laboratory simulations and parameterization of the primary marine aerosol production. *Journal of Geophysical Research: Atmospheres*, *108*(D9), n/a-n/a. https://doi.org/10.1029/2002JD002263

Martin, A. C., Cornwell, G. C., Atwood, S. A., Moore, K. A., Rothfuss, N. E., Taylor, H., … Prather, K. A. (2017). Transport of pollution to a remote coastal site during gap flow from California's interior: impacts on aerosol composition, clouds, and radiative balance. *Atmospheric Chemistry and Physics*, *17*(2), 1491–1509. https://doi.org/10.5194/acp-17-1491-2017

Mayol, E., Jiménez, M. A., Herndl, G. J., Duarte, C. M., & Arrieta, J. M. (2014). Resolving the abundance and air- sea fluxes of airborne microorganisms in the North Atlantic Ocean. *Frontiers in Microbiology*, *5*(OCT), 1–9. https://doi.org/10.3389/fmicb.2014.00557

McCluskey, C. S., Hill, T. C. J., Malfatti, F., Sultana, C. M., Lee, C., Santander, M. V., … DeMott, P. J. (2017). A dynamic link between ice nucleating particles released in nascent sea spray aerosol and oceanic biological activity during two mesocosm experiments. *Journal of the Atmospheric Sciences*, *74*(2017), JAS-D-16-0087.1. https://doi.org/10.1175/JAS-D-16-0087.1

McCluskey, C. S., Hill, T. C. J., Sultana, C. M., Laskina, O., Trueblood, J., Santander, M. V., … DeMott, P. J. (2018). A mesocosm double feature: Insights into the chemical make-up of marine ice nucleating particles. *Journal of the Atmospheric Sciences*. https://doi.org/10.1175/JAS-D-15-0370.1

McCluskey, C. S., Ovadnevaite, J., Rinaldi, M., Atkinson, J., Franco, B., Ceburnis, D., … Demott, P. J. (2018). Marine and Terrestrial Organic Ice Nucleating Particles in Pristine Marine to Continentally-Influenced Northeast Atlantic Air Masses. *Journal of Geophysical Research: Atmospheres*, *123*, 1–17. https://doi.org/10.1029/2017JD028033

Migon, C., Sandroni, V., Marty, J. C., Gasser, B., & Miquel, J. C. (2002). Transfer of atmospheric matter through the euphotic layer in the northwestern Mediterranean: Seasonal pattern and driving forces. *Deep-Sea Research Part II: Topical Studies in Oceanography*, *49*(11), 2125–2141. https://doi.org/10.1016/S0967-0645(02)00031-0

Monahan, E. C., Spiel, D. E., & Davidson, K. L. (1986). A Model of Marine Aerosol Generation

Via Whitecaps and Wave Disruption. In E. C. Monahan & G. Mac Niocaill (Eds.), *Oceanic Whitecaps: And Their Role in Air-Sea Exchange Processes* (pp. 167–174). Dordrecht: Springer Netherlands. https://doi.org/10.1007/978-94-009-4668-2_16

Neale, R. B., Gettelman, A., Park, S., Chen, C., Lauritzen, P. H., Williamson, D. L., … Taylor, M. a. (2012). Description of the NCAR Community Atmosphere Model (CAM 5.0). NCAR Technical Notes. *Ncar/Tn-464+Str*, 214. https://doi.org/10.5065/D6N877R0.

Niemand, M., Möhler, O., Vogel, B., Vogel, H., Hoose, C., Connolly, P., … Leisner, T. (2012). A Particle-Surface-Area-Based Parameterization of Immersion Freezing on Desert Dust Particles. *Journal of the Atmospheric Sciences*, *69*(10), 3077–3092. https://doi.org/10.1175/JAS-D-11-0249.1

O'Sullivan, D., Murray, B. J., Malkin, T. L., Whale, T. F., Umo, N. S., Atkinson, J. D., … Webb, M. E. (2014). Ice nucleation by fertile soil dusts: Relative importance of mineral and biogenic components. *Atmospheric Chemistry and Physics*, *14*(4), 1853–1867. https://doi.org/10.5194/acp-14-1853-2014

O'Sullivan, D., Murray, B. J., Ross, J. F., & Webb, M. E. (2016). The adsorption of fungal ice-nucleating proteins on mineral dusts: A terrestrial reservoir of atmospheric ice-nucleating particles. *Atmospheric Chemistry and Physics*, *16*(12), 7879–7887. https://doi.org/10.5194/acp-16-7879-2016

Ohnemus, D. C., & Lam, P. J. (2015). Cycling of lithogenic marine particles in the US GEOTRACES North Atlantic transect. *Deep-Sea Research Part II: Topical Studies in Oceanography*, *116*, 283–302. https://doi.org/10.1016/j.dsr2.2014.11.019

Pruppacher, H. R., & Klett, J. (2010). *Microphysics of Clouds and Precipitation* (Vol. 18). https://doi.org/10.1007/978-0-306-48100-0

R. Lewis, E., & Schwartz, S. (2004). Sea Salt Aerosol Production: Mechanisms, Methods, Measurements and Models—A Critical Review. *Washington DC American Geophysical Union Geophysical Monograph Series*, *152*, 3719-.

Rogers, D. C., DeMott, P. J., Kreidenweis, S. M., & Chen, Y. (2001). A continuous-flow diffusion chamber for airborne measurements of ice nuclei. *Journal of Atmospheric and Oceanic Technology*, *18*(5), 725–741. https://doi.org/10.1175/1520-0426(2001)018<0725:ACFDCF>2.0.CO;2

Schnell, R. C., & Vali, G. (1976). Biogenic Ice Nuclei: Part I. Terrestrial and Marine Sources. *Journal of the Atmospheric Sciences*. https://doi.org/10.1175/1520-0469(1976)033<1554:BINPIT>2.0.CO;2

Silva, P. J., Carlin, R. a, & Prather, K. a. (2000). Single particle analysis of suspended soil dust from Southern California. *Atmospheric Environment*, *34*(11), 1811–1820. https://doi.org/10.1016/S1352-2310(99)00338-6

Song, X. H., Hopke, P. K., Fergenson, D. P., & Prather, K. a. (1999). Classification of single particles analyzed by ATOFMS using an artificial neural network, ART-2A. *Analytical Chemistry*, *71*(4), 860–865. https://doi.org/10.1021/ac9809682

Stokes, M. D., Deane, G., Collins, D. B., Cappa, C., Bertram, T., Dommer, A., … Survilo, M. (2016). A miniature Marine Aerosol Reference Tank (miniMART) as a compact breaking wave analogue. *Atmospheric Measurement Techniques*, *9*(9), 4257–4267. https://doi.org/10.5194/amt-9-4257-2016

Sullivan, R. C., Guazzotti, S. A., Sodeman, D. A., & Prather, K. A. (2007). Direct observations of the atmospheric processing of Asian mineral dust. *Atmospheric Chemistry and Physics*, *7*(3), 1213–1236. https://doi.org/10.5194/acpd-6-4109-2006

Sullivan, R. C., Guazzotti, S. A., Sodeman, D. A., Tang, Y., Carmichael, G. R., & Prather, K. A. (2007). Mineral dust is a sink for chlorine in the marine boundary layer. *Atmospheric Environment*, *41*(34), 7166–7179. https://doi.org/10.1016/j.atmosenv.2007.05.047

Sultana, C. M., Collins, D. B., & Prather, K. A. (2017). The Effect of Structural Heterogeneity in Chemical Composition on Online Single Particle Mass Spectrometry Analysis of Sea Spray Aerosol Particles. *Environmental Science & Technology*. https://doi.org/10.1021/acs.est.6b06399

Sultana, C. M., Cornwell, G. C., Rodriguez, P., & Prather, K. A. (2017). FATES: a flexible analysis toolkit for the exploration of single-particle mass spectrometer data. *Atmospheric Measurement Techniques*, *10*(4), 1323–1334. https://doi.org/10.5194/amt-10-1323-2017

Ternon, E., Guieu, C., Löye-Pilot, M. D., Leblond, N., Bosc, E., Gasser, B., … Martín, J. (2010). The impact of Saharan dust on the particulate export in the water column of the North Western Mediterranean Sea. *Biogeosciences*, *7*(3), 809–826. https://doi.org/10.5194/bg-7-809-2010

Tobo, Y., Demott, P. J., Hill, T. C. J., Prenni, A. J., Swoboda-Colberg, N. G., Franc, G. D., & Kreidenweis, S. M. (2014). Organic matter matters for ice nuclei of agricultural soil origin. *Atmospheric Chemistry and Physics*, *14*(16), 8521–8531. https://doi.org/10.5194/acp-14-8521-2014

Vergara-Temprado, J., Miltenberger, A. K., Furtado, K., Grosvenor, D. P., Shipway, B. J., Hill, A. A., … Carslaw, K. S. (2018). Strong control of Southern Ocean cloud reflectivity by ice-nucleating particles. *Proceedings of the National Academy of Sciences*, 201721627. https://doi.org/10.1073/pnas.1721627115

Vergara-Temprado, J., Murray, B. J., Wilson, T. W., O'Sullivan, D., Browse, J., Pringle, K. J., … Carslaw, K. S. (2017). Contribution of feldspar and marine organic aerosols to global ice nucleating particle concentrations. *Atmospheric Chemistry and Physics*, *17*(5), 3637–3658. https://doi.org/10.5194/acp-17-3637-2017

Wallace, G. T., & Duce, R. A. (1975). Concentration of particulate trace metals and particulate organic carbon in marine surface waters by a bubble flotation mechanism. *Marine Chemistry*, *3*(2), 157–181. https://doi.org/10.1016/0304-4203(75)90020-1

Wallace, G. T., & Duce, R. A. (1978). Open-ocean transport of particulate trace metals by bubbles. *Deep-Sea Research*, *25*(9), 827–835. https://doi.org/10.1016/0146-6291(78)90026-7

Wang, X., Deane, G. B., Moore, K. A., Ryder, O. S., Stokes, M. D., Beall, C. M., … Prather, K. A. (2017). The role of jet and film drops in controlling the mixing state of submicron sea spray aerosol particles. *Proceedings of the National Academy of Sciences*, *114*(27), 6978–6983. https://doi.org/10.1073/pnas.1702420114

Weisel, C. P., Duce, R. A., Fasching, J. L., & Heaton, R. W. (1984). Estimates of the transport of trace metals from the ocean to the atmosphere. *Journal of Geophysical Research: Atmospheres*, *89*(D7), 11607–11618. https://doi.org/10.1029/JD089iD07p11607

Welti, A., Müller, K., Fleming, Z. L., & Stratmann, F. (2018). Concentration and variability of ice nuclei in the subtropical maritime boundary layer. *Atmospheric Chemistry and Physics*, *18*(8), 5307–5320. https://doi.org/10.5194/acp-18-5307-2018

Wilson, T. W., Ladino, L. A., Alpert, P. A., Breckels, M. N., Brooks, I. M., Browse, J., … Murray, B. J. (2015). A marine biogenic source of atmospheric ice-nucleating particles. *Nature*, *525*(7568), 234–238. https://doi.org/10.1038/nature14986

Chapter 8. Conclusions

8.1 Synopsis

This dissertation investigates the effects of different aerosol sources on clouds and precipitation in coastal systems, with a strong focus on the sources and impact of ice nucleating particles (INPs). Chapter 2 describes the transport of anthropogenic aerosol from the interior of California to a coastal site and potential climatic effects. Chapter 3 uses precipitation samples, droplet freezing assays, atmospheric transport simulations, and hydrometeor phase measured by polarimetric radar to determine sources of INPs at a pair of coastal and mountain sites in California. Chapter 4 uses single particle measurements of dust and bioaerosol standards to develop a framework for the improved discrimination between the two particle types in ambient data. Chapters 5 and 6 use single particle composition measurements to directly measure and estimate sources of INPs at a coastal site in California. Finally, Chapter 7 investigates the resuspension of dust from the ocean and whether this process could be a novel source of marine INPs.

8.2 Conclusions

8.2.1 Transport of Pollution to a Remote Coastal Site during Gap Flow from California's Interior: Impacts on Aerosol Composition, Clouds and Radiative Balance

Measurements taken at Bodega Bay, CA during the CalWater-2015 intensive observing period were used to investigate the impacts of the Petaluma Gap Flow conditions (PGF; Neiman et al., 2006) upon local air quality and marine cloud albedo. Vertically resolved lower tropospheric wind observations and carbon monoxide concentration were used to identify PGF conditions. Several measures of anthropogenic pollution, including CO, NO_x condensation nuclei (CN), and black carbon mass concentrations, were consistently elevated when compared to non-PGF periods.

Submicron particle particles increased by 110%, while supermicron particle ranges decreased by 84% during PGF conditions.

Single particle chemical mixing state during PGF events was investigated using UF-ATOFMS and ATOFMS Measurements. It was found that submicron particle populations change during PGF to favor carbonaceous particle types at the expense of sea spray aerosol. The analysis of secondary aging also showed that carbonaceous particles are more likely to contain elemental carbon than organic carbon during PGF episodes. Aethalometer measurements also suggested that soot was less aged during PGF periods and total absorption and total black carbon mass were greater than during non-PGF periods. These results suggest that PGF conditions could lead to an increase in absorption of solar shortwave radiation by black carbon aerosol.

Particle hygroscopicity, calculated from size-resolved cloud condensation nuclei (CCN) concentrations, was nearly invariant between PGF and non-PGF periods. Cloud droplet number concentrations (CDNC) were estimated using the methodology of Cohard et al. (1998), and increases in CDNC were determined to be stable across a wide range of updraft velocities. The marine cloud albedo change in response to PGF CCN was estimated using MODIS level 2 cloud products and equation 7 from Platnick and Twomey (1994). To first order (assuming constant liquid water path) it was estimated that near shore marine clouds will brighten by 16% to 28% percent (interquartile range) in visible wavelengths during PGF events. This finding supports the hypothesis that PGF conditions may lead to a brightening in near-shore marine stratocumulus clouds through the cloud albedo indirect effect. These results demonstrate that PGF can impact aerosol number, chemical aging pathways, shortwave absorption and the number of CCN available to near-shore marine clouds. Further study of the chemical composition of continental outflow in

other regions is necessary to refine understanding of the anthropogenic impact upon the environment.

8.2.2 Contrasting Local and Long-Range Transported Warm Ice-Nucleating Particles During an Atmospheric River in Coastal California, USA

This study examined the freezing spectra of time-resolved rainfall samples from two Northern CA sites, one coastal (BBY) and one inland (CZC), during an atmospheric river (AR) with significant regional impact. We compared these spectra and their warm INP concentration (INP_{-10}) across sites with varying cloud depth, airmass source and transport mechanisms.

The precipitation collection sites were both located downwind of marine particle sources for the entire storm and the cloud layers above each site receive significant airmass contribution from the marine boundary layer during all storm periods. However, only CZC showed warm INPs in precipitation during all periods, while the only difference in airmass influence between the cloud layers over the two sites is that inflowing air to mixed phase clouds over CZC passes through the terrestrial boundary layer before arriving. When warm INPs are present in BBY precipitation, their presence can be explained mechanistically by transport patterns and cloud top altitude favorable for LRT aerosols to become injected at cloud top.

The KDAX radar was used to estimate hydrometeor phase of clouds located over the two sites. The precipitating hydrometeor phase in clouds with $-10\ ^{\circ}C < T \leq 0\ ^{\circ}C$ was significantly different above CZC than above BBY, with a higher probability of frozen hydrometeors over CZC. Warm INPs were also consistently more numerous, by as much as a factor of 10, in CZC precipitation. We can thus hypothesize that terrestrial warm INPs became injected into mixed-phase clouds over CZC and impacted cloud hydrometeor populations through in-situ ice-phase microphysics. Future studies into the impact of aerosols on cloud microphysics may benefit from

targeted polarimetric radar observations conducted in tandem with tropospheric soundings and laboratory analysis of cloud and precipitation material to further understand how aerosols affect precipitation.

8.2.3 Improved discrimination between dust and bioaerosol by aerosol time-of-flight mass spectrometry

Laboratory samples for dust and cellular bioaerosol standards were measured and characterized by the ATOFMS in order to better identify cellular bioaerosol in ambient datasets. The mass spectral landscape of these particles was explored as a function of TPII and a comprehensive series of characteristic ion markers useful for identifying cellular particles were identified. A decision tree was developed in order to identify these particles at a coastal site in California ("*Cell-type*"). *Cell-type* particles were defined by elevated markers for many of the mass spectral features identified in the lab studies, including nucleobases (66^-, 71^-, 90^-, 117^-, $131\text{-}134^-$), negative phosphates ($^{159}H(PO_3)_2^-$, $^{199}NaH_2P_2O_7^-$), quaternatry amines associated with bacteria ($^{59}N(CH_3)_3^+$, $^{74}N(CH_3)_4^+$), and positive potassium clusters ($^{104}K_2CN^+$, $^{157}K_2PO_3^+$, $^{175}K_2HSO_4$).

Ambient *Cell-type* particles were correlated with bioaerosol concentrations measured by a wideband integrated bioaerosol sensor (WIBS). Two particle classes, the FP and FBAP types (Gabey, Stanley, Gallagher, & Kaye, 2011), showed weak correlations with *Cell-type* particles (r^2 values of 0.137 and 0.247), while the FP3 (Wright, Hader, McMeeking, & Petters, 2014b) subclass correlated moderately well with *Cell-type* particles (r^2 of 0.525). This correlation between *Cell-type* particles and the FP3 class may be significant because the FP3 type has been strongly implicated in INP studies (Suski et al., 2018; Wright, Hader, McMeeking, & Petters, 2014a).

Indeed, we observed that temporal profiles of ambient warm INP (T = -15 ºC) concentrations generally followed those of *Cell-type* particles at a coastal site in California (r^2 =

0.533). The sum of this evidence suggests that whole or fragmented cells comprise a significant fraction of the FP3 particle class, and that this population likely contributes significantly to the warm INP population at the observation site. The work presented in this study presents a new approach to identify biological particles which will be applicable to the SPMS field as a whole.

8.2.4 Direct on-line mass spectrometry measurements of ice nucleating particles at a coastal site

The Colorado State University continuous flow diffusion chamber (CFDC; Eidhammer et al., 2010; Rogers et al., 1998) was integrated with an aerosol time-of-flight mass spectrometer (ATOFMS; Gard et al., 1997) to directly measure INP composition. A pumped counterflow virtual impactor (PCVI; Brechtel Manufacturing Inc., Model 8100) was used to isolate ice crystals from non-activated particles. Validation experiments confirmed that the ATOFMS only detected particles when the CFDC chamber was producing ice crystals, with a typical detection efficiency of 3.10×10^{-4}.

The CFDC-PCVI-ATOFMS system was deployed to measure INP_{-30} composition at a coastal site in Bodega Bay, CA. Ice crystal residuals were enriched with dust particles compared to ambient measurements, which were dominated by SSA. Ice crystal residuals were also comprised of SSA and bioparticles, though in lower abundance than dust. Primary bioparticles were also enriched in INP_{-30} relative to ambient while SSA was not. The SSA particles found in the ice residual samples were found to be enriched in organic species relative to ambient SSA. While the IN-activity of SSA has previously been tied to organic species produced by biological activity in lab (DeMott et al., 2016; McCluskey et al., 2018b) and field experiments (McCluskey et al., 2018a; Wilson et al., 2015), this is the first time that it has been directly measured in ambient particles. Finally, the active site density (n_s) for all, dust, and SSA particles were calculated using

the CFDC-PCVI-ATOFMS. The SSA n_s agreed well with the ambient SSA parameterization from McCluskey et al. (2018b). The dust n_s agreed better with values estimated from ambient data on dust off of Africa (Price et al., 2018) but were lower than a laboratory-based parameterization (Niemand et al., 2012). The CFDC-PCVI-ATOFMS technique developed and validated in this study illustrates promise for determining the composition and sources of INPs in ambient environments due to its ability to classify individual particles as well as its ability to probe particle mixing state.

8.2.5 Assessing contributions to ice nucleating particle concentrations at a coastal site in California using single particle measurements

Tandem measurements of particle composition, number, and size were used to estimate the contribution of dust, SSA, and biological particles to INP_{-20} concentrations at BML. Particle surface areas for dust and SSA were calculated using combined measurements of an ATOFMS and an aerodynamic particle sizer (APS; TSI Inc.), and then active site density parameterization used to predict their relative contribution to INP_{-20}. Bioaerosol contributions to INP_{-20} concentrations were estimated using the WIBS. Predicted INP_{-20} concentrations were constrained to ambient concentrations measured by droplet freezing assays and were found to generally agree well.

Over the course of the study, bioaerosol were determined to be the major source of INP_{-20}. Dust was determined to be a relatively minor source overall, while SSA concentrations were negligible. The greatest increase in $INP_{-20}$was observed shortly after precipitation events and can be directly attributed to increases in bioaerosol. This work presents a novel new way to estimate INP sources without using direct measurements of their composition and could be useful for future studies to estimate INP sources without necessitating direct measurements of their composition.

8.2.6 Resuspension of dust as a novel source of ice nucleating particles

A series of lab experiments conducted using realistic sea spray generation methodologies showed that dust can be resuspended during wave breaking. Dust deposition events 9 g m^{-2} were simulated and their single-particle composition monitored with an ATOFMS. Dust was shown to be aerosolized during all of these experiments. The strong relationship between sea spray particle size and the likelihood that it contained dust indicated that these whole dust particles and not dissolved elements.

Online and offline measurements of INP concentrations showed that this resuspended dust was still IN-active at concentrations significantly higher than lab-generated SSA or ambient measurements. The relatively weak IN-activity of sea spray and the well-documented IN-activity of dust means that even modest amounts of dust ejected from the ocean may significantly affect INP concentrations over remote marine regions.

The global prevalence of this process was modelled using the Community Earth System Model (CESM 1.2.2; Hurrell et al., 2013) and effects upon INP concentrations were estimated using an active site density parameterization for dust (Niemand et al., 2012). The spatial distribution of ejected dust was similar across all simulations, while the total magnitude changed based upon the input parameters. The fraction of dust particles that get resuspended was highest in regions with high sea spray emissions such as the SO and south of Greenland. The calculated INP_{-25} concentration in the surface layer of the model is highest in regions downwind of major dust sources including the Caribbean and the Arabian sea. However, resuspended dust particles make up the greatest fraction of relative to all dust in the atmosphere in the SO. Coupled with the fact that the SO is predicted to have low INP contributions from other sources, the effect of dust resuspension on atmospheric INPs is expected to be the greatest in the SO (Vergara-Temprado et

al., 2017, 2018). Due to the uncertainty in marine INP identity and the magnitude of their effects upon climate, if dust resuspension contributes significantly to their emission then it is critical that this process be accounted for in future studies.

8.3 Future directions

8.3.1 Determining how meteorological conditions impact ability of aerosol to be incorporated into clouds and precipitation

Chapter 2 investigated how meteorology can affect ambient aerosol size, number, and composition while Chapter 3 investigated how transport conditions can affect which aerosols get incorporated into clouds. The role of meteorology in modulating aerosol source, transport and incorporation into clouds is complex. As shown in Chapter 3, contributing factors may include synoptic weather patterns, kinematic forcing mechanisms such as barrier and low-level jets, and the availability of moisture near cloud top. Atmospheric rivers (ARs) as important storms for their ability to transport vast amounts of water vapor to the state of California. for the removal of trace atmospheric constituents of remote origin and the impact of terrestrial and marine warm INPs on mixed-phase clouds and precipitation are topics deserving further study.

Chapter 3 also demonstrated that polarimetric precipitation radar can be a useful tool to study cloud microphysics given well-constrained conditions. The ability to probe cloud phase is a very useful tool to have when trying to determine the impact of INPs upon a storm. Previous studies have done so using precipitation profiling radars (Ault et al., 2011) or in-situ measurements using airborne platforms (Creamean et al., 2013). Future studies into the impact of aerosols on cloud microphysics could benefit from polarimetric radar observations, which have an extensive spatial coverage in the United States. Thus, the methodology employed here can be extended to measure analyze different meteorological scenarios and/or regions.

8.3.2 Identifying cellular particles in ambient aircraft datasets

Chapter 4 of this dissertation described mass spectral features associated with dust and cellular particles. This information was used to identify a relatively rare cellular particle type (*Cell-type)* that correlated well with warm INP concentrations. The abundance of biological particles at altitudes where they influence mixed-phase clouds is still relatively unknown (Perring et al., 2014; Twohy et al., 2016). A number of flight campaigns investigating the composition of cloud seeds have been conducted using the ATOFMS (see ICE-L, ICE-T, CalWater-2011, and CalWater-2015). These datasets should be investigated using the information gleaned from this chapter in in order to better understand the potential of these cellular particles to affect cloud properties.

8.3.3 Further study of INP source using the ATOFMS

Chapters 5 and 6 of this dissertation employed two different analysis methods for the ATOFMS to investigate the source of INPs during the CalWater-2015 field campaign. However, these results have so far been confined to a singular measurement context. These methodologies should both be extended to other sites and systems in order to better understand how particle composition affects IN-activity.

8.3.4 Further study of the resuspension of dust from the ocean

In Chapter 7 of this dissertation, the resuspension of dust from bubble bursting processes as a novel source of oceanic ice nucleating particles was shown through lab experiments. One aspect that was relatively unexplored through this work was what additional factors may affect dust resuspension. For example, particle size and density may affect how long dust particles remain suspended at a depth where they may be aerosolized. Their size and composition will also affect their dissolution rates (Mackey et al., 2015) and organic compounds in seawater may affect how efficiently dust particles are scavenged by rising bubbles.

The global relevance of dust resuspension from the ocean was explored by through modeling simulations performed in the Community Atmospheric Model (CAM5.0), the atmospheric component of the Community Earth System Model (CESM 1.2.2; Hurrell et al., 2013; Neale et al., 2012). These simulations were constrained using measurements of single particle composition at Bodega Bay. Specifically, the mixing state of dust particles was probed to determine whether or not they contained sodium chloride. It was assumed that all salt found on the particle could be attributed to it being resuspended. However, cloud processing of dust and sea salt can also lead to internally mixed dust with sodium chloride (Andreae et al., 1986; Niimura et al., 1998; Sullivan et al., 2007; Zhang et al., 2003). Hydroxymethanesulfonate (HMS; $^{111}CH_3SO_4^-$) has previously been identified as a tracer for identifying cloud processed particles using the ATOFMS (Whiteaker & Prather, 2003). The formation of HMS was shown to be highly dependent upon both the pH of the particle, and the concentrations of formaldehyde. Thus, while using HMS to identify cloud-processed particles in highly polluted regions may be appropriate, it may not be suitable for relatively pristine, marine environments such as Bodega Bay. The establishment of alternative ion markers for cloud-processing of particles in marine environments would allow for the better constraint on the phenomenon of dust resuspension from the ocean.

8.4 References

Andreae, M. O., Charlson, R. J., Bruynseels, F., Storms, H., Van Grieken, R., & Maenhaut, W. (1986). Internal Mixture of Sea Salt, Silicates, and Excess Sulfate in Marine Aerosols. Science, 232(4758), 9–12. https://doi.org/10.1126/science.232.4758.1620

Ault, A. P., Williams, C. R., White, A. B., Neiman, P. J., Creamean, J. M., Gaston, C. J., … Prather, K. a. (2011). Detection of Asian dust in California orographic precipitation. Journal of Geophysical Research, 116(D16205), 1–15. https://doi.org/10.1029/2010JD015351

Cohard, J.-M., Pinty, J.-P., & Bedos, C. (1998). Extending Twomey's Analytical Estimate of Nucleated Cloud Droplet Concentrations from CCN Spectra. Journal of the Atmospheric Sciences, 55(October 2015), 3348–3357. https://doi.org/10.1175/1520-0469(1998)055<3348:ETSAEO>2.0.CO;2

Creamean, J. M., Suski, K. J., Rosenfeld, D., Cazorla, A., DeMott, P. J., Sullivan, R. C., … Prather, K. a. (2013). Dust and biological aerosols from the Sahara and Asia influence precipitation in the western U.S. Science (New York, N.Y.), 339(2013), 1572–8. https://doi.org/10.1126/science.1227279

DeMott, P. J., Hill, T. C. J., McCluskey, C. S., Prather, K. A., Collins, D. B., Sullivan, R. C., … Franc, G. D. (2016). Sea spray aerosol as a unique source of ice nucleating particles. Proceedings of the National Academy of Sciences, 113(21), 5797–5803. https://doi.org/10.1073/pnas.1514034112

Eidhammer, T., DeMott, P. J., Prenni, A. J., Petters, M. D., Twohy, C. H., Rogers, D. C., … Kreidenweis, S. M. (2010). Ice Initiation by Aerosol Particles: Measured and Predicted Ice Nuclei Concentrations versus Measured Ice Crystal Concentrations in an Orographic Wave Cloud. Journal of the Atmospheric Sciences, 67(8), 2417–2436. https://doi.org/10.1175/2010JAS3266.1

Gabey, A. M., Stanley, W. R., Gallagher, M. W., & Kaye, P. H. (2011). The fluorescence properties of aerosol larger than 0.8 μ in urban and tropical rainforest locations. Atmospheric Chemistry and Physics, 11(11), 5491–5504. https://doi.org/10.5194/acp-11-5491-2011

Gard, E., Mayer, J. E., Morrical, B. D., Dienes, T., Fergenson, D. P., & Prather, K. A. (1997). Real-Time Analysis of Individual Atmospheric Aerosol Particles: Design and Performance of a Portable ATOFMS. Analytical Chemistry, 69(20), 4083–4091. https://doi.org/10.1021/ac970540n

Hurrell, J. W., Holland, M. M., Gent, P. R., Ghan, S., Kay, J. E., Kushner, P. J., … Marshall, S. (2013). The community earth system model: A framework for collaborative research. Bulletin of the American Meteorological Society, 94(9), 1339–1360. https://doi.org/10.1175/BAMS-D-12-00121.1

Hurrell, J. W., M., H. M., Gent, P. R., S., G., Kay, J. E., Kushner, P. J., … Long, M. C. (2013). The Community Earth System Model. Bulletin of the American Meteorological Society, (September), 1339–1360. https://doi.org/10.1175/BAMS-D-12-00121.1

McCluskey, C. S., Hill, T. C. J., Sultana, C. M., Laskina, O., Trueblood, J., Santander, M. V., … DeMott, P. J. (2018). A Mesocosm Double Feature: Insights into the Chemical Makeup of Marine Ice Nucleating Particles. Journal of the Atmospheric Sciences, 75(7), 2405–2423. https://doi.org/10.1175/JAS-D-17-0155.1

McCluskey, C. S., Ovadnevaite, J., Rinaldi, M., Atkinson, J., Franco, B., Ceburnis, D., … Demott, P. J. (2018). Marine and Terrestrial Organic Ice Nucleating Particles in Pristine Marine to Continentally-Influenced Northeast Atlantic Air Masses. Journal of Geophysical Research: Atmospheres, 123, 1–17. https://doi.org/10.1029/2017JD028033

Neale, R. B., Gettelman, A., Park, S., Chen, C., Lauritzen, P. H., Williamson, D. L., … Taylor, M. a. (2012). Description of the NCAR Community Atmosphere Model (CAM 5.0). NCAR Technical Notes. Ncar/Tn-464+Str, 214. https://doi.org/10.5065/D6N877R0.

Neiman, P. J., Ralph, F. M., White, A. B., Parrish, D. D., Holloway, J. S., & Bartels, D. L. (2006). A Multiwinter Analysis of Channeled Flow through a Prominent Gap along the Northern California Coast during CALJET and PACJET. Monthly Weather Review, 134, 1815–1841. https://doi.org/10.1175/MWR3148.1

Niemand, M., Möhler, O., Vogel, B., Vogel, H., Hoose, C., Connolly, P., … Leisner, T. (2012). A Particle-Surface-Area-Based Parameterization of Immersion Freezing on Desert Dust Particles. Journal of the Atmospheric Sciences, 69(10), 3077–3092. https://doi.org/10.1175/JAS-D-11-0249.1

Niimura, N., Okada, K., Fan, X. B., Kai, K., Arao, K., Shi, G. Y., & Takahashi, S. (1998). Formation of Asian dust-storm particles mixed internally with sea salt in the atmosphere. Journal of the Meteorological Society of Japan, 76(2), 275–288. https://doi.org/10.2151/jmsj1965.76.2_275

Perring, A. E., Schwarz, J. P., Baumgardner, D. G., Hernandez, M. T., Spracklen, D. V., Heald, C. L., … Fahey, D. W. (2014). Airborne observations of regional variation in fluorescent aerosol across the United States. Journal of Geophysical Research: Atmospheres, 120, 1153–1170. https://doi.org/10.1002/2013JD020225.Received

Platnick, S., & Twomey, S. (1994). Determining the susceptibility of Cloud Albedo to Changes in Droplet Concentration with the Advanced Very High Resolution Radiometer. Journal of Applied Meteorology, 33, 334–347.

Price, H. C., Baustian, K. J., McQuaid, J. B., Blyth, A., Bower, K. N., Choularton, T., … Murray, B. J. (2018). Atmospheric Ice-Nucleating Particles in the Dusty Tropical Atlantic. Journal of Geophysical Research: Atmospheres, 123(4), 2175–2193. https://doi.org/10.1002/2017JD027560

Rogers, D. C., DeMott, P. J., Kreidenweis, S. M., & Chen, Y. (1998). Measurements of ice nucleating aerosols during SUCCESS. Geophysical Research Letters, 25(9), 1383–1386. https://doi.org/10.1029/97GL03478

Sullivan, R. C., Guazzotti, S. A., Sodeman, D. A., Tang, Y., Carmichael, G. R., & Prather, K. A. (2007). Mineral dust is a sink for chlorine in the marine boundary layer. Atmospheric Environment, 41(34), 7166–7179. https://doi.org/10.1016/j.atmosenv.2007.05.047

Suski, K. J., Hill, T. C. J., Levin, E. J. T., Miller, A., DeMott, P. J., & Kreidenweis, S. M. (2018). Agricultural harvesting emissions of ice-nucleating particles. Atmospheric Chemistry and Physics, 18(18), 13755–13771. https://doi.org/10.5194/acp-18-13755-2018

Twohy, C. H., McMeeking, G. R., DeMott, P. J., McCluskey, C. S., Hill, T. C. J., Burrows, S. M., … Toohey, D. W. (2016). Abundance of fluorescent biological aerosol particles at temperatures conducive to the formation of mixed-phase and cirrus clouds. Atmospheric Chemistry and Physics, 16(13), 8205–8225. https://doi.org/10.5194/acp-16-8205-2016

Vergara-Temprado, J., Miltenberger, A. K., Furtado, K., Grosvenor, D. P., Shipway, B. J., Hill, A. A., … Carslaw, K. S. (2018). Strong control of Southern Ocean cloud reflectivity by ice-nucleating particles. Proceedings of the National Academy of Sciences, 201721627. https://doi.org/10.1073/pnas.1721627115

Vergara-Temprado, J., Murray, B. J., Wilson, T. W., O'Sullivan, D., Browse, J., Pringle, K. J., … Carslaw, K. S. (2017). Contribution of feldspar and marine organic aerosols to global ice nucleating particle concentrations. Atmospheric Chemistry and Physics, 17(5), 3637–3658. https://doi.org/10.5194/acp-17-3637-2017

Whiteaker, J. R., & Prather, K. a. (2003). Hydroxymethanesulfonate as a tracer for fog processing of individual aerosol particles. Atmospheric Environment, 37, 1033–1043. https://doi.org/10.1016/S1352-2310(02)01029-4

Wilson, T. W., Ladino, L. A., Alpert, P. A., Breckels, M. N., Brooks, I. M., Browse, J., … Murray, B. J. (2015). A marine biogenic source of atmospheric ice-nucleating particles. Nature, 525(7568), 234–238. https://doi.org/10.1038/nature14986

Wright, T. P., Hader, J. D., McMeeking, G. R., & Petters, M. D. (2014a). High relative humidity as a trigger for widespread release of ice nuclei. Aerosol Science and Technology, 48(11), i–v. https://doi.org/10.1080/02786826.2014.968244

Wright, T. P., Hader, J. D., McMeeking, G. R., & Petters, M. D. (2014b). High Relative Humidity as a Trigger for Widespread Release of Ice Nuclei. Aerosol Science and Technology, 48(11), i–v. https://doi.org/10.1080/02786826.2014.968244

Zhang, D., Zang, J., Shi, G., Iwasaka, Y., Matsuki, A., & Trochkine, D. (2003). Mixture state of individual Asian dust particles at a coastal site of Qingdao, China. Atmospheric Environment, 37(28), 3895–3901. https://doi.org/10.1016/S1352-2310(03)00506-5